Title
Stimulated Raman Spectroscopy Characterization of Wavepackets in Solids and on Rapidly Evolving Potential Energy Surfaces

Author
Ellis, Scott Randall

Publication Date
2017

Peer reviewed|Thesis/dissertation

Stimulated Raman Spectroscopy Characterization of Wavepackets in Solids and on Rapidly Evolving Potential Energy Surfaces

by

Scott Randall Ellis

A dissertation submitted in partial satisfaction of the

requirements for the degree of

Doctor of Philosophy

in

Chemistry

in the

Graduate Division

of the

University of California, Berkeley

Committee in charge:

Professor Richard A. Mathies, Chair
Professor Richard J. Saykally
Professor Roger W. Falcone

Fall 2017

Stimulated Raman Spectroscopy Characterization of Wavepackets in Solids and on Rapidly Evolving Potential Energy Surfaces

Abstract

Stimulated Raman Spectroscopy Characterization of Wavepackets in Solids and on Rapidly Evolving Potential Energy Surfaces

by

Scott Randall Ellis

Doctor of Philosophy in Chemistry

University of California, Berkeley

Professor Richard A. Mathies, Chair

The aim of this dissertation is to describe how Raman spectroscopies can be used to track photoinitiated reactivity. Spectroscopy is the primary tool that allows us to measure the states of matter to understand how they interact. We can then use this understanding to build and innovate systems that fulfill human needs. There is a paradox that studying systems that yield the most fundamental understanding (i.e. gas phase low temperature spectroscopy) are often farthest removed from useful applications (e.g. solar panels, transistors etc.). This work explores both practical and fundamental research where the more fundamental results are presented in the early chapters and more application based results appear in later chapters. In short, we have developed a powerful spectroscopic technique, two-dimensional excited state femtosecond stimulated Raman spectroscopy (2D-ES-FSRS). By pushing FSRS to higher time resolution we can measure couplings between Raman active vibrations that were previously undetectable. Despite our experimental capability, the theoretical interpretation of the signal remains a challenge.

Chapter 1 succinctly summarizes spectroscopic signals with focus on vibronic absorption[1], resonance Raman spectroscopy[2, 3], and stimulated Raman[4]. Chapter 2 presents an analysis of the two-dimensional excited state femtosecond stimulated Raman spectrum of the charge transfer complex H_4-TCNQ:1,2,4,5-tetramethylbenzene. These initial results were interpreted in the context of excited state anharmonicity between low and high frequency Raman vibrations. Chapter 3 presents the high time resolution transient absorption and FSRS analysis of another charge transfer complex tetracyanoethylene:1-chloronapthalene and provides theoretical and experimental evidence for the prevalence of the difference bands in resonant FSRS of small symmetric chromophores. Chapter 4 presents a reevaluation of the analysis of H_4-TCNQ:1,2,4,5-tetramethylbenzene from chapter two. Additional excited state data are presented on the fluorinated analogue F_4-TCNQ to confirm vibration reassignments. A formula for the fifth-order 2D-ES-FSRS polarization is derived.

We then apply vibronic analysis to systems with more useful applications. Chapter 5 investigates the resonance Raman intensities and vibronic properties of the promising singlet

fission sensitizing material, crystalline tetracene. The reorganization energy is diminished in the crystalline system relative to the monomer by a factor of seven indicating that the exciton is delocalized onto about seven tetracene molecules. In Chapter 6 examples of the reciprocal relation between polaron binding energy and polaron size are discussed. In Chapter 7 transient absorption spectroscopy is used to help deduce the molecular mechanism of photocatalysis of an allylic 1,3-photorearrangement of 1-cinnamylalkylammonium ions by a super molecular assembly.

The main points of this dissertation can be summarized as follows:

•In efficient optical photochemical reactions in the condensed phase low frequency vibrational coherences and the multimode phase relations thereof often determine the branching ratio between reaction pathways.

•A resonance Raman spectrum projects the action of the lowest order derivative of the resonant excited state potential energy surface(s) at the ground state geometry onto the ground state vibrational coordinates. Through clever use of resonance conditions these projections allow us to determine the coordinates of proximate conical intersections, those that are reached first by the excited state Raman wavepacket.

•The amount of energy that is deposited into vibrational reorganization energy immediately after excitation scales as the reciprocal of the exciton delocalization. The exciton size and therefore the polaron size can sometimes be estimated by a comparison of the magnitude of the Stokes shift.

•The time resolution of the amplitudes observed in a femtosecond stimulated Raman spectrum is the cross correlation of the actinic pump and probe pulses and in principal can be sub-10 fs. The time resolution of a frequency observed in a stimulated Raman spectrum is convolved over the duration of the Raman pump pulse or the vibrational dephasing time where the shorter of the two is effectively limiting.

•A fifth-order 2D-FSRS signal can be resonantly enhanced relative to a cascading third-order FSRS signal if the last four transient dipole-field interactions are many times more intense than the first two. This is observed when an impulsive pump pulse is resonant with a weak ground state absorption while the Raman pump and Stokes probe pulses are resonant with an intense excited state absorption.

To Dr. Joyce Huber and Dr. Randall Ellis

for instilling me with curiosity and a sense of purpose.

Contents

List of Figures

List of Tables

List of Schemes

Acknowledgments

This work was made possible by the scientists who built the blue and red stimulated Raman laser tables. They would be happy to know that the lasers never broke but rather the procurement of flash lamps became prohibitively difficult and expensive; Professor Richard Mathies who gave me the freedom and resolve to study systems that are import to science; Dr. David P. Hoffman and Dr. Daniel Dietze for innumerable assistance; Dr. Mark Creelman and Dr. David T. Valley who instructed me on how to operate the laser tables; Myeongkee Park for sharing his outlooks with me; Kathleen Durkins in the Molecular Graphics Facility for assisting with computations; and the Matt Francis Lab for generous use of the fluorimeter.

The thing that doesn't fit is the thing that's the most interesting: the part that doesn't go according to what you expected.

—Richard P. Feynman

Chapter 1

A Practical Introduction to Vibronic Spectroscopy

1.1 Foreword

It is an exciting time to be studying spectroscopy. In the last few decades scientists have pioneered dozens of new spectroscopic techniques that allow us to measure the states of matter in almost any energy regime.[5–11] The field is also moving towards higher-order spectroscopies which allow us to measure more intricate correlations between states and in some cases shine light on new states that were previously dark. Spectroscopists face a formidable challenge in keeping track of all the different spectroscopic techniques and their applications. Before delving into the many ways each pathway is different it is practical to understand how they are similar and interrelated. The subsequent chapters exploit the interrelatedness between a multitude of spectra to tease out subtle properties and dynamics of the molecular systems.

To this end, this first chapter is written as a handbook intended for beginning graduate student. For more generalized scientists I recommend the time tested textbooks by Harris and by Griffiths.[12, 13] A rigorous and well illustrated textbook on molecular spectroscopy has recently been published by McHale.[3] A more advanced yet highly tractable description of non-linear spectroscopy can be found in the work of Peter Hamm.[14] My colleague Dr. Daniel Dietze recently published a most comprehensive review of femtosecond stimulated Raman spectroscopy (FSRS) with an emphasis on advances in instrumentation and the diverse body of applications to which it has been used.[15] This work does not focus on FSRS instrumentation since it has been covered in great detail in the dissertations of Dr. David Hoffman and Dr. Mark Creelman with regards to the red and blue laser tables respectively.[16, 17]

1.2 Steady-State Spectroscopic Signals

We begin by considering optical processes that occur with incoherent light where there is no phase relationship between the incident photons and no phase relationship between each molecule in the ensemble. We highlight these signals with diagrammatic perturbation theory.[18] Diagrammatic perturbation theory is a powerful theoretical tool that allow us to clearly define and make comparisons between optical pathways. Figure 1.1 presents the double sided Feynman Diagrams (DSF) and wave mixing energy level diagrams (WMEL) of six optical processes that occur under ambient light conditions. Collectively, these pathways are referred to as linear or steady state spectroscopies.

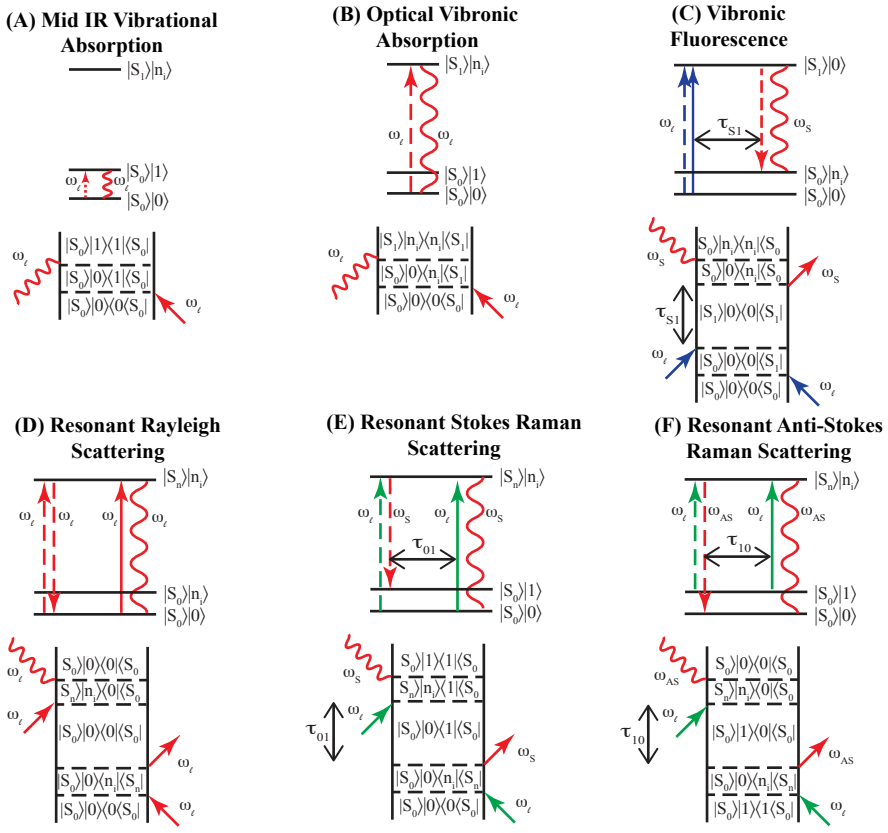

Figure 1.1: Double sided Feynman diagrams and wave mixing energy level diagrams of six optical processes that occur commonly under ambient light. Pathway (A) and (B) are absorption pathways that occur through $\chi^{(1)}$. The latter four pathways (C)-(F) occur through $\chi^{(3)}$. The notation used here $|S_0\rangle$, $|S_1\rangle$ denote the ground and first excited electronic state respectively. The vibrational state within the manifold of a given electronic state is denoted as $|0\rangle$, $|1\rangle$ or $|n_i\rangle$. The action of the incident light field (ω_ℓ), and the Stokes shifted light field (ω_S) on the left and right side of the density matrix are indicated with solid and dashed arrow, respectively. The lifetime of the excited state population is denoted τ_{S_1} and the dephasing time of the vibrational coherence state is labeled τ_{01}.

The WMEL and DSF diagrams represent perturbations on a density matrix by electric fields that impart a polarization into the sample. The density matrix begins in the ground vibrational and electronic state $|S_0\rangle|0\rangle\langle 0|\langle S_0|$. The solid and dashed lines represent the action of the fields on the right and left hand side of the density matrix. Each field has a frequency denoted ω_ℓ for the incident light or a lower frequency ω_S which is Stokes shifted by one or more vibrational frequencies, a pulse envelope (continuous wave, Gaussian, exponential profile), and a wavevector ($\pm k_1$, $\pm k_2$ etc.). The actions of the fields can create a population if the bra and the ket are the same. These correspond to diagonal elements of the density matrix. These elements decay with rate of Γ or a lifetime τ. When the bra is not the same state as the ket this is called a coherence state and corresponds to a off-diagonal density matrix element. Between the action of the fields, a coherence state oscillates in and out of the complex plane under the action of the Hamiltonian with it's transition frequency.

$$\omega_{ba} = \frac{E_b - E_a}{\hbar} \tag{1.1}$$

Coherent states also decay in a process called dephasing. When a field acts upward on the ket side of the density matrix or downward on the bra side, it imparts a wave vector into the polarization of $+k_i$. Conversely, if a field acts downward on the ket or upward on the bra it imparts a wavevector of $-k_i$ into the material polarization. The wavy line in the WMEL diagrams denote the signal that is emitted by the induced polarization. After the emission of a signal, the system must reside in a population state. Having developed a framework with which we can understand spectroscopic pathways we can inspect the steady state spectroscopic signals.

Vibrational Absorption

Pathway (A) is a vibrational absorption that occurs within the manifold of the ground electronic state. Fundamental vibrational transitions occur in the frequency range of 10 - 4200 cm^{-1}. The perturbed density matrix

$$[\rho^{(1)}(t)]_{IR-Abs} = \frac{1}{i\hbar}\int_{-\infty}^{t} \rho H'_{S_0,0,S_0,1}(E_\ell^*, t_1) e^{-i(\omega_{10}+\Gamma_{01})(t-t_1)} dt_1 \tag{1.2}$$

H' is an off diagonal matrix elements that determines the projection of the states by a given time dependent perturbation.

$$H'_{S_0,0,S_1,1}(E_\ell^*, t_1) = -E_\ell^* \langle S_0|\langle 0|\mu|1\rangle|S_0\rangle e^{i\omega_\ell(t_1 - k_1/c)} \tag{1.3}$$

The first order polarization is generated with closure of the density matrix.

$$P^{(1)}(\omega_\ell)_{IR-Abs} = |E_\ell|^2 \Gamma_{01} \left| \frac{\langle S_0|\langle 0|\mu|1\rangle|S_0\rangle}{\omega_\ell - \omega_{10} + i\Gamma_{01}} \right|^2 e^{-i\omega_\ell k_1/c} \delta(\omega - \omega_\ell) \tag{1.4}$$

In an absorption event, the field acts on the density matrix just once. Thus the polarization generates a signal with the same frequency and wavevector as the incident field but with the opposite phase. All spectroscopic signals can be thought of as constructive and destructive interferences with the sample. Since the electronic state is unchanged, the overlap integral of the vibrational wave functions determines the IR absorption cross-section. The operator $\hat{\mu}$ has ungerade parity meaning it is a function that is antisymmetric with respect to inversion. The overlap integral over all space is only non-zero within the harmonic approximation if the vibrational wave functions also have ungerade parity.

$$\langle 0|\mu|1\rangle = \int_{-\infty}^{\infty} \Psi_0 \hat{\mu} \Psi_1 dQ_i \tag{1.5}$$

When a vibration has ungerade parity the dipole changes with respect to a vibrational coordinate at the ground state geometry.

$$\hat{\mu} = \sum_{i=1}^{3N-6} \left(\frac{\partial \mu}{\partial Q_i}\right)_0 Q_i \neq 0. \tag{1.6}$$

The position operator is proportional to the sum of the raising and lowering operators.

$$\hat{X} = \sqrt{\frac{\hbar}{2m\omega}}(a + a^\dagger) \tag{1.7}$$

Therefore IR transitions are only allowed for fundamentals ($\Delta\nu = \pm 1$). When anharmonicity is introduced into the wave functions both the parity and the one quantum selection rule break down and gerade vibrations as well as combination bands, and overtones appear with weak intensity in an IR spectrum.

Electronic and Vibronic Absorption

Pathway (B) describes an absorption from the ground state $|S_0\rangle$ to the lowest excited singlet state $|S_1\rangle$. The transition is allowed if the electronic state changes parity and there is significant orbital overlap between the occupied and unoccupied orbitals from which the transition originates. In additionally, vibronic absorption bands appear blue of the electronic origin transition energy. Since the parity is accounted for by the electron wavefunctions these vibronic absorption bands are built on gerade vibrations. The Born-Oppenheimer approximation says that the electron moves much faster than the vibrations. Therefore, when an electron is excited, the ground state nuclear geometry is projected by it's Frank-Condon factors onto the excited electronic state. The absorption cross section can be written in a sum-over-states picture as:[19]

$$\sigma_A(\omega_\ell) = \frac{4\pi e^2 \omega_\ell |\mu_{S_1S_0}|^2}{3cn\hbar^2} \sum_{n_i} \Gamma_{S_1S_0} \left| \frac{\langle n_i|0\rangle}{\omega_\ell - n_i\omega_{10} - \omega_{S_1S_0} + i\Gamma_{S_1S_0}} \right|^2. \tag{1.8}$$

The parameter e is the elementary charge, n is the material refractive index, ω_ℓ is the incident light frequency. $\omega_{S_1S_0}$, is the electronic origin or zero-zero transition frequency, ω_i is the frequency of the excited state vibration and n_i is the quanta of energy in that coordinate. The value $\mu_{S_1S_0}$ is the elctronic transition dipole. The absorption cross section in 1.8 can be extended to multidimensional potential energy surfaces by taking a product over all Franck-Condon factors and the sum extended all coordinates.

The absorption cross section is proportional to the molar absorptivity as:

$$\sigma_A = 1000ln(10)\frac{\epsilon}{N_A} \tag{1.9}$$

The absorption cross section can be related to the classical oscillator strength as:

$$f = \frac{m_e c^2}{\pi e^2}\int_{band}\sigma_A(\omega)d\omega \tag{1.10}$$

While the absorption cross section and molar absorptivity are defined at each frequency the oscillator strength integrates over a electronic transition band and therefore can be easily be related to theoretical calculations.

Fluorescence

In a fluorescence process three fields act on the density matrix. The first two prepare and excited state population. Kasha's rule says that the excited state population in typical cases relaxes to the lowest energy electronic state ($|S_1\rangle|0\rangle\langle 0|\langle S_1|$) before emission occurs. The emission from the excited state is initiated by coupling to isotropically oriented vacuum fluctuation fields of frequency ω_s which occurs at any time during the excited state lifetime τ_{S_1}. The rate of fluorescence at a given Stokes frequency can be written in a sum-over-states formulation.[19]

$$k_{Em} = \frac{2ne^2|\mu_{S_1S_0}|^2}{3\pi\hbar c^3}\int d\omega_S\omega_S^3\sum_{n_j}\Gamma_{S_1S_0}\left|\frac{\langle n_j|0\rangle}{\omega_S - n_j\omega_j + \omega_{S_1S_0} + i\Gamma}\right|^2 \tag{1.11}$$

The fluorescence wavevector and polarization are aniostropic at early times before molecular or electronic rotation of the transition dipole, $\mu_{S_1S_0}$. A fluorescence anisotropy analysis is given in E.6. After vibrational energy redistribution the transition dipole and the magnitude of the Stokes field are constant. Therefore the excited state lifetime can be approximated from the fluorescence intensity via the Stickler-Berg relation.[20]

$$\tau_{S_1} = \Phi * \tau_{rad} \tag{1.12}$$

$$\tau_{rad} = g_{S_0}/g_{S_1}\frac{1}{8000ln(10)\pi N_A n^2}\frac{\int I_f(\omega_S)\omega_S^{-3}d\omega_S}{\int I_f(\omega_S)d\omega_S\int\epsilon(\omega_\ell)d(ln(\omega_\ell))} \tag{1.13}$$

When the lowest excited state is dipole allowed and in the absence of excited state frequency shifts and changes in the normal coordinate basis set (Duschinsky rotations), the Franck-Condon factors of the absorption and fluorescence cross section are equal. This results in a mirror reflection symmetry of the absorption and fluorescence vibronic lineshapes (see Fig. 5.1). Finally a measure of the reorganization energy can be estimated by the offset between the absorption band and the fluorescence band called the Stokes shift (see D.2).

1.3 Raman Spectroscopy

Pathway (D) corresponds to elastic resonant Rayleigh scattering in which no energy is transferred to the matter. Pathways (E) and (F) are Stokes and anti-Stokes Raman scattering pathways whereby a fraction of the energy from incident monochromatic light is transferred to or from the sample, respectively. The scattered light carries with it new wavelengths at a Raman shifted frequencies from the incident light. In a classical description the off-resonant Raman transition probability is determined by the coordinate dependence of the polarizability $|\partial\alpha/\partial Q|^2$. The resonance Raman transition polarizability is derived in Appendix F. The resonance Raman cross section is:

$$\sigma_R(\omega_\ell) = \frac{8\pi e^4 \omega_S^3 \omega_\ell |\mu_{S_1S_0}|^4}{9c^4} \sum_{n_i} \left| \frac{\Gamma\langle 1|n_j\rangle\langle n_j|0\rangle}{\omega_\ell - n_j\omega_{10} - \omega_{S_1S_0} + i\Gamma} \right|^2 \tag{1.14}$$

Just like spontaneous fluorescence, the Raman transition are coupled by spontaneous vacuum fluctuation fields of frequency ω_S. However unlike fluorescence the Raman process must be coupled from the coherence state which persists for <100 fs in polyatomic molecules in the condensed phase. As such, the spontaneous Raman transition probability is extremely small. While an absorption event may have a cross section of $\sigma_A = 1\text{Å}^2$ an off-resonant Raman event occurs with a cross-section of typically $\sigma_R = 10^{-13}\text{Å}^2$. The fluorescence signal which obscures the Raman signal has a cross section proportional to the the product of the absorption cross section and the fluorescence quantum yield ($\sigma_F = \sigma_A * \Phi_f$) and can vary by many orders of magnitude depending on the lifetime of the excited state population. However, when the incident light is resonant with an electronic transition, the Raman scattering cross section can be is enhanced by four orders of magnitude. A Raman cross section on resonance is typically around $\sigma_{RR} = 10^{-9}\text{Å}^2$.

Raman spectroscopy has many applications. The application of ordinary off-resonant Raman spectroscopy is usually structural identification and as a spectroscopic marker. Resonance Raman spectroscopy (RRS) has far more interesting applications. The resonance enhancement allows for vibrational characterization of chromophore even when they are embedded in a macromolecule such as a protein. Resonance Raman intensities can be used to determine the excited state nuclear geometry.[21, 22] When the absorption is unstructured and contains overlapping electronic states the RRS can be used to identify which electronic states are operative in a given absorption transition and at what energies. When a photo-

chemical reaction occurs on a timescale concurrent with multimode dephasing, RRS can be used to identify the vibrational coordinates along which the reaction occurs.[23–25] Finally on resonance with electronic states that are close in energy, RRS yields information about vibronic coupling between states (see section 1.4).

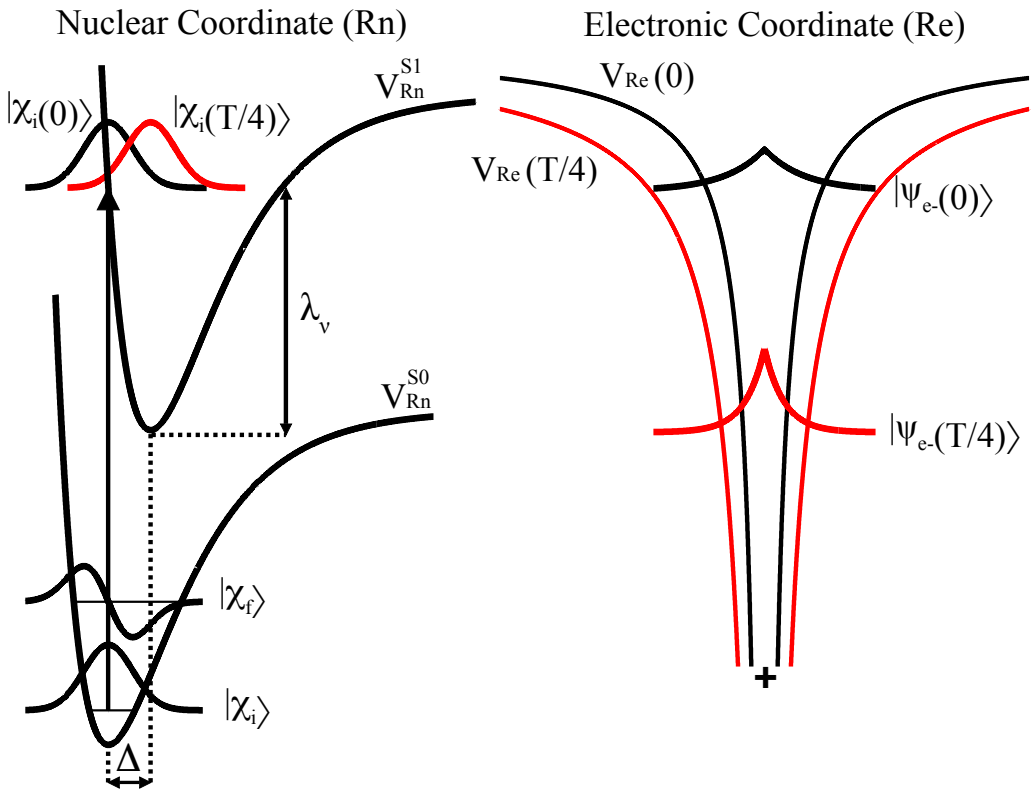

Figure 1.2: Time dependent wavepacket on a one-dimensional displaced anharmonic oscillator. At t = 0 (black) the ground state wave function $|\chi_i\rangle$ is projected on the excited state potential energy surface $V_{Rn}^{S_1}$. After a quarter period $t \approx T/4$ the wavepacket (red) has evolved to a new geometry displaced by Δ. The effect of and the driving force for the nuclear reorganization is a localization of the excited state electronic wave function $|\psi_{e^-}\rangle$ depicted as a radial hydrogenic probability distribution.

Time-Dependent Wavepacket Model

Thus far we have used a sum-over-states description with resonant frequencies for absorption fluorescence and resonance Raman scattering. An equivalent time-dependent picture which exemplifies the interrelatedness of these signals is derived by performing the inverse Fourier transform of the resonance frequency denominator and collecting the time-dependence of the vibrational wave function.[1, 19, 26]

$$\sigma_A = \frac{4\pi\omega_\ell|\mu_{S_1S_0}|^2}{3\hbar cn}\left[\int_0^\infty \langle\chi_i|\chi_i(t)\rangle exp\left[i\left(\omega_\ell - \omega_{S_1S_0} + n_j\omega_j\right)t\right]e^{-\frac{(\Gamma+i\lambda_s/2)|t|}{\hbar}}dt\right]^2 \tag{1.15}$$

$$\sigma_R = \frac{8\pi\omega_S^3\omega_\ell|\mu_{S_1S_0}|^4}{9\hbar^2c^4}\left[\int_0^\infty \langle\chi_f|\chi_i(t)\rangle exp\left[i\left(\omega_\ell - \omega_{S_1S_0} + n_j\omega_j\right)t\right]e^{-\frac{(\Gamma+i\lambda_s/2)|t|}{\hbar}}dt\right]^2 \tag{1.16}$$

$$k_{Em} \propto \omega_S^3\left[\int_0^\infty \langle\chi_w|\chi_w(t)\rangle exp\left[i\left(-\omega_S + \omega_{S_1S_0} + n_w\omega_w\right)t\right]e^{-\frac{(\Gamma+i\lambda_s/2)|t|}{\hbar}}dt\right]^2 \tag{1.17}$$

Where $\mu_{S_1S_0}$ is the electronic transition dipole length, $\omega_{S_1S_0}$ is the electronic origin zero-zero transition frequency, $n_j\omega_j$ and $n_w\omega_w$ are the vibrational frequencies of the initial states usually assumed to be zero. Γ is the damping factor in the time domain equivalent to the homogenous line-width in the frequency domain. λ_s is the solvent relaxation energy. To account for inhomogeneity, the cross-section lineshapes are typically numerically convolved with a Gaussian of standard deviation θ. The absolute cross-sections of the absorption, σ_A, and Raman transitions, σ_R, are largely determined by multidimensional Franck-Condon overlaps of the ground state wavepacket propagating under the excited state Hamiltonian $|\chi_i(t)\rangle = exp(-iH_{et}/\hbar)|\chi_i\rangle$, or, in the case of emission rate, k_{Em}, an excited state wavepacket propagating under the action of the ground state Hamiltonian, $|\chi_w(t)\rangle = exp(-iH_g t/\hbar)|\chi_w\rangle$.[1] In the case where the potential energy surfaces are harmonic with equal ground and excited state vibrational frequencies, the two wavepackets $|\chi_i(t)\rangle$ and $|\chi_w(t)\rangle$, are equivalent and the multidimensional overlaps can be expressed as:[1]

$$\langle\chi_i|\chi_i(t)\rangle = \prod_{j=1}^{N} Exp\left[-\frac{\Delta_j}{\sqrt{2}}[1 - exp(-i\omega_j t)]\right] \tag{1.18}$$

$$\langle\chi_f|\chi_i(t)\rangle = \frac{\Delta_j}{\sqrt{2}}(e^{-i\omega_1} - 1)\prod_{j=1}^{N} Exp\left[-\frac{\Delta_j}{\sqrt{2}}[1 - exp(-i\omega_j t)]\right] \tag{1.19}$$

The Δ_j are the dimensionless displacements of the ground and excited state harmonic potential minima for the vibrational modes with frequencies ω_j. The mode specific reorganization energy, λ_ν, can be calculated as:

$$\lambda_\nu = \frac{\hbar\omega_j\Delta^2}{2} \tag{1.20}$$

A schematic representation of the time-dependent wavepacket model is presented in Figure 1.2 where both the nuclear coordinate and radial electronic wavefunction are considered.

In this depiction the vibration has a period of T. At time zero the wavepacket is projected by its Frank Condon factors onto S_1 electronic potential energy surface in a maximally displaced position and begins to accelerate. The driving force for and the result of the wavepacket motion is the localization of the electron in the newly occupied orbital and the delocalization of the electron in the recently vacated hole orbital. The electron reaches a maximum localization at time delays of $\Delta t = (2n + 1)T/4$ where n is a non-negative integer and then delocalizes reaching a minimum localization at time delays of $\Delta t = (nT)/2$. This can be understood by considering that the nuclear geometry that stabilizes the electronic occupation is that which allows the electron to reside as close the the nuclei as possible. We will see in subsequent chapters that the localization of the electron can effect excited state processes like electron transfer and singlet fission.

1.4 Vibronic Coupling and the Identification of Conical Intersections

Conical intersections are hyperlines in the multidimensional nuclear coordinate and momentum space where there is a degeneracy between electronic potential energy surfaces. Conical intersections are of great importance because they often dictate photochemical and solid state reactivity.[28] The nuclear coordinate/momentum space is vast and highly dimensional. There are most likely multiple conical intersections or else a long conical intersection that twists and winds along the space. Most of this space is unimportant because it will not be sampled by the molecule within the excited state lifetime. Thus the critical parameter is the nuclear geometry of the conical intersection most proximate to the ground state geometry that is sampled first by the ballistic trajectory of the excited state Raman wavepacket. When a conical intersection is reached before the multimode dephasing (<100 fs)[1], the coordinates along which the conical intersection resides are projected down onto the ground state vibrational coordinates and can easily be measured in a resonance Raman spectrum. The effect of a conical intersection has the most pronounce effect when the excitation wavelength is tuned to resonance with a vibronically mixed state, while resonance with the pure electronic states is weak or dipole forbidden.

In the past, scientists preferred to work in a sum-over-states formulation rather than an equivalent time-dependent wavepacket formulation. In the sum-over-state picture the non-adiabatic perturbation of electronic states that describes a conical intersection is called vibronic coupling. The time-dependent wavepacket formulation described above accounts for the Albrecht A term in the sum-over-states picture presented in Appendix G. Vibronic coupling leads to Raman activity though the Albrecht B,C,D terms. The vibration along coordinates Q_m acts as a perturbation of the electronic wave function which is a solution to the unperturbed Hamiltonian H_e^0 at equilibrium nuclear geometry Q_0. In this formulation, the vibration causes the mixing of the electronic state; however, it is equally valid to say that the mixing of electronic states promotes the vibration. The two processes must occur

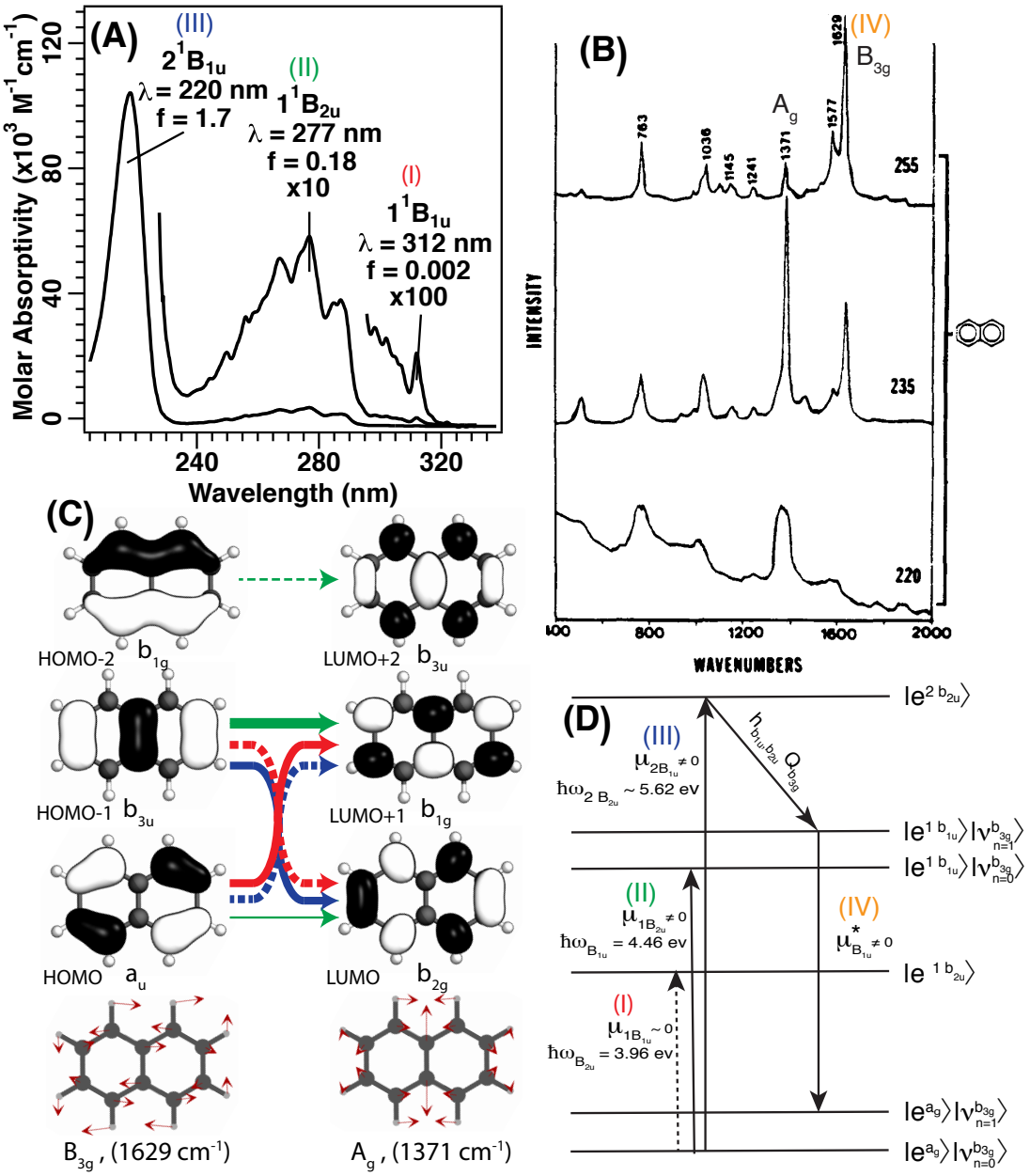

Figure 1.3: (A) Ultraviolet absorption spectrum of naphthalene. The assignment of electronic states is indicated along with the symmetries, energies and oscillator strengths of the transitions. (B) Resonance Raman spectra of $5\times10^{-}5$ M naphthalene in acetonitrile at wavelengths of 255, 235 and 220 nm reproduced with permission from Ref. [27]. Copyright 1984. American Chemical Society. (C) Molecular orbitals that contribute to contribute to the $1B_{1u}$, $1B_{2u}$ and $2B_{1u}$ transitions. The transition amplitudes are indicated by the thickness of the red, green, and blue lineshapes, where dashed arrows indicate negative transition amplitudes. (D) Diagram that indicates how vibronic coupling from the $2B_{1u}$ and $1B_{2u}$ leads to resonance Raman enhancement of the b_{3g} 1629 cm^{-1} vibration.

simultaneously with a positive feed back until the virtual wavepacket reaches a real electronic state or projects down to the ground state.

There are certain resonance conditions with which the effect of vibronic coupling is clearly observed a Raman spectrum. When the excitation light is on resonance with a dipole allowed state the A-term will dominate the Raman signal while the higher order terms are weakly observable. When the resonance with a pure electronic state is weak the higher order terms in the vibronic coupling expansion will dominate. This is the case when the excitation light source is tuned to resonance in-between optically active states that are energetically separated leading B-term scattering.

A clear example of B-term scattering is presented in Figure 1.3 for naphthalene. Figure 1.3(A) presents the lowest energy electronic transitions with symmetries $1B_{1u}$, $1B_{2u}$ and $2B_{1u}$.[29, 30] The $2B_{1u}$ transition is many times more intense than the other two transitions.[31][1] In the resonance Raman spectra of naphthalene (Fig. 1.3(B)) the non-totally symmetric b_{3g} modes gains tremendous intensity both preresonantly and at energies between the $2B_{1u}$ and $1B_{2u}$ states.[27, 32] Non-totally symmetric modes cannot be displaced between a single electronic states as was described by the time-dependent wavepacket model. In b_{3g} modes the lack of rotational symmetry about the short and long molecular axis requires that the initial direction of a distortion along a b_{3g} coordinate be arbitrary. Indeed both the phase of the transition density and the phase of the non-totally symmetric nuclear distortion are arbitrary, but because of the feedback between the two effects, momentum is imparted into the excited state wavepacket even though none of the electronic states are displaced along the b_{3g} coordinate. The b_{3g} vibrations have the correct symmetry to mix the B_{2u} and B_{1u} states and complete the product of irreducable representations to produce the totally symmetric representation necessary to complete a Raman transition: $B_{2u}\times B_{3g}\times B_{1u} = A_g$. In the 255 nm UV resonance Raman spectrum of naphthalene, the high frequency b_{3g} mode at 1629 cm^{-1} is about five times more intense than the totally symmetric a_g ring breathing mode at 1371 cm^{-1}.

Another striking example of vibronic coupling is observed in the electronic states of benzene with symmetries of B_{2u}, B_{1u} and E_{1u} in order of increasing energies (Fig. 1.4(A)). Inspection of the D_{6h} character table reveals that the B_{1u} and B_{2u} transitions are symmetry forbidden while the E_{1u} transition is strongly allowed. The Raman spectrum of benzene (Fig. 1.4(B)) on resonance with the B_{1u} transition at 212.8 nm displays a multitude of overtones and combination bands involving the e_{2g} modes. As before, the non-totally symmetric vibration serves as a perturbation of the upper electronic state; however, because the lower energy electronic states are dipole forbidden if a Raman transition is to be completed a second perturbation is required. Thus scattering occurs through the D-term at 212.8 nm resonance in benzene. We inspect the symmetries of the perturbative operators: $E_{1u}\times E_{2g}\ni B_{1u}$ and $E_{1u}\times E_{2g}\times E_{2g}\times E_{1u}\ni A_{1g}+A_{2g}$ To put this another way a E_{2g} perturbation is the only way to mix the electronic state $|e^{e_{1u}}\rangle$ with $|e^{b_{1u}}\rangle$ with which the 212.8 nm light is resonant. A

[1] Throughout this dissertation we will use the convention that the molecule lies in the YZ plane and the long a molecular axis is defined by Z.

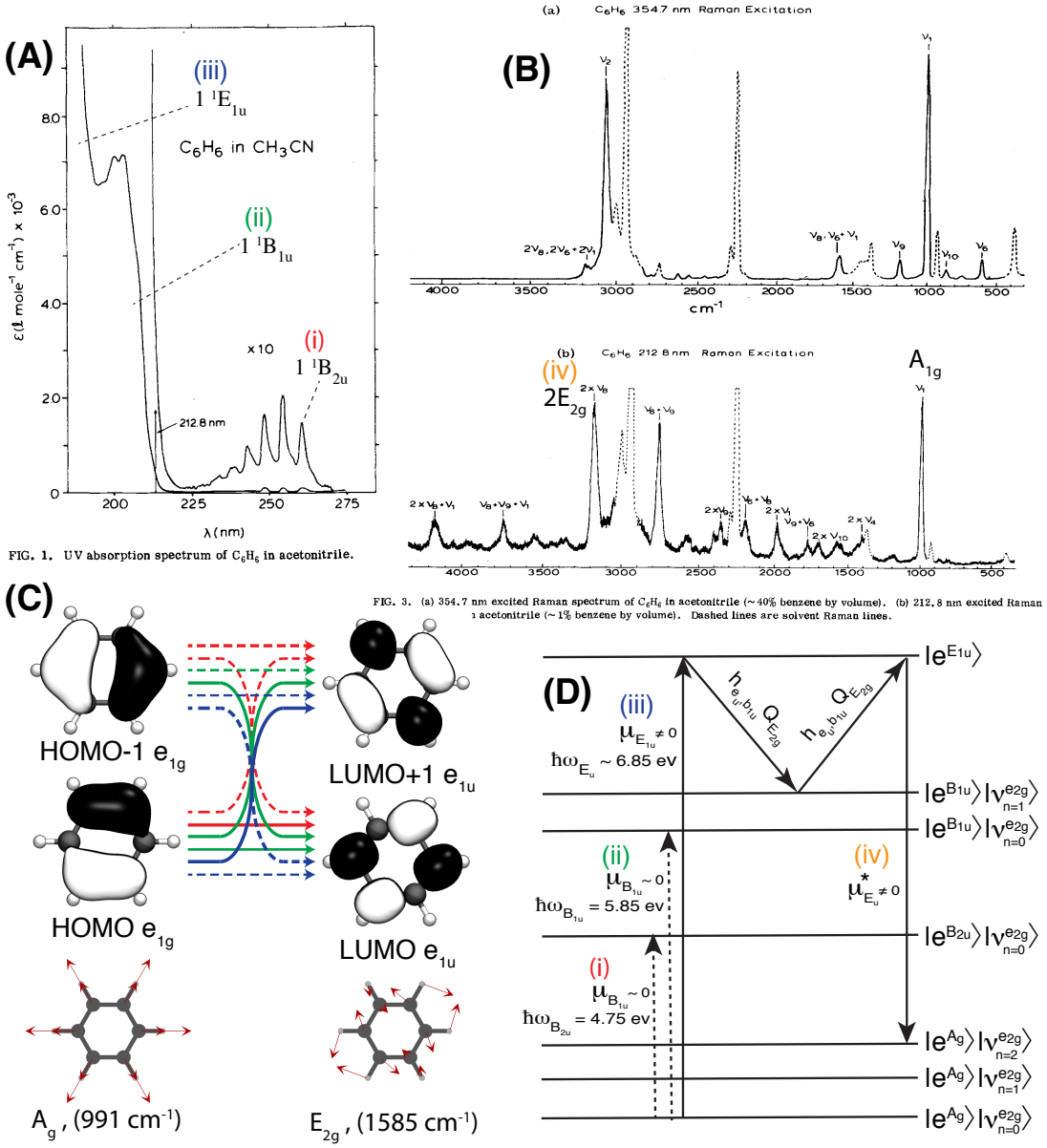

FIG. 1. UV absorption spectrum of C_6H_6 in acetonitrile.

FIG. 3. (a) 354.7 nm excited Raman spectrum of C_6H_6 in acetonitrile (~40% benzene by volume). (b) 212.8 nm excited Raman ı acetonitrile (~1% benzene by volume). Dashed lines are solvent Raman lines.

Figure 1.4: (A) Ultraviolet absorption spectrum of benzene. The assignment of electronic states is indicated along with the symmetries, energies and oscillator strengths of the transitions. (B) Resonance Raman spectra of 4.5 M benzene in acetonitrile at wavelengths of 354.7 and 212.8 nm reproduced with permission from Ref. [21]. Copyright 1981. The Journal of Chemical Physics. (C) Molecular orbitals that contribute to contribute to the B_{1u}, B_{2u} and E_{1u} transitions. The transition amplitudes are indicated by the thickness of the red, green, and blue arrows, where dashed arrows indicate negative transition amplitudes. (D) Diagram that indicates how vibronic coupling of E_{1u} and B_{1u} states lead to resonance Raman enhancement of the even overtones and combinations of the e_{2g} vibrations.

second E_{2g} perturbation is necessary to unmix the states if the transition is to resonantly couple down again through the intense E_{1u} transition dipole. As always, the product of perturbative operators contains the totally symmetric tensors representations.

In summary, the coordinates of a conical intersection can be easily measured via resonance Raman spectroscopy. When vibronic coupling between states occurs on a timescale shorter than multi-mode dephasing, the action of the conical intersection has a pronounced impact on the Raman intensities of non-totally symmetric modes. In the following chapters our work focuses on develop a spectroscopic technique for identifying conical intersections in systems of lower symmetry or when the action of the vibronic coupling is weaker.

1.5 Non-linear Spectroscopy

Figure 1.5 presents twelve non-linear pathways each corresponding to a different technique. We will not go into each pathway at length here but some globalizing points should be made. These pathways are distinct from the steady state pathways in Figure 1.1 as they are only accessible via high photon density light pulses. Some of these pathways are time and frequency domain analogues of the steady state pathways from Figure 1.1; for example, pathways (VI) and (IX) are both analogous to resonance Stokes Raman pathway (E) where the Stokes field (ω_S) is explicitly applied with a defined polarization and wave vector. Although they contain the same information, due to experimental requirements it is usually easier to measure low-frequency Raman vibrations in the time-domain[24, 33] via (VI) and high-frequency Raman vibrations in the frequency domain via (IX).[9, 34] Other non-linear pathways allow us to measure different states of matter or how the states of matter project onto other states in different ways. For example, the sum frequency generation pathway (I) is probes vibrations that are both Raman active and IR active.[35] On the other hand, hyper-Raman pathway (XII) is sensitive to vibrations that are neither Raman active or IR active within the two photon selection rule.[36]

All of the pathways except for (I), (II) and (X) result in signal emission collinear with a probe pulse. Especially, when the wavevector matching isn't employed to separate the unique non-linear pathways the resulting signal will have contributions of many different non-linear pathways and it can be difficult to determine precisely from which states the measured signal originates. Using knowledge of the system and its lower order spectroscopic signals a clever spectroscopist can rule out some pathways and find evidence for one pathway or one class of pathways being dominate. Spectroscopies are most powerful when applied together to form multipoint correlations that can uniquely distinguish between models. Therefore in order to effectively characterize excited state FSRS spectra in subsequent chapters a multitude of lower order spectroscopies are employed and all data are considered holistically.

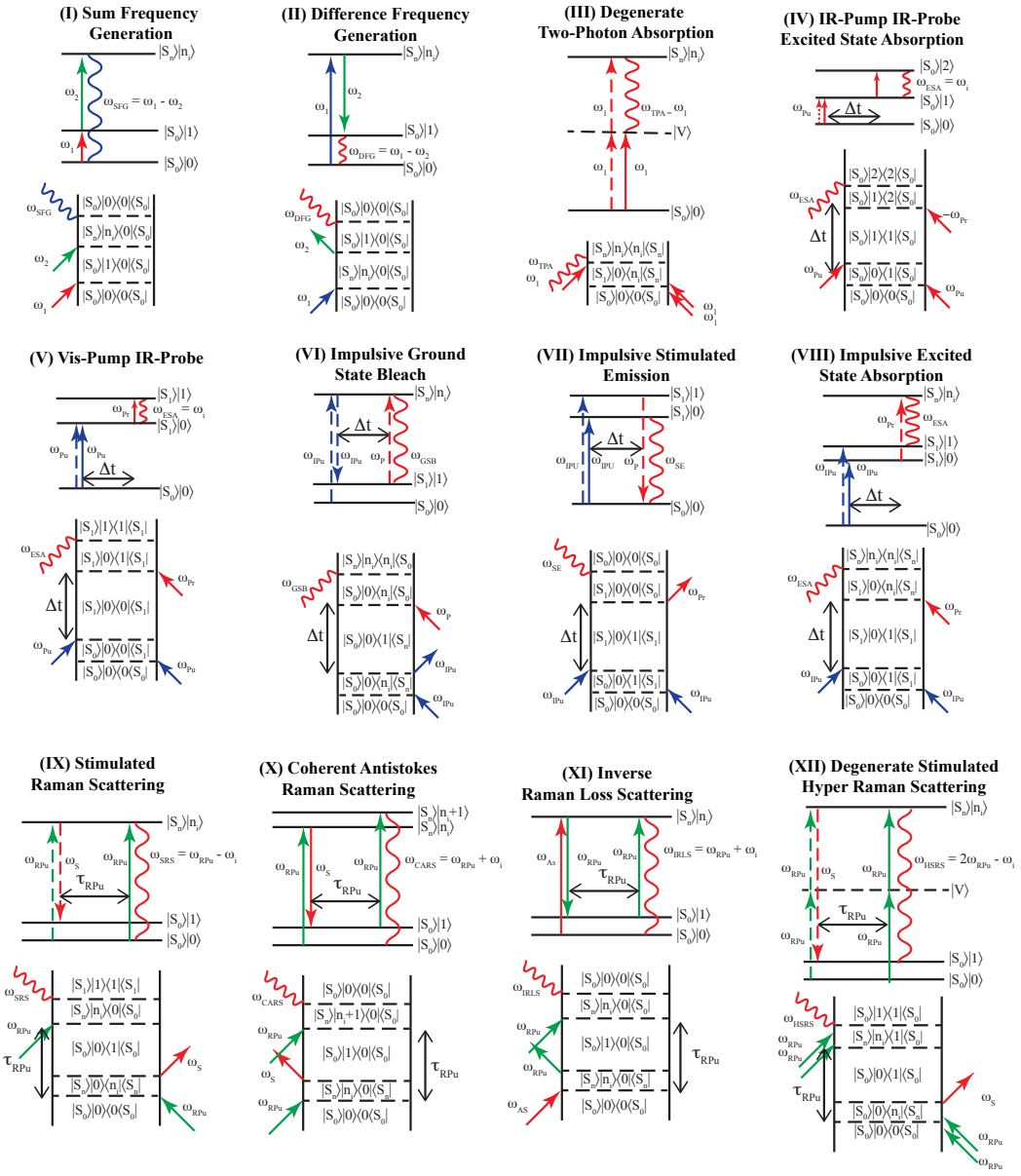

Figure 1.5: Double sided Feynman diagrams and wave mixing energy level diagrams of twelve non-linear pathways. Pathway (A) and (B) are $\chi^{(2)}$ pathways. Pathways (C)-(G) are time domain techniques that occur through $\chi^{(3)}$. The notation used is the same as before. $|S_0\rangle$, $|S_1\rangle$ and $|S_n\rangle$ denote the ground state, first excited electronic state and some arbitrary higher lying electronic state respectively. The vibrational state within the manifold of a given electronic state is denoted as $|0\rangle$, $|1\rangle$ or $|n_i\rangle$. The time delay between the actinic or impulsive pump pulse is is denoted Δt and the duration of the Raman pump pulse or the dephasing time of the vibrational coherence state is labeled τ_{RPu}.

Chapter 2

Characterization of a Conical Intersection in a Charge Transfer Dimer with Two-Dimensional Time Resolved Stimulated Raman Spectroscopy

2.1 Abstract

Photochemical reactions are mediated by conical intersections (CI), which are difficult to directly probe and characterize. To gain insight into CIs, two-dimensional femtosecond stimulated Raman spectroscopy (2D-FSRS) is used to examine a model excited-state charge-transfer (CT) complex consisting of an electron donor, tetramethylbenzene (TMB), and an acceptor, tetracyanoquinodimethane (TCNQ). Following impulsive excitation, the excited-state transient absorption reveals largeamplitude excited-state wave packet motion along low-frequency modes, in particular TCNQ's totally symmetric 323 cm^{-1} CCN bend, which persist for $\sim$ 5 ps. These low frequency coherences modulate the intensity and peak frequencies of the excited-state FSRS vibrational spectra. In particular, large-magnitude oscillations at 323 cm^{-1} are observed in the peak frequency ($\Delta\omega$ = 2 and intensity (ΔOD = 1.5 mOD) of the nontotally symmetric 1271 cm^{-1} C=C rocking mode. The magnitude of these oscillations is analyzed to determine the first-order anharmonic coupling between the high- and lowfrequency degrees of freedom in the excited state. The anharmonic coupling between the totally symmetric 323 cm^{-1} and the nontotally symmetric 1271 cm^{-1} modes is estimated to be in excess of 50 cm^{-1}, strongly suggesting that they are the tuning and coupling modes, respectively, for the CI that connects the CT excited state to the neutral ground state and controls charge recombination internal conversion.

2.2 Introduction

Conical intersections (CIs)[37, 38] are ubiquitous features of photochemical reactions but by their very nature they are difficult to observe and characterize. CIs occur when two Born-Oppenheimer (adiabatic) nuclear potential energy surfaces (PES) are degenerate in energy. At and near this point, the electronic and nuclear degrees of freedom are strongly coupled. Due to the high dimensionality of phase space and the double cone topology of CIs, the system will be effectively trapped on the lower surface once it has "hopped" from the upper one. This efficient, fast, and irreversible internal conversion lies at the heart of many important classes of photochemical reactions such as isomerizations, electron transfer, and proton transfer.[39] Given the importance of CIs for understanding photochemistry, methods that directly characterize the nuclear motions that couple the electronic states are needed.

Charge recombination following photoinduced charge transfer in organic materials is a specific type of reaction where CIs play a major role. The fluorescence of these systems is very weak or undetectable,[26] suggesting that internal conversion to the ground state is fast and efficient. For many materials, such as those used in photovoltaics,[40] this recombination is undesirable. An understanding of which structural changes promote charge separation and impede recombination may allow for the rational design of superior materials.

The model system explored here consists of an electron donor, tetramethylbenzene (TMB), and an electron acceptor, tetracyanoquinodimethane (TCNQ). When combined in solution they form a π-stacked molecular charge transfer (CT) complex; upon absorption of a photon

an electron is transferred from the HOMO of the TMB to the LUMO of the TCNQ. The electron is transferred back to the TMB in a 10 ps process concomitant with internal conversion to the ground state. Charge-transfer complexes have been extensively studied with resonance Raman spectroscopy[26, 41–43] which offers insight into which modes are initially excited and promote the photoinduced charge separation. Most efforts at probing the ultrafast kinetics following Franck-Condon (FC) relaxation have relied on pump-probe electronic spectroscopy,[44–46] but these techniques do not have the energy resolution needed to provide direct evidence as to the precise nuclear rearrangements that mediate charge recombination.

To obtain the structural information necessary to characterize the CI responsible for charge recombination, we have used femtosecond stimulated Raman spectroscopy (FSRS) to study the TMB:TCNQ CT complex. FSRS offers the unique ability to record vibrational structural changes that occur faster than the vibrational dephasing time.[9, 47, 48] FSRS has been applied to a diverse range of systems such as rhodopsin,[9] GFP,[49] azobenzene,[34] charge-transfer systems,[24, 50, 51] and many others.[52–54] In particular, the observation of time-dependent oscillations in the excited-state vibrational frequencies of GFP revealed the importance of low-frequency motions[49] in controlling excited-state reactive dynamics. These observations for GFP prompted us to seek an electron-transfer system with high spectral quality that might enable an even more detailed exploration of this novel observation. The observation of such oscillations would provide "two-dimensional" data that report on the anharmonic coupling between different normal modes. Such 2D experiments have been attempted previously on neat solvents but have been plagued by third-order cascades,[55–57] which we have mitigated in this work (see the Supporting Information (SI) for details).

In this report, we exploit the novel capabilities of 2D-FSRS to measure the anharmonic coupling between the totally symmetric 323 cm^{-1} CCN bending mode and the nontotally symmetric 1271 cm^{-1} C=C rocking mode of the TCNQ in the TMB:TCNQ CT complex. Transient absorption and resonance Raman measurements reveal that the 323 cm^{-1} CCN bending mode is strongly impulsively excited upon electronic excitation and its coherent wave packet motion persists for $\sim$5 ps. Interestingly, these large-amplitude low-frequency motions modulate the intensities and frequencies of the other excited-state Raman peaks, in particular, the intensity and frequency of the 1271 cm^{-1} mode. We focus on the remarkable oscillations in the peak center frequencies, instead of their amplitudes, because the change in frequency is an intensive property. Furthermore, the magnitude of the peak center frequency oscillations can be directly related to the anharmonic coupling between modes using theory developed here and elsewhere.[57–59] CIs are formed by two key modes: a totally symmetric tuning mode that tunes the energy gap between the two surfaces and a nontotally symmetric coupling mode that distorts the nuclear symmetry allowing the different symmetry electronic surfaces to cross. The large anharmonic coupling between the symmetric 323 cm^{-1} and the nontotally symmetric 1271 cm^{-1} modes strongly suggests that their characters dominate the tuning and coupling modes, respectively, defining the CI that mediates charge recombination in the TMB:TCNQ charge-transfer complex.

2.3 Materials and Methods

Sample Preparation

7,7,8,8-Tetracyanoquinodimethane (TCNQ, 98%, TCI America), 1,2,4,5-tetramethylbenzene (TMB, 99%, Sigma-Aldrich), and dichloromethane (DCM, 99.9%, EMD) were used as received. Excess TMB was necessary to solubilize the TCNQ and achieve the desired optical density of 0.15 OD per 1.5 mm and 0.7 OD per 500 μm at 530 nm for the spontaneous Raman and femtosecond stimulated Raman experiments, respectively. For stimulated Raman measurements, the CT complex was formed in a solution of $\sim$1 M TMB and 0.02 M TCNQ and for the spontaneous Raman experiments a solution of 33 mM TMB and 33 mM TCNQ was used. Solutions were filtered through a 0.45 μm Teflon filter. The radical anion of TCNQ was prepared according to the literature procedures.[60] Briefly, TCNQ (1 mmol) and $KI_{(s)}$ (2.5 mmol) were added to 10 mL of acetonitrile (99.9 %, EMD) with stirring for 20 min at room temperature. After drying, the $TCNQ^{-}K^{+}$ salt formed as a purple powder with 88% yield. The product was subsequently recrystallized from acetonitrile. Solutions of the anion in acetonitrile were prepared and spontaneous Raman and steady-state absorption measurements were performed immediately because the radical anion is known to slowly react with oxygen. Acetonitrile was used because the $TCNQ^{-}K^{+}$ salt is not soluble in DCM.

Spontaneous Raman

Samples were circulated through a 1.5 mm capillary tube at 2 m/s using a peristaltic pump and irradiated with 10 mW of 413, 514, and 647 nm light. The parallel polarized scattering was collected in the standard 90^{o} geometry and focused onto the entrance slit of a 2 m Spex 1401 double spectrograph. Spectra were imaged on a liquid nitrogen cooled CCD (Roper Scientific LN/CCD 1100). Spectra were corrected for self-absorption effects and cyclohexane was used to calibrate the Raman shift.

Femtosecond Stimulated Raman

The instrument has been described in detail previously. [61] Briefly, ultrashort pulses are generated by a home-built Kerr lens mode-locked Ti:sapphire oscillator (30 fs, 5.3 nJ/pulse, 91 MHz) that seeds a Ti:sapphire regenerative amplifier (B.M. Industries, Alpha 1000 US, λ_{max} = 790 nm, 70 fs, 0.9 mJ/pulse, 991 Hz) pumped by a Q-switched Nd:YLF (B.M. Industries, 621-D). The fundamental output is split into three pulses. The actinic pump (λ_{max} = 530 nm, 60 fs, 150 nJ/pulse) is generated with a home-built noncollinear optical parametric amplifier (NOPA) and compressed by an F2 prism pair (ThorLabs). A portion of the fundamental is spectrally filtered and temporally shaped by a Fabry-Perot etalon (TecOptics, design A6) forming the narrow band Raman pump pulse (λ_{max} = 795 nm, 100 nJ/pulse, fwhm = 2.8 cm^{-1}). [24] The probe pulse (8 fs, 5 nJ/pulse, λ_{max} = 883 nm) is produced by generating a continuum in a 3 mm thick sapphire plate followed by temporal

compression in a BK7 prism pair. Both the Raman pump and probe pulses are polarized parallel to the table. For short-delay experiments, the actinic pump is polarized parallel to the Raman beams for maximum signal-to-noise while for long delay experiments it is polarized at the magic angle to mitigate the effects of rotational diffusion on the kinetics. All beams are focused into the sample and overlapped both spatially and temporally.

After the sample, the probe pulse is isolated, recollimated, and directed into a spectrograph which disperses the beam onto a fast CCD (Princeton Instruments, PIXIS 100F). A phase locked chopper (Newport, 3501) blocks every other Raman pump pulse, allowing the Raman gain to be calculated, shot-to-shot, as $\ln(probe_{\text{Raman pump on}}/probe_{\text{Raman pump off}})$. The shot-to-shot fluctuations of the probe are less than 0.1% circumventing the need for a reference beam. A computerized delay stage controls the timing between the actinic pump and the Raman pulse pair. Ground-state stimulated Raman spectra are collected by intermittently shuttering the actinic pump. Near-IR transient absorption spectra are calculated as $-\log(probe_{\text{actinic pump on}}/probe_{\text{actinic pump off}})$. All data collection and initial data processing is performed with a custom LabVIEW program.[62]

Data Analysis

Raman spectra have had the solvent contributions removed after appropriate averaging. For the spontaneous data the baselines were removed manually. For the time-resolved stimulated Raman spectra the peaks and baselines were fit simultaneously across the following spectral regions: 750-900, 900-1850, 2130-2910, and 2870-3030 cm^{-1}. A cubic polynomial was used to model the baseline in all regions except for the last one where a constant offset was used. All peaks were modeled with a Lorentzian line shape except for the 1194, 1388, and 1599 cm^{-1} transitions, which were modeled with a dispersive Lorentzian, eq 2.1.

$$I(\nu) = \frac{A + B\nu}{\nu^2 + 1} \tag{2.1}$$

Here A is the intensity of the real part, B is the intensity of the dispersive part, and ν is defined by eq 2.2.

$$\nu = \frac{\omega - \omega_0}{\Gamma/2} \tag{2.2}$$

where ω is the frequency, ω_0 is the frequency of the vibrational transition, and Γ is the full width at half-maximum (fwhm). The baselines in the intermediate spectral regions were removed manually for presentation. To analyze the oscillatory components in the transient absorption and Raman data, the slowly varying, exponential, population dynamics were removed using standard nonlinear curve fitting to the appropriate exponential decay. The residual oscillatory signals were subsequently analyzed using a linear prediction with singular value decomposition (LPSVD) algorithm,[63–65] which converts the normally nonlinear least-squares problem of fitting the data to a sum of damped cosinusoids into a linear one,

ensuring that the global optimum is found. Extracted model parameters were then converted into frequency domain spectra. All data analysis is performed in IGOR Pro using custom-developed procedures.[66]

2.4 Results

Electronic Probing of Charge-Transfer Dynamics

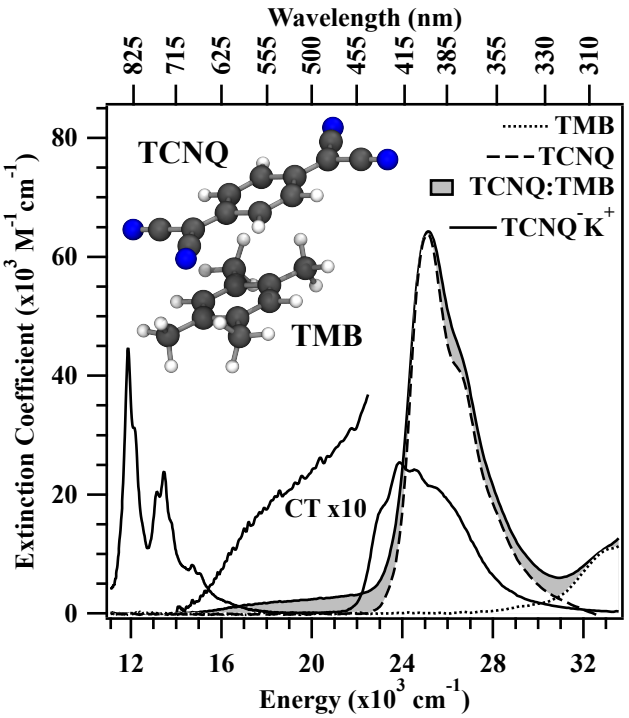

Figure 2.1: Absorption spectra of 7,7,8,8-tetracyanoquinodimethane (TCNQ, dashed, electron acceptor), 1,2,4,5-tetramethylbenzene (TMB, dotted, electron donor), the TMB:TCNQ complex (shaded), and the chemically generated TCNQ anion ($TCNQ^-K^+$, solid) in dichloromethane. The charge-transfer band of the complex has been magnified by a factor of 10 for visualization. The inset shows the calculated C_1 complex structure.

Figure 2.1 presents the ground-state visible absorption spectra of TMB (dotted line), TCNQ (dashed line), the complex (shaded curve), and the chemically generated TCNQ anion (solid line). The TMB:TCNQ complex has a broad, featureless charge-transfer (CT) absorption band in the 600-450 nm region. The CT transition is characterized by an intermolecular excitation from the HOMO of the TMB to the LUMO of the TCNQ. Binding properties of the complex in DCM were determined via the Benesi-Hildebrand method: [67] $K_{eq} = 0.25 \pm 0.03$ M^{-1}, $\epsilon_{530} = 4300 \pm 400$ M^{-1} cm^{-1}. When TCNQ is chemically reduced,

the radical anion $TCNQ^{\bullet -}$ (solid line) shows an intense B_{1u} absorption band[68] with sharp vibronic features: λ_{max} = 843 nm, ϵ_{843} = 44000 M^{-1} cm^{-1}. Vibronic progressions due to the 323, 1271, and 1616 cm^{-1} modes are clearly visible. Two distinct stable intermolecular conformers, one with C_s symmetry (not shown) and the other with C_1 symmetry (inset of Figure 2.1), were identified with DFT calculations using the ωB97x-D functional and the 6-311++G(d,p) basis set.[69] When modeled in vacuum, the C_s conformer is about 80 cm^{-1} more stable than the C_1 conformer. However, time-dependent DFT calculations suggest that the lowest energy singlet transition of the C_s conformer is symmetry forbidden while that of the C_1 conformer has an oscillator strength 20 times greater. In addition, the ground-state dipole moment of the C_1 conformer is predicted to be 3.5-fold that of the C_s conformer suggesting that, with proper inclusion of polar solvation effects, the C_1 conformer should be lower energy. Thus, while both conformers likely exist in the sample at room temperature, it is probable that only the lower symmetry C_1 conformer contributes to the excited-state signal.

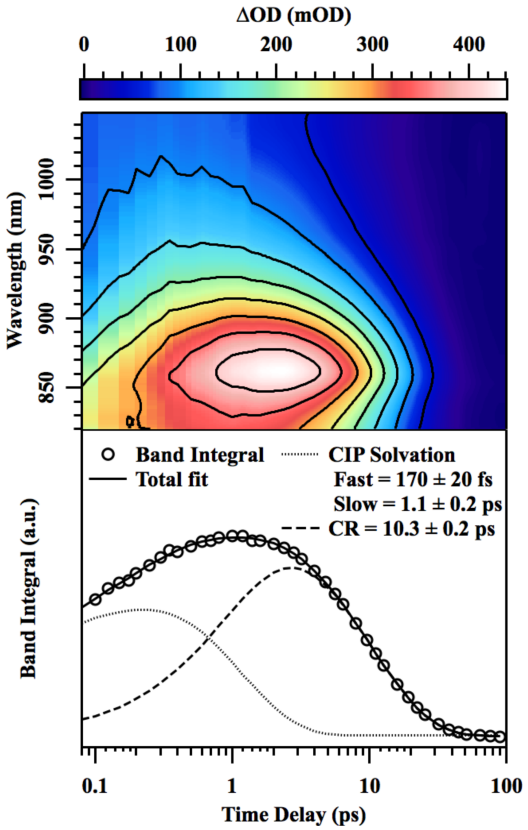

Figure 2.2: (Top) Dispersed transient absorption of the TMB:TCNQ complex from 0.05 to 90 ps in the 830-1450 nm region. The band integral over this region (circles) along with a three-component exponential fit (solid line) is shown at the bottom. The two fast components (dotted line) correspond to polar solvation of the contact ion pair and the slow component (dashed line) is assigned to charge recombination.

The dispersed transient absorption (TA) of the TNCQ:TMB complex over the 830-1450 nm region following excitation at 530 nm is presented at the top of Figure 2.2 with time delays from 50 fs to 90 ps on a logarithmic scale. An increase in absorbance and red shift in the maximum is observed at early times followed by a slight blue shift and a slow decay at longer times. The transient spectra are peaked around ∼860 nm, and the bandwidth and position are consistent with the ground-state radical anion absorption albeit broadened and shifted to longer wavelengths. To simplify the subsequent analysis and remove the effect of spectral shifts, the TA was integrated over the entire probe window; the results are presented at the bottom of Figure 2.2 as open circles. The band integral was best modeled by a three-component exponential convoluted with a Gaussian instrument response function (IRF), solid line. Two of the components correspond to intensity increases and had time constants of 170 ± 20 fs and 1.1 ± 0.2 ps, respectively. Both decay constants quantitatively match the reported solvation times of coumarin 153 in DCM: 144 fs and 1.04 ps. [70] Due to this correspondence, these dynamics have been assigned to solvation of the nascent contact ion pair (CIP). The longest measured decay component has a time constant of 10.3 ± 0.2 ps and corresponds to the complete disappearance of the TA signal due to back electron transfer (i.e., charge recombination).

Figure 2.3a presents the dispersed TA of the complex in the 870-930 nm region following excitation at 530 nm from -500 to 2500 fs with 20 fs steps. Oscillations visible in the contour lines are due to coherent wave packet motion in the excited state. Oscillations due to impulsively excited ground-state wave packets can be ruled out due to the large energy separation between the ground- and excited-state absorption bands. To analyze these oscillations, the TA was integrated over the region of interest and the resulting band integral is presented in Figure 2.3b as the gray line. The 870-930 nm region was chosen because this is where the slopes of the transient spectra are steepest, which has been shown, both theoretically and experimentally, to give the highest signal-to-noise.[71] To extract the oscillatory signal, the slowly varying population decay was modeled by a three-component exponential decay convoluted with a Gaussian IRF, shown as the black line, and removed. The extracted oscillatory signal is shown as a gray line and the LPSVD[63–65] fit is shown as the black line in Figure 2.3c. The residuals between the data and fit are shown as dots offset below.

Before conversion to the frequency domain, the magnitudes of the oscillatory signal are corrected for damping due to the finite duration of the pump and probe. Equation 2.3 displays the functional form of a damped oscillatory signal obtained in the limit of delta function pulses. eq 2.3

$$S(t) = e^{-t/\tau} \cos(\omega t)\theta(t) \tag{2.3}$$

where τ is the dephasing time, ω is the angular frequency of oscillation, Θ is the Heaviside step function, and t is the delay between the actinic pump and the probe. To model the effect of nondelta function pulses, it is necessary to convolve eq 2.3 with the Gaussian IRF. While there is no closed form solution for this convolution, one does exist for an undamped

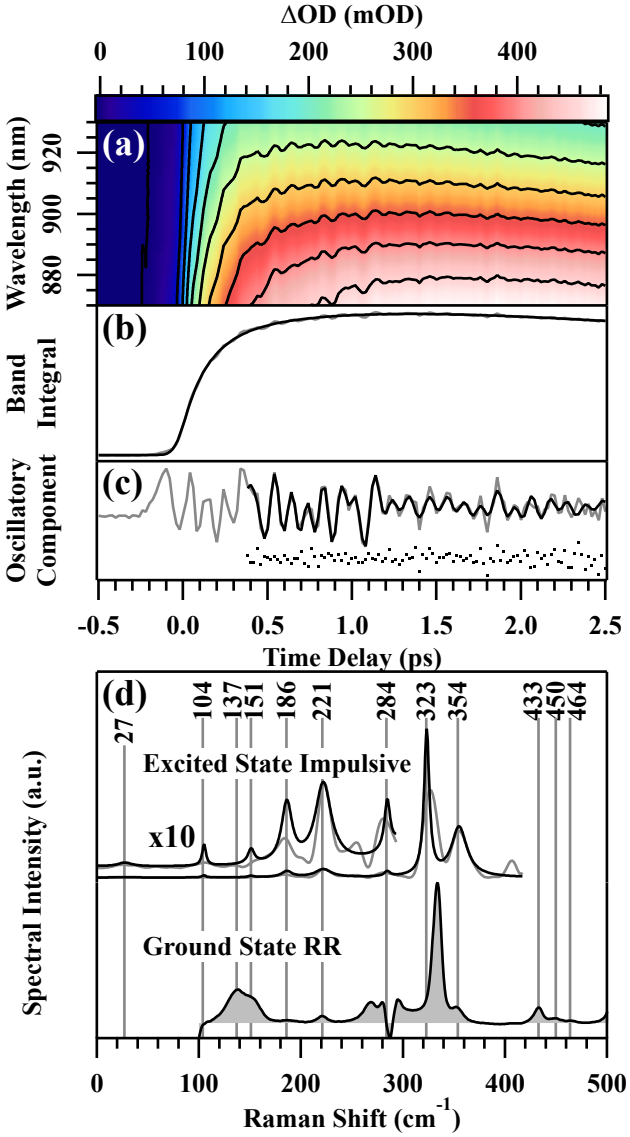

Figure 2.3: (a) Dispersed transient absorption of the TMB:TCNQ complex from âĹŠ0.5 to 2.5 ps with 20 fs steps over the 870-930 nm region. (b) The integral of the TA over the region shown in (a) (gray line) along with a fit to a three-component exponential decay convoluted with a Gaussian instrument response function (black line). (c) The oscillatory component of (b) (gray line) is fit to eight exponentially decaying sinusoids using the LPSVD algorithm (black line). The residuals of the fit are shown as dots. (d) Frequency domain reconstruction of the LPSVD parameters (black line) and an FFT analysis of the oscillations in (c) (gray line) along with the low-frequency resonance Raman spectrum of the complex acquired with 514 nm excitation (shaded). Magnitudes of the time domain data have been corrected for the finite duration of the pump and probe using eq 2.4 as described in the text, and data below 300 cm^{-1} has been magnified by a factor of 10 for clarity. Frequencies of the LPSVD model are indicated.

sinusoid convoluted with a Gaussian; in this case the oscillatory magnitude is damped by the factor shown in eq 2.4

$$Exp\left(-\frac{1}{2}\sigma^2\omega^2\right) \tag{2.4}$$

Here σ is the standard deviation of the Gaussian IRF and ω is the angular frequency of the sinusoid. Numerical convolutions of eq 2.3 with a Gaussian (see SI) show a reduction in magnitude identical to eq 2.4 as long as the delays chosen are longer than the full width at half-maximum (fwhm) of the Gaussian function. Therefore, eq 2.4 was used to scale all LPSVD magnitudes and FFT spectra before presentation. Figure 2.3d presents the frequency domain representation of the LPSVD parameters (black line), an FFT of the raw data (gray line), and the low-frequency resonance Raman (RR) spectrum of the TMB:TCNQ complex ground state taken with Raman excitation at 514 nm (shaded). Both of the frequency domain spectra have been scaled to correct for the effects of finite pulse widths, as described above. The LPSVD and FFT agree well with one another. A total of eight peaks are observed below 500 cm^{-1} in the RR and oscillatory TA data. Normal modes are assigned with the aid of DFT calculations and the literature[72–74] and complete descriptions, with respect to the axes and carbon numbering in Figure 2.4, can be found in the SI. One mode is highlighted here: the 323 (333) cm^{-1} mode, which can be described as an A_g CCN in-plane bend combined with $C_{2,4}$=$C_{3,5}$ stretches (see the movies in the SI). The excited-state impulsive and the ground-state RR spectra are similar except for the slight shift in the 323 cm^{-1} mode and the large shift of the 137 cm^{-1} mode in the ground state to 104 cm^{-1} in the excited state.

Raman Spectroscopy of the Charge-Transfer Excited State

Figure 2.4 presents the ground-state RR spectra of (a) TMB, (b) the complex, (c) TCNQ, and (d) the TCNQ anion along with (e) the excited-state stimulated Raman spectrum of the complex 2 ps after excitation. Axes and carbon numbering used for mode characterizations are depicted in the upper right corner. Spectra of the anion and the excited state display a multitude of overtones and combination bands. Moreover, the striking similarity between spectra (d) and (e)—all frequencies are within 10 cm^{-1} of one another-indicates that the excited state of the complex can be accurately described as a transient biradical species, i.e., $TCNQ^{\bullet-}TMB^{\bullet+}$. No modes of the $TMB^{\bullet+}$ cation are observed in spectrum (e) because the Raman pump at 795 nm is strongly resonant with the $S_1 \rightarrow S_2$ excited-state absorption band that is localized on TCNQ. While the spectra of the TCNQ monomer and excited-state complex are similar, there is a consistent blue shift in modes that involve the benzene ring—at 722, 976, and 1616 cm^{-1}—and a large red shift in the 1388 cm^{-1} C_2=C_3 stretching mode upon reduction of the TNCQ. This observation is consistent with an extra electron being placed in the $\pi*$ antibonding orbital, which has a distinct node centered on the C_2=C_3 bond. In Figure 2.4 there are eight fundamental vibrations above 500 cm^{-1} in the excited-state spectrum which have A_g symmetry and are localized on the TCNQ. The 2198 cm^{-1} mode corresponds to a symmetric stretch of all CN groups. The 1616 cm^{-1} mode is a C_4=C_5

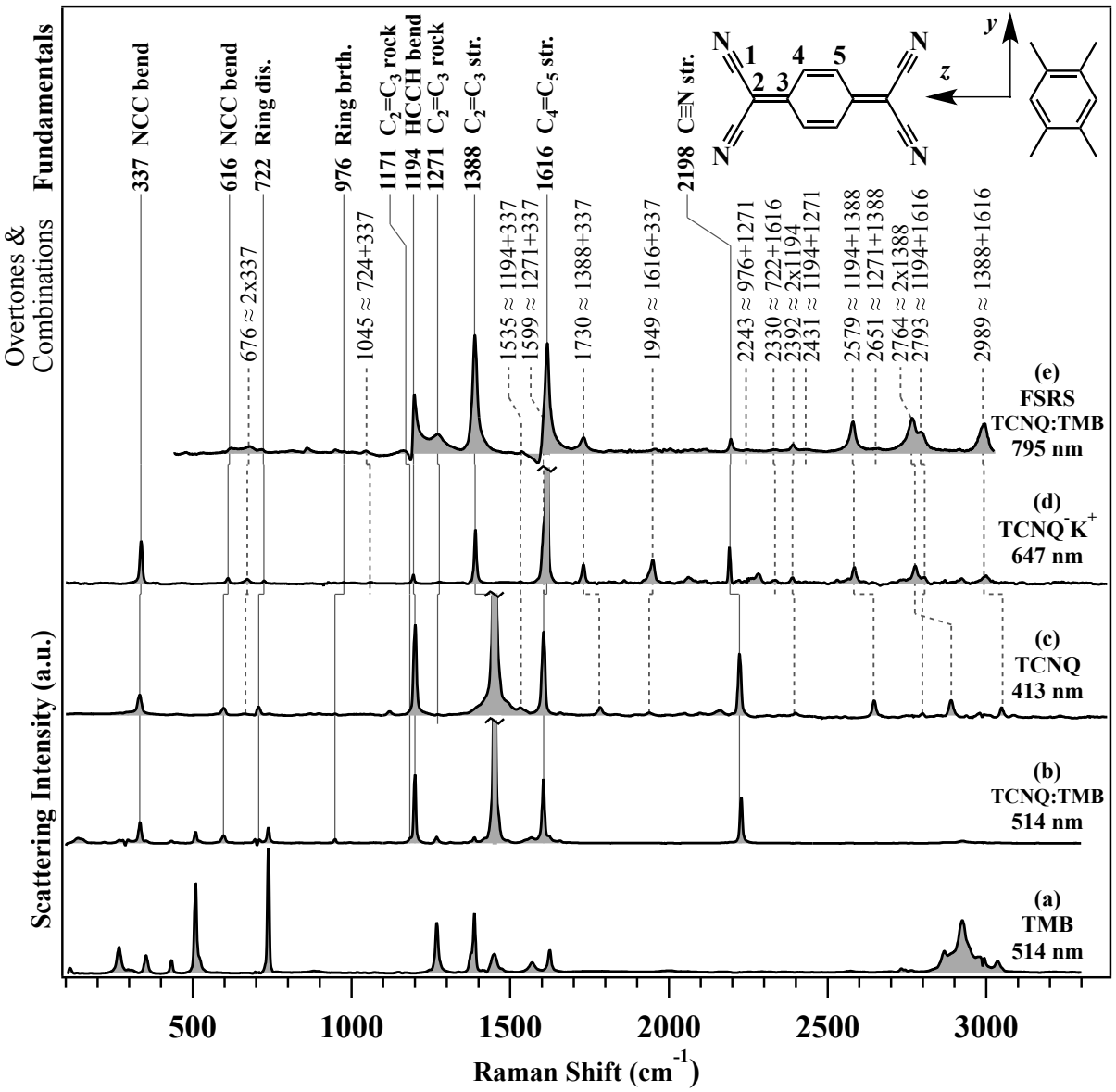

Figure 2.4: Spontaneous Raman spectra of (a) TMB with excitation at 514 nm, (b) the TMB:TCNQ charge-transfer complex with excitation at 514 nm, (c) TCNQ with excitation at 405 nm, and (d) the chemically generated TCNQ anion ($TCNQ^{-}K^{+}$) with excitation at 647 nm. (e) Excited-state stimulated Raman spectrum of the TMB:TCNQ complex 2 ps after actinic excitation at 530 nm with Raman probing at 795 nm. Fundamental positions are marked by solid lines and overtone and combination bands are marked by dashed lines. Large peaks in (b), (c), and (d) have been truncated, as indicated, in order to make the weaker signals visible. Frequencies and assignments are listed at the top along with the structures of the monomers, the carbon numbering, and the axes used to characterize the normal modes.

stretch on the benzene ring. The 1388 cm^{-1} mode is a C_2=C_3 stretching motion. The 1271 cm^{-1} motion is of B_{3g} symmetry and is an in-phase hydrogen rock coupled with C_2=C_3 rocking motion in which the $C_1C_2C_3$ and $C_2C_3C_4$ angles are alternately enlarged and compressed. The 1194 cm^{-1} mode is an in-phase hydrogen rock. The 1171 cm^{-1} mode is similar to the 1271 cm^{-1} mode but the carbon and hydrogen motions are more strongly coupled. The 976 cm^{-1} peak corresponds to a ring breathing coupled to a CCN bending motion. The 722 cm^{-1} mode is a ring compression motion along the y axis. The 616 cm^{-1} motion is a localized CCN bend.

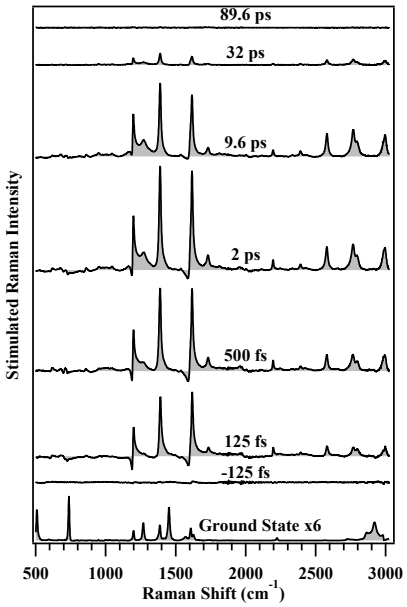

Figure 2.5: Stimulated Raman spectra of the TMB:TCNQ complex at selected time delays after excitation at 530 nm. Signals due to the solvent and residual ground state have been removed and the background has been corrected. The peak amplitudes increase at early times and then decrease in tandem with the TA, see Figure S2 in the SI. A magnified ground-state spectrum is shown at the bottom for reference and contains large contributions from the TMB monomer. Oscillatory Excited-State Raman Signals

Figure 2.5 presents excited-state stimulated Raman spectra of the complex for selected time delays after actinic excitation along with a magnified ground-state spectrum for reference. At each time delay the transient Raman spectrum was fit to a sum of Lorentzians and a baseline function. The peaks at 1194, 1388, and 1599 cm^{-1} are not purely positive and are modeled by a dispersive Lorentzian line shape. Dispersive line shapes have been observed in FSRS before[54, 75] and are due to resonant transitions through nonlinear pathways other than RRS(I).[54, 76, 77] For long delays, the kinetics of the fitted amplitudes strongly mirror those of the TA, see Figure S2 in the SI. For the short delay data, taken with 20 fs time steps, the extracted center frequencies and amplitudes reveal more interesting dynamics.

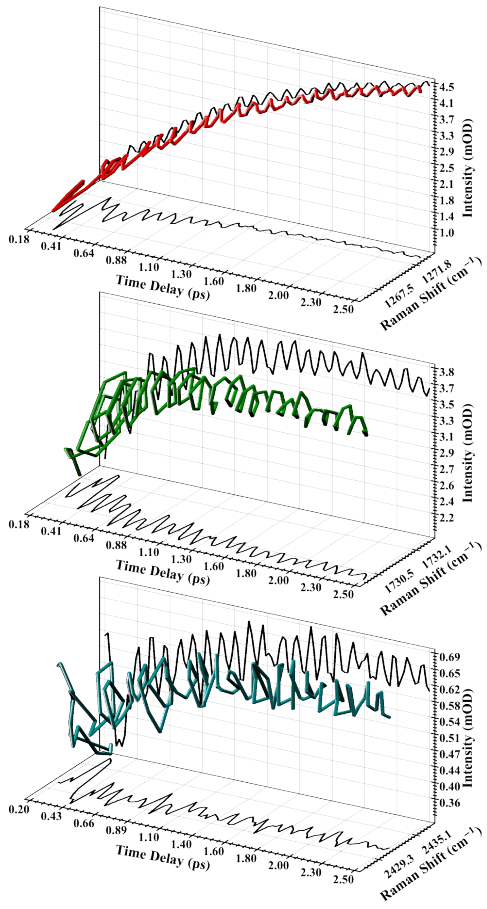

Figure 2.6: Intensity-frequency trajectories for three representative peaks; 1271 (top), 1730 (middle), and 2431 cm^{-1} (bottom). The amplitudes and peak positions are on the back and bottom axes, respectively. Oscillations in both amplitude and peak position are visible and their phase and frequency relation results in a corkscrew-like trajectory.

Figure 2.6 presents three representative intensity-frequency trajectories for the 1271 (top), 1730 (middle), and 2431 (bottom) cm^{-1} modes. Data are displayed as colored tubes, and projections of the peak position and the peak amplitude are shown on the bottom and back, respectively. High signal-to-noise oscillations are visible in both components for all three peaks with magnitudes of 2 cm^{-1} and 1.5 mOD for the 1271 cm^{-1} mode; 0.75 cm^{-1} and 2.1 mOD for the 1730 cm^{-1} mode; and 5 cm^{-1} and 0.05 mOD for the 2431 cm^{-1} mode. Note that all three trajectories evolve in a corkscrew pattern indicating that the peak amplitudes and centers both oscillate with the same frequencies and have a fixed $\pi/2$ phase relationship suggesting that they are modulated by the same underlying phenomenon. Stimulated Raman intensities may depend on many different parameters including the shape of all potential energy surfaces (PES) involved in the Raman process.(47) On the other hand, peak frequencies are the direct measure of the curvature of the PES of interest. For this reason,

the rest of the discussion will focus on the temporal oscillations of the peak frequencies.

Analysis of the oscillatory peak frequencies followed the framework outlined for the oscillatory TA signal. First, the slowly varying population dynamics were removed after which the isolated oscillatory signal was modeled using the LPSVD algorithm. The data analysis steps for the 1271 cm^{-1} mode are demonstrated in Figure 2.7 (figures for the 1730 and 2431 cm^{-1} modes are presented in the SI). Again, the LPSVD and FFT have excellent agreement and oscillatory components due to the 104, 151, 323, and 354 cm^{-1} modes are observed.

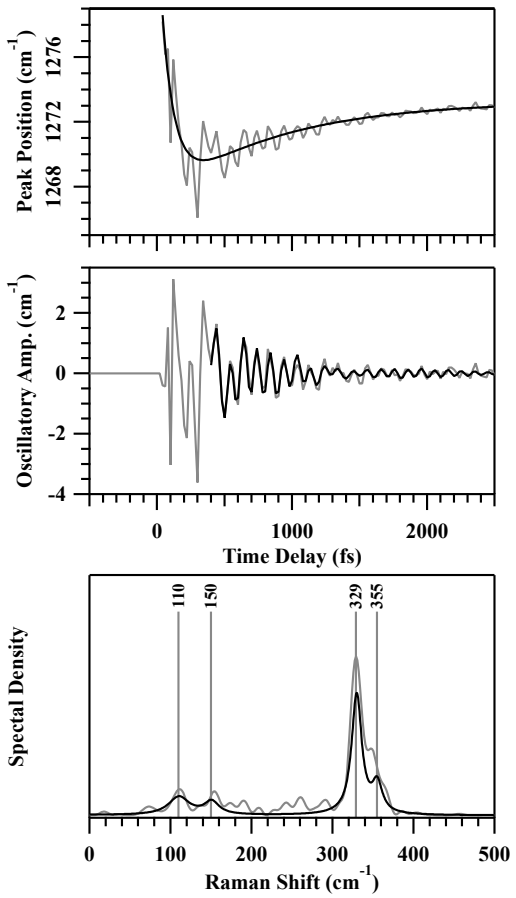

Figure 2.7: Extracted center frequency of the 1271 cm^{-1} peak as a function of time (top, gray line) along with a fit to an exponential decay (black line). The residual oscillatory component is shown in the middle (gray line) along with an LPSVD fit to four exponentially decaying cosinusoids (black line). A frequency domain reconstruction of the extracted model parameters is shown below (black line) along with an FFT analysis of the oscillatory component (gray line). These data have not been scaled by eq 2.4 or 2.9.

Figure 2.8 presents the extracted oscillatory parameters for all the peaks in the transient Raman spectra of the TMB:TCNQ complex. Each circle represents a detected oscillatory component and its abscissa, ordinate, and size represent the frequency of oscillation, the

position of the excited-state peak, and the relative intrinsic magnitude of the oscillation with respect to the average center frequency, respectively. The excited-state impulsive Raman spectrum from Figure 2.3d is shown along with vertical gray lines marking the peak centers for reference. The ordinates of the circles are fixed by definition to the peak positions of the transient Raman spectrum obtained 2 ps after excitation, which is shown at the right along with horizontal gray lines marking the peak positions, for reference.

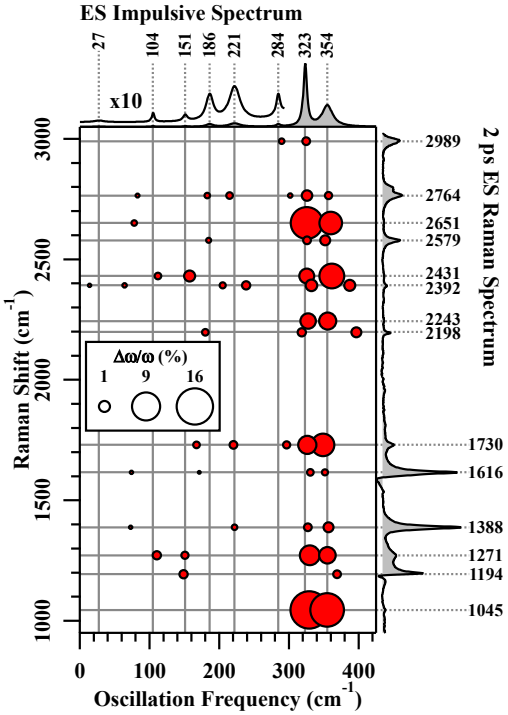

Figure 2.8: Correlations between the oscillatory peak center frequencies measured with time-resolved stimulated Raman and the impulsively excited low-frequency vibrations measured by transient absorption of the TMB:TCNQ complex. Each circle's ordinate is locked to the center frequencies of the peaks in the excited-state complex spectrum (2 ps after excitation). The abscissas are the measured frequency with which the peak centers oscillate and are not determined by the excited-state impulsive data. The LPSVD reconstruction of the coherent TA oscillations is shown at the top. The areas of the circles indicate the relative magnitude of the peak center frequency oscillations with respect to the average FSRS peak position. The peak center frequency was examined as opposed to the peak amplitude because it is an intensive property. These magnitudes have been corrected for the effects of the finite durations of the actinic pump and Raman probe and for the effect of averaging over the effective vibrational dephasing time. Note that the 1271 cm^{-1} mode and its overtones and combinations and those of the 323 cm^{-1} mode have large oscillatory magnitudes on the order of 5% (50 cm^{-1}).

The intrinsic magnitudes of the FSRS peak center frequency oscillations, shown in Figure 2.8, are significantly larger than the observed magnitudes, shown in Figure 2.7, because of the

effect of finite pulse durations (discussed above) and averaging over the vibrational coherence dephasing time.[1] The damping due to the latter effect can be corrected for by calculating the average value of the instantaneous frequency as a function of actinic pump-Raman probe delay. The instantaneous frequency (defined as the derivative of the phase) of an oscillating high-frequency mode modulated by a low-frequency one can be modeled as:

$$\frac{\partial \phi}{\partial t} = \omega(t) = \omega_{h,0} + Ae^{-t/\tau_{\mathrm{CO}}} \cos(\omega t) \tag{2.5}$$

where ω_{h},0 is the average center frequency of the high-energy FSRS peak, ω_{l} is the frequency of the low-energy normal mode causing the modulation, A is the intrinsic magnitude of the modulation, and τ_{co} is the dephasing time of the impulsively excited low-frequency vibrational coherence. In the limit of delta function actinic and probe pulses, the dephasing of the Raman pump induced vibrational coherence can be modeled as

$$W(t) = e^{-t/\tau_{peak}} \tag{2.6}$$

where τ_{peak} is the dephasing time due to the Raman pump pulse shape and the intrinsic decay of the molecular system. With eqs 2.5 and 2.6 the average change in frequency of the high-frequency vibration becomes

$$\begin{aligned} \langle \Delta\omega(t) \rangle (\Delta t) &= \frac{\int_0^\infty (\omega(t+\Delta t) - \omega_{h,0}) W(t) dt}{\int_0^\infty W(t) dt} \\ &= \frac{Ae^{-t/\tau_{\mathrm{CO}}} \cos(\omega_l \Delta t - \alpha)}{\sqrt{(\omega_l \tau_{peak})^2 + \left(\frac{\tau_{peak}}{\tau_{\mathrm{CO}}} + 1\right)^2}} \end{aligned} \tag{2.7}$$

where Δt is the time delay between the actinic pump and the Raman pulse pair, t is the time between the initial and final field couplings which generate the vibrational coherence,[52] and α is a phase shift defined in eq 2.8.

$$\alpha = \arctan\left(\frac{-\omega_l}{\frac{1}{\tau_{peak}} - \frac{1}{\tau_{\mathrm{CO}}}}\right) \tag{2.8}$$

Equation 2.7 demonstrates that the FSRS center peak frequency will oscillate at frequency ω_{l} as a function of Δt but that the observed magnitude of modulation will be strongly damped and the observed phase will be different than the intrinsic phase. The intrinsic modulation magnitude may be obtained from experimentally observed parameters using eq 2.9.

$$A = A_{obs} \sqrt{\left(\frac{2\nu_l}{\Gamma_{peak}}\right)^2 + \left(\frac{\Gamma_{\mathrm{CO}}}{\Gamma_{\mathrm{peak}}} + 1\right)^2} \tag{2.9}$$

[1] The observed vibrational coherence time is the convolution of the intrinsic molecular dephasing time and decay time of the Raman pump. In the frequency domain these linewidths are additive.

Here A_{obs} is the observed modulation magnitude, and we have replaced the dephasing times by the corresponding line widths ($\pi\Gamma = 1/\tau$) and the angular frequency with the regular frequency. All four of these parameters are readily available from the experiment and eq 2.9 has been used to scale the magnitude data presented in Figure 2.8; Figure S5 in the SI presents the raw data in the same format as Figure 2.8.

The 2D-FSRS plot in Figure 2.8 provides a direct measure of the large anharmonic couplings, some in excess of 100 cm^{-1}, between the low- and high-frequency degrees of freedom in the excited-state CIP after the charge-transfer reaction. In general, there is excellent agreement between the frequencies of the FSRS peak center oscillations and the TA oscillations. In particular, the 1271 cm^{-1} C_2=C_3 rocking mode is the only visible fundamental that displays significant (>50 cm^{-1}) couplings to the 323 and 355 cm^{-1} modes, which are a CCN bend and an out-of-plane deformation of the TMB, respectively. As a consequence, combination tones of the 1271 cm^{-1} mode (the 2243, 2431, and 2651 cm^{-1} modes) also have large (>50 cm^{-1}) magnitude oscillations. In addition, combination tones of the 323 cm^{-1} mode (the 1045 and 1730 cm^{-1} modes) are strongly modulated, which indirectly indicates a strong self-modulation of the 323 cm^{-1} mode. Previous results[53, 54] have indicated that low-frequency modes are often self-modulated. In addition, the 1271 cm^{-1} mode is the only observable fundamental to have detectable coupling to the 105 or 151 cm^{-1} modes, both of which involve deformations of the CCN angle. Interestingly, the weaker and broader Raman modes ($\Gamma > 40$ cm^{-1}) tend to have the largest couplings, with estimated intrinsic oscillatory magnitudes in excess of 50 cm^{-1}, to the low-frequency degrees of freedom while the totally symmetric modes that are most Franck-Condon active (and have the most energy deposited into them during electronic excitation) have the smallest.

2.5 Discussion

Femtosecond stimulated Raman has been used to shed new light on the excited-state dynamics, PES shape, and charge recombination mechanism of the TMB:TCNQ charge-transfer complex. Based on a comparison of the Raman spectra, the excited-state structure of the acceptor, TCNQ, is identical to that of the chemically prepared radical anion and is formed almost immediately following photoexcitation. Solvent reorganization stabilizes the nascent CIP, and charge recombination occurs in ∼10 ps. At times earlier than 5 ps, while the excited-state wave packet is still coherent and well-defined, oscillations in both the transient absorption and the stimulated Raman frequencies and intensities corresponding to low-frequency TCNQ and interdimer motions are observed. We have determined that the oscillations in the excited-state Raman peak frequencies are the signature of a fifth-order process meaning that they are directly related to anharmonic couplings between the low- and high-frequency modes; see SI for more information. Using this implementation of 2D-FSRS, we have characterized many cross couplings, some of which have intrinsic magnitudes that are estimated to be in excess of 50 cm^{-1}. These anharmonic couplings are of great

value for understanding the mechanism of charge recombination (i.e., internal conversion) as discussed in more detail below.

Resonance Raman intensity data indicates which nuclear motions are strongly coupled to the initial photoinduced charge separation process.[26, 41, 42] Figure 2.4 shows that the 323 cm^{-1} CCN bending, 1194 cm^{-1} hydrogen rocking, 1388 cm^{-1} C_2=C_3 stretching, and 1616 cm^{-1} C_4=C_5 stretching modes of TCNQ experience the largest geometry changes following electronic excitation. From Figure 2.5 we see that as early as 125 fs the excited-state spectra look nearly identical to the chemically produced anion spectrum (Figure 2.4d). The growth kinetics of both the TA and the Raman quantitatively match those of polar solvation.[70] These results are very similar to those reported earlier[51] showing that the charge transfer occurs during the photoexcitation process and the subsequent solvent reorganization stabilizes the CIP. On the other hand, the 2D-FSRS data presented in Figure 2.8 offers new information on the structure of and wave packet dynamics on the excited-state PES and the resulting mechanism of the charge recombination reaction.

2D-FSRS Reveals Anharmonic Coupling

Two-dimensional FSRS allows the direct measurement of anharmonic couplings between various modes on the reactive excited-state surface. The intrinsic oscillatory magnitudes presented in Figure 2.8 may be related to the anharmonic coupling by eq 2.10, the derivation of which can be found in the SI.

$$\frac{\Delta\omega(t)}{\omega_{h,0}} = \frac{\omega(t) - \omega_{h,0}}{\omega_{h,0}} = -\frac{1}{2}\chi\Delta\cos(\omega_l t) \tag{2.10}$$

Here ω_h is the measured frequency of the high-frequency mode as a function of actinic pump-Raman probe delay, $\omega_{h,0}$ is the average frequency, ω_l is the frequency of the low-energy mode, Δ is the dimensionless displacement of the excited-state equilibrium geometry from the ground-state equilibrium geometry along the low-frequency normal coordinate, and χ is the first-order dimensionless anharmonic coupling between the low- and high-frequency degrees of freedom. Using eq 2.10, anharmonic couplings may be determined directly from the size of the circles in Figure 2.8 together with the Δ's of the low-frequency modes, which can be extracted from the impulsive (Figure 2.3) or resonance Raman (Figure 2.4) data. Due to the nature of the TMB:TCNQ complex, it is difficult to determine the complex concentration with high precision, limiting our ability to determine absolute Δ's directly. However, we can estimate the Δ of the 323 cm^{-1} mode to be approximately 2, assuming that the TMB:TCNQ CN stretch has approximately the same Δ as that of the tetracyanoethylene:hexamethylbenzene complex.[26] This indicates that the largest observed couplings, i.e., between the 323 and 1271 cm^{-1} modes, are on the order of 0.05 while the couplings between the 323 cm^{-1} mode and the rest of the fundamentals are on the order of 0.01. To put this into perspective, the coupling between the C-Cl stretch and the CCl_3 bend in chloroform[57] and the intermolecular couplings in guanosine 5'-monophosphate[78] predicted by DFT are on

the order of 0.03. Measured diagonal anharmonicities in diatomics are usually in the range of 0.01-0.02.

The observation that modes with weak broad lines in the excited-state FSRS spectra couple strongly, while the Raman active modes do not, is crucial to understanding the vibrational dynamics. Inspection of the spectra in Figure 2.5 shows that the 1271 cm^{-1} mode is by far the broadest fundamental with a fwhm of $\sim$55 cm^{-1}. A vibrational normal mode's breadth can be due to two underlying phenomena: heterogeneity of ground-state conformations or intrinsically fast dephasing of the vibrational coherence. Heterogeneity leads to Gaussian broadening while fast dephasing retains solely Lorentzian character. As the 1271 cm^{-1} mode is Lorentzian (within experimental error), it is likely that its breadth is due to quick damping ($\sim$200 fs) of the vibrational coherence. Fast dephasing is, in general, a sign of strong coupling to other system or bath degrees of freedom. While the width of the mode can indicate whether or not it is strongly coupled, it cannot, in general, reveal to which other modes it is coupled. However, the 2D-FSRS data offers deep insight into the mode-specific coupling within this molecular complex revealing that the 1271 cm^{-1} C_2=C_3 rocking mode is strongly anharmonically coupled to the 323 cm^{-1} CCN bending and the 354 cm^{-1} TMB out-of-plane deformation modes.

The direct measurement of mode-specific anharmonic couplings in the excited state reveals the mechanism for the charge recombination internal conversion back to the neutral ground state. Figure 2.9 depicts a mechanism that involves a CI connecting the CT excited state with the ground state. At least two modes are necessary to form a CI: a totally symmetric (TS) mode that "tunes" the energy gap between the two states (known as the tuning mode) and a nontotally symmetric (NTS) mode that bridges the symmetry "gap" between them (known as the coupling mode). In Figure 2.9 the ground state is depicted as the gray surface while the CT state is shown in yellow. Both surfaces intersect at the CI, indicated by the green sphere. The TS degree of freedom is indicated by the black arrow and NTS by the magenta one. Slices of the PES along the NTS mode are shown in magenta. Note the large displacement between the tuning mode's equilibrium position on the ground and excited state. The subspace of all nuclear motion spanned by the TS and NTS modes is termed the branching space. In this space, the degeneracy between the two electronic states is lifted, and the two electronic surfaces do not touch, except at one point, the CI. However, at the CI (green sphere) the two electronic states are degenerate along all nuclear degrees of freedom.

In order to cross from the CT state to the ground state, the NTS mode must distort the molecular system to lower the electronic symmetry and couple the states but to do so it must gain some energy. However, the NTS mode is not vibrationally excited upon electronic excitation and, because the potential is relatively harmonic in the FC region, the wave function is initially totally symmetric (blue wave function). It is clear from Figure 2.9 that the adiabatic electronic surfaces in the branching space are not harmonic in the region about the CI. This anharmonicity allows energy to be transferred from the initially excited TS mode to the NTS mode,[79] as indicated by the change in the NTS wave function when moving along the red arrow from the FC region to the CI (red wave function). The

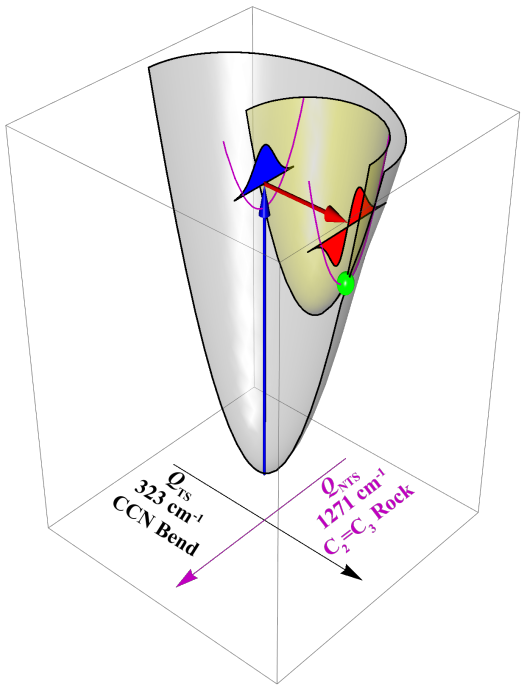

Figure 2.9: Schematic potential energy surfaces (PES) for the ground (gray) and charge-transfer excited (yellow) states in terms of the totally symmetric (TS) tuning mode (black) and the nontotally symmetric (NTS) coupling mode (magenta). Vibrational wave functions for the coupling mode are shown both in the Franck-Condon region (blue) and near the conical intersection (red). Near the conical intersection (green sphere) the adiabatic potentials are no longer harmonic and energy can be transferred through the anharmonicity between the initially excited tuning mode to the coupling mode as indicated by the change in the NTS wave function. Such a transfer of energy is necessary to surmount the symmetry barrier between the ground and excited states.

coupling and tuning modes must be strongly coupled to each other and exchange energy if the system is to access the CI and internally convert to the ground state. This fact means that the data presented in Figure 2.8 and knowledge of the mode symmetry can be used to determine which excited-state motions form a CI between the CT excited state and the neutral ground state. Only one pair of modes have the required coupling and symmetries; the totally symmetric 323 cm^{-1} CCN bending/ring deformation mode is the tuning mode and the nontotally symmetric 1271 cm^{-1} C_2=C_3 rocking mode is the coupling mode that together define the branching space and drive the charge recombination internal conversion. Moreover, these assignments can be rationalized on the basis of molecular orbital theory; initially, the TCNQ C_2=C_3 is at a 60° angle with respect to the TMB's z-axis, meaning that the lobes of the LUMO are skewed 60° with respect to those of the HOMO. In order for radiationless charge recombination to occur, these lobes must overlap well. For this to happen, the C_2=C_3 bond must lengthen and the CCC angles must distort to better match TMB's benzene ring; this job is performed by the 323 cm^{-1} mode. Furthermore, the skew

must be reduced; this distortion is achieved by the 1271 cm^{-1} mode.

2.6 Conclusions

Two-dimensional FSRS has been successfully implemented and used to measure multiple anharmonic couplings between the high- and low-frequency degrees of freedom in an excited-state charge-transfer complex. These multiple anharmonic couplings have been directly observed in the excited state of a condensed-phase system. While most couplings are on the order of 10-15 cm^{-1}, some, in particular those between the 323 and the 1271 cm^{-1} modes, are nearly an order of magnitude larger, indicating their importance for mechanistically relevant energy transfer. This observation combined with the fact that the 323 cm^{-1} CCN bending mode is totally symmetric and the 1271 cm^{-1} C_2=C_3 rocking mode is nontotally symmetric strongly suggests that these modes span the branching space of the conical intersection between the charge-transfer excited state and the ground state thereby promoting the charge recombination reaction.

Another striking observation is that the vibrational spectra exhibit significant intensity and frequency oscillations that persist to at least 5 ps after excitation. This observation shows that the internal conversion process is mediated by localized wave packet dynamics rather than full phase space randomization. With modern laser systems and careful choice of resonance conditions, it should be possible to probe the mode-specific couplings between all Raman active degrees of freedom in many more excited-state systems. Furthermore, we predict that as more systems are studied it will become clear that all fast ($<$10 ps) internal conversion processes are mediated by vibrationally coherent localized phase space evolutions. These coherences are a tool that can be leveraged by 2D-FSRS to characterize conical intersections in photoreactive systems. Our results suggest more generally that localized PES regions and specific early time coherent nuclear dynamics play a critical role in reactive internal conversion processes.

Acknowledgements

This work was supported by the Mathies Royalty Fund. DFT calculations were carried out with the support of the NSF Grant CHE-0840505. The authors thank David T. Valley, David W. McCamant, and Philipp Kukura for stimulating discussions.

Chapter 3

Difference Bands in Time Resolved Femtosecond Stimulated Raman Spectra of Photoexcited Intermolecular Electron Transfer from Chloronapthalene to Tetracyanoetheylene

This work will be submitted to the *The Journal of Physical Chemistry A* by Scott R. Ellis, David P. Hoffman, Myeongkee Park and Richard A. Mathies

3.1 Abstract

The time resolved femtosecond stimulated Raman spectra (FSRS) of a charge transfer (CT) excited non-covalent dimer 1-choronapthalene:tetracyanoethylene (ClN:TCNE) in dichloromethane (DCM) is reported with 40 fs time resolution. In the frequency domain, five FSRS peaks are observed with frequencies of 534, 858, 1064, 1392 and 1926 cm^{-1}. The most intense peaks at 534 and 1392 cm^{-1} correspond to fundamentals while the features at 858, 1069 and 1926 cm^{-1} are attributed to a difference frequency, an overtone and a combination frequency of the fundamentals, respectively. The frequency of the 1392 cm^{-1} fundamental corresponding to the central C=C stretch of $TCNE^{\bullet -}$ is redshifted from the frequency of the steady state radical due to the close proximity and electron affinity of the counter cation. The observation of a FSRS band at a difference frequency is analyzed. This analysis lends evidence for alternative non-linear pathways of inverse Raman gain scattering (IRGS) or vertical-FSRS (VFSRS) which may contribute to the time-evolving FSRS spectrum on-resonance. Measurements of the complex are presented in the time domain showing coherent oscillations in the stimulated emission with frequencies of 153, 278, and 534 cm^{-1}. The 278 cm^{-1} mode corresponds to Cl bending of the dichloromethane solvent. The center frequency of the 278 cm^{-1} mode is modulated by a frequency of $\sim$30 cm^{-1} which is attributed to the effect of librational motion of the dichloromethane solvent as it reorganizes around the nascent contact ion pair. The 153 $\pm$ 15 cm^{-1} mode corresponds to an out-of-plane bending motion of TCNE. This motion modulates the intermolecular separation of the contact ion pair and thereby the overlap of the frontier orbitals which is crucial for rapid charge recombination in 5.9 $\pm$ 0.2 ps. High time-frequency resolution provides molecular details accompanying charge localization and charge recombination that would otherwise be missed.

3.2 Introduction

Since the advent of time resolved femtosecond stimulated Raman spectroscopy, scientists have realized a multitude of non-linear pathways may contribute to FSRS spectra especially when the Raman pump and Stokes probe pulse are tuned to resonance with an excited state absorption or stimulated emission band.[15, 80–83] Unequivocal identification of which non-linear pathways that contribute the greatest intensity remains a significant challenge. Furthermore, when the aforementioned resonant electronic transition is localized on a small, highly-symmetric chromophore, the nuclear displacement becomes strongly leveraged on a few vibrational coordinates. In such cases combination bands, overtones and difference bands of the highly displaced coordinates may gain substantial Franck-Condon activity. Difference bands are only weakly observable in ground state spontaneous resonance Raman spectra because they must originate from a vibrationally excited state but they can display pronounced intensity in the excited state femtosecond stimulated Raman spectrum under resonance conditions.

At the same time, the analysis of high order non-linear pathways is only important and interesting insofaras it informs us about molecular dynamics.[84] To this end we conducted a spectroscopic analysis of 1-chloronapthalene:TCNE intermolecular charge transfer complex to understand the effect of specific vibrational coherences in modulating the back electron transfer. TCNE is a prototypical electron acceptor. It has only ten atoms and D_{2h} symmetry allowing for both the observation of and clear assignment of the overtones, combination and difference bands.

The electron rich compound 1-chloronapthalene (ClN) forms an intermolecular donor:acceptor (DA) complex with TCNE through partial donation of electron density. DA complexes are characterize by a broad weak charge transfer (CT) absorption band corresponding to an excitation from the HOMO localized on the donor to the LUMO localized on the acceptor. CT absorption bands typically have a weak molar absorptivity, a result of the weak intermolecular orbital overlap. The broad lineshape of CT bands arises from the inhomogeneity of non-covalent complex as well as a large intramolecular and solvent reorganization energies which accompany charged excited state species.[26] Finally CT states are typically non-fluorescent due to their short excited state lifetimes and weak intermolecular orbital overlaps which determines the transition dipole.

The energy of the charge transfer band can be related to the electrochemical reduction and oxidation potentials by:

$$\hbar\omega_0 = E^o_{D^+/D} - E^o_{A/A^-} + C \tag{3.1}$$

Where ω_0 is the electronic origin transition frequency, $E^o_{D^+/D}$ is the oxidation potential of the donor, E^o_{A/A^-} reduction potential of the acceptor and C is a semi-emperical correction to account for the difference in the Coulombic screening of the solvent due to the close proximity of the contact ion pair.[85] Cyclic voltammetetry of TCNE shows a half-reduction wave at voltages in the range of 0.15 - 0.25 V depending on the solvent.[86] The oxidation potential of naphthalene has been reported to be 1.80 V verse SCE in acetonitrile.[87] The oxidation potential of chloronapthalene is expected to be ∼0.06 V higher than that of naphthalene due to the inductively withdrawing effect of the chloro group.[88]. Values for the Coulombic screening term C vary between 0.06 and 0.3 V depending on the dielectric constant of the solvent and the distance between the donor and acceptor.[26, 89] To first approximation, the rate of charge recombination is governed by Marcus dynamics.[90] Charge recombination of photoexcited charge transfer systems are often exergonic and accompany large nuclear reorganization energies.[26] As a result charge recombination transitions are often energetically near or beyond the Marcus inverted region where the barrier between charged and neutral states ($\Delta G^{\ddagger}$) is small and the process occurs efficiently.[91]

At a higher level of theory, it has long been anticipated that specific vibrational modes may facilitate the biradical charge recombination.[92–95] Specifically an intermolecular librational coordinate must modulate the distance between the donor and the acceptor orbitals and therefore the electronic coupling between initial and final states. The DA librational frequency has been calculated in the range of 40-60 cm^{-1} for TCNE:hexamethylbenzene

and is likely over-damped in the solution phase, perhaps appearing as part of the solvent response.[96] Although never observed in the solution phase, the DA libration may be observable as a low-frequency phonon mode in a DA mixed crystals of TCNE:hexamethylbenzene with frequencies of 50 or 68 cm^{-1}.[97]

It has also recently been shown that intramolecular vibrational motion can have a marked effect on the charge recombination. A thorough Raman intensity analysis of the TCNE:hexamethylbenzene complex has been conducted and the mode specific reorganization energies have been reported.[26] The UV-Vis and resonance Raman spectra of $TCNE^{\bullet-}$ radical anion prepared chemically and through voltammetric methods have been reported.[68, 98] The impulsive stimulated Raman spectrum shows that coherent vibrational oscillations with a frequency of 162 cm^{-1} modulate the ground state bleach signal.[44, 92] Oscillations of a similar frequency of 153 ± 4 cm^{-1} were resolved in the time-resolved fluorescence up conversion experiment ensuring that this signal originates from vibrational coherences of the excited charge transfer state, S_1.[93] The symmetry of this excited state coherence has remarkably been assigned to an out-of-plane bending motion that is not Raman active in the monomer but becomes active in the lower order symmetry of the complex. Spectral integration of the fluorescence upconversion signal indicates that the out-of-plane bending mode modulates the transition dipole moment.[93] Taking these data as a whole a cohesive picture becomes clear. When neutral TCNE is photoreduced, displacements are found along coordinates of frequencies 165, 534, 1565 cm^{-1} (Δ of 0.82, 0.54 and 0.94 respectively).[26] With reduction these vibrations have frequencies of 153, 534 and 1421 cm^{-1} in solution phase.[86] Of note, the 1421 cm^{-1} mode corresponding to the central C=C stretch of $TCNE^{\bullet-}$ is sensitive to the nature and proximity of counter ion.[99]

In what follows, we use a sub-50 femtosecond impulsive pump pulse to excite the complex to a biradical species $TCNE^{\bullet-}ClN^{\bullet+}$ and generate a vibrational wavepacket. Through the oscillations in the stimulated emission we identify specific excited state vibrational coordinates that allow the electron to localize in the LUMO of the TCNE. We find evidence for vibrational coherences in the photoexcited solvent shell. We then use FSRS to observe the effect that charge localization has on other Raman active vibrations. Finally we highlight the presence of a difference band in the excited state FSRS spectra and find evidence for alternative non-linear pathways inherent to the FSRS pulse sequence.

3.3 Materials and Methods

Sample Preparation

1-chloronapthlene (90%, ∼10% 2-chloronaphthalene, Sigma Aldrich), tetracyanoethylene (98%, Sigma Aldrich) and dichloromethane (DCM, 99.9%, EMD) were used as received. Solutions of the complex were prepared with an optical density of 0.9 per 1 mm path-length at 530 nm. Solutions were filtered though a 40 μm teflon filter. The concentration of the solutions were ∼0.1 M ClN and ∼0.1 M TCNE in the FSRS experiments.

Femtosecond Stimulated Raman Spectroscopy

The FSRS instrument has been described in detail previously.[61] Briefly, ultrashort pulses are generated by a home-built Kerr lens mode-locked Ti:sapphire oscillator (30 fs, 5.3 nJ/pulse, 91 MHz) that seeds a Ti:sapphire regenerative amplifier (B.M. Industries, Alpha 1000 US, $\lambda_{\max}$ = 790 nm, 70 fs, 0.9 mJ/pulse, 991 Hz) pumped by a Q-switched Nd:YLF (B.M. Industries, 621-D). The fundamental output is split into three pulses. The actinic pump ($\lambda_{\max}$ = 530 nm, 40 fs, 150 nJ/pulse) is generated with a home-built noncollinear optical parametric amplifier (NOPA) and compressed by an F2 prism pair (ThorLabs). A portion of the fundamental is spectrally filtered and temporally shaped by a Fabry-Perot etalon (TecOptics, design A6) forming the narrow band Raman pump pulse ($\lambda_{\max}$ = 795 nm, 1.7 μJ/pulse, fwhm = 2.8 cm^{-1},τ_{RPu} = 3.8 ps). [24] The probe pulse (8 fs, 5 nJ/pulse, $\lambda_{\max}$ = 883 nm) is produced by generating a continuum in a 3-mm thick sapphire plate followed by temporal compression in a BK7 prism pair. Both the Raman pump and probe pulses are polarized parallel to the table. For long-delay experiments, the actinic pump is polarized at magic angle with respect to the Raman beams to mitigate the effects of rotational diffusion on the kinetics. All beams are focused into the sample and overlapped both spatially and temporally.

After the sample, the probe pulse is isolated, recollimated, and directed into a spectrograph which disperses the beam onto a fast CCD (Princeton Instruments, PIXIS 100F). A phase locked chopper (Newport, 3501) blocks every other Raman pump pulse, allowing the Raman gain to be calculated, shot-to-shot, as $\ln(probe_{\text{Raman pump on}}/probe_{\text{Raman pump off}})$. The shot-to-shot fluctuations of the probe are less than 0.1% circumventing the need for a reference beam. A computerized delay stage controls the timing between the actinic pump and the Raman pulse pair. Ground-state stimulated Raman spectra are collected by intermittently shuttering the actinic pump. Near-IR transient absorption spectra are calculated as $-\log(probe_{\text{actinic pump on}}/probe_{\text{actinic pump off}})$. All data collection and initial data processing is performed with a custom LabVIEW program.[62]

Spontaneous Raman

Samples were circulated through a 1.5 mm capillary tube at 2 cm/s using a peristaltic pump and irradiated with 5 mW of 457, 488, and 514 nm light. The parallel polarized scattering was collected in the standard 90$^{\text{o}}$ geometry and focused onto the entrance slit of a 2 m Spex 1401 double spectrograph. Spectra were imaged on a liquid nitrogen cooled CCD (Roper Scientific LN/CCD 1100). The peaks of cyclohexane was used to calibrate the Raman shift. The spontaneous Raman spectrum of TCNE was acquired in acetonitrile rather than DCM because the higher solubility afforded a detectable off-resonant scattering signal. Once the signal from neutral TCNE had been optimized, a small aliquot of 1 M KI or 1 M NaI in acetonitrile was added to reduce the contents of the sample reservoir as it circulated through the beam path. The spectra of $TCNE^{\bullet-}Na^{+}$ and $TCNE^{\bullet-}K^{+}$ were extracted from the

difference spectrum before and after the addition of iodide. In this way the spectrum was acquired before the sample was able to appreciably oxidize and degrade.

Data Analysis

The femtosecond stimulated Raman spectra were averaged for 150 s over 20 scans through 60 time delays of the actinic pump. The ground state spectra were scaled to the same amplitude of the 703 cm^{-1} DCM peak as that in the actinic excited spectra and then subtracted to extract the contributions of the pure excited state signals. For the time-resolved stimulated Raman spectra, the peaks and baselines were fit in separate spectral regions using a linear baseline. All peaks were modeled with a Lorentzian line shape except for the 534 cm^{-1} peak, which was modeled as a dispersive Lorentzian, eq. 3.2.

$$I(\nu) = \frac{A + B\nu}{\nu^2 + 1} \tag{3.2}$$

Here A is the intensity of the real part, B is the intensity of the dispersive part, and ν is defined by eq. 3.3.

$$\nu = \frac{\omega - \omega_0}{\Gamma/2} \tag{3.3}$$

where ω is the frequency, ω_0 is the frequency of the vibrational transition, and Γ is the full width at half-maximum (fwhm). To analyze the oscillatory components in the transient absorption and Raman data, the slowly varying, exponential, population dynamics were removed using standard nonlinear curve fitting to the appropriate exponential decay. The residual oscillatory signals were subsequently analyzed using a linear prediction with singular value decomposition (LPSVD) algorithm,[63–65] All data analysis was performed using IGOR Pro and custom-developed procedures.[66].

Theory of Difference Frequencies in FSRS

Difference frequencies are provided for by the quantum theory of stimulated Raman spectroscopy which has been described excellently in published literature.[100, 101] The FSRS pulse sequence permits for multiple non-linear pathways designated femtosecond stimulated Raman (FSRS), inverse Raman gain scattering (IRGS), and vertical femtosecond stimulated Raman scattering (VFSRS). Figure 3.1 presents three non-linear pathways which result in a narrow band gain feature at a Raman shift of a difference frequency on the Stokes side of a narrow band Raman pump pulse. The notation used here $|S_0\rangle$, $|S_1\rangle$ and $|S_n\rangle$ denote the ground electronic state the first excited electronic state and a general higher lying electronic state, respectively. The vibrational state within the manifold of a given electronic state is denoted as $|\nu_{low}, \nu_{hi}\rangle$ and the conjugate transpose as $\langle\nu_{low}, \nu_{hi}|$. State $|0,0\rangle$ has no quanta of energy. State $|1,0\rangle$ has one quanta of energy ($\hbar\omega_{low}$) in the low frequency vibration. State $|0,1\rangle$ has one quanta of energy ($\hbar\omega_{hi}$) in the high frequency vibration. State $|1,1\rangle$ has one

quanta of energy in each vibration. The state $|n_i, n_j\rangle$ has a general quanta of energy in each vibration indicating that the specific vibrational state is not critical to the activation of the non-linear pathway.

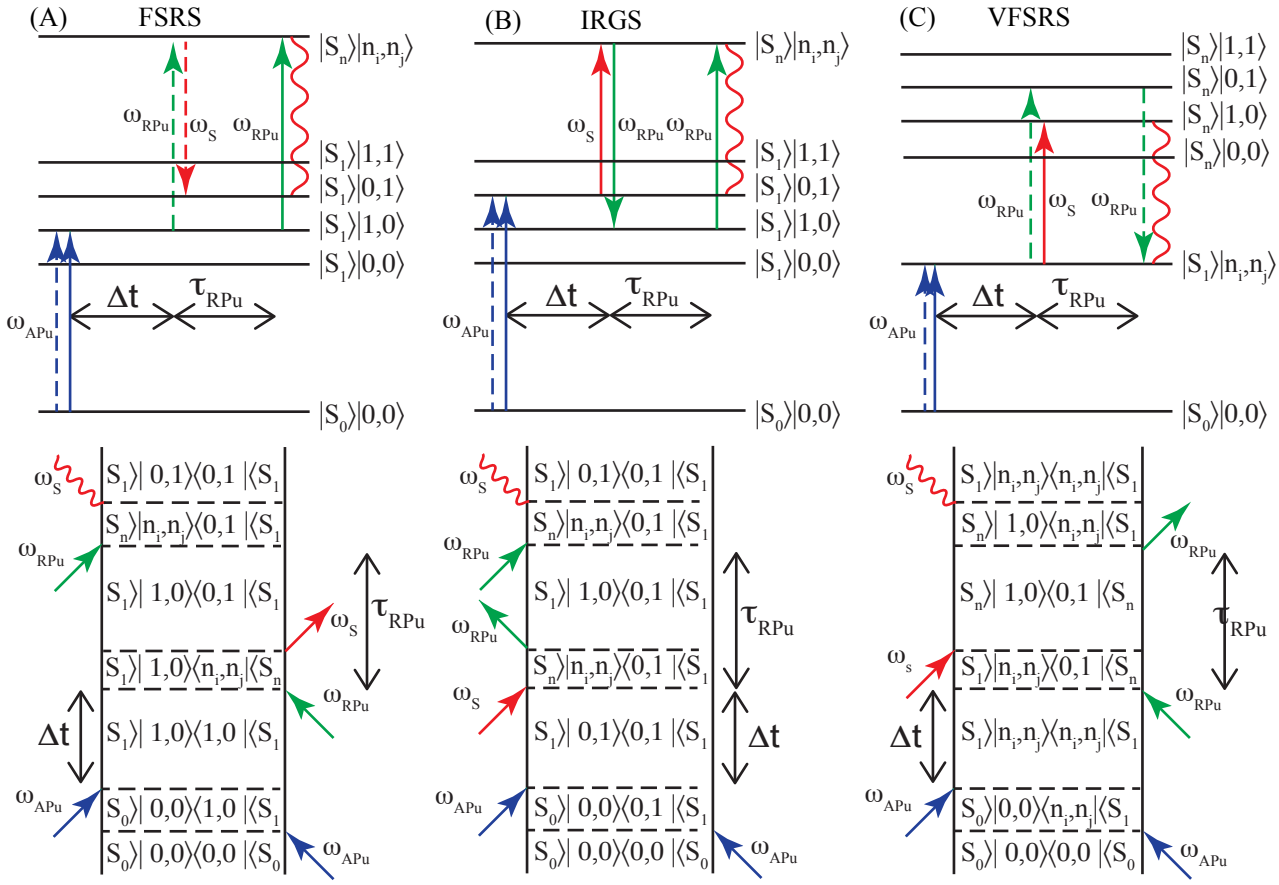

Figure 3.1: Wave-mixing energy level diagrams and double sided Feynman diagrams for three fully resonant non-linear pathways that result in narrow band gain features at a difference frequency on the Stokes side of a narrow band Raman pump ($\omega_s = \omega_{RPu} - \omega_{hi} + \omega_{low}$). The notation used here $|S_0\rangle$, $|S_1\rangle$ and $|S_n\rangle$ denote the ground electronic state, the first excited electronic state, and a general higher lying electronic state, respectively. The vibrational state within the manifold of a given electronic state is denoted as $|\nu_{low}, \nu_{hi}\rangle$ and the conjugate transpose as $\langle\nu_{low}, \nu_{hi}|$. The action of the actinic pump (APu, blue), Raman pump (RPu, green) and Stokes Probe (S, red) on the left and right side of the density matrix are indicated with solid and dashed arrows, respectively. The population evolution time is denoted Δt and the picosecond Raman pump pulse duration is labeled τ_{RPu}.

The action of the femtosecond actinic pump on the right and the left of the density matrix prepares a population on the first excited singlet state. If the actinic pump is broad or resonant on the blue side of the absorption band a fraction of the excited state population will be vibrationally excited along the low frequency coordinate ($|S_1\rangle|1,0\rangle\langle 1,0|\langle S_1|$). This excited state population decays with two rates Γ_{1010} and $\Gamma_{S_0S_1}$ over time delay Δt. Γ_{1010} is the vibrational energy redistribution out of the low frequency vibration and $\Gamma_{S_0S_1}$ corresponds to the rate of internal conversion (in this case charge recombination). The Raman pump and the Stokes probe then act together and on resonance with the states $|S_n\rangle|n_i,n_j\rangle$ to prepare a vibrational coherence ($|S_1\rangle|1,0\rangle\langle 0,1|\langle S_1|$). The electronic resonance condition is necessary to observe a difference frequency because the superposition on $|S_n\rangle$ must be allowed to evolve for sufficient time to find two coordinate overlap. Only fundamental Raman transitions are allowed off-resonance. Furthermore combination bands, difference bands and overtones are commonly observed when the electronic transition of $\mu_{S_1S_0}$ is localized on a few symmetric bonds such that the multimode dephasing ($\sim$ 15 fs) has not occurred by the time the wavepacket finds two coordinate overlap. At time delays concurrent with the dephasing of the two coordinate vibrational coherence ($1/\pi\Gamma_{1001} \approx \tau_{RPu}$), the Raman pump pulse may act on the system again, stimulating a narrow band gain signal in the direction of the probe at a Raman shift frequency $\omega_{FSRS} = \omega_{RPu} - \omega_{hi} + \omega_{low}$.

The standard time resolved FSRS pathway (A) is evaluated in the SI yielding a fifth order polarization of the form:

$$
\begin{aligned}
&P^{(5)}_{(A)}(\omega_{FSRS},\Delta t)\\
&= (\frac{1}{i\hbar})^5 C(\ell,\tau_{APu},\omega_{APu},\tau_S,\omega_S,\omega_{RPu})\,|E_{APu}|^2\,|E_{RPu}|^2\,E_S^*\\
&\times \frac{|\mu_{S_1S_0}|^2\,|\mu_{S_nS_1}|^4}{\omega_{FSRS}-\omega_{RPu}-\omega_{hi}+\omega_{low}-i\Gamma_{1001}}\\
&\times \left|\frac{\langle 1,0^{S_1}|0,0^{S_0}\rangle}{(\omega_{APu}+\omega_{S_1S_0}-\omega_{low}-i\Gamma_{S_1S_0})}\right|^2 \sum_{n_i,n_j}\left|\frac{\langle 1,0^{S_1}|n_i,n_j^{S_n}\rangle\langle n_i,n_j^{S_n}|0,1^{S_1}\rangle}{\omega_{RPu}-\omega_{S_nS_1}-(n_i+1)\omega_{low}-n_j\omega_{hi}-i\Gamma_{S_nS_1}}\right|^2\\
&\times e^{-(\Gamma_{1010}+\Gamma_{S_1S_1})\Delta t}
\end{aligned}
\tag{3.4}
$$

The parameter $\Gamma_{S_1S_n}$ is the rate of electronic dephasing which is generally much faster than vibrational dephasing Γ_{1001}. The value C is a constant which contains experimental parameters such as sample pathlength ℓ and the frequency and duration of the light pulses. To simplify the notation we have assumed that the low and high frequencies are unchanged on the S_0, S_1 and S_n states although this is not generally the case.

The pathway labeled (B) is an inverse Raman gain pathway. The actinic pump prepares vibrationally hot excited state population with one quanta in the high frequency mode ($|S_1\rangle|0,1\rangle\langle 0,1|\langle S_1|$). Subsequently, the probe acts first on the bra side to drive the state upward while the pump simultaneously acts on the bra to drive the state downward preparing the same coherence state as in pathway (A). As before, interaction of the Raman pump pulse

stimulates a gain signal in the direction of the probe. The inverse Raman pathways are commonly observed as a loss signal on the anti-Stokes side of the Raman pump; however, as Figure 3.1 shows, when the probe are tuned to resonance with an excited state absorption, the inverse Raman gain pathway can produce a gain signal.[83, 102] Furthermore if the inverse Raman gain pathway is initiated from a vibrationally hot state it can produce a gain signal on the Stokes side of the Raman pump pulse.

The pathway labeled (C) has been called 'vertical FSRS' by Ernsting and coworkers highlighting the fact that it prepares a vibrational coherence on the excited state vertically above the ground state geometry.[82, 103] In this case, the difference transition is accessible from any vibrational state of S_1 $|n_i, n_j\rangle$. The Raman pump and Stokes probe pulses act on opposite sides of the density matrix to prepare a coherence on the electronic excited state with which they are resonant ($|S_n\rangle|1,0\rangle\langle 0,1|\langle S_n|$). At a later time delays a second interaction with the picosecond Raman pump pulse projects the state downward generating a narrow band gain signal in the direction of the probe with a frequency of $\omega_{RPu} - \omega_{hi}^{S_n} + \omega_{low}^{S_n}$ where the superscripts indicates vibrational frequencies of electronic state $|S_n\rangle$.

Distinguishing which among these three non-linear pathways contributes to our measured signal presents a formidable challenge. All three pathways are enhanced as $(\mu_{S_1S0})^2 (\mu_{S_nS1})^4$. Furthermore these pathways involve projections onto vibronic states with the same Franck-Condon factors e.g. $\langle 1, 0^{S_n}|0, 0^{S_1}\rangle = \langle 1, 0^{S_1}|0, 0^{S_n}\rangle$. In principal, any or all of these pathways could be contributing to the signal with a similar intensity at a given resonant wavelength. We'll note that pathway (C) can readily be distinguished from pathways (A) and (B) because the frequency $\omega_{hi}^{S_n} + \omega_{low}^{S_n}$ may be different from $\omega_{hi}^{S_1} + \omega_{low}^{S_1}$. Furthermore pathways (B) and (C) require that both the Raman pump pulse and the Stokes probe pulses are both on resonance with vibronic states $|0, 1^{S_n}\rangle$ and $|1, 0^{S_n}\rangle$, respectively, while pathway (A) is accessible under preresonance conditions where the Raman pump pulse is on resonance with state $|0, 0^{S_n}\rangle$ while the probe pulse might be in a spectrally clear wavelength region.[104] In other words, the signals from pathways (A) is expected to peak at redder Raman pump wavelengths than that of pathways (B) or (C). All of this must be considered in the subsequent analysis of the photoexcited ClN:TCNE CT complex.

3.4 Results

Steady-State Charge Transfer Absorption

Figure 3.2 presents the absorption spectra of the TCNE:ClN CT complex and its components. Free 1-chloronapthalene (ClN) in DCM only absorbs at wavelengths below 390 nm. Neutral TCNE does not absorb at visible wavelengths. Two charge transfer bands appear when ClN is mixed in solution with TCNE. The CT bands with maxima at 408 and 537 nm correspond to transitions from different occupied π orbitals of ClN (symmetries of a_u and b_{1u} in the quasi D_{2h} point group of naphthalene).[88] The binding properties of the complex were determined

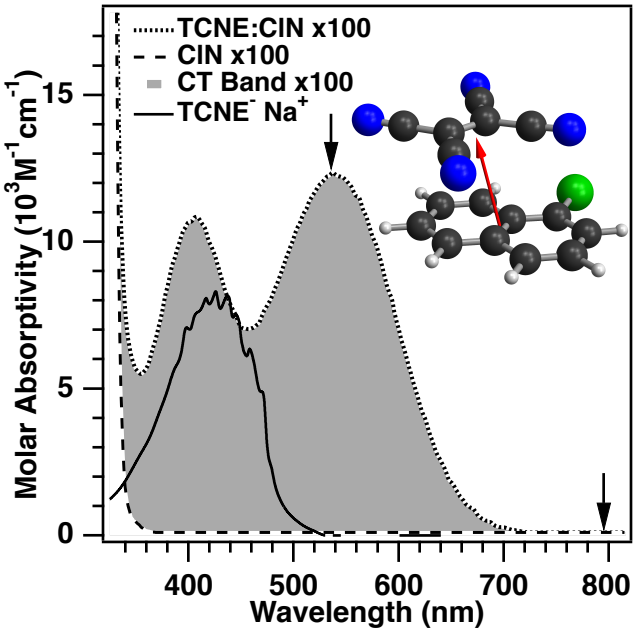

Figure 3.2: UV-Vis absorption spectrum of TCNE:ClN CT complex (dotted line, grey filled), unbound ClN (dashed line) and Na^+TCNE^- (solid line, digitized from ref. [105]). The molar absorptivity of the complex has been multiplied by 100. The center wavelengths of the actinic and Raman pump are indicated by arrows at 530 and 795 nm, respectively. The DFT optimized structure of the TCNE:ClN dimer is included. The transition dipole moment for the lowest energy charge transfer band is presented as a red arrow.

via the Benesi-Hildebrand method: $K_{eq} = 7.3 \pm 1.3$ M^{-1}, $\epsilon_{537} = 120 \pm 20$ $M^{-1}cm^{-1}$, $\epsilon_{408} = 100 \pm 20$ $M^{-1}cm^{-1}$.[67, 106].

The binding conformation of the TCNE:ClN complex (Figure 3.2, inset) was modeled via a density functional theory geometry optimization using the restricted ωB97x-D functionals and the 6-311++G(d,p) basis set. The electronic transition energies were then calculated using time-dependent DFT at the same level of approximation. The calculations showed that there are multiple stable conformers with energies varying by less than thermal energy. The confomer presented in Figure 3.2 was chosen because it was the most stable, and additionally the TD-DFT calculation of this conformer accurately predicted the relative absorptivity of the charge transfer bands originating from the a_u and b_{1u} orbitals of ClN. The lowest energy charge transfer band is calculated to occur at 537 nm with a transition dipole length of 0.37 Å (red arrow).

$TCNE^{\bullet-}$ is an analogue of the photoexcited charge transfer state with the major distinction being that there is no spin correlated counter ion. The solid black line presents the absorption spectrum of chemically prepared $TCNE^{\bullet-}Na^+$ in solution of 2-methyltetrahydrofuran. The anion absorption at 425 nm displays strong vibronic progression with a spacing of ~534 cm^{-1}.[86, 105] The structure of $TCNE^{\bullet-}$ was modeled along with the vibrational and optical transitions using TD-DFT with uB3LYP functionals. The lowest

energy transition dipole of the radical anion is oriented along the C=C double bond.

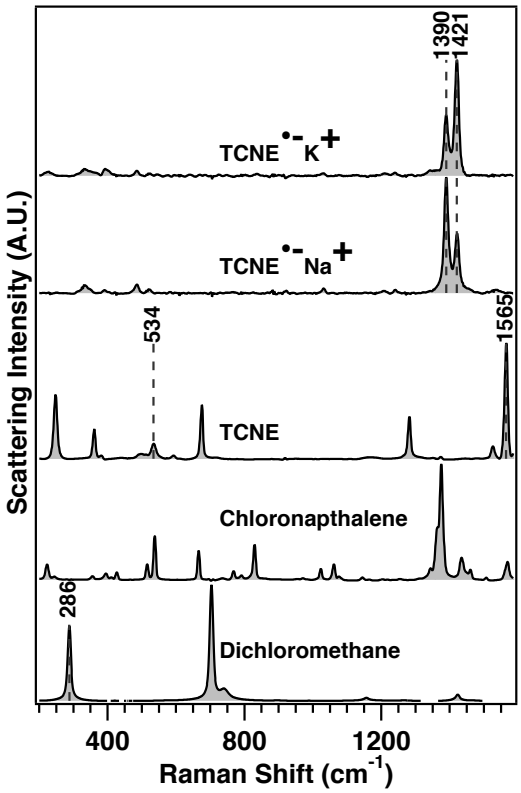

Figure 3.3: Ground state spontaneous Raman spectra of DCM (514 nm, neat), chloronaphthalene (488 nm, DCM), TCNE (514 nm, acetonitrile), $TCNE^{\bullet-}Na^{+}$ (457 nm, acetonitrile), and $TCNE^{\bullet-}K^{+}$ (457 nm, acetonitrile). In the spectra of the solutes, the solvent and the broad featureless baselines have been subtracted for clarity. Important peaks have been labeled.

Spontaneous Raman Analysis

The ground state spontaneous Raman spectra of the components of the CT complex are presented in Figure 3.3. The central C=C stretching mode of neutral TCNE appears at 1565 cm^{-1}. When TCNE is reduced by potassium iodide or sodium iodide two peaks are observed at 1390 and 1421 cm^{-1}. The 1421 cm^{-1} peak agrees closely with the frequency calculated from DFT (Table A.1); however, the peak at 1390 cm^{-1} is not accounted for by the calculated structure which is optimized in the gas phase. These peaks likely correspond to the C=C stretch of the $TCNE^{\bullet-}$ with and without a counter cation in the inner sphere solvation shell. Figure 3.4 presents mass weighted vibrational coordinates of $TCNE^{\bullet-}$ and DCM that are displaced in the initial charge transfer excitation.[26, 86]. Importantly, when $TCNE^{\bullet-}Na^{+}$ is prepared instead of $TCNE^{\bullet-}K^{+}$ the relative intensity of 1390 cm^{-1} mode increases relative to the 1421 cm^{-1} by a factor of 4. This shift intensity may be attributed to

the shift in equilibrium of free $TCNE^{\bullet-}$ verses the $TCNE^{\bullet-}M^{+}$ contact ion pair. We will later show that in the FSRS spectra of photoexcited TCNE:ClN only one peak at ∼1390 cm^{-1} appears because the close proximity of the contact ion pair is enforced by the rapid charge transfer excitation.

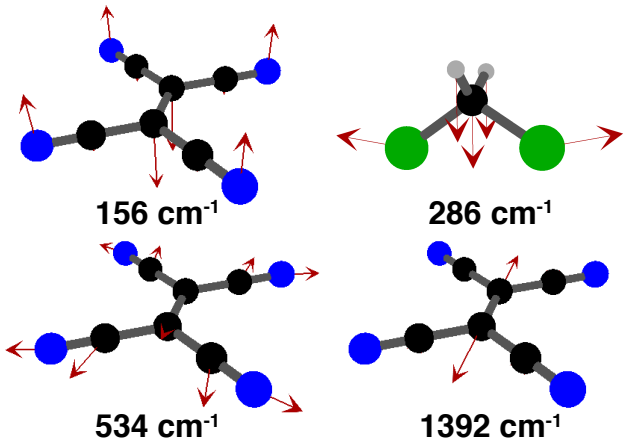

Figure 3.4: Mass weighted normal coordinates of $TCNE^{\bullet-}$ and dichloromethane from DFT. The calculated frequencies are 149.9, 283.3, 534.6 and 1424.6 cm^{-1}, respectively.

Polarized Transient Absorption

The wavelength dispersed transient absorption spectrum after the excitation of the CT band at 530 nm with magic angle polarization is presented in Figure 3.5(a). A stimulated emission band appears in the blue region of the probe window. The band integrals from 825-835 nm for parallel, magic angle and perpendicular polarizations are presented in Figure 3.5(b). The stimulated emission decay is well fit as a monotonic bi-exponential decay with time constants of 0.11 ± 0.01 and 1.4 ± 0.2 ps. These time constants correspond closely with DCM solvation times.[70, 107] The signal at magic angle polarization is not monotonic. As the stimulated emission decays an excited state absorption band is revealed which persists longer than the stimulated emission. This excited state absorption signal then decays with a third time constant of 5.9 ± 0.2 ps corresponding to the charge recombination of the radical contact ion pair $TCNE^{\bullet-}ClN^{\bullet+}$. An analysis of the perpendicular polarized signal and the time resolved anisotropy is presented in the SI.

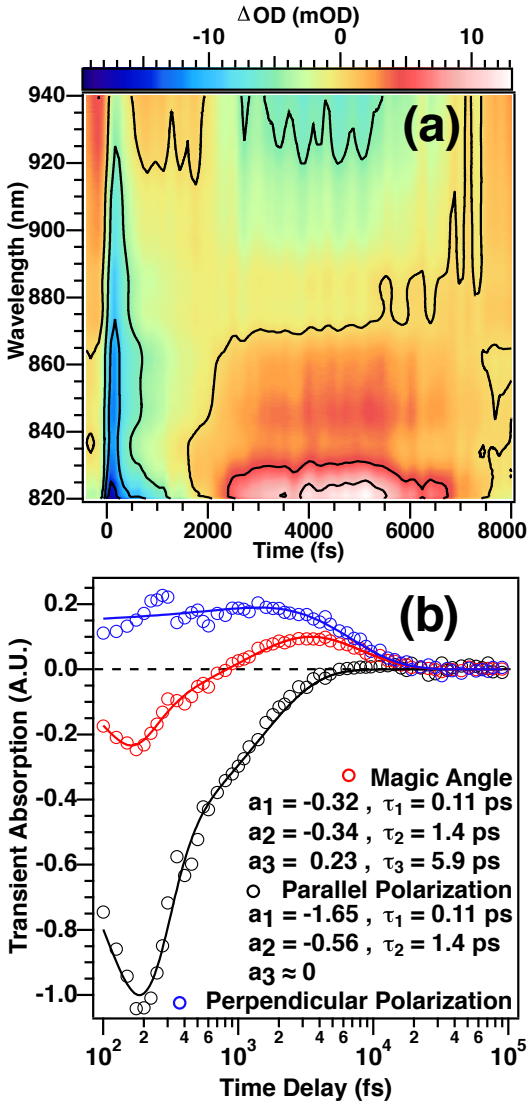

Figure 3.5: (a) Contour plot of dispersed transient absorption signal with magic angle polarization of ClN:TCNE in the region of 820 - 940 nm after excitation with 530 nm light. (b) Time evolution of the transient absorption signal (825 - 835 nm) on the probe pulse in parallel (black), magic angle (red) and perpendicular (blue) polarizations.

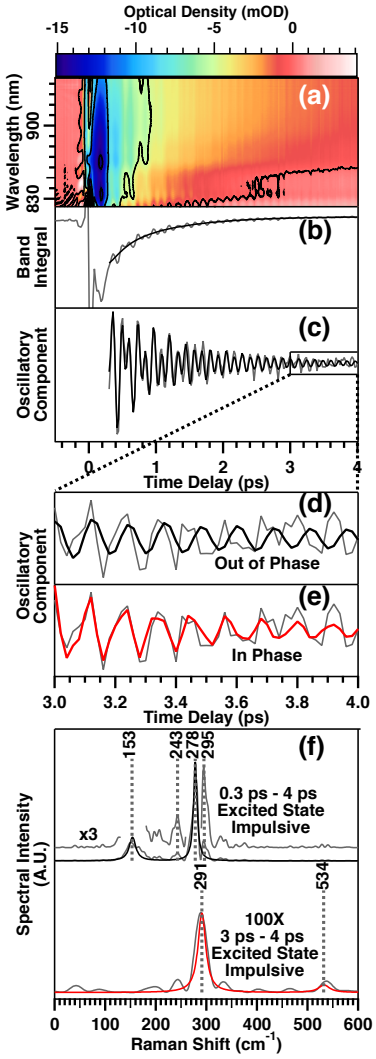

Figure 3.6: (a) Dispersed stimulated emission in parallel polarization. (b) Band integral of the stimulated emission over the region of 825-835 nm (gray line) along with a fit to a two-component exponential decay convolved with a Gaussian instrument response function (black line). (c) The oscillatory component from 0.3 ps to 4 ps (gray line) is fit to a signal of two exponentially decaying sinusoids using the LPSVD algorithm (black line). (d) A magnified view of the oscillatory component in the time interval of 3 - 4 ps (grey line) and the fit (black line) as shown above. (e) A second LPSVD fit (red line) exclusively to the signal in 3 - 4 ps temporal window. (f, top) Frequency domain reconstruction of the LPSVD parameters (black spectrum) and an FFT analysis from 0.3 ps to 4 ps of the oscillatory component (gray spectrum). The smaller peaks of the FFT spectrum have been scaled by a factor of 3. (f, bottom) LPSVD reconstruction (red spectrum) and FFT (grey spectrum) of signal from 3 - 4 ps.

Impulsive Stimulated Emission Analysis

The short time decay of the parallel polarized emission band is presented in Figure 3.6. At very early times a coherent artifact is observed after which oscillations are observed modulating the emission band integral (825-835 nm). LPSVD analysis shows that the signal is dominated by two frequencies of 153 ± 12 cm^{-1} and 278 ± 5 cm^{-1}. The fit in the early time region is so good that the difference between the data and the fit cannot be discerned. The 153 cm^{-1} oscillation corresponds to an excited state b_{1u} out-of-plane bending mode which is displaced in the initial charge transfer excitation of the complex but should not be Raman active in the monomer alone. The 153 cm^{-1} mode has a short dephasing time of 0.67 ps (FWHM = 16 ± 4 cm^{-1}) suggesting that it is strongly coupled to the solvent degrees of freedom. The 278 cm^{-1} oscillations (Fig. 3.6F) correspond to a symmetric chlorine bending mode of the DCM solvent. The LPSVD analysis was unable to reproduce side bands at 243 and 295 cm^{-1} (Fig. 3.6 F, grey) suggesting that more complicated dynamics than pure dephasing may be at play (Fig. 3.6 F, black).

The exemplary fit that reproduces the oscillations at early times fails at later time delays from 3 - 4 ps (Fig. 3.6 (d)). To account for this a second LPSVD fit was performed exclusively to the signal from 3 - 4 ps (Fig. 3.6 (e), red). Remarkably two new frequencies are observed with frequencies of 291 and 534 cm^{-1}. The 534 cm^{-1} peak is a symmetric in-plane bending of the CN groups (Fig 3.4). The 278 cm^{-1} mode is shown to shift in frequency to 291 cm^{-1} over the course of the solvent reorganization.

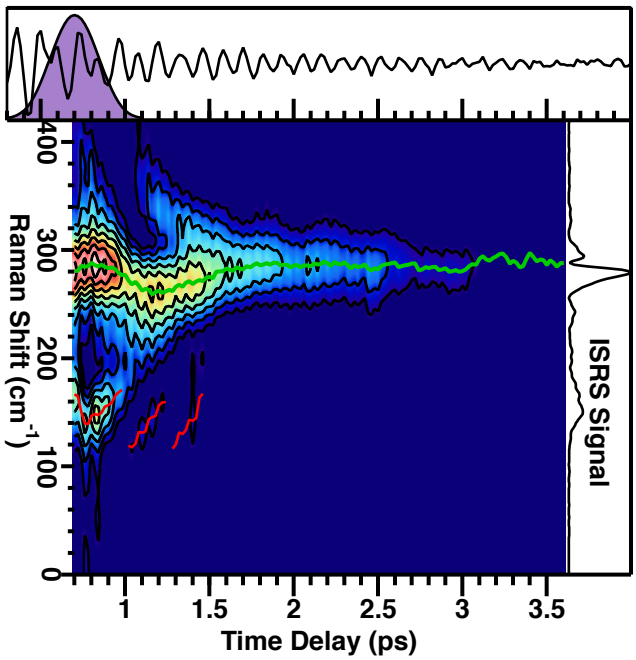

Figure 3.7: Spectrogram of oscillatory stimulated emission band in the region of 825 - 835 nm. The time domain signal is shown on top along with a Blackman window function of FWHM = 0.325 ps (purple). The Fourier transform over the full 0.3 - 4 ps window is shown on the right. The green line shows the peak maximum of the ∼278 cm^{-1} signal while the red line shows the peak maximum of the ∼153 cm^{-1} signal

A sliding Fourier transform was applied to the free induction decay (Fig. 3.7). The peak maximum of the ∼278 cm^{-1} signal (green line) undergoes a blue-shift from 0.7-1.1 ps and then a red shift at later time delays. Frequency modulated free induction decays have been well characterized in literature for years[108, 109]; however, this is the first record of a frequency modulation of a solvent coordinate. Next it will be shown that the intramolecular vibration of coordinates of TCNE are also frequency modulated over the timescales of dynamic solvation.

Time Resolved FSRS

The time-resolved stimulated Raman spectrum of photoexcited TCNE:ClN is presented in Figure 3.8 with magic angle polarization of the actinic pump. The spectrum appears with the instrument response, limited by the actinic pump duration of 40 fs. The spectrum consists to 5 peaks corresponding two well characterized fundamental frequencies at 534 and 1392 cm^{-1} of the radical anion $TCNE^{\bullet-}$ and three weaker combination bands and overtones involving these coordinates at 858, 1067 and 1920 cm^{-1}. Assignments were made based on density functional theory and consideration of all relevant literature. Importantly the DFT indicates that $TCNE^{\bullet-}$ has no normal modes with frequencies in the range of 640 - 1000 cm^{-1} making the assignment of the difference frequency at 858 cm^{-1} straight forward (Fig. A.1). The amplitude and peak center frequencies evolve at early time delays (Fig. 3.9). The

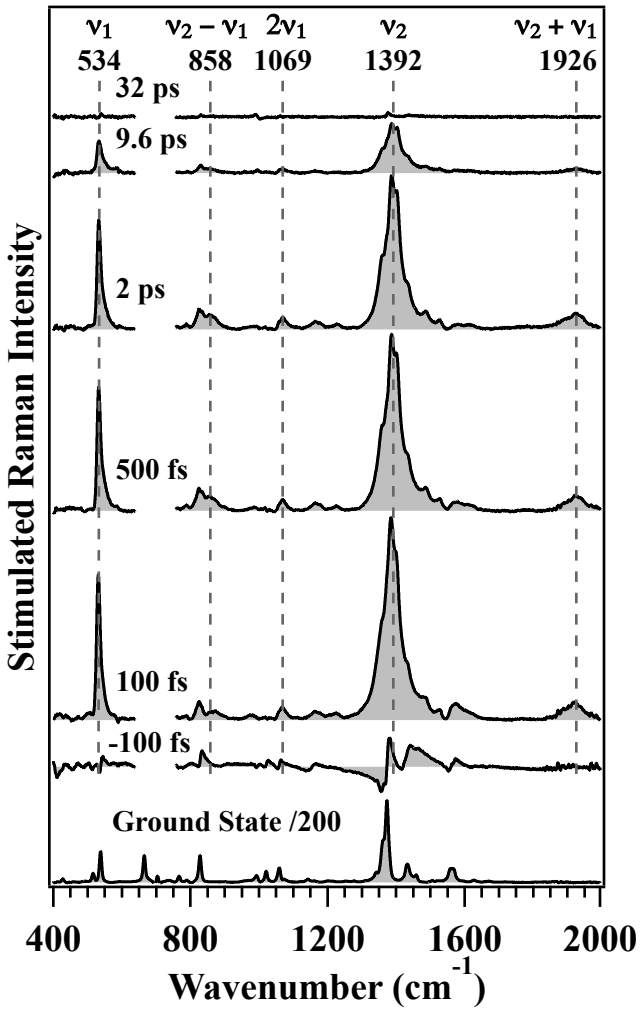

Figure 3.8: Evolution of excited state femtosecond stimulated Raman spectrum of TCNE:ClN at selected timepoints. The intense ground state spectrum corresponding primarily to uncomplexed ClN and DCM is shown below scaled by 1/200 for comparison.

reported frequencies are those measured at a time delay of 2 ps after the peak frequencies have mostly stabilized. The FSRS amplitudes Figure 3.9(left) are well fit by a three component exponential function. The time constants of $\tau_1 = 0.11$, $\tau_2 = 1.4$ and $\tau_2 = 5.9$ ps are the same as those observed in the excited state absorption signal (Fig 3.5(b)). The center frequencies of the peaks shift with the two faster time constants (τ_1 and τ_2) concurrent with dynamic solvation and the decay of the stimulated emission in the near infrared window.[44]

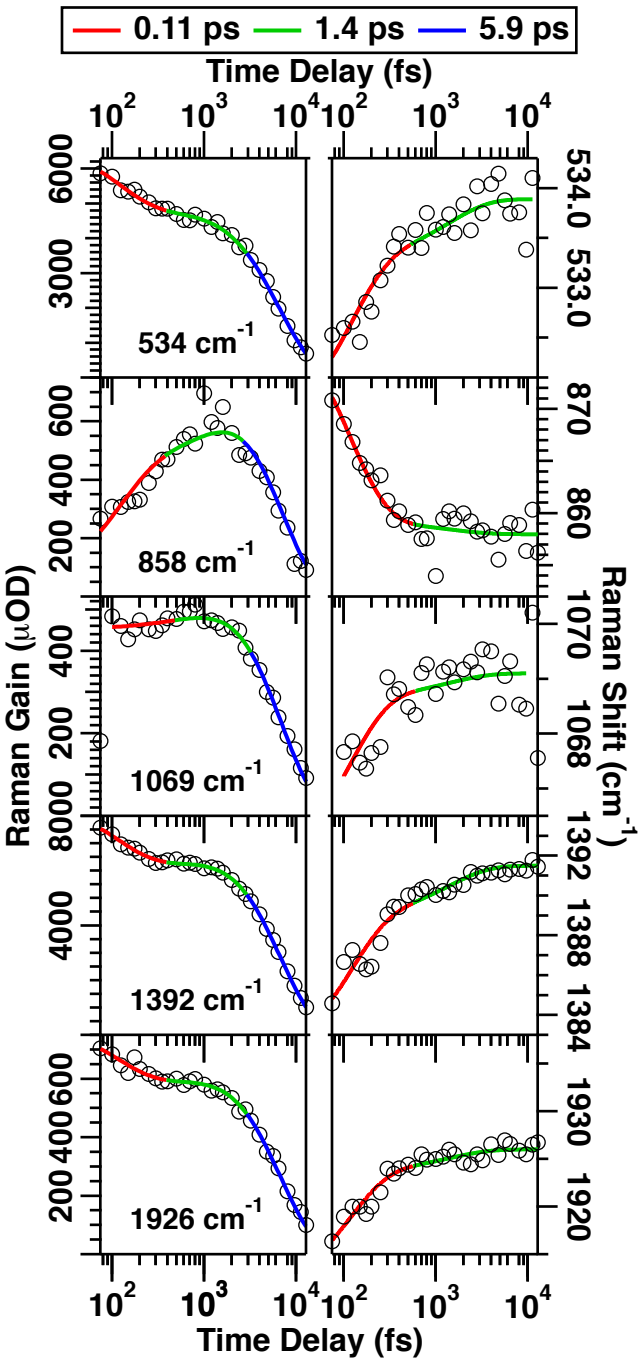

Figure 3.9: Kinetics of peak amplitudes (left) and center frequencies (right) of five transient FSRS peaks. The time constants for the three processes are shown above.

		τ_1 (fs)	τ_1 (fs)	τ_2 (fs)	τ_2 (fs)
		110	110	1400	1400
		Γ_1 (cm^{-1})	Γ_1 (cm^{-1})	Γ_2 (cm^{-1})	Γ_2 (cm^{-1})
		97	97	8	8
ω_0 (cm^{-1})	Γ_{peak} (cm^{-1})	$A_{1,obs}$ (cm^{-1})	$A_{1,inst}$ (cm^{-1})	$A_{2,obs}$ (cm^{-1})	$A_{2,inst}$ (cm^{-1})
534	13	1.8±1.7	16±14	0.6±0.5	1.0±0.8
858	50	-19.6±1.7	-57±5	-4.2±0.5	-4.9±0.6
1068	25	3.4±2.1	17±10	0.5±0.5	0.6±0.6
1392	55	7.7±1.7	21±5	2.7±0.5	3.1±0.6
1926	71	13.4±1.7	32±4	2.5±0.5	2.8±0.5
1392-534			0.8±15		-0.4±0.9
2x534			31±20		2.0±1.0
1392+534			37±15		4.1±0.9

Table 3.1: FSRS peak shift fit parameters from Fig. 3.9. The center frequency of each peak at a time delay of 2 ps is label ω_0. The FWHM of each peak is labeled Γ_{peak}. The time constants and corresponding bandwidths of the dynamic processes are labeled as τ_i and Γ_i, respectively, where $\pi\Gamma = 1/\tau$. The fit parameters A_{obs} are the magnitudes of the peak shifts determined directly from the global fitting while A_{inst} are those values after a scaling factor of $(\Gamma_i/\Gamma_{peak}+1)$ has been applied to account for Fourier uncertainty. The difference, harmonic double and sum of the instantaneous peak shifts of the fundamental modes is presented at the bottom.

The peak widths and the magnitude of the peak shifts are present in Table 3.1. Importantly a FSRS spectrum does not measure an instantaneous frequency. Rather the observed frequency is convolved with subsequent frequencies over the dephasing of the vibrational coherence or the duration of the Raman pump pulse (See SI). Therefore a scaling factor must be applied to extract the true magnitude of a peak shift.

$$A^{peak}_{inst,i} = A^{peak}_{obs,i}\left(\frac{\Gamma_i}{\Gamma_{peak}} + 1\right) \tag{3.5}$$

Γ_i is the bandwidth of the dynamic process and Γ_{peak} is the bandwidth of a given FSRS peak. The observed and adjusted peak shifts are denoted A_{obs} and A_{inst} respectively. The FWHM of the five peaks at a time delay of 2 ps are 13 ± 0.2, 50 ± 8, 25 ± 0.9, 55 ± 0.9 and 71 ± 3 cm^{-1} in ascending order of Raman shift frequency. The bandwidth of the 534 cm^{-1} mode and it's overtone at 1068 cm^{-1} are narrower than peaks involving the 1392 cm^{-1} coordinate suggesting that the C=C stretch is much more strongly coupled to other vibrational coordinates than is the in-plane bending of the cyano groups.

All the peaks blue-shift over the early solvation time except for the difference frequency at 858 cm^{-1} which red-shifts. The observed blue-shift of the 534 cm^{-1} fundamental ($A^{534}_{1,obs} = 1.8 \pm 1.7$) is much smaller than that of the 1392 cm^{-1} fundamental ($A^{1392}_{1,obs} = 7.7 \pm 1.7$ cm^{-1}) before accounting for convolution. With the scaling factors is applied, the frequency shifts

of the two fundamentals are similar in magnitude ($A^{534}_{1,inst}$ = 16 ± 14 cm^{-1} and $A^{1392}_{1,inst}$ =21 ± 5 cm^{-1}). Furthermore the sum of peak shifts of the fundamentals agree with the peak shift of the combination band at 1926 cm^{-1} ($A^{534}_{1,inst} + A^{1392}_{1,inst} \approx A^{1926}_{1,inst}$ cm^{-1}). The peak shift of the overtone of the 534 also shows coarse agreement with the shift of fundamental multiplied by two. This result lends credence to both the assignment and our analysis technique. The difference peak at 858 cm^{-1} red-shifts by 60 cm^{-1} more than would be expected by the difference of the fundamental peak shifts ($A^{1392}_{1,inst} - A^{534}_{1,inst} > A^{858}_{1,inst}$).

Interestingly, the peak at 858 cm^{-1} also shows a intensity gain over the time delays of 1.4 ps while the other peaks decay over this period. The relative intensity of the difference band at 858 cm^{-1} to that of the combination band at 1926 cm^{-1} is analyzed in the SI. At early times a relative intensity of ∼0.4 is measured which quickly increases to ∼1.0 with a time constant of ∼300 fs. An interpretation of these data will be discussed in the context of non-linear stimulated Raman pathways.

3.5 Discussion

The Effect of Solvation on Electronic Coupling

We state by discussing the effect of specific vibrational coherences on the intermolecular electronic coupling and the rate of charge recombination. It is proposed that the 153 cm^{-1} mode may increase the electronic coupling while reorganization of solvent may actually decrease it by localizing the excited electron. Next we discuss the effect that the reorganization of the solvent shell has on the intramolecular TCNE vibrations. Finally, the behavior of the excited state FSRS difference band is characterized.

The parallel and magic angle polarization of the transient absorption signal (Fig. 3.5(b)) evolve with the same two fast time constants (0.11 and 1.4 ps). These time constants match literature values for the reorganization of the DCM solvent shell.[70, 107] Dynamic solvation results in the decay of the stimulated emission on a timescale faster than the decay of the excited state population ($\Gamma_{S_1S_0} = 5.9 \pm 0.2$ ps) indicating that the transition dipole moment is sensitive to the solvent coordinate. We postulate that the restructuring of the solvent shell around the nascent contact ion pair results in a localization of the electron on TCNE and the hole on ClN, a process often called charge localization or polaron formation.[51] The localization of the electron decreases the intermolecular orbital overlap and accordingly decreases the transition dipole, $\mu_{S0S1}(q_S(\Delta t))$. The generalized solvent coordinate, $q_S(\Delta t)$, is a function of time delay after the initial excitation. The same solvation which induces a localization of the electron in the LUMO of the acceptor would also result in a increase in an excited state absorption transition dipole, μ_{S_nS1}, if that transition involves $\pi* \leftarrow \pi$ orbitals which are themselves localized on the acceptor. The latter result has been observed in our previous work on a similar charge transfer complex.[107] Using time-dependent DFT, the orientation of the stimulated emission transition dipole μ_{S1S0} was calculated to lie between the ClN and TCNE molecules. The excited state absorption is not observed with parallel

polarization and persists longer than the stimulated emission in the near infrared. The transition dipole, μ_{S_nS1} must therefore lie normal to the initial excitation, approximately in the plane of the molecules.

Having established the orientation of the excited state absorption in the molecular frame we seek to understand the electronic character of the transition. Similar anisotropic excited state absorption dynamics were observed in CT complexes of pyrene:TCNE and hexamethylbenzene:TCNE suggesting that the signal originates from $TCNE^{\bullet-}$.[44, 92] The FSRS peaks correspond to vibrations that are localized on TCNE. Their amplitudes (Fig 3.9) track the 5.9 ps decay of the excited state absorption. This suggests that the electronic transition is also localized on TCNE. The most promising assignment of the excited state absorption is to a transition similar to the $D_1 \leftarrow D_0$ transition of the $TCNE^{\bullet-}$ radical anion. A unrestricted time dependent DFT calculation of $TCNE^{\bullet-}$ shows that this transition dipole, $\mu_{D_1D_0}$ is oriented along the C=C bond of TCNE in the plane of the molecule congruent with the polarized transient absorption results. On the ground state the onset of this transition is observed at 490 nm which is much higher in energy than the onset of the excited state absorption at ∼860 nm. A possible explanation is that the correlation between the electrons of the nascent contact ion pair is responsible for a large redshift of the doublet absorption band of $TCNE^{\bullet-}$.

Excited State Vibrational Analysis

The oscillatory signal with frequencies of 153 and 534 cm^{-1} originate from excited state coherences localized on $TCNE^{\bullet-}$. The 534 cm^{-1} peak most likely has a longer dephasing time than the other peaks and therefore becomes more pronounced at longer time delays. The 278 and 291 cm^{-1} signals correspond to coherent motion localized on DCM although it is not completely clear whether these are excited or ground state vibrational wavepackets. It has been shown that Raman vibrations of the solvent proximate to a chromophore can be resonantly enhanced through a molecular near-field effect.[110–112] Therefore an excited state Raman wavepacket must also be launched along those solvent coordinates that stabilize the redistribution of electron density. To stabilize the nascent contact ion pair, both the intramolecular Cl-bending mode at 278 cm^{-1} and various inhomogenious librational coordinates with frequencies around ∼30 cm^{-1} must be coherently displaced after CT excitation. The sliding window Fourier transform analysis (Fig. 3.7) indicates that the 278 cm^{-1} mode is indeed frequency modulated, leading to side bands in the full-window FFT. This is to be expected since the time-constants with which the stimulated emission decays ($\tau_1 = 0.11$ ps, $\tau_2 = 1.4$ ps) correspond to energies of 300 and 24 cm^{-1} respectively. The dielectric response of dichloromethane has a resonance frequency at 30 cm^{-1} consistent with the splitting of the observed side bands in the impulsive spectrum.[113]. Direct observation of the 30 cm^{-1} librational coordinate is likely obscured by the biexponential population decay. This is a clear cut example of a frequency modulated free induction decay which highlights the limitation of the full-window Fourier transform in analyzing excited state impulsive time domain data.[114]

The fundamental FSRS frequencies at 534 and 1392 cm^{-1} in Figure 3.8 correspond to an in-plane bending of the TCNE cyano groups and the symmetric stretch of the central C=C double bond, respectively. The ground state solution phase resonance Raman reports that the frequency of the C=C stretch decreases from 1565 in neutral TCNE to 1421 cm^{-1} in $TCNE^{\bullet-}$ (Fig 3.3).[68] A second peak is observed with a frequency of 1390 cm^{-1} corresponding to the C=C stretch of the distorted contact ion pair. This assignment is validated by examination of the literature.[99] In crystals of $TCNE^{-}K^{+}$ and $TCNE^{-}Na^{+}$, a doublet is observed at 1421 and 1370 cm^{-1} and at 1430 and 1380 cm^{-1}, respectively. The red-shift of the doublet when the cation ion is changed indicates that the C=C stretching frequency is sensitive to the proximity and electron affinity of the counter ion. The doublet itself arises from crystal field splitting of the two different $TCNE^{\bullet-}$ molecules within the unit cell.[99] When the resonant excitation wavelength is changed from 514.5 nm to 488 nm, the relative intensity of the 1421 cm^{-1} mode to the 1370 cm^{-1} mode is increased by a factor of $\sim$5 indicating that this coordinate is coupled to the electronic transition of the radical anion salt. In other crystal morphologies, such as $TCNE^{-}Rb^{+}$, only one TCNE molecule is present per unit cell and correspondingly a single C=C stretching band at 1431 cm^{-1} is observed.[115]

In the time-resolved FSRS spectra, the close proximity of the $TCNE^{\bullet-}$ to the $ClN^{\bullet+}$ counter ion is enforced by the resonant excitation of charge transfer band. In the FSRS spectrum a broad C=C stretching band is observed at the average frequency of this C=C stretching doublet (1392 $cm^{-1} \approx (1370\ cm^{-1} + 1421\ cm^{-1})/2$) but red-shifted from the solution phase frequency by 29 cm^{-1}. The redshift of the C=C stretching frequency can be related to the effect of contact ion pair formation. Indeed the sensitivity of the C=C stretch frequency to the inhomogeneous distribution of orientations of contact ion pair might explain the disparity in peak widths of the 1392 cm^{-1} mode (FWHM $\approx$ 55) and the 534 cm^{-1} mode (FWHM $\approx$ 13). Finally we propose that the 29 cm^{-1} redshift of the C=C stretching frequency can in part be attributed to the out-ouf-plane distortion along the 153 cm^{-1} b_{1u} coordinate. Were this the case, the frequency of the C=C stretching coordinate should oscillate with the frequency of 153 cm^{-1} through a 2D-FSRS pathway as has been characterized previously.[49, 104, 107, 116]

Analysis of Difference Bands

We set about analyzing the contribution to the signal by the three non-linear pathways by considering the combination band at 1920 cm^{-1} (939 nm) as an internal standard with which to analyze the features of the 858 cm^{-1} difference band (854 nm). Figure 3.5(a) shows that the excited state absorption is present at 854 nm but has diminished by 939 nm. Therefore pathways (B) and (C) are accessible at the resonant wavelength of the difference band but not at the wavelength of the combination band which must arise from pathway (A). If the combination band or difference band were to arise purely from pathway (A), a comparison of their intensities can be understood analytically since their transition polarizabilities are approximately equal. This is a result of the commutative property of the Franck-Condon factors (see SI). However via pathway (A) the Raman portion of the difference band transition

can only be initiated from $|1,0\rangle$ while a combination band can be initiated from $|0,0\rangle$. As such pathway (A) will favor the combination band. On the ground state the ratio of intensities through pathway (A) would be:

$$I_{1,1\leftarrow 0,0}/I_{0,1\leftarrow 1,0} = e^{\frac{-\hbar\omega_{low}}{k_B T}} = 0.08. \tag{3.6}$$

However the prepared state in this time resolved experiment is generated by actinic excitation. At time delays earlier than vibrational energy redistribution (typically on the order of 10 ps)[117, 118] to zeroth order approximation if a white light actinic pump is used ratio of intensities through pathway (A) follows as:

$$\begin{aligned} \frac{I_{0,1\leftarrow 1,0}}{I_{1,1\leftarrow 1,0}} &= \left| \frac{\langle 1, 0^{S_1} | 0, 0^{S_0} \rangle}{\langle 0, 0^{S_1} | 0, 0^{S_0} \rangle} \right|^2 \\ &= \frac{|\Delta|^2}{2} \end{aligned} \tag{3.7}$$

The dimensionless displacement of the 534 cm^{-1} coordinate has been reported for a similar charge transfer system TCNE:hexamethylbenzene at 0.54.[26] Therefore a ratio of the intensity of the difference band to that of the combination band should be $\sim$0.15. From Figure A.2, at early times (75 fs) we measure a relative intensity of $\sim$0.4. The relative intensity rapidly increases to a value of $\sim$1 with a time constant of 300 $\pm$ 70 fs. The ratio of intensities is not consistent with coupling through pathway (A) exclusively. We propose that dynamic solvation on this time scale induces a shift in the excited state absorption resonance condition ($\omega_{S_n S_1}$) which causes pathway (B) or (C) to be enhanced while pathway (A) which contributes to the combination band is diminished.

Evidence for alternative FSRS pathways can also be found by analyzing the shift of the instantaneous frequencies (Table 3.1). This is the first self-consistent check of our ability to measure dynamic peak shifts in a FSRS spectrum. The instantaneous frequency of the combination band at 1926 cm^{-1} blue-shifts by a total of 34 $\pm$ 5 cm^{-1}. This value agrees with the sum of the blue-shifts of the fundamentals (41 $\pm$ 15 cm^{-1}). The overtone at 1068 cm^{-1} also shows a net blue-shift in coarse agreement with twice the shift of the 534 cm^{-1} peak. However the difference band at 858 cm^{-1} red-shifts by 60 cm^{-1} more than would be expected by the difference of the fundamentals. This behavior could indicate the presence of pathway (C) gaining intensity relative to pathways (A) and (B) over the course of dynamic solvation. As mentioned earlier, pathway (C) prepares a coherence on electronic state S_n with frequencies that are commonly redshifted because the nuclei have not relaxed at the time of the Raman emission. The preparation of coherent difference frequencies can originate from any vibrational state $|S_1\rangle|n_i, n_j\rangle$ via the VFSRS pathway (C), but can only be accesses from vibrationally hot states $|S_1\rangle|1,0\rangle$ and $|S_1\rangle|0,1\rangle$ via pathways (A) and (B), respectively.

We can not unequivocally identify which non-linear pathways are contributing to the observed signal and with what magnitudes. However through careful experimentation their contribution may be resolved. If the actinic pump is tuned to the red edge of the CT

band (700 nm) then only the ground vibrational state $|S_1\rangle|0,0\rangle$ is prepared. If pathway (A) is operative then the combination band will have intensity but the difference band will be diminished. On the other hand if pathway (B) is exclusively operative, neither the combination band nor the difference band will have intensity since they originate from $|S_1\rangle|0,1\rangle$ and $|S_1\rangle|1,1\rangle$, respectively. Finally if pathway (C) is operative then the frequency of the VFSRS peaks will red-shift as the Raman pump is tuned to bluer wavelengths because higher-lying anharmonic vibronic transitions are stimulated. On the other hand the FSRS and IRGS frequencies stimulated via pathways (A) and (B) are insensitive to Raman pump wavelength.

The presence of alternative non-linear pathways in a time evolving FSRS spectrum has important implications beyond the appearance difference frequencies. When the state prepared after actinic excitation is vibrationally excited, fundamental scattering from the inverse Raman gain pathway (B) may contribute as a gain or possibly a loss signal on the Stokes side of the Raman pump. Likewise the standard FSRS pathway initiated from vibrationally excited states may appear on the anti-Stokes side of the Raman pump analogous to spontaneous anti-Stokes Raman. Furthermore most time-resolved FSRS experiments rely on resonance enhancement of the excited state signal. When both the Raman pump and Stokes probe are on-resonance with an excited state absorption or stimulated emission, the VFSRS pathway may be operative. As the Raman pump is swept to bluer wavelengths this VFSRS signal should redshift as higher vibronic coherences are prepared. When FSRS instruments are built with more widely tunable blue and UV Raman pump pulses that are resonant with more localized electronic states, it is likely that combination bands and difference frequencies will become more important to analyzing time evolving stimulated Raman signals.

A few illuminating points can also be made about instantaneous frequencies. The observed frequency of a combination band may not be equal exactly the sum or difference of the fundamentals if there is a disparity in the peak widths and a large peak shift. For example, suppose two fundamentals with a narrow bandwidths were red-shifting. If the corresponding combination band were broad, it would appear with an observed frequency higher than the sum of the fundamentals because it samples a different part of the free induction decay. A FSRS peak shift might be caused by a change in a harmonic frequency or it could be the result of a change in anharmonicity. A blue-shift of the harmonic frequency of the high frequency fundamental causes both the combination band and difference band to blue-shift. A blue-shift in the harmonic frequency of the low frequency mode causes the combination band to blue-shift and the difference band to red-shift. Finally a decrease in anharmonicity between the coordinates causes the combination band to blue-shift but does not affect the difference frequency. Therefore careful comparison of combination and difference frequencies allows for measurement of time-dependent excited state anharmonicity.

3.6 Conclusion

In the photoexcited TCNE:ClN complex, three low frequency coordinates were indicated to induce a localization of the electron. These coordinates have frequencies of ∼30, 153 and 278 cm^{-1} corresponding to the librational frequency of the DCM solvent shell, a b_{1u} out-of-plane bending mode of TCNE and the symmetric Cl bending mode of DCM, respectively. After the vibrational wavepacket has mostly dephased, the excited state distortion still has a marked effect on the rate of the charge recombination by altering the intermolecular orbital overlap.[45] The time-resolved FSRS spectra display two important reporter modes. The central C=C stretching frequency of $TCNE^{\bullet-}ClN^{\bullet+}$ at 1392 cm^{-1} is redshifted from that of free $TCNE^{\bullet-}$ due to the proximity of the contact ion pair. Difference bands, combination bands and overtones are observed in FSRS spectra when the Raman pump is strongly resonant with a localized high symmetry electronic transitions such as those afforded by charge transfer excited radical dimers. By accounting for the fundamental time-frequency trade off, the frequency shift of the combination band can be related to the frequency shift the fundamentals. The unusual intensity and frequency behavior of the difference band is interpreted in the context of alternative FSRS pathways including inverse Raman gain scattering and vertical femtosecond stimulated Raman scattering.

Chapter 4

Reevaluation of Resonance Enhanced Two-Dimensional Excited State Femtosecond Stimulated Raman Spectroscopy of Photoexcited Charge Transfer to H_4-TCNQ and F_4-TCNQ: Fifth-Order Coupling Within the Harmonic Approximation

This work will be submitted to the *The Journal of Physical Chemistry A* by Scott R. Ellis, Daniel R. Dietze, Myeongkee Park and Richard A. Mathies

4.1 Abstract

The time resolved femtosecond stimulated Raman spectrum of F_4-TCNQ:1,3,5-trimethylbenzene (3MB) is presented. The two-dimensional excited state femtosecond stimulated Raman spectrum (2D-ES-FSRS) of the H_4-TCNQ: 1,2,4,5-tetramethylbenzene (4MB) complex is reevaluted within a more precise theoretical framework. In both systems the excited state signals are dominated by four analogous totally symmetric fundamentals consisting of an elongation of the double bonds, and in-plane bending of the cyano groups and fluorines (or hydrogens) and the overtones, combination band and difference bands involving these four coordinates. The 2D-ES-FSRS spectrum reveals that the combination and difference bands involving the low frequency mode that has been impulsively excited are oscillating more intensely than the other three fundamental vibrations. This new analysis indicates that cross-peaks in a *resonant* 2D-ES-FSRS spectrum may appear because two vibrational coordinates are coupled to the same electronic transition and does not necessarily implicate anharmonicity between the vibrations.

4.2 Introduction

Direct measurement of anharmonic coupling between Raman active degrees of freedom has long been of great interest.[119] Measuring coherent Raman couplings on an excited electronic state would provide even more interesting information as the excited state potential energy surface can be strongly anharmonic in the vicinity of a conical intersection or reaction coordinate.[49, 116] The first measurement of 2D-ES-FSRS signal was in of wild type green fluorescent protein in 2009 by Fang et al.[49] The C=O stretching mode of the chromophore phenol ring at $\sim$1280 cm^{-1} and C=N stretching mode of the imidazole at $\sim$1585 cm^{-1} were shown to oscillate out of phase with a period of 280 fs cooresponding to a low frequency wagging motion of the chromophore. Also in 2009, Wilson et al. showed that the 2D-FSRS signals were too weak to be observed on the ground state in bulk solvents as they were obscured by a much stronger cascading third-order signal.[55] In 2011, Weigel et al. observed the oscillations in a 300 cm^{-1} FSRS peak of flavin adenine dinucleotide with it's own frequency thus resolving the first diagonal 2D-ES-FSRS peak.[54] Unfortunately assignment of this excited state vibration eluded them.

In our past report, we presented the 2D-ES-FSRS of a photoexcited intermolecular charge transfer complex H_4-TCNQ:4MB. An intense peak at 1271 cm^{-1} displayed strong frequency and amplitude oscillations. The initial assignment of this 1271 cm^{-1} signal was to a non-totally symmetric b_{3g} coordinate. However, our recent work provided experimental evidence and theory for the presence of difference bands in excited state FSRS spectra via a vibrationally hot excited state population FSRS pathways (ES-P-FSRS).[15, 120] This prompts an assignment of this 1271 cm^{-1} mode to a difference frequency of symmetric fundamental vibrations (1616 - 345) cm^{-1} which is more reasonable given that non-totally symmetric vibrations cannot be displaced in an electronic transition when symmetry is maintained.

In light of this reassignment the 2D-ES-FSRS adopts new significance. In this report we show that couplings are strongest at combination band frequencies and difference frequencies of the coordinates involving the low frequency mode that is impulsively excited. We present an alternative explanation that the measured couplings are not the result of a anharmonicity near a conical intersection. Rather, we find that the observed coupling are more general, appearing when two coordinates are displace along a given resonant electronic transition such as a excited state absorption. In reactive systems, where the excited state lifetime is shorter than the vibrational dephasing, the 2D-ES-FSRS may indeed report on anharmonicity that is critical to the photochemical reaction; however this deduction is not supported by our current results.

Theory of 2D-Excited State FSRS

The theory of prepared FSRS[100] and 2D-ground state FSRS[101, 121] have been described previous. Also in our previous work we showed that under resonance with a localized highly symmetric electronic transition a combination, difference and overtone bands can become gain substantial intensity if via a second-plus third-order pathway.[120] Here we will summarize some nuances inherent to the fifth-order 2D-ES-FSRS pathway using three different color pulses each resonant with an electronic transition.

The FSRS pulse sequence is presented in Figure 4.1. Along with an example of a one coordinate displaced vibronic system. In the subsequent wave energy level mixing diagrams and double-sided Feynman diagrams we invoke a two coordinate displaced vibronic system. The vibrational state within the manifold of a given electronic state is denoted as $|\nu_{low}, \nu_{hi}\rangle$ or the conjugate transpose as $\langle\nu_{low}, \nu_{hi}|$. Here ν_{low} is the quanta of energy in the low frequency mode and ν_{hi} is the quanta of energy in the high frequency mode.

In all of the above pathways initial impulsive pump pulse must be shorter than the period of a low frequency vibration so as to create a vibrational coherence on the excited electronic state such as $|S_1\rangle|1,0\rangle\langle 0,0|\langle S_1|$. Pathway (A) is a impulsive excited state absorption that appears in the third-order susceptibility and has been described previously.[71] The phase of the coherence state over the time delay Δt determines the overlap integral of the projection onto an higher lying excited electronic state. Pathway (A) is included here for comparison with the higher order 2D-Stimulated Raman pathways (B) (C) and (D) in which the phase acquired over Δt effects the lineshape of the signal in the subsequent stimulated Raman process.

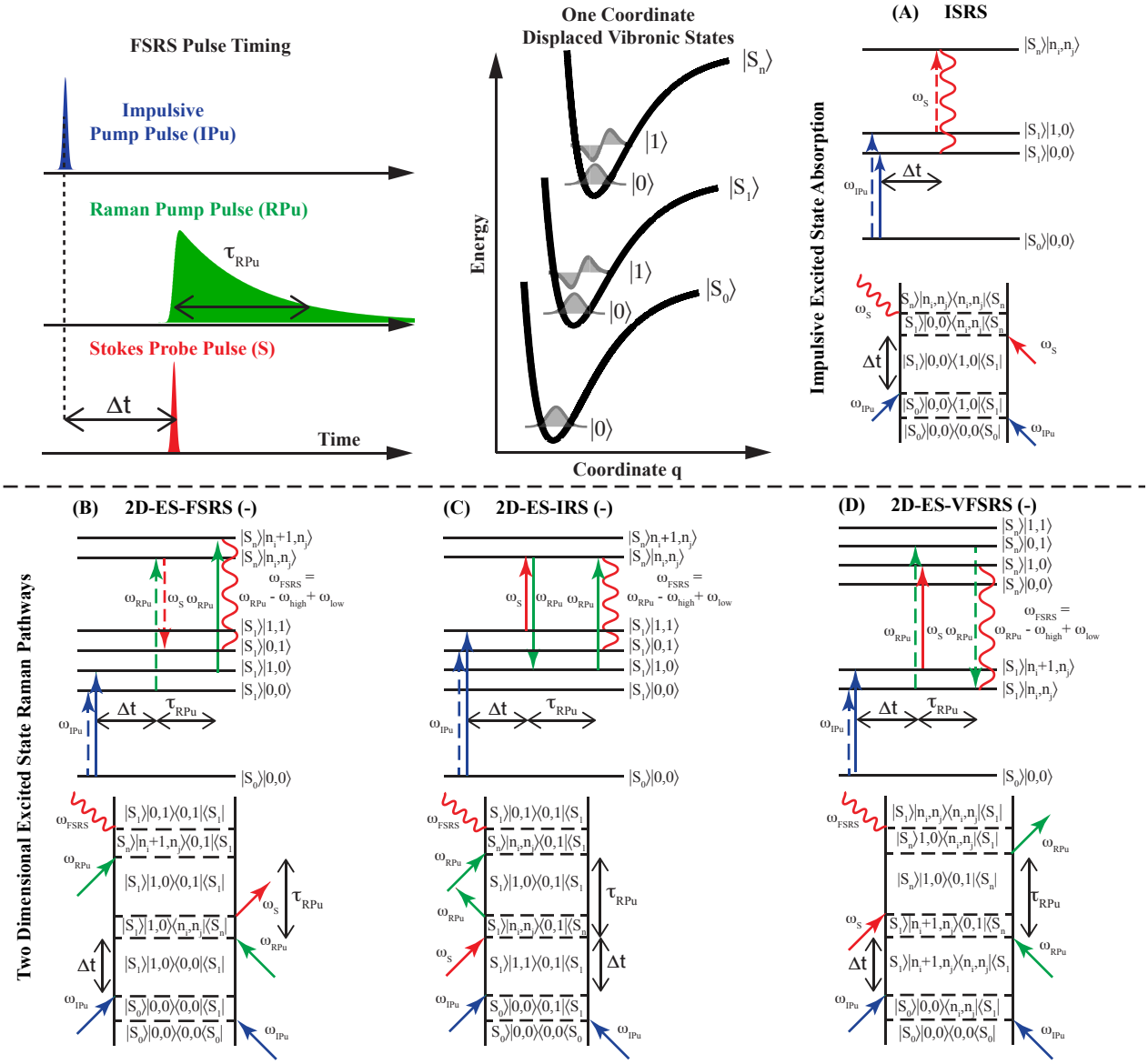

Figure 4.1: FSRS pulse sequence (top left) and one-coordinate potential energy surfaces of three displaced anharmonic electronic states $|S_0\rangle$, $|S_1\rangle$ and $|S_n\rangle$. Wave-mixing energy level diagrams and double sided Feynman diagrams (A)-(D) relevant to this work. Pathway (A) corresponds to an oscillatory excited state absorption loss signal. Pathways (B) (C) and (D) resulting in oscillating narrow band dispersive Lorentzian signals at a difference Raman shift frequency. The vibrational state within the manifold of a given electronic state is denoted as $|\nu_{low}, \nu_{hi}\rangle$ or the conjugate transpose as $\langle\nu_{low}, \nu_{hi}|$. The action of the impulsive pump (IPu, blue), Raman pump (RPu, green) and Stokes Probe (S, red) on the left and right side of the density matrix are indicated with solid and dash arrow respectively. The coherence evolution time is denoted Δt and the picosecond Raman pump pulse duration is labeled τ_{RPu}.

The time evolution of the density matrix via pathway (B) can be written as follow:

$$
\begin{aligned}
&[\rho^{(5)}(t)]_{2D-ES-FSRS} \\
&= (\frac{1}{i\hbar})^5 \int_{-\infty}^{t} dt_1 \int_{-\infty}^{t_1} dt_2 \int_{-\infty}^{t_2} dt_3 \int_{-\infty}^{t_3} dt_4 \int_{-\infty}^{t_4} dt_5 \sum_{n_i,n_j} \\
&\times e^{(i(\omega_{S_n S_1}+(n-1)\omega_{hi}+(n+1)\omega_{low})-\Gamma_{S_n S_1})(t-t_1)} H'_{S_n,n_j+1,n,S_1,1,0}(E_{RPu},t_1) \\
&\times e^{(i\omega_{low}-\Gamma_{1000})(t_3-t_4)} H'_{S_1,1,0,S_1,0,0}(E_{IPu},t_4) \\
&\times \rho \\
&\times H'_{S_0,0,0,S_1,0,0}(E^*_{IPu},t_5) e^{-(i\omega_{S_1 S_0}+\Gamma_{S_0 S_1})(t_4-t_5)} \\
&\times H'_{S_1,1,0,S_n,n_j,n}(E^*_{RPu},t_3) e^{-(i(\omega_{S_n S_1}+(n-1)\omega_{low}+n\omega_{hi})+\Gamma_{S_1 S_n})(t_2-t_3)} \\
&\times H'_{S_n,n_j,n,S_1,0,1}(E^*_{S},t_2) e^{(-(i(\omega_{hi}-\omega_{low})+\Gamma_{1001})(t_1-t_2)}
\end{aligned}
\tag{4.1}
$$

For simplicity of notation we have assumed that the frequency of the vibrations are the same on all the electronic states. The dephasing rate of the low frequency vibration, the high frequency vibation, the difference band and the combination band are denoted as $\Gamma_{1000}, \Gamma_{0100}, \Gamma_{1001}, \Gamma_{0011}$, respectively. The dephasing of a state has a electronic and vibrational component for example the state $|S_1\rangle|1,0\rangle\langle 0,0|\langle S_0|$ dephases with a rate $\Gamma_{S_1S_0}+\Gamma_{1000}$. It is generally observed that electronic dephasing occurs much faster than vibrational dephasing which in turn is faster than electronic population relaxation ($\Gamma_{S_1S_0} > \Gamma_{0010} > \Gamma_{S_1S_1}$). We have used the approximation:

$$\Gamma_{S_1S_0} + \Gamma_{1000} \approx \Gamma_{S_1S_0} \tag{4.2}$$

$$\Gamma_{S_1S_1} + \Gamma_{1000} \approx \Gamma_{1000} \tag{4.3}$$

Equation 4.1 simplifies by approximating that the Raman pump pulse is a continuous wave electric field while the impulsive pump and Stokes probe pulses are ultrashort Gaussian pulses with a spectral bandwidth which spans ω_{low}. Note also that the first coherence time delay between the impulsive pump and pulse the first interaction of the Raman pump given by $t_3 - t_4$ in Equation 4.1 is the time delay Δt that is explicitly swept out in a FSRS experiment (Fig. 4.1). We assume no coordinate dependence of the electronic transition dipoles allowing us to extract the two coordinate Franck-Condon factors. The values H' are off diagonal matrix elements that determine the projection of the states by a given time dependent perturbation.

$$H'_{S_0,0,0,S_1,0,0}(E^*_{IPu},t_5) = -E^*_{IPu}\mu_{S0S1}\langle 0,0|0,0\rangle\sqrt{2\pi}\tau_S e^{(-t_5-z/c)^2\tau^2_{IPu}/2} e^{i\omega_{IPu}(t_5-z/c)} \tag{4.4}$$

$$H'_{S_1,1,0,S_0,0,0}(E_{IPu},t_4) = -E_{IPu}\mu_{S1S0}\langle 1,0|0,0\rangle\sqrt{2\pi}\tau_S e^{(-t_4-z/c)^2\tau_{IPu}^2/2}e^{-i\omega_{IPu}(t_4-z/c)} \tag{4.5}$$

$$H'_{S_1,0,1,S_n,n_i,n_j}(E^*_{RPu},t_3) = -E^*_{RPu}\mu_{S1Sn}\langle 0,0|n_i,n_j\rangle e^{i\omega_{RPu}(t_3-z/c)} \tag{4.6}$$

$$\begin{aligned} &H'_{S_n,n_i,n_j,S_1,0,1}(E^*_S,t_2) \\ &= -E^*_S\mu_{S_nS1}\langle n_i,n_j|0,1\rangle\sqrt{2\pi}\tau_S e^{(-t_2-z/c)^2\tau_S^2/2}e^{-i\omega_S(t_2-z/c)} \end{aligned} \tag{4.7}$$

$$H'_{S_1,1,0,S_n,n_i,n_j}(E_{RPu},t_1) = -E_{RPu}\mu_{S1S_n}\langle 1,0|n_i+1,n_j\rangle e^{-i\omega_{RPu}(t_1-z/c)} \tag{4.8}$$

The polarization emits the signal by the closure of the density matrix.

$$\begin{aligned} &P^{(5)}_{(A)}(t,\Delta t) \\ &= (\frac{1}{i\hbar})^5 C(\ell,\tau_{IPu},\omega_{IPu},\tau_S,\omega_S,\omega_{RPu})\,|E_{IPu}|^2\,|E_{RPu}|^2\,E^*_S \\ &\times |\mu_{S_1S_0}|^2\,|\mu_{S_nS_1}|^4 \\ &\times \sum_{n_i,n_j}\frac{\langle 0,1^{S_1}|n_i+1,n_j^{S_n}\rangle\langle n_i+1,n_j^{S_n}|1,0^{S_1}\rangle}{\omega_{RPu}-\omega_{S_nS_1}-n_i\omega_{low}-n_j\omega_{hi}-i\Gamma_{S_nS_1}} \\ &\times \frac{\langle 1,0^{S_1}|0,0^{S_0}\rangle\ \langle 0,0^{S_0}|0,0^{S_1}\rangle}{(\omega_{IPu}-\omega_{S_1S_0}-\omega_{low}-i\Gamma_{S_1S_0})(\omega_{IPu}-\omega_{S_1S_0}+i\Gamma_{S_1S_0})} \\ &\times \frac{\langle 0,0^{S_1}|n_i,n_j^{S_n}\rangle\langle n_i,n_j^{S_n}|0,1^{S_1}\rangle}{\omega_{RPu}-\omega_{S_nS_1}-n_i\omega_{low}-n_j\omega_{hi}+i\Gamma_{S_nS_1}} \\ &\times e^{(i(\omega_{RPu}-\omega_{hi}+\omega_{low})-\Gamma_{1001})t}e^{(i\omega_{low}-\Gamma_{1000})\Delta t} \end{aligned} \tag{4.9}$$

The Fourier transform is performed across t. The 2D-ES-FSRS signal at each time delay Δt is:

$$\begin{aligned} &P^{(5)}_{(A)}(\omega_{FSRS},\Delta t) \\ &\propto \frac{(\cos(\omega_{low}\Delta t)+\mathrm{i}\,\sin(\omega_{low}\Delta t))(\omega_{FSRS}-\omega_{RPu}-\omega_{hi}+\omega_{low}+i\Gamma_{1001})e^{-\Gamma_{1000}\Delta t}H(\Delta t,0)}{(\omega_{FSRS}-\omega_{RPu}-\omega_{hi}+\omega_{low})^2+\Gamma^2_{1001}} \end{aligned} \tag{4.10}$$

Here $H(\Delta t,0)$ is the Heaviside step function. The signal arises from the imaginary part of the induced polarization which acquires a phase over Δt. Equation 4.10 is evaluated and presented in Figure 4.2.

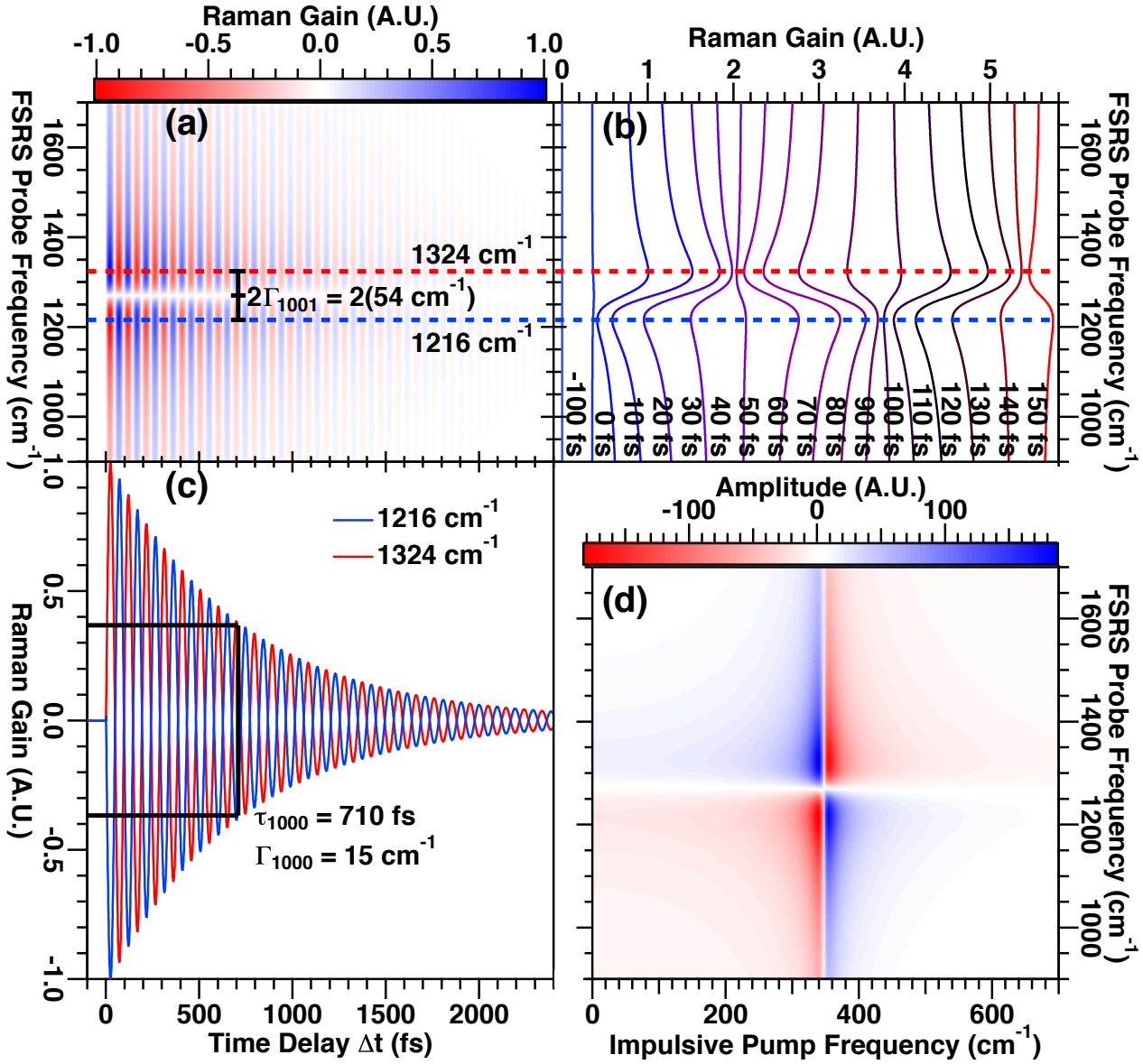

Figure 4.2: (a) 2D-ES-FSRS spectrum simulated from Eq. 4.10 with parameters $\omega_{low} = 345$ cm^{-1}, $\omega_{hi} = 1616$ cm^{-1}, $\Gamma_{1000} = 15$ cm^{-1}, $\Gamma_{1001} = 54$ cm^{-1}. A dispersive Lorentzian centered around $\omega_{hi} - \omega_{low}$ oscillates and decays as a function of Δt. (b) Selected 2D-ES-FSRS spectra at 10 fs intervals over the first period and a half of the low frequency coordinate. The maxima and minima of the dispersive signal are indicated by blue and red dashed lines at $\omega_{hi} - \omega_{low} \pm \Gamma_{1001}$. (c) The time evolution of the signal at a Raman shift frequencies of 1216 cm^{-1} and 1326 cm^{-1}. The rate of decay is indicated by solid black lines. (d) The 2D-ER-FSRS spectrum where the real amplitude Fourier transform has been performed over Δt producing the impulsive pump frequency axis and a two-dimensional dispersive Lorentzian signal.

At early times the signal from pathway (B) appears as a dispersive Lorentzian (the first derivative of a Lorentzian function) centered around $\omega_{RPu} - \omega_{hi} + \omega_{low}$ which oscillates with a frequency of ω_{low} as a function of Δt. Analogous 2D-ES-FSRS (F) and (+) pathways are presented in the SI. The 2D-ES-FSRS (F) pathway describe scattering at a fundamental frequency of $\omega_{RPu} - \omega_{hi}$ and 2D-ES-FSRS (+) pathway describes a signal at a combination frequency $\omega_{RPu} - \omega_{hi} - \omega_{low}$, respectively. The net amplitude of the 2D-ES-FSRS signals are zero which is distinct from the usual excited state population FSRS pathway which contribute a real Lorentzian amplitude to the signal. If the 2D-ES-FSRS signals were added to a real lorentzian signal from an excited state population it would appear that the peak center frequency were oscillating in time.

Many features arise from this theoretical analysis. The 2D-ES-FSRS signal goes a $\mu_{S_nS_1}^4 \mu_{S_1S_0}^2$ while a cascading third-order signal goes at $\mu_{S_1S_0}^6$ of the solute or as the solvent polarizability raised to the third power. Systems can be explored with two electronic transitions where the final four dipole field interactions are much more intense than the first two ($\mu_{S_nS_1} > \mu_{S_1S_0}$). This resonantly enhances the 2D-ES-FSRS pathway relative to the third-order cascading ground state Raman signal.

Under off-resonant conditions 2D-FSRS coupling between the states $|1,0\rangle$ and $|0,1\rangle$ occurs exclusively through anharmonicity of the vibrational wavefunctions.[57, 119] However, if three resonant electronic states are employed, the 2D-ES-FSRS pathway can be accessed within the harmonic approximation. This can be understood by noting that all the Franck-Condon factors in equation 4.9 is non-vanishing if the S_0 and S_1 states are displaced along Q_{low} and S_1 and S_n state are displaced along both Q_{low} and Q_{hi}. These same conditions also produce difference bands and combination bands via the usual ES-P-FSRS pathways described in our previous work.[120] The resonance conditions further enhance the 2D-ES-FSRS signal by effectively coupling the vibrational states.

There are some additional difference between the 2D-ES-FSRS pathway and the standard excited state population FSRS. The ES-P-FSRS pathway couples through a single vibronic resonance, the resonance condition for the 2D-ES-FSRS pathway (B) is spread out over two different vibronic states of S_n. Also the ES-P-FSRS pathway displays a gain feature at the same frequency as the Stokes field (ω_S) that stimulated it in the fourth dipole field interaction. However in pathway (B) the fourth dipole-field interaction occurs at a frequency different from the resulting 2D-ES-FSRS signal. Wilson et al. accounted for this effect by scaling the side bands by the square root of the ratio of the probe spectrum at the stimulating and detected wavelengths.[55]

Recent measurements[81–83, 102] indicate that there are likely alternative nonlinear pathways (C) and (D) which result in a similar oscillating dispersive signal at a difference frequency shift for the Raman pump under resonance conditions. A 2D-ES-Inverse Raman Scattering pathway (C) arises from a higher energy vibronic coherence being prepared by the impulsive pump pulse ($|S_1\rangle|1,1\rangle\langle 0,1|\langle S_1|$). The upward action of the Stokes probe pulse first and the downward action Raman pump field creates a second coherence state that is lower in energy than the first ($|S_1\rangle|1,0\rangle\langle 0,1|\langle S_1|$). The interference between these two coherences is unconverted in the frequency domain by a second action of the Raman pump

pulse.

The 2D-ES-Vertical FSRS pathway (D) can be understood by analogy to the prepared population VFSRS pathway. As before the impulsive pump pulse prepare any low frequency vibrational coherence ($|S_1\rangle|n_i+1, n_j\rangle\langle n_i, n_j|\langle S_1|$). The action of the Raman pump and Stokes probe pulses on opposite sides of the density matrix then prepares a second coherence on the S_n electronic state ($|S_n\rangle|1, 0\rangle\langle 0, 1|\langle S_n|$). Again the interference is upconverted by a second action of the Raman pump after τ_{RPu}. In a wavepacket description, the 2D-vertical FSRS pathway constitutes probing the curvature of the S_n potential energy surface from coordinates sampled by a wavepacket as it evolves from the ground state nuclear geometry Q_{S0} to the distorted excited state geometry. Such a signal could be useful albeit difficult to interpret.

All three pathways are coupled by the same transition dipoles and similar vibronic states.[54] For a given system there are subtle differences in the resonance denominator that would result in the contribution of each to vary based on the wavelengths of the pulses used.

4.3 Materials and Methods

Measurements of F_4-TCNQ

The methods employed in this work are the same as those reported in our previous works.[107, 120]. A solution with excess F_4-TCNQ in DCM was prepared. 1,3,5-trimethylbenzene was added slowly with stirring until an optical density of 0.7/mm at 540 nm was achieved. The solution was then filtered through the a 40 μm teflon filter to remove the excess F_4-TCNQ. The resulting solution has concentrations of 10 uM F_4-TCNQ and 0.4 M 1,3,5-trimethylbenzene, respectively. The solution was pumped through a 500 μm quartz cuvette. The pulse energies of the impulsive pump, Raman pump and Stokes probe pulses were, 180, 1300 nJ and 2.2 nJ respectively. In impulsive transient absorption experiments, the impulsive pump was chopped shot to shot. In excited state FSRS experiments, the Raman pump was chopped shot to shot and while the impulsive pump was shuttered once per temporal scan producing a few ground state spectra interspersed between many more excited state spectra.

Data Analysis

In our previous work we employed a least squares peak fitting to the FSRS probe spectrum at each time delay.[107] The oscillatory signal was then resolved in the fit peak frequencies and amplitudes. In this work, the 2D-FSRS spectrum is resolved directly and with fewer model specific assumptions by fitting each FSRS probe frequency to a second order exponential decay and Fourier transforming the oscillatory residual signal. In this way we can plot the excited state FSRS spectrum as it oscillate at a given frequency with a given phase. A illustration of this analysis procedure is presented in the SI.

4.4 Results

UV-Vis analysis of F_4-TCNQ:3MB

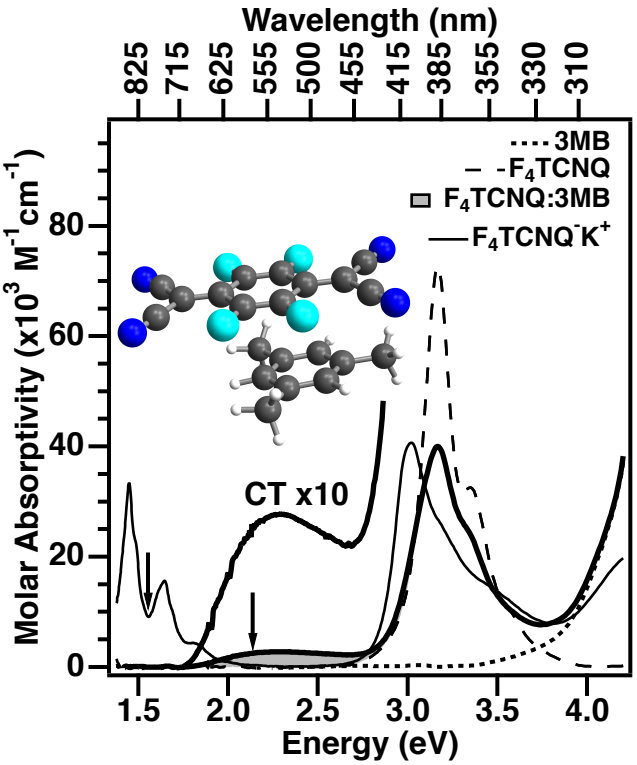

Figure 4.3: Ground state absorption spectra of 3MB (fine dashed line) F_4-TCNQ (coarse dashed line) isolated in solutions of DCM. The thick solid line shows the same concentration of F_4-TCNQ as a mixture in solution saturated with 3MB. The region of the charge transfer ban 450-750 nm has been shaded grey and also scaled by a factor of 10. of The absorption of chemically prepared K^+F_4-$TCNQ^-$ in acetonitrile (thin solid line) shows an absorption band with well resolved vibronic structure in the near IR. The molar absorptivity units of the Y-axis is analytical for all chemical species except for the charge transfer complex and the 3MB which have a molar absorption coefficients of $\epsilon_{535nm} = 5000 \pm 3000$ $M^{-1}cm^{-1}$ and $\epsilon_{280nm} = 28$ $M^{-1}cm^{-1}$, respectively. The DFT optimized structure of the complex is included. The fluorine atoms are represented by teal spheres. The center wavelength of the broadband impulsive pump and narrow band Raman pump pulses are indicated with arrows at 560 and 795.5 nm, respectively.

The nuclear and electronic structure of F_4-TCNQ is similar to that of H_4-TCNQ. One important difference is that the fluorine atoms are more inductively electron withdrawing than the hydrogen atoms. The inductive withdrawing effect lowers the reduction potential from 0.25 V in H_4-TCNQ to 0.16 V in F_4-TCNQ.[85] A decrease in reduction potential accompanies a redshifts the charge transfer band of complexes formed with F_4-TCNQ

(Eqn. 3.1). To offset this effect, the electron donor molecule was substituted from 1,2,4,5-tetramethylbenzene to 1,3,5-trimethylbenzene. The removal of an inductively donating methyl group increase the oxidation potential such that the steady state CT absorption of the complex would not redshift.

Figure 4.3 presents the absorption spectra of F_4-TCNQ and 3MB as a monomers in DCM. When the F_4-TCNQ solution is diluted with a DCM solution of saturated 3MB, a broad charge transfer band appears at 535 nm. The optical and binding properties of the F_4-TCNQ:3MB complex in DCM were determined by the Benisi-Hildebrand experiment to be $\epsilon_{535} = 5000 \pm 3000$ and $K_{eq} = 0.8 \pm 0.6$. In addition to the appearance of the charge transfer band interactions with the 3MB diminishes the molar absorptivity of the $\pi^* \leftarrow \pi$ absorption band of the F_4-TCNQ. This likely be a result of a partial donation of electron density from the HOMO of 3MB to the LUMO of the F_4-TCNQ.

When F_4-TCNQ is reduced with potassium iodide the solution turns green and a strong absorption band appears in the near IR ($\lambda_{max} = 856$ nm, thin solid line). This transition involves a $\pi^* \leftarrow \pi$ orbitals similar to that observed in neutral F_4-TCNQ at 391 nm and redshifted by 1.7 eV. This redshift is likely a result of the destabilization of ground state electron configuration by adding an unpaired spin as well as a stabilization of the excited state electron configuration by pairing the spin of the electron in the antibonding orbital. In the subsequent time-resolved optical experiments we will excite the charge transfer band with a very short impulsive pump pulse. This creates a vibrational coherenece on a transient intermolecular bi-radical species where the anion largely resides on the F_4-TCNQ.[120] The Raman pump and Stokes probe fields are then coupled with an excited state absorption transition with electronic character similar to that of radical anion absorption band in the near IR.

Impulsive Excited State Absorption Analysis of F_4-TCNQ:3MB

Figure 4.4 presents the transient absorption signal of F_4-TCNQ:3MB in the near infrared probe window. The excited state absorption signal gains intensity over the first picosecond with time constants of 0.12 ± 0.02 and 1.1 ± 0.2 ps before decaying with a time constant of 9 ± 2 ps. The increase in intensity of excited state absorption is likely due vibrational and librational reorganization of the solvent shell allowing for charge localization in the π^* orbital of F_4-TCNQ. The time-constant for charge recombination ($\tau_3 = 9\pm 2$ ps) is similar to the time constant in H_4-TCNQ:4MB of ($\tau_3 = 10.3\pm 0.2$ ps). This indicates that swapping the hydrogens for fluorines and removing a methyl group only weakly perturbs the intermolecular π-orbital overlap that determines the charge recombination. While the excited state population dynamics of the two systems are similar, the excited state vibration coherences are different.

The oscillatory component of the band integral over the region of 840 - 850 nm was extracted from three component exponential population dynamics. The signal is dominated by two frequencies of 298 and 343 cm^{-1} corresponding to totally symmetric bending vibrations of the cyano and fluorine groups of F_4-$TCNQ^{\bullet-}$ that are displaced in the initial charge transfer

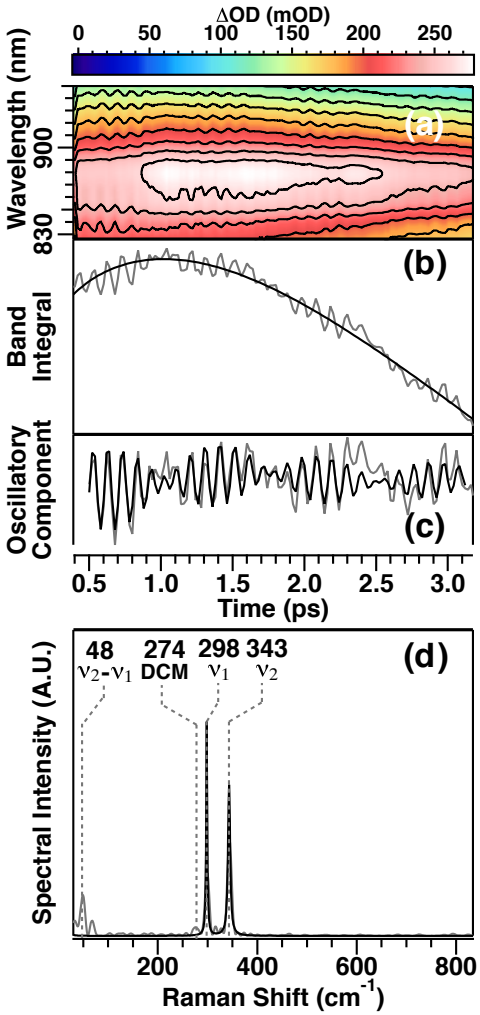

Figure 4.4: (a) Dispersed parallel polarized transient absorption of F_4-TCNQ:3MB from 0.4 ps to 3.2 ps with 20 fs steps over the 825 âĂŞ 950 nm region. (b) The integrated TA signal (grey line) over the region of 840 - 850 nm where the slope of the absorption is the steepest along with a fit to a three-component exponential decay convoluted with a Gaussian instrument response function (black line). (c) The oscillatory component of (b) (gray line) is fit to two damped sinusoids using the LPSVD algorithm (black). The residuals to the LPSVD fit are shown as dots. (d) Frequency domain representation of the LPSVD fit (black line) as well as the Fourier transform of the oscillatory signal in (c) (grey).

transition. The mass weighted vibrational coordinates of these modes, labeled ν_1 and ν_2, are presented in Figure 4.8. The oscillatory signal does not dephase significantly within the 3.2 ps temporal window. The FWHM of these oscillations is certainly less than 8 cm^{-1}. LPSVD analysis indicates a FWHM of 2.5 and 5 cm^{-1} may be attributed to the 298 and 343 cm^{-1} oscillations, respectively although these values are highly uncertain given the temporal window. Additionally, there are two peaks not well reproduced by the LPSVD analysis at

48 and 274 cm^{-1}. The 48 cm^{-1} mode corresponds to the difference frequency of the two impulsively excited low frequency modes ($\nu_2 - \nu_1$). The 274 cm^{-1} peak is attributed to Cl bending of the dichloromethane solvent which has been observed in our previous work.[120] These assignments are discussed.

Excited FSRS Analysis of F_4-TCNQ:3MB

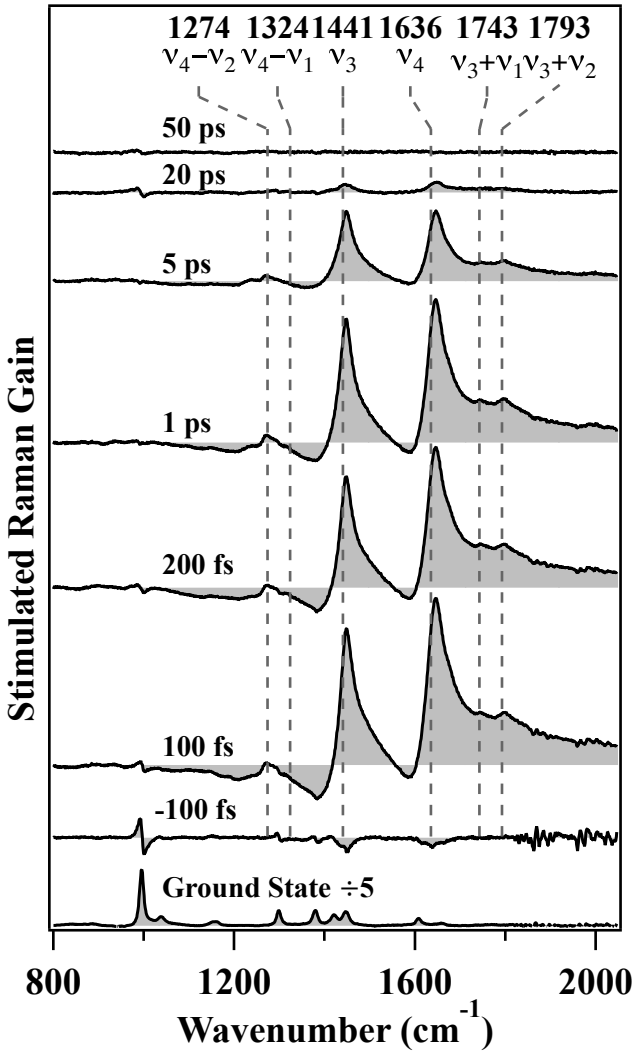

Figure 4.5: Evolution of excited state femtosecond stimulated Raman spectrum of F_4-TCNQ:3MB at select timepoints. The grounds state spectrum corresponding primarily to DCM and uncomplexed 3MB is shown below scaled by 1/5 so that it could be shown along side the weaker excited state Raman signal. The center frequency as determined by dispersive Lorentzian peak fitting is indicated.

The excite state FSRS spectrum of F_4-TCNQ:3MB is presented in Figure 4.5. The spectrum is dominated by two peaks (ν_3 and ν_4) with frequencies of 1441 and 1636 cm^{-1}

corresponding to stretching of the C_2=C_3 and C_4=C_5 coordinates. The excited state fundamentals have a dispersive lineshape and FWHM of 45 cm^{-1}. These properties are inherent to the molecular system and the nonlinear pathways since the Raman pump used in this experiment had a real Lorentzian profile with a FWHM of 11.5 cm^{-1}.[24] There are also smaller features at 1274, 1324, 1743 and 1793 cm^{-1}. These coordinates appear at the difference frequency and combination frequency of the high frequency mode (ν_4) with the two low frequency modes measured in the time domain (ν_1 and ν_2).

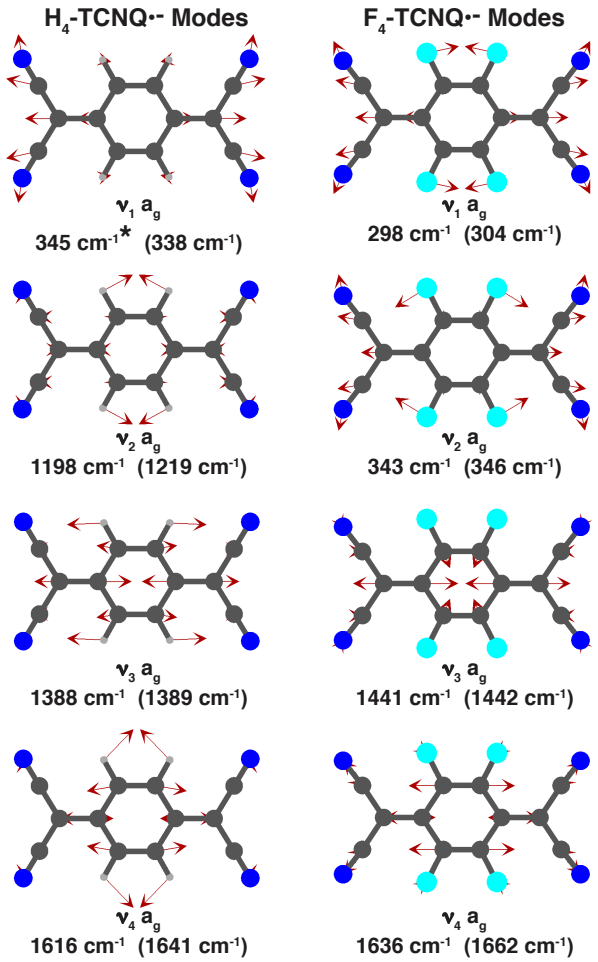

Figure 4.6: Mass weighted vibrational coordinates of H_4-TCNQ (left) and F_4-TCNQ (right) which produce intense Raman scattering in the time and/or frequency domains after broad band charge transfer excitation. The measured frequencies were extracted from the FSRS spectra at a time delay of 2 ps. The value in parenthesis is the frequency of calculated form DFT using uB3LYP functionals. No frequency scaling factor was applied.

Impulsive Excited State Absorption Analysis of H_4-TCNQ:3MB

The observation of difference bands in an excited state spectra of F_4-TCNQ:3MB prompts a reevaluation of our previous results on H_4-TCNQ:4MB. Figure 4.7 presents a spectrogram of the impulsive excited state absorption band over the region of 870 - 930 nm. The Fourier transform spectrum is dominated by four peaks with frequencies of 184, 223, 323, and 353 cm^{-1}. The most intense peak is identifiable as bending of the $C_1{\equiv}N$ groups (ν_1). The sliding window FFT indicates that this peak red-shifts and then blue-shifts over the course of the free induction decay to a resulting frequency of 345 cm^{-1} at 2 ps. This effect is modeled in the supporting information. The peaks at 184 and 223 cm^{-1} may be assigned to difference frequencies between high frequency vibrations $\nu_3 - \nu_2$ and $\nu_4 - \nu_3$, respectively. The 223 cm^{-1} mode could alternatively be assigned to a B_{3u} out of plane bending motion analogous to that observed in tetracyanoethylene.[92, 122]

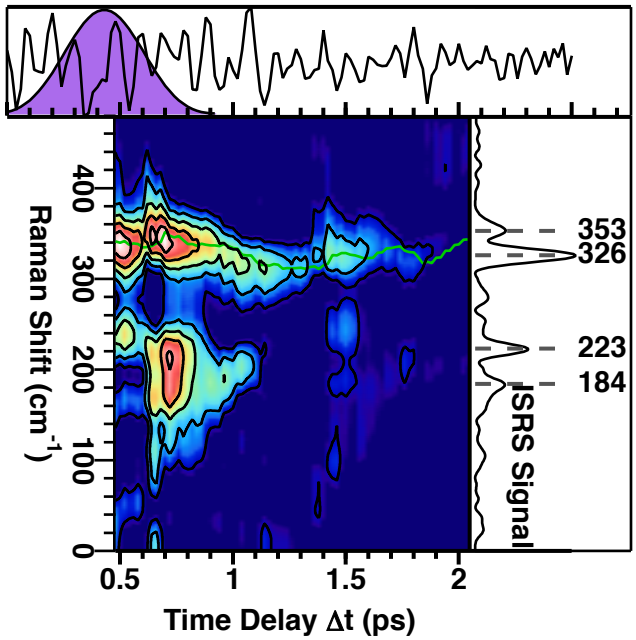

Figure 4.7: Spectrogram of oscillatory excited state band integral of H_4-TCNQ from Fig 2.3 over the region of 870 - 930 nm. The time domain signal is shown on top along with a Blackman window function of FWHM = 0.300 ps (purple). The Fourier transform over the full 0.2 - 2.5 ps window is shown on the right. The green line shows the peak maximum of the ~345 cm^{-1} signal.

Excited FSRS Analysis of H_4-TCNQ:4MB

Figure 4.8 presents the excited state FSRS spectrum of H_4-TCNQ:4MB in DCM at a time delay of 2 ps. This spectrum has four fundamental peaks at 1198, 1388, 1616, 2198 cm^{-1} which correspond to frequencies of the radical anion H_4-$TCNQ^{\bullet-}$. The peaks at 1388 in

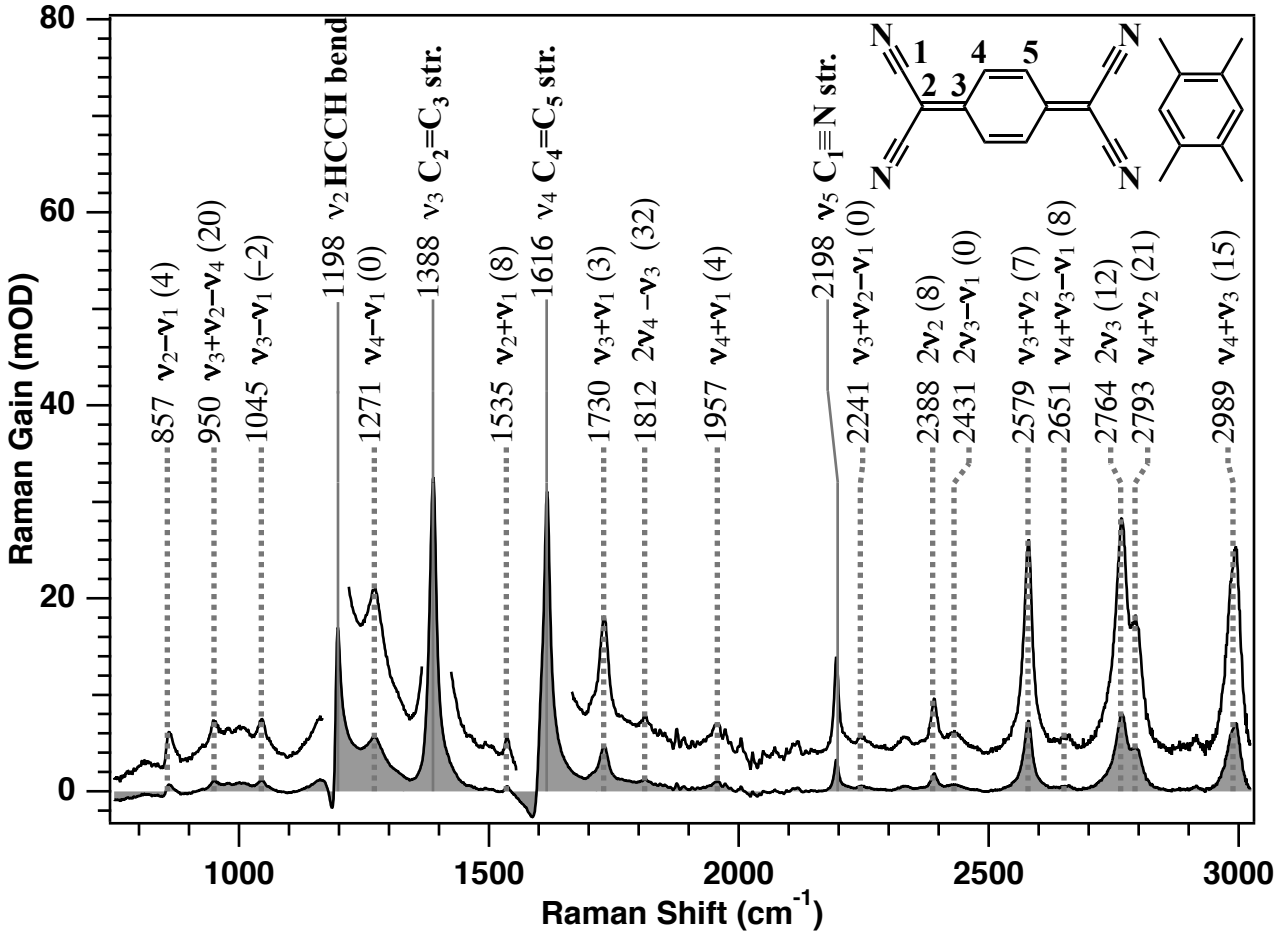

Figure 4.8: Excited state FSRS spectrum of H_4-TCNQ:4MB in DCM at a time delay of 2 ps. The center frequency fundamentals are indicated by a solid line. The center frequencies of combination bands, overtones and difference bands are labeled with a dashed line. Assignments of the coordinates (ν_1 - ν_5) is offered by the molecular drawing (inset) and also by Figure 4.6. The anharmonicity of inherent to each the assignment is given in parenthesis.

H_4-TCNQ has C_2=C_3 stretching character approximately the same as that of F_4-TCNQ at 1441. Likewise the 1616 cm^{-1} mode of H_4-TCNQ has the same C_4=C_5 stretching character as the 1636 cm^{-1} coordinate of F_4-TCNQ. The peak at 1198 cm^{-1} in H_4-TCNQ corresponds to a hydrogen bending mode which has similar character to the mode of F_4-TCNQ at 298 cm^{-1}. The large increase in frequency of this mode in the hydrogenated analogue is the result of the decreased mass of the hydrogen atoms verses the fluorine atoms leading to a blueshift of $\omega_H \approx \omega_F \times \sqrt{19}$. The peak at 2198 cm^{-1} corresponds to a symmetric stretching of the C_1≡N groups.

In addition to the fundamental peaks we find sixteen peaks corresponding to difference bands, combination bands and overtones involving four totally symmetric modes presented in Figure 4.6. Of the sixteen higher order peaks ten of them involve the low frequency coor-

dinate ν_1. Importantly, the 1271 cm^{-1} mode, formerly attributed to a non totally symmetric hydrogen rocking mode is more aptly attributed to a difference frequency of the intense 1616 and 345 cm^{-1} fundamentals. This same low frequency coordinate was observed in the oscillations of the excited state absorption, therefore the 345 cm^{-1} coordinate is displaced between the S_0 and S_1 states and also between the S_1 and S_n states. Combination band and overtones are anharmonically redshifted while the anharmonicity does not affect difference bands.[120]

Two-Dimensional Excited State FSRS Analysis of H_4-TCNQ:4MB

The two-dimensional excited state FSRS spectrum is presented in Figure 4.9(A). The Fourier transform has been performed across the time delay Δt and the signal extracted as described previously. Important peak frequencies are indicated by a grey dashed lines. A magnified view of the 2D-ES-FSRS in the region of (333, 1388) cm^{-1} is presented in top right corner (D). The coupling between the low and high frequency modes results in a two-dimensional dispersive Lorentzian amplitude which agrees well with the theoretically derived model (Fig. 4.2 (d)).

Slices of the 2D spectrum along the impulsive pump axis and the FSRS probe axis are presented in (B) and (C), respectively. The slice along the 333 cm^{-1} frequency shows a multitude of dispersive Lorentzian features. The most intense feature is the C_2=C_3 stretching stretching fundamental at 1388 cm^{-1}. This feature is much more intense than the cross peaks at the other fundamental frequencies of 1198 and 1616 cm^{-1}. The next most intense peaks are at 1730 and 1957 cm^{-1} correspond to combination bands with the 345 cm^{-1} mode. In fact every combination and difference frequencies involving the low 345 cm^{-1} mode and the three high frequency modes which could be observed in our FSRS probe window is present in the 345 cm^{-1} impulsive slice and with the same sign of the dispersion (down then up). When the 223 cm^{-1} slice is inspected we find that the combination bands and difference bands involving the 345 cm^{-1} mode are no longer present instead we find a real Lorentzian signal with frequencies of the fundamentals.

In the other dimension a slice is performed across the FSRS probe axis with a frequency 1271, 1537, 1730 or 1957 cm^{-1} the impulsive pump lineshape in the region of 345 cm^{-1} frequency is complicated. There is a negative feature at $\sim$323 cm^{-1}, a positive feature at $\sim$335 cm^{-1} and then a second positive feature at $\sim$345 cm^{-1}. This complicated lineshape is likely the result of the dispersive nature of the 2D-FSRS signal as well as the frequency shift of the 345 cm^{-1} excited state vibration. The 223 cm^{-1} peak has appreciable intensity along the FSRS probe frequencies of fundamentals, not appearing when slices are made along difference frequencies, combination frequencies and overtones.

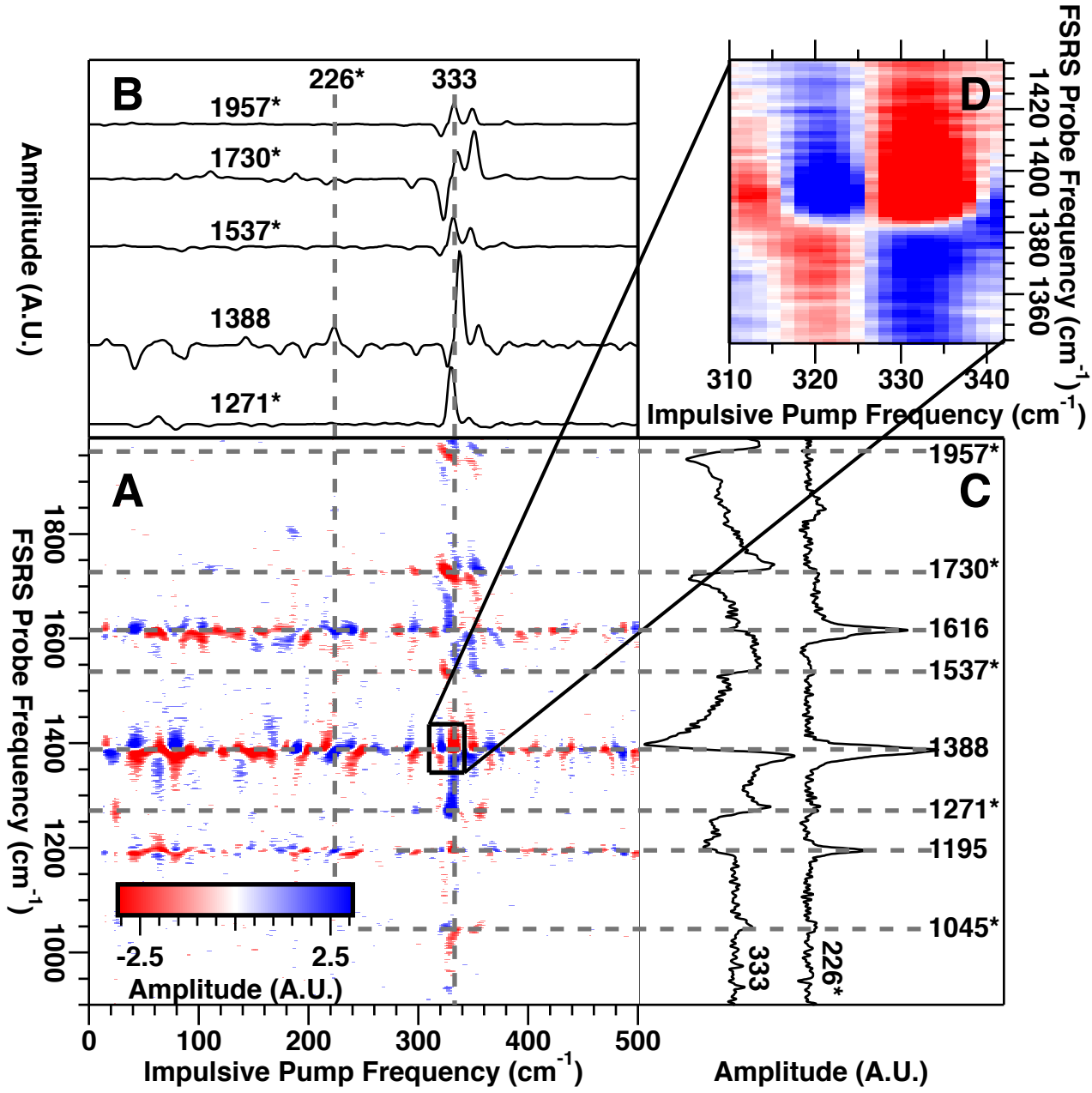

Figure 4.9: (A) Two-dimensional excited state FSRS spectrum of H_4-TCNQ:4MB. Dashed lines indicate important peak frequencies. (B) Slices takes across the FSRS probe frequency axis presenting the impulsive pump spectrum that are coupled to a given excited state FSRS peak. (C) Slices taken across FSRS probe spectrum showing which excited state FSRS peaks are coupled to a given impulsively excited vibration. (D) Magnified view of the 2D-ES-FSRS spectrum in the region of the 323 cm^{-1} and the intense 1388 cm^{-1}. Combination and difference frequencies are indicated with an asterix.

4.5 Discussion

The results presented here are consistent with our previous work differing by the assignment of peaks and by the theoretical interpretation of fifth-order coupling intensity.[107] In both H_4-TCNQ and F_4-TCNQ the peaks in the time domain and frequency domain are accounted for by four totally symmetric fundamentals of the radical anion species, and their difference bands, combination bands and overtones. The coordinates of these fundamentals are analogous in H_4-TCNQ and F_4-TCNQ differing primarily by the frequency of the in-plane bending of the hydrogens or fluorines (Fig. 4.6).

The impulsive oscillations in the excited state absorption are described by non-linear pathway (A) (Fig. 4.1). The diagram shows a low frequency fundamental coherence being prepared by the impulsive excitation, but an excited state difference frequency coherence state can also be prepared on the excited state if two coordinates are displaced and the impulsive pump spectrum spans the vibronic energy levels. Therefore difference bands are observed in the impulsive signal at 48 cm^{-1} in F_4-TCNQ:3MB and at 184 and 223 cm^{-1} in H_4-TCNQ:4MB. The red-shift of the 345 cm^{-1} $C_1{\equiv}N$ bending fundamental over the course of the free induction decay may be the result of solvation altering the harmonic frequency. Peak shifts such as this are well established in the literature, but can be overlooked if the phase of the signal is not scrutinized.[108, 109, 123]

Perhaps the most interesting result of the F_4-TCNQ:3MB analysis is the disparity between the excited state peak widths as measured in the time domain ($\Gamma < 8$ cm^{-1}) and that measured with FSRS ($\Gamma = 44$ cm^{-1}). There is no reason that totally symmetric vibration on the same electronic state should have such drastically different dephasing times. This is clear evidence for the contribution from alternative non-linear pathways contributing to the FSRS signal on the Stokes side of the Raman pump.[120] Vertical-FSRS pathways which prepare coherences on the S_n electronic state. The S_n state could have a very short lifetime which could account for the large width of the VFSRS signals. The contribution of alternative non-linear pathways also account for the dispersive lineshape of the fundamentals.

The FSRS peaks that appear at frequencies corresponding to the radical anion F_4-$TCNQ^{\bullet-}$ and H_4-$TCNQ^{\bullet-}$. This indicates that the signals originate from a fifth-order polarizability. There is no indication of a cascading third-order signal involving ground state frequencies.[107] In the 2D-ES-FSRS spectrum of H_4-TCNQ:4MB, There is a strong coupling between the 345 cm^{-1} mode and the 1388 cm^{-1} mode while coupling with the 1198 and 1616 cm^{-1} fundamentals is weaker. Additionally, the combinations and difference frequencies involving the 345 cm^{-1} mode show intense dispersive Lorentzian features consistent with the proposed 2D-ES-FSRS signal. On the other hand coupling with the 223 cm^{-1} mode shows a positive Lorentzian lineshape at the fundamental FSRS frequencies. This would be consistent with a modulation of the coordinate dependence of the transition dipole. This B_{3u} mode has been shown to modulate charge density in a similar charge transfer system.[122]

In principal either vibronic coupling or excited state anharmonicity could be involved with the observed coupling intensities; however, a simpler explanation is that the six Franck-

Condon factors of the form of Equation 4.9 determine the intensity of a given 2D-FSRS peak. In off-resonance 2D-FSRS there can be non-zero overlap between the vibrational states $|1,0\rangle$ and $|0,1\rangle$ exclusively through anharmonicity between the two coordinate wave function. However, in the resonant case terms like $\sum_{n_i,n_j}\langle 0,1^{S_1}|n_i+1,n_j^{S_n}\rangle\langle n_i+1,n_j^{S_n}|1,0^{S_1}\rangle$ leads to intensity if the $S_n \leftarrow S_1$ states are displaced along both the low and high frequency coordinate. This is the same effect that allows combination bands and overtones to gain substantial intensity intensity in a Raman spectrum under resonance conditions. Resonance enhancement of the 2D-FSRS pathway efficiently couples the states and permits for the signal to be measured; however, the resonant couplings no longer occurs exclusively through anharmonicity. In previous works it has been shown that anharmonic couplings are too weak to be observed by the current FSRS instrumentation and are dominated by a more intense third-order cascading signal.[57] Indeed in more reactive systems, especially those in which the rate of internal conversion is faster the dephasing of the impulsively excited vibrations the excited state anharmonicity may be very large and the 2D-ES-FSRS signal may be strong in the off resonance case.[116]

Although the peaks in the 2D-ES-FSRS don't necessarily report on excited state anharmonicity they still bare useful information. A cross peak indicates the coordinates are coupled by one or more electronic transition. In a small system involving one chromophone and one a single electronic relaxation pathway this statement seems trivial, but when this technique is applied to more complicated systems a cross peak in a 2D-ES-FSRS spectrum could be used to identify that two excited state FSRS signals are on the same chromophore or that one excited state vibration continues modulate an subsequent vibrational transition after an internal conversion or excited state reaction. Excited state FSRS experimentation will be an invaluable tool for future spectroscopists.

The peaks in the 2D-ES-FSRS spectrum yield phase information about the excited state vibrations that is lost with lower time resolution. The absolute sign of the peak dispersion in Figure 4.9(C) varies depending on the time delay at which we start the Fourier transform. The coherent artifact prevent acquiring a signal at $\Delta t = 0$. If the signal were extrapolated back to $\Delta t = 0$ the absolute phase of the signal would likely depend on the resonance denominators in equation the frequency of the Raman pump with respect to the most resonant state. A preliminary inspection of the relative phase reveals that the combination band and difference bands involving the low frequency 345 cm^{-1} have the same dispersive lineshape. The fundamentals in the slice along the 345 cm^{-1} have the opposite lineshape. Finally in the 223 cm^{-1} slice along the pump axis we find the fundamentals appear as real Lorentzians lineshapes while the FSRS combination bands are not present. The real Lorentzian lineshape could be the result of a modulation of the transition dipole. These results together indicate that the relative phase between peaks lineshape may contain useful information. This is but one example of how going to higher order spectroscopies can produce powerful new insight.

4.6 Conclusion

Difference bands, combination bands and overtones are ubiquitous in FSRS spectra when the Raman pump is resonant with a localized high symmetry electronic transitions such as those afforded by charge transfer excited radical dimers. The disparity in the peak widths measured in the impulsive time domain and those measured with FSRS is an indication that alternative non-linear pathways such as Vertical-FSRS may contribute to the signal under resonance conditions.

We have reevaluated the 2D-ES-FSRS of H_4-TCNQ:4MB in light of more precise theoretical considerations. To isolate a 2D-ES-FSRS signal it is advantageous design an experiment where each subsequent dipole-field interaction is more strongly resonant than the last. Agreement is found between the experiment and the theoretically predicted 2D-ES-FSRS signal. Strong coupling is observed between the 345 cm^{-1} and the combination bands and difference bands involving this coordinate. This challenges the assumption that coupling between Raman active vibrations occurs exclusively through excited state anharmonicity under resonance conditions. Coupling the Raman pump and Stokes probe fields through an excited state absorption band permits the vibrational states to find two coordinate overlap yielding cross peaks in the 2D-ES-FSRS spectrum. Cross peaks in resonant 2D-ES-FSRS indicate that the two coordinates are coupled through the same electronic transition and therefore they must be proximate to the same electron density. 2D-ES-FSRS will be an invaluable tool for identifying excited state reactivity especially in systems where internal conversion precedes the dephasing of vibrational coherences.

Chapter 5

Resonance Raman Characterization of Tetracene Monomer and Nanocrystals: Excited State Lattice Distortions Concurrent with Efficient Singlet Fission

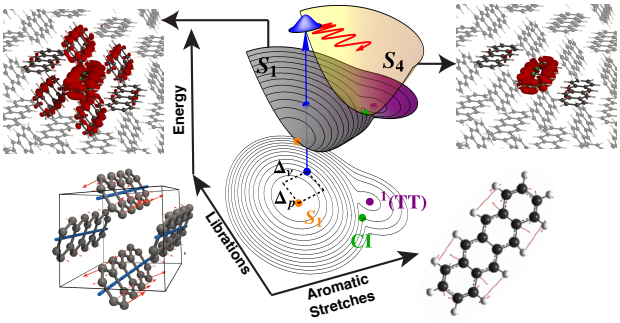

This work will be submitted to *Physical Chemistry Chemical Physics*
Scott R. Ellis[1], Daniel R. Dietze[1,†], Tonatiuh Rangel[2], Florian Brown-Altvater[1], Jeffrey B. Neaton[2,*] and Richard A. Mathies[1,*]

[1] *Department of Chemistry, MC 1460, University of California at Berkeley, Berkeley, California 94720, USA*

[2] *Department of Physics, MC 7300, University of California at Berkeley, Berkeley, California 94720, USA*

*Corresponding authors, jbneaton@lbl.gov (JN) and ramathies@berkeley.edu (RM).

†Current address: OSRAM Opto-Semiconductors GmbH, 93055 Regensburg, Germany

5.1 Abstract

Characterization of the specific intramolecular vibrations, phonon modes and exciton states that lead to efficient singlet fission (SF) may be instrumental in the design of the next generation of high efficiency photovoltaic devices. To this end we analyze the absolute resonance Raman (RR) cross-sections for tetracene (Tc) both as a monomer in solution and as a crystalline solid in an aqueous suspension of nanocrystals. For both systems, a time-dependent wavepacket model is developed that is consistent with the absolute RR cross-sections, the magnitude of the absorption cross-sections, and the vibronic lineshapes of the fluorescence. In the monomer, the intramolecular reorganization energy is 1760 cm^{-1} and the solvent reorganization energy is 70 cm^{-1}. In nanocrystals, the total reorganization is diminished to less than 600 cm^{-1}. The lowest energy exciton has an estimated intramolecular reorganization energy between 300 cm^{-1} and 500 cm^{-1} while intermolecular librational phonons have a reorganization energy of about 130 cm^{-1}. The diminished reorganization energy of the nanocrystal is interpreted in the context of the delocalization of the band-edge exciton onto about $\sim$7 molecules. By including electron and electron-hole correlations within many-body perturbation theory, the polarized absorption spectra of crystalline Tc are calculated and found to be in agreement with experiment. The low-lying exciton states and optically active phonons that contribute to the polarized crystal absorption are identified.

5.2 Introduction

Singlet fission (SF) is a spin allowed process whereby a singlet exciton decays into a pair of spin-coupled triplet excitons. Singlet fission is potentially useful in photovoltaic energy harvesting as a means to circumvent the Shockley-Queisser limit of 33.7 % energy capture efficiency for single band-gap semiconductors. Tetracene (Tc) and other polyacenes have been extensively used as a model system to study singlet fission.[124] Recent spectroscopic measurements have bolstered interest in polyacene SF by showing that in a related system, polycrystalline 6,13-bis(triisopropylsilylethynyl)pentacene thin films, SF occurs on an 80 fs timescale through a conical intersection in vibrational phase space with near perfect efficency.[28, 125] Other studies have focused on determining the exciton size[126], energy[127], mobility[128] and lifetime.[129–131] However, the importance of excited state nuclear motion in the singlet fission process has received less attention experimentally.

The SF process in crystalline Tc is somewhat less efficient and more complicated than in pentacene derivatives. In Tc, the combined 0-0 energies of the triplets (T_1+T_1) is higher than that of the lowest singlet exciton state (S_1) by $\sim$0.2 eV.[127, 132–134] Transient absorption experiments on Tc have revealed two timescales for SF: an efficient sub-200 fs process which comprises about half of the total SF quantum yield, and a slower SF process with reported time constants ranging from 40 ps to 170 ps.[129–131] There are conflicting reports as to whether the slower SF process is in fact thermally activated.[135] This inconsistency likely arises from differences in sample morphology. In samples with smaller crystal domains the

slower SF process proceeds with a time constant of 70 ps at room temperature and with very minimal temperature dependence while in large single crystals a SF time constant of 170 ps is more typical and SF shows strong thermal activation.[136] This observation is consistent with exciton diffusion to modified defect sites where singlet fission is more efficient. The germinate pair of triplet excitons then dissociates into free excitons which diffuse apart or the triplet pair may also recombine, producing a delayed fluorescence signal from the singlet product state.[131, 135, 137, 138]

RR intensities can be used to decipher the vibronic spectral density and understand the aforementioned ultrafast electronic dynamics in the context of specific nuclear motion and excited state structure. A resonant coherent anti-Stokes Raman intensity analysis has been reported on Tc monomer in benzene exploring the 1000 - 1600 cm^{-1} region.[139] The absorption spectrum of Tc monomer was measured in the gas phase at ultra-cold temperatures such that the vibronic peaks could be resolved.[140] The gas phase absorption showed that in Tc monomer the S_1 potential energy surface is strongly displaced along totally symmetric aromatic ring-breathing modes but also reveals vibronic activity involving non-totally symmetric b_{3g} ring-distortion modes. The off-resonance spontaneous Raman spectra of Tc monomer in solution[141, 142] and crystalline Tc have been reported.[30, 143–145] The impulsive Raman spectrum of crystalline Tc has also been measured in the time-domain under preresonance conditions with a four-pulse transient-grating experiment[126] and under resonance conditions with femtosecond transient absorption.[146] Both experiments show that the third-order polarizability is strongly modulated at a frequency of $\sim$120 cm^{-1}, while the impulsive transient absorption experiment also identified three other ground state oscillations with frequencies of 58, 130 and 312 cm^{-1}. Furthermore, by using a femtosecond pulse train with a periodicity of 225 fs (ω = 143 cm^{-1}), the authors were able increase the T_1-T_n excited state absorption signal by 20%, while only increasing the time-integrated emission signal by 2%. These results suggest that a phonon mode with a similar frequency determines the branching ratio between singlet and triplet formation. Collectively, these works suggest that local deformation of the crystal lattice along specific Raman active coordinates may facilitate efficient SF, motivating a more detailed vibronic characterization.

Tetracene monomer is planar in solution and has D_{2h} symmetry (see Fig. 5.1). The lowest energy electronic transition dipole (B_{2u}) is polarized along the short molecular axis M.[147] The B_{2u} transition is well separated in energy from the next optically allowed absorption band by about 1.2 eV.[29] Tc forms a triclinic crystal structure with the space group $P\bar{1}$ showing inversion symmetry. Tc crystals have two molecules per unit cell in a herringbone structure, which offers an energetic compromise between dispersion forces (π-stacking) and T-shaped C-H to p_z quadrupole interactions. The many-bodied sum and difference of transition dipole interactions on and between the two Tc molecules in the unit cell results in two polarized absorption bands called the lower and upper Davydov states abbreviated LDS and UDS, respectively.[148, 149] The LDS and UDS have been shown to be polarized 71^o with respect to one another and oriented approximately along the a and b crystal axes, respectively.[147]

Recent theoretical efforts on molecular crystals have focused on understanding their geometrical properties and excited state phenomena including SF. It has been shown that

accounting for van der Waals (vdW) interactions within density functional theory (DFT) improves predicted geometries[150, 151] and phonon band structures.[152, 153] Moreover, excited state phenomena in periodic solids can be accessed with ab initio many-body perturbation theory approaches, such as the GW approximation and the Bethe-Salpether equation (BSE).[154] In particular, GW-BSE has proven successful in characterizing the low-lying excitations of the oligoacene family.[150, 151, 155–157] Although previous theoretical calculations on Tc have established aspects of Tc excited states,[150, 151] calculations of phonons and the lowest energy neutral excitations of Tc based on state-of-the-art DFT and GW-BSE methods continue to be needed to enhance our understanding of excited state processes of Tc such as SF and RR scattering.

Here we present the measurement and modeling of the absolute RR cross-sections of the vibrations of Tc monomer and nanocrystals. A wavepacket model is developed which is self-consistent with the absorption, fluorescence, and RR data. This model allows us to parse the reorganization energy into specific intramolecular and lattice distortions that occur immediately after photoexcitation. Furthermore, we use van der Waals based DFT with periodic boundary conditions to characterize the phonon modes and intramolecular vibrations that contribute substantially to the vibronic spectral density. The low-energy polarized absorption spectra of crystalline Tc are calculated with ab initio GW-BSE, and the computed low-energy exciton states that participate in the SF process are analyzed. This combined experimental and theoretical analysis elucidates the short-time ($<$100 fs) wavepacket dynamics of photoexcited Tc which likely determines the branching ratio between the efficient and slow SF processes.

5.3 Materials & Methods

Sample preparation

Tetracene (2,3-benzanthracene, 98%, Sigma Aldrich) was used as received. Tc was dissolved in acetone (99.6%, Fisher), benzene (99.7%, EMD) and dichloromethane (99.5%, EMD) to an optical density of 0.15 at the excitation wavelength for Raman measurements of the monomer. Tetracene nanocrystals were prepared following the reprecipitation method.[158] Briefly (19.6 mg, 86 μmol) of Tc was dissolved in 100 mL tetrahydrofuran (HPLC grade, Fisher) to form a saturated solution. Saturated Tc in THF (16 mL) was added slowly to MilliQ filtered water (200 mL) in a round bottom flask with rapid stirring for 10 minutes at room temperature. The solution was then evaporated under reduced pressure at 60 oC from 216 to $\sim$25 mL.

The molar absorptivity of the nanocrystals was initially determined by precipitating a known concentration of Tc tetrahydrofuran solution into a known volume of water. When the suspension was poured out of the round bottom the walls of the round bottom were transparent indicating that a negligible amount of Tc was lost to the container in the precipitation process. The UV-Vis spectrum of the Tc nanocrystal suspension in water was immediately

acquired. Once the absorptivity had been determined the concentration of subsequent Tc nanocrystal suspensions were determined from their optical density at 520 nm.

Tc nanocrystals were imaged using a scanning electron microscope (FEI Quanta 3D FIB, 30 kV, 280 pA). The Tc nanocrystal suspension (900 μM) was drop cast on a silicon substrate and sputtered with a 4 nm gold layer. The nanocrystals were polydisperse polyhedrons with edge lengths ranging from 150 - 800 nm (Fig. C.4).[158] The polydispersivity of the nanocrystals does not present a significant challenge for this work as the optical properties do not show confinement effects and only show a small increase in inhomogeneity (see Section C). Studying nanocrystals rather than thin films or single crystals presents the distinct advantage that the optical properties can be assumed to be an isotropic average over all crystal orientations thereby simplifying the analysis.

Sodium 2-naphthalenesulfonate (SNS, TCI >95%) was used as an internal standard for Raman intensity measurements of the nanocrystals. SNS was chosen because typical ionic intensity standards such as Na_2SO_4 caused the nanocrystals to aggregate and precipitate. SNS served as a surfactant stabilizing the suspension for more than five hours. The Tc nanocrystal suspension was diluted with 0.13 M aqueous SNS solution to an optical density of 0.15 OD per path length at the excitation wavelength.

Broadband stimulated resonance Raman measurements

The details of the stimulated Raman setup have been described elsewhere.[159] In short, the picosecond Raman pump and femtosecond probe pulses are generated from an 800 nm fundamental out of a homebuilt Ti:Sapphire oscillator and 1 kHz regenerative amplifier. The Raman pump is generated from two sequential non-collinear optical parametric amplifiers (NOPA). The first NOPA is seeded by a broadband continuum. The broadband output pulse is then spectrally filtered and serves as a seed for the second NOPA producing a 220 μW narrow-band (FWHM = 38 cm^{-1}) pulse at 520 nm. The femtosecond broadband probe pulse is generated in a thin piece of sapphire and is compressed to less than 60 fs in the spectral region where stimulated Raman measurements are made. The two pulses are polarized parallel to one another and are overlapped spatially and temporally in the sample generating a coherent signal in the direction of the probe. The Raman pump is optically chopped at 500 Hz yielding Raman gain features as

$$Gain = ln\left(\frac{Probe_{RamanPumpOn}}{Probe_{RamanPumpOff}}\right) \tag{5.1}$$

Tc nanocrystal samples were measured in a 2-mm path length cuvette that was translated perpendicular to the beam at a rate of 0.5 mm/s to mitigate photoalteration effects.

Spontaneous resonance Raman measurement

Spontaneous Raman measurements were excited with light from argon and krypton gas lasers (Spectra-Physics 2020). The parallel-polarized light was collected in a 90o scattering geom-

etry and through a double subtractive dispersion spectrograph (Spex 1401) with effective spectral resolution of 7 cm^{-1} and imaged onto a liquid nitrogen cooled CCD (Roper Scientific 1100). All measurements were made with less than 15 mW of incident intensity focused to a 5 μm beam waist in the center of the sample. The solutions of Tc monomer were flowed at a rate of 2 cm/s through a 1.5 mm diameter capillary tube to mitigate photoalteration. Because excessive agitation causes nanocrystal suspensions to aggregate, the suspension was gently fed into the capillary tubes and then translated perpendicular to the beam at a rate of 0.5 mm/s.

Fluorescence measurements

Fluorescence spectra were acquired with a Horiba FluoroMax-4 spectrofluorometer, excited with 413 nm light (3 nm slit) and resolved with 1 nm resolution. Tetracene monomer solution in acetone was prepared at a concentration 1.4×10^{-5} M. The Tc nanocrystal suspension was diluted to an optical density of 0.1 at 520 nm.

Data analysis

All Raman spectra were corrected for the wavelength dependence of self-absorption in the sample following Equation 5.2:

$$\frac{I_t(\lambda)}{I_0(\lambda)} = 10^{\epsilon(\lambda) l_{eff} C_{Tc}} \tag{5.2}$$

The original signal I_0 is recovered from the transmitted signal It by considering the molar absorptivity, $\epsilon(\lambda)$; the Tc concentration, C_{Tc}; and an effective pathlength, l_{eff}; of the light escaping from the sample for a given geometry.

Spontaneous RR peaks were fit simultaneously as a sum of Lorentzian functions in regions where the baseline was approximately linear. The stimulated RR peaks were fit to a dispersive Gaussian function of the form (see Fig. C.7 & C.5):

$$f(\omega) = A\left(cos(\phi) + sin(\phi)(\omega - \omega_i)\right) exp\left(\frac{-(\omega - \omega_i)^2}{2\sigma^2}\right) \tag{5.3}$$

Dispersive Gaussian features arise from the truncation of the free induction decay by convolution with the shortened temporal envelope of the Raman pump pulse.[61] The intensity of each peak was then determined by numerical integration of its absolute value.

$$I = \int_{\omega_i - 4\sigma}^{\omega_i + 4\sigma} d\omega |f(\omega)| \tag{5.4}$$

The absolute Raman cross-sections of Tc monomer and Tc nanocrystal were determined by comparison with the integrated peak area of internal standards. The monomer peaks were measured relative to acetone's CCC bending band at 786 cm^{-1} ($\partial\sigma_{std}/\partial\Omega = 6.5 \pm 0.7 \times 10^{-14} \text{Å}^2$/molecule/steradian at 488 nm).[160] The Tc nanocrystal spectra were measured

against the aromatic stretching mode of aqueous naphthalene 2-sulfonante (SNS) at 772 cm^{-1}, ($\partial\sigma_{std}/\partial\Omega = 2.4 \pm 0.5 \times 10^{-14}$Å^2/molecule/steradian at 488 nm). The absolute Raman cross-section of the 772 cm^{-1} band of SNS was determined by comparison with the sulfate 981 cm^{-1} symmetric stretching mode (Fig. C.8).[161] These cross-sections were extrapolated using the established $\omega_s\omega_l^3$ frequency dependence of off-resonance Raman intensities. Once the relative intensities were measured, the absolute Raman cross-sections of Tc could be determined as:

$$\sigma_{Tc} = \frac{8\pi}{3}\left(\frac{1+2\rho}{1+\rho}\right)\left[\left(\frac{\omega_l - \omega_{Tc}}{\omega_l - \omega_{std}}\right)^2\left(\frac{I_{Tc}}{I_{std}}\right)\left(\frac{c_{std}}{c_{Tc}}\right)\left(\frac{\partial\sigma_{std}}{\partial\Omega}\right)\right] \tag{5.5}$$

where A is the area of the peaks, c is the concentration of Tc and the internal standard as indicated, ω_l is the frequency of the incident photons, $\omega_l - \omega_{Tc}$ is the frequency of scattered photons. The depolarization ratio ρ was taken to be 1/3 for the totally symmetric modes of the resonant Raman spectra because only one transition dipole coupling dominates in the polarizability tensor at the relevant excitation energies.

The measured cross sections were modeled using the dynamic wavepacket model developed by Heller[162] and detailed by Kelly.[4, 19, 26] Specifics of the dynamic wavepacket model are given in the SI. The model describes a Gaussian wavepacket propagating on a fifteen dimensional displaced harmonic potential energy surface. The absorption and Raman cross-sections are given by a correlation function, $\langle X_n | X_i(t) \rangle$, of an excited state wavepacket with the relevant ground state vibronic wavefunctions. If the ground and excited states are separable harmonic surfaces with equal vibrational frequencies and no Duchinsky rotations are present then the lineshape of the relaxed emission spectrum can also be calculated from the correlation function of a ground state wavepacket with the excited state vibronic wavefunctions.

An upper bound for the total reorganization energy can be established by integrating the Stokes shift over the envelope of the emission band intensity and normalizing.

$$\lambda_{net} = \int_0^\infty \frac{I_F \times (\omega_S - \omega_0)}{\omega_S^3} d\omega_S \Big/ \int_0^\infty \frac{I_F}{\omega_S^3} d\omega_S \tag{5.6}$$

In Equation 5.6, ω_S is the emission frequency which appears at a Stokes shift from the zero-zero electronic transition frequency ω_0. I_F is the fluroescence intensity. The denominator of ω_S^3 accounts for the fact that higher frequency transitions are favored by the frequency dependence of the refractive index.

Theoretical excited state calculations

Low-lying singlet excitations of Tc crystals were computed with ab initio many-body perturbation theory within the GW approximation and BSE approach. Our calculations proceed with a structural optimization of the two-molecule unit cell with DFT using the Perdew-Burke-Ernzerhof (PBE) functional.[163] The ABINIT code[164] is employed for our DFT

calculations. Experimental lattice constants, taken from Ref. [165], are held fixed while internal coordinates are relaxed. Once the structure is optimized, we generate neutral excitations in a two-step procedure. First, the self-energy-corrected electronic bandstructure is calculated perturbatively within the GW approximation, where G is the Green's function of the system and W is the screened Coulomb potential. Second, our DFT wavefunctions and GW-corrected eigenvalues are used to solve a two-particle electron-hole Hamiltonian with the BSE approach, leading to singlet excitation energies that include electron-hole interactions. For these one-shot G0W0 and BSE calculations, we use the BerkeleyGW package[166]; the ABINIT code[164] to construct the DFT starting point. A standard one-shot GW calculation is used to correct the eigenvalues of the initial DFT-PBE calculations, following Ref. [151]; the frequency dependence of the dielectric function is approximated by the plasmon-pole model of Hybertsen- Louie[167] as implemented in BerkeleyGW.[166] The GW sums are truncated in reciprocal space up to an energy cutoff of 10 Ry, and up to a number of unoccupied bands equivalent to an energy range of 30 eV and a 5 x 4 x 2 k-grid. To construct the BSE kernel, a coarse k-grid is implemented, equivalent to the one used at the GW step. Later the kernel, wavefunctions, and GW energies are interpolated to a finer k-grid of 10 x 8 x 5 to calculate the absorption spectra. Full diagonalization of BSE Hamiltonian, beyond the Tamm-Dancoff approximation, is performed with 10 occupied and 10 empty bands, as implemented in BerkeleyGW.[168] These settings ensure that our excited state energies are converged to about 0.1 eV in the low-energy range (up to 3 eV). Isosurfaces for the electron density are computed by averaging the density corresponding to high-probability hole positions: on the lobes of the p_z-type orbitals of the 18 carbon atoms of a central tetracene molecule. Following prior work,[151] the isovalues are set to plot 40% of the electronic density.

Theoretical phonon calculations

The phonon frequencies and coordinates were calculated in the harmonic approximation using a finite differences approach and a van der Waals dispersion-corrected functional. For our phonon calculations, total-energy calculations were performed with the Quantum ESPRESSO code v5.1.1.[169] Lattice parameters and internal coordinates were fully relaxed with a Monkhorst-Pack k-grid of $4 \times 3 \times 2$ using the vdW-DF-cx functional[170] and PBEsol ultra-soft pseudopotentials,[171] as in previous work.[151] The plane-wave basis is expanded up to an energy-cutoff of 55 Ry. The Hellmann-Feynman forces are converged to 2×10^{-5} Ry/Bohr and the total energy to 10^{-8} Ry. To ensure accurate forces, the convergence threshold for all self-consistent calculations is set to 10^{-12} Ry. The same k-grid is used as for the prior relaxation, and each atom is displaced in each dimension by 0.01 Å to generate the force constants. The frequency spectrum is obtained by diagonalizing the Fourier transform of the real-space force-constant matrix, the eigenvectors providing the corresponding displacement vectors for each mode. The acoustic sum rule is enforced.

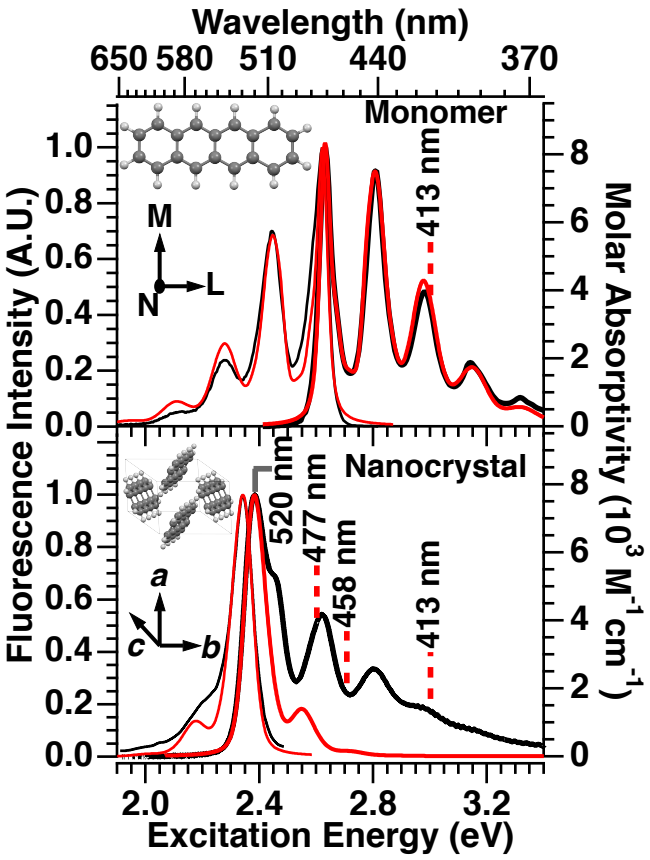

Figure 5.1: Absorption and emission spectra (black lines) of tetracene monomer in acetone and nanocrystal suspension in water compared to time dependent absorption and emission wavepacket model calculations (red lines) of the vibronic lineshapes in which agreement with the Raman cross sections have been found. Excitation wavelengths used for spontaneous Raman measurements are given by red dashed lines while the excitation wavelength in the stimulated Raman measurement is given by a grey line.

5.4 Results

Figure 5.1 compares the measured absorption and fluorescence spectra (black lines) of Tc monomer dissolved in acetone and Tc nanocrystals as a suspension in water. The monomer absorption spectrum shows a clear vibronic progression with spacing of 1440 cm^{-1} while the fluorescence spectrum has a mirrored vibronic progression with a spacing of about 1420 cm^{-1}. The mirror reflection symmetry of the absorption and emission validates the approximation that Duschinsky rotations do not significantly affect the vibronic spectral density. This observation can be further validated by inspecting the gas phase absorption and fluorescence spectra of Tc monomer at 4 K.[140]

The spontaneous RR spectra of Tc monomer and nanocrystals (Figure 5.2) were acquired

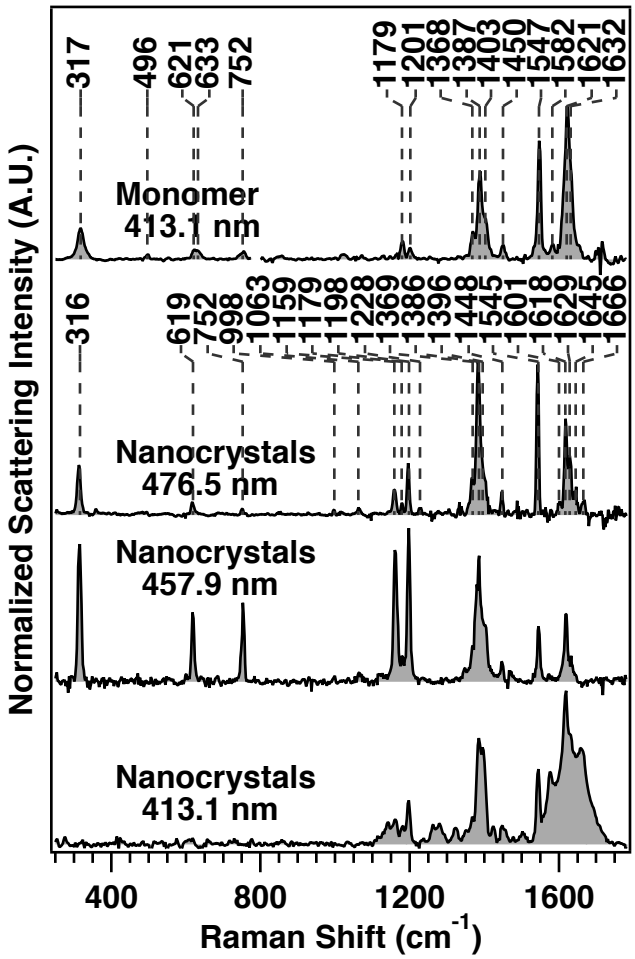

Figure 5.2: Spontaneous resonance Raman spectra of tetracene monomer (top) in acetone excited at 413.1 nm and tetracene nanocrystals suspended in water at three excitation wavelengths blue of the onset of the fluorescence. Regions obstructed by solvent scattering have been excluded for clarity.Spontaneous resonance Raman spectra of tetracene monomer (top) in acetone excited at 413.1 nm and tetracene nanocrystals suspended in water at three excitation wavelengths blue of the onset of the fluorescence. Regions obstructed by solvent scattering have been excluded for clarity.

in the spectral region blue of the onset of the fluorescence signal.[142] Although a number of Raman measurements have been reported on Tc monomer and nanocrystals, these are the first spontaneous Raman measurements made on resonance in both systems.[139, 141–144] The contributions of scattering from the solvent and the broad featureless baselines have been subtracted. The time dependent wavepacket model was used to model to the absorption, fluorescence and Raman spectra in acetone. Details of this fitting procedure are given in the SI. The magnitude of the dimensionless displacements are initially determined by the measured cross sections and then iteratively refined to fit the width of the absorption and the 0-1 and 0-2 vibronic peak intensity relative to that of the 0-0 peak at 2.62 eV. A comparison

Table 5.1: Reorganization energies for Raman active modes of tetracene monomer

Mode	Raman Shift (cm^{-1})	Calc. Cross Section σ_R($\times 10^{11}$ Å^2)	Meas. Cross Section σ_R($\times 10^{11}$ Å^2)	Reorganization Energy λ_ν (cm^{-1})	Symmetry
ν_1	316	119	119 ± 86	75	A_g
ν_2	494†	10	10 ± 7	6	B_{3g}
ν_3	621	17	17 ± 12	12	A_g
$2\nu_2$	631	24	27 ± 19		A_g
ν_4	752	34	38 ± 27	34	A_g
ν_5	1179	33	59 ± 42	372	A_g
ν_6	1200	25	34 ± 25	118	A_g
ν_7	1367	36	33 ± 24	74	A_g
ν_8	1386	259	210 ± 151	455	A_g
ν_9	1402	68	66 ± 48	107	A_g
ν_{10}	1446	16	16 ± 11	18	
ν_{11}	1547	342	328 ± 237	234	A_g
ν_{12}	1582	20	20 ± 14	11	
ν_{13}	1621†	374	364 ± 263	201	B_{3g}
ν_{14}	1632†	127	112 ± 88	69	B_{3g}

Fit to spectra measured in acetone solution. Fit parameters: Excitation Wavelength, 413.1 nm; Electronic Origin Transition Energy, E_{00}= 472.1 nm; Transition Dipole Length, M = 0.647 Å; Homogeneous Linewidth, Γ = 95 cm^{-1}; Inhomogenous Linewidth, Θ = 97 cm^{-1}; Solvent Reorganization Energy, λ_s = 70 cm^{-1}; Phonon Reorganization Energy, λ_p = 0 cm^{-1}; Intramolecular Reorganization Energy, λ_ν = 1760 cm^{-1}; Refractive Index, n = 1.370; † The b_{3g} modes were treated phenomenologically as displaced harmonic surfaces although literature suggests higher order vibronic coupling. The calculation of 95 % confidence intervals is described in the SI.

between the measured and calculated Raman cross-sections with 413.1 nm excitation is presented in Table 5.1. Excellent agreement is found between the absolute magnitudes of the absorption and Raman cross-sections for the majority of the modes indicating that the excited state of the monomer is well described by this 15-mode displaced harmonic surface and a single transition dipole coupling.

Previous vibronic analyses of the Tc monomer indicated that certain aromatic stretching modes at 316, 1179, 1200, 1386 and 1547 cm^{-1} were highly displaced.[140, 172] However, the large contribution to the vibronic lineshape by the 1621 and 1632 cm^{-1} non-totally symmetric b_{3g} modes determined from the Raman intensity analysis is less obvious. Tc monomer's rigid aromatic frame results in the absence of low frequency vibrational modes with ω_j <170 cm^{-1}. The Stokes shift between the absorption and fluorescence maxima must therefore be

accounted for by solvent relaxation. Furthermore, the lack of permanent dipoles on either ground or excited states results in a very small solvent relaxation energy (λ_s = 71 cm^{-1}) compared to other aromatic systems.[19, 172]

The absorption and emission properties of Tc nanocrystals are very similar to those of Tc single crystals after accounting for isotropic averaging over transition dipole orientations (see Fig. C.2 & C.3).[147] In Tc nanocrystals, the absorption spectrum extends 0.5 eV blue of the electronic origin at 2.34 eV while the fluorescence tails-off 0.3 eV red of the origin. The Tc nanocrystal absorption spectrum shows two additional peaks at 2.62 and 2.79 eV that are not mirrored in the fluorescence spectrum. The fluorescence displays only a shoulder at about 2.2 eV. The modeled spectra (red solid and blue dashed lines) are time-dependent wavepacket fits to the vibronic structure.

Table 5.2: Reorganization energies for Raman active modes of tetracene nanocrystals consistent with measured cross sections (red fit)

Mode	Raman Shift (cm^{-1})	Calc. Cross Section σ_R (×10^{11} Å^2)	Meas. Cross Section σ_R (×10^{11} Å^2)	FWHM (cm^{-1})	Reorganiz -ation Energy λ_v (cm^{-1})
ν_1	58	85			37
ν_2	123	143			30
ν_3	130	324			65
ν_4	316	884			99
ν_5	619	20	20 ± 16	52	3
ν_6	752	10	10 ± 7	46	2
ν_7	998	10	10 ± 6	52	2
ν_8	1159	59	}		19
ν_9	1179	10	} 155 ± 101	67	6
ν_{10}	1198	87	}		29
ν_{11}	1369	17	}		7
ν_{12}	1386	204	} 282 ± 64	61	85
ν_{13}	1396	62	}		25
ν_{14}	1448	42	42 ± 22	56	19
ν_{15}	1545	63	63 ± 14	42	31

Fit to S_1 exciton of nanocrystal suspension in water. Fit parameters: Excitation Wavelength, 520 nm; Electronic Origin Transition Energy, E_{00} = 525.1 nm; Transition Dipole Length, M = 0.46 Å; Homogeneous Linewidth, Γ = 135 cm^{-1}; Inhomogenous Linewidth,Θ = 140 cm^{-1}, Solvent Reorganization Energy, λ_s = 0 cm^{-1}; Phonon Reorganization Energy, λ_p = 130 cm^{-1}; Intramolecular Reorganization Energy, λ_ν = 330 cm^{-1}; Refractive Index, n = 1.72[31]; The calculation of 95 % confidence intervals is described in the SI.

The red spectra in Figure 5.1 are fits in which agreement is found with the measured

Raman cross sections (Table 5.2). The absorption spectrum of the nanocrystals can be satisfactorily fit with the wavepacket model at the red-edge but the model fails at bluer wavelengths. The reason for this will be discussed at length, but in short the reproduction of the full absorption lineshape requires consideration of multiple electronic states which can interact and lead to interference terms in both the absorption and the Raman scattering that complicates the analysis.[173] The fit to the Raman cross sections more closely reproduces the fluorescence spectrum but still diverges in the region of 565 nm. Following Eq. 5.6, an upper bound for the total nuclear reorganization energy of the emissive singlet states is determined to be λ_{net} <600 cm^{-1}.

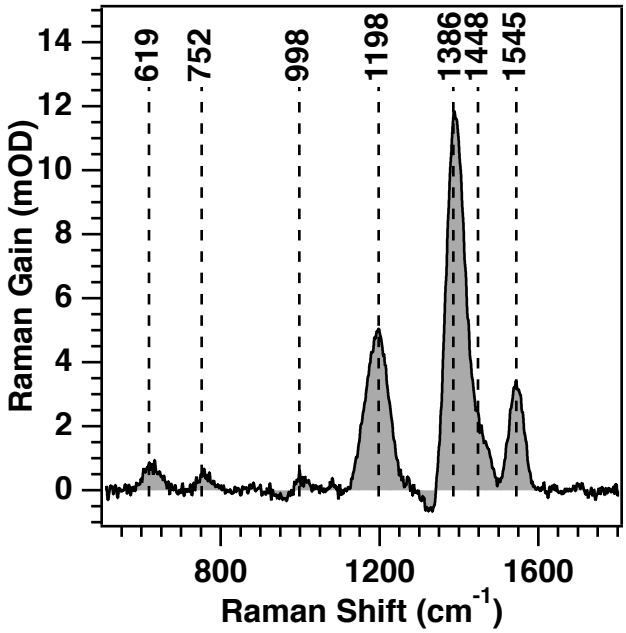

Figure 5.3: Femtosecond stimulated resonance Raman spectrum of tetracene nanocrystals suspended in water excited at 520 nm.

Figure 5.3 presents the femtosecond stimulated Raman spectrum of Tc nanocrystals in water resonantly excited at the absorption maximum of 520 nm. With 520 nm excitation, a fluorescence quantum yield of ∼0.002 results in a florescence intensity more than a hundred-fold greater than that of the strongest spontaneous resonance Raman band (calculation in SI).[132] Stimulated Raman spectroscopy is preferable to the spontaneous Raman spectroscopy in this circumstance because the stimulated signal is free of the isotropically emitted fluorescence background. The contribution of ground state bleaching by the Raman pump in the low frequency region of the spectrum has been subtracted for clarity (see Fig. C.5). The remaining signal consists of seven dispersive Gaussian features of well characterized totally symmetric intramolecular Raman active modes.[144] Table 5.2 presents a comparison of the measured and calculated Raman cross-sections as well as the parameters used to calculate Raman cross sections and the magnitude of the absorption cross section. The satisfactory fit

to the lowest energy absorption band as well as to the emission band indicates that the red edge of the absorption is dominated by a single electronic transition dipole of length M_{S0S1} = 0.46 Å. The deviation of the emission lineshape will be discussed below.

Due to the finite bandwidth of the stimulated Raman pump pulse (λ= 520 nm, FWHM = 37 cm^{-1}) used for the Tc nanocrystal experiments, the contributions of closely spaced peaks in the regions of 1159 - 1198 cm^{-1} and 1369- 1396 cm^{-1} could not be fully resolved (Table 5.2). The model was fit such that the sum of the calculated cross sections in these regions equals the measured cross section of the broad peaks. The relative cross sections of the unresolved peaks in these regions were taken to be consistent with the relative intensities of the peaks in the 476.5 nm Raman spectrum of the nanocrystals (Fig. 5.2).

The offset of the fluorescence maximum from the electronic origin, often referred to as the Stokes shift, is greater in Tc nanocrystals than it is in Tc monomer (see Figure 5.1). The origin for the shift does not come from solvent relaxation or surface trapped states because the same emission lineshape is observed in tetracene single crystals and thin films (see Figures C.2 & C.3).[131, 147, 158] This emission band appears at a highly red-shifted position in less than 300 fs after excitation and then blue shifts through the lifetime of the excited singlet state.[131, 135] Therefore the Stokes shift cannot be attributed to exciton diffusion to defect sites and the solvent reorganization energy (λ_s) is taken to be zero in Tc nanocrystals. The observed Stokes shift must instead be attributed to nuclear relaxation along low frequency phonon modes (λ_p = 130 cm^{-1}).

In the wavepacket model for Tc nanocrystals we incorporate the three Raman active intermolecular phonon modes observed at 58, 123 and 130 cm^{-1} as well as the intramolecular mode at 316 cm^{-1} which were reported under resonance conditions in Ref. [146]. The model was fit by first assuming rapid multimode dephasing leading to the approximate relative intensity relation I $\propto \Delta^2\omega^2$.[1] Next, the displacements of these low frequency modes were scaled together to reproduce the magnitude of the observed Stokes shift. The displacements of the high frequency modes were then adjusted to fit the stimulated Raman cross-sections. Finally, the relative displacements of the low frequency modes were again adjusted such that the relative calculated intensity was consistent with the spectral power density reported in Grumstrup et al.[146] Through this fitting procedure we were able to parse the total reorganization energy into contributions from specific vibrations. We estimate that the low frequency phonon modes have a reorganization energy of 130 cm^{-1} while the intramolecular vibrations have a reorganization energy consistent with the Raman intensities has a reorganization energy of 330 cm^{-1}.

In addition to stimulated RR spectra, spontaneous RR spectra of Tc nanocrystals were also obtained at three different bluer excitation wavelengths resonant with the higher energy exciton states (Fig. 5.2). The analysis of these three spectra is complicated by interfering electronic states. Importantly, all of the fundamental intramolecular Raman active modes found in the Tc monomer spectrum can be found in the Tc nanocrystal spectrum with only weakly perturbed frequencies ($\sim \pm 3$ cm^{-1}).

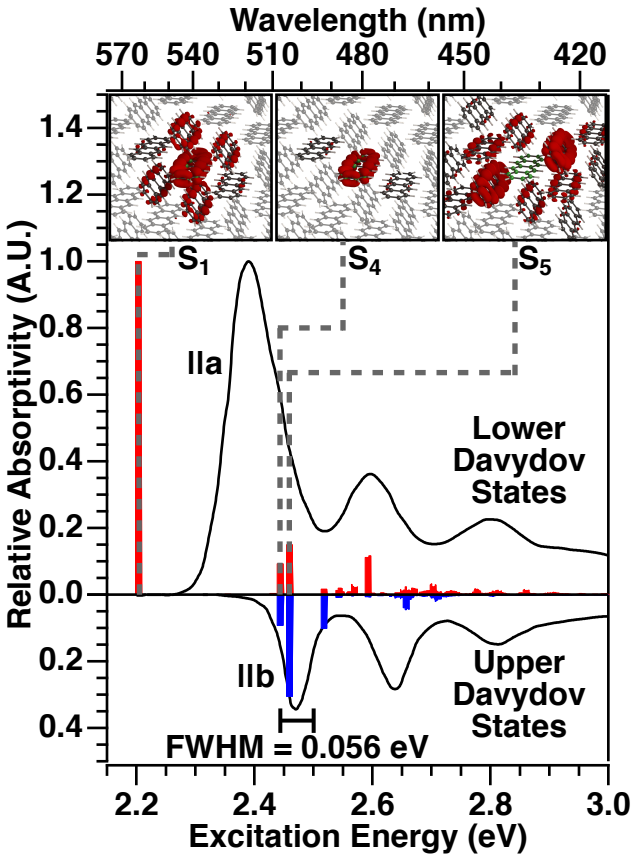

Figure 5.4: Comparison of experimental polarized absorption from Ref. [145] with calculated oscillator strengths of the contributing exciton eigenstates with a-polarization (top) and b-polarization (bottom). The exciton electron density surfaces (red) are connected to the eigenstates contributing to the absorption with dashed lines. The 40% electronic density surfaces were calculated for a hole that is equally distributed over the 18 p_z-type orbitals of the carbons on the central tetracene molecule depicted with green circles.

Theoretical calculations of phonons and excited-states of crystalline Tc

To better understand the higher energy exciton states of crystalline Tc, GW-BSE calculations were performed to compute them, and then analyzed to identify the optical absorption polarization dependence of each exciton eigenstate and to visualize the important electronic orbitals. Figure 5.5 presents a comparison of the polarized absorption of Tc single crystals as reported in Ref. [147] and as calculated with GW-BSE. The a and b-polarized exciton absorption bands are indicated as red and blue lines, respectively. The Lower Davydov State (LDS) corresponding to the a-polarized absorption is presented on top with grey lines connecting the calculated exciton energies with the corresponding orbital isosurfaces. The GW-BSE calculations performed herein suggest that in the low energy region of 2 - 3 eV

there are over 150 singlet exciton states, but most of these are weakly absorbing or optically dark transitions leaving only three exciton states (S_1, S_4, S_5) with appreciable oscillator strengths. The calculated energy of S_1 at 2.20 eV is lower than the measured electronic origin transition energy of E_{00} = 2.36 eV presented in Table 5.2. A mean absolute error of 0.16 eV is typical for GW-BSE excited state calculations of polyacenes.[151] A significant portion of this error can arises from a DFT starting-point issue, which underestimates the band gap and therefore overestimates the dielectric screening. Importantly only one exciton transition (S_1) dominates the red edge of the LDS. The second lowest energy exciton state (S_2) is calculated to be 0.15 eV higher in energy and is optically dark (with zero oscillator strength). Therefore, when the Raman pump is tuned to the red edge of the lowest energy exciton, only one electronic potential energy surface dictates the motion of the vibrational wavepacket and interference effects which have been shown to arise due to overlapping electronic resonances may be negligible.[174] Figure 5.4 indicates that the manifold of closely spaced exciton states (S_n) blue of the lowest energy exciton (S_1) accounts for the lack of mirror image symmetry of the absorption and emission.

The exciton states are comprised primarily of linear combinations of excitations and de-excitations involving the original a_u (occupied) and b_{2g} (unoccupied) molecular orbitals of the unperturbed monomer. The transitions to the lowest energy exciton (S_1) are strongly polarized along the LDS transition dipole. The electronic isosurface shows that the S_1 exciton is delocalized over approximately seven molecules for the isosurface value of 40%. This calculation suggests that the exciton size is much smaller than the nanocrystal size. Accordingly, confinement and local field effects in the nanocrystals are negligible and the optical properties of the macroscopic single crystal are largely preserved.[175] In the energy range of 0.15 - 0.22 eV above S_1 there are two optically dark exciton states, S_2 & S_3, presented in Figure C.1. The fourth and fifth exciton bands (S_4 & S_5) are calculated to have similar energies of 2.44 and 2.46 eV respectively. S_4 and S_5 have appreciable oscillator strengths along both LDS and UDS transition dipoles. S_4 is highly localized with the electron and the hole residing on the same central molecule. By contrast the S_5 exciton appears to have charge transfer character with the electron and hole residing on adjacent molecules.

Figure 5.5(A) presents a model wavepacket analysis that illustrates how delocalization of an excitation uniformly across ξ molecules affects the emission lineshape. The model uses the same fit parameters presented in Table 5.1 for $\xi = 1$. As ξ is incremented each displaced coordinate in the monomer becomes ξ-fold degenerate with a displacement of $\Delta_{monomer}/\xi$. Additionally the homogenous linewidth parameter Γ was incremented linearly from 95 cm^{-1} at $\xi = 1$ to 280 cm^{-1} at $\xi = 7$. Adjusting the homogenous linewidth is justified since displaced phonon modes were omitted from this analysis. Incrementing the homogenous linewidth parameter and inclusion of the phonons modes have similar effects in that both serve to dephase the multimode wavepacket. The measured emission from the monomer and the nanocrystals is given as solid and dashed black lines, respectively in Fig. 5.5(A). As ξ is incremented the fit emission lineshape increasingly resembles that of the nanocrystals. The best fit is found in the interval between $\xi = 5$ and $\xi = 6$ suggesting that the S_1 exciton is delocalized over about $\sim$5.5 molecules consistent with the S_1 electron density depiction in

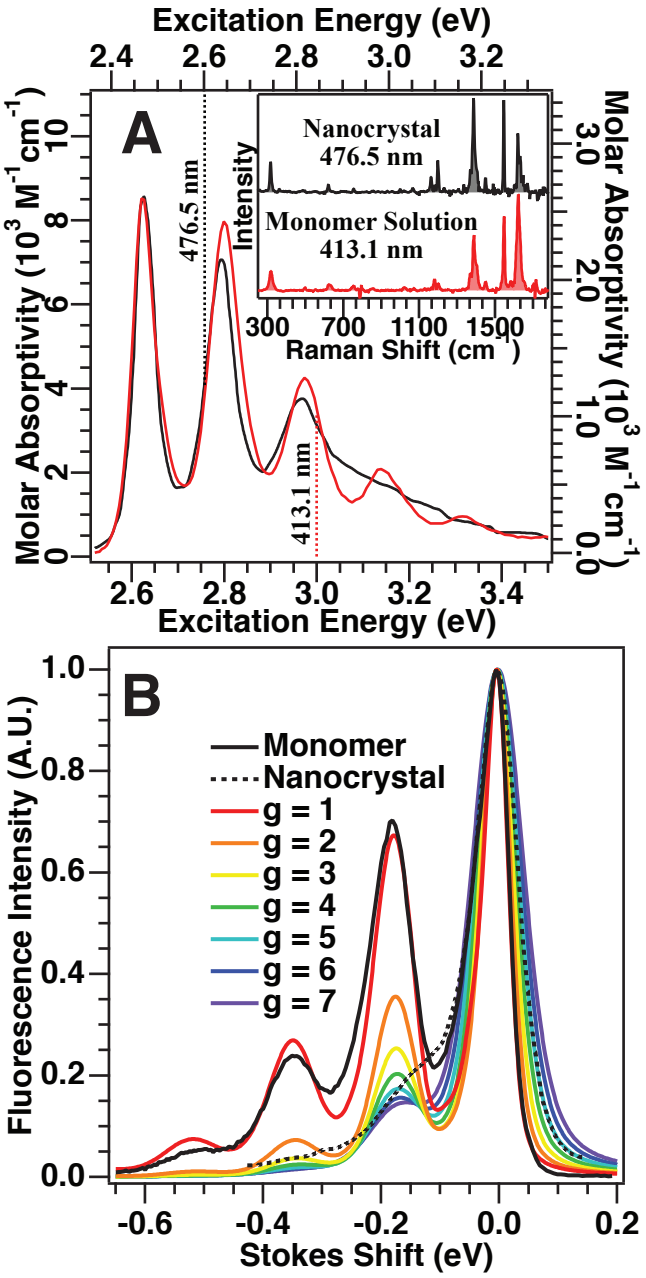

Figure 5.5: **(A)** Model of the effect of wavepacket delocalization on the emission lineshape of a molecular crystal. The black solid line is the measured emission spectrum of tetracene monomer in acetone while the black dashed line is the measured emission from the nanocrystal (from Fig. 5.1). The red line is the wavepacket fit to the monomer emission with displacements Δ_i given in Table 5.1. The colored lines present calculated emission spectra in which the excitation is delocalized over ξ molecules each with a displacement of Δ_i/ξ. **(B)** Absorption lineshape of monomeric tetracene in acetone (black) and the b-polarized component corresponding to the upper Davydov states of crystalline tetracene (red) from Ref. [145]. The excitation energy axes have been offset but the scaling is the same. (Inset) Resonance Raman spectra of Tc monomer (bottom) and Tc nanocrystals (top).

Figure 5.4.

Figure 5.5(B) presents a comparison of the absorption lineshape of the monomer and the ||b polarized absorption of the crystal corresponding to transitions to the upper Davydov states (S_n). Both absorption spectra appear to have similar vibronic structure corresponding to aromatic stretching frequencies ($\Delta\omega$ = 1386 cm^{-1}). A comparison of the spontaneous RR spectra of Tc monomer with 413.1 nm excitation and Tc nanocrystals with 476.5 nm excitation is presented in Figure 5.2. Despite the different resonance conditions, the two spectra show similar Raman intensities at the same peak frequencies. This suggests that the vibronic spectral density of states on S_n more closely resembles that of the monomer than that of the S_1 exciton in the crystal; this observation is consistent with the more localized character of S_4.

The vibrational character of the highly displaced Raman active phonon modes of tetracene is presented in Figure 5.6. Assignments of these phonon modes were made by comparing the vdW DFT calculated zone center frequencies and parities with all relevant literature.[126, 143, 144, 146, 176] The 58 cm^{-1} mode corresponds to a libration about the short molecular axis (M) while the 123 and 130 cm^{-1} modes correspond to librations about the long molecular axis (L) on two different molecules.

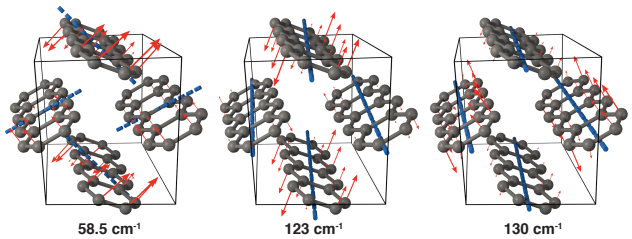

Figure 5.6: Character of the displaced librational phonon modes in tetracene single crystal as viewed from the ab crystal plane. The blue dashed lines correspond to the axis of rotation.

5.5 Discussion

The monomer absorption and Raman properties are precisely fit, but this constitutes only a preliminary analysis as only one excitation wavelength was used. The b_{3g} modes were treated phenomenologically as displace harmonic coordinates; however, it is well-known that a b_{3g} mode cannot be displaced. The lack of rotational symmetry about the short and long molecular axis requires that the initial direction of a distortion along a b_{3g} coordinate be arbitrary. The b_{3g} modes resonance enhancement consistent with B-term vibronic coupling with the optically active high energy B_{1u} state analogous to the vibronic coupling of states in naphthalene (Section 1.4).[27, 29, 30] These data suggests that excitation above of the lowest energy B_{2u} state or the exciton states comprised there of produces a mixed excited state at very early times which is anharmonic along the b_{3g} coordinates in both Tc monomer

and nanocrystals (see Sections 1.4 & C.1). Unfortunately to our knowledge no time-domain model has been developed that incorporates B-term Raman cross-sections.

We have developed a 15-mode vibronic model that describes the absorption and emission lineshapes as well as the RR cross sections for both Tc monomer and Tc nanocrystals. Returning to the crystalline system, a more physically realistic model might include a distribution of displacements on a cluster of degenerate vibrations surrounding the excitation; however, at this time there is no easy experimental way of determining this distribution. While a single displaced coordinate is not physically realistic in a crystal, the energy dissipated along all of the degenerate vibrations in the distribution for each mode must sum to the calculated reorganization energies presented in Table 5.2. For the rest of the discussion we will focus on the mode specific reorganization energies that occur after Frank-Condon absorption.

In the Tc monomer there is a reorganization energy of 1760 cm^{-1} along intramolecular aromatic stretching coordinates and a solvent reorganization energy of 70 cm^{-1} along generalized solvent coordinates in acetone. By contrast the Tc nanocrystal undergoes a distortion of the crystal lattice in the proximity of the exciton with a diminished net reorganization energy. Integration of the fluorescence band (Eq. 5.6) yields an upper bound of 600 cm^{-1} for the total reorganization energy. From the Raman intensities, we find that much of this reorganization energy (330 cm^{-1}) is accounted for by a wavepacket along totally symmetric coordinates that is generated within the first 100 fs after excitation.

From the shift of the emission peak maximum an estimate of about 130 cm^{-1} is made for the librational phonon reorganization energy. A concern is whether the Stokes shift in Tc nanocrystals (Fig. 5.1) can be attributed purely to vibrational reorganization energy or if there is a significant contribution from defect states.[136, 177, 178] The stimulated emission band appears at a highly Stokes shifted position at a time delay of 300 fs and then blue shifts throughout the duration of the excited state lifetime ($\sim$170 ps).[131, 135] The apparent Stokes shift is thus most accurately a consequence of the reorganization energy along specific Raman active coordinates immediately after excitation. The remaining energy (0 - 200 cm^{-1}) in the emission band may arise from slower thermally activated distortions or exciton diffusion to modified defect sites or indirect band-gap transitions which occur on time scales longer than wavepacket dephasing. Indeed the fluorescence lineshape varies depending on temperature and sample morphology.[135, 136] These results highlight the importance of resonance Raman measurements and multidimensional wavepacket analysis for developing an understanding of vibronic coupling in complex periodic systems.

It is important to understand why the wavepacket fit to the Raman intensities of the nanocrystals (Table 5.2) deviates from the measured emission lineshape in the region of 565 nm (red line Fig. 5.1). The fit accurately reflects the majority of the fluorescence intensity which is polarized along the LDS transition dipole; however, the fit deviates in the wavelength region of a weak emission band polarized along the UDS.[147, 173, 179] This anomalous UDS-polarized emission violates Kasha's rule which would predict that all emission intensity is polarized along the lowest energy dipole coupled transition.[180] Weak anomalously polarized emission is similarly observed in molecular crystals of rubrene.[181] This weak UDS-polarized

emission has been postulated to occur through thermal population different points within the exciton band structure.[173] Indeed the calculated emission lineshape presented in Figure 5.1 (red lines) more closely resembles the measured emission lineshape at 4 K when minimal thermal population occurs than the emission lineshape at 298 K.[158] Alternatively, when the unpolarized fluorescence lineshape is used for fitting (blue dashed line), the Raman cross-sections of the mid-frequency modes (619, 752 and 998 cm^{-1}) are over-estimated by an order of magnitude. A more accurate model could be established by fitting exclusively to the emission lineshape polarized along the lower Davydov band; however, spectral leakage and self-absorption make such measurements difficult.[181]

When comparing excitations of the monomer and nanocrystal, the nanocrystal experiences about one-fifth the total reorganization energy while at the same time the nanocrystal experiences about twice as much intermolecular reorganization energy. A more delocalized excitation acts on more vibrational coordinates but the displacement of each coordinate is proportional to the change in electron density (bond order) acting across specific bonds. To first approximation if an exciton is equally distributed on ξ molecules in a crystal, the intramolecular reorganization energy should scale reciprocally with ξ. The analysis presented in Figure 5.5(A) indicates that this decrease in intramolecular reorganization energy in the crystal is a result of delocalization of the S_1 exciton onto about $\sim$5.5 molecules. The isosurfaces in Figure 5.4 suggest an unequal distribution of electron density across $\sim$7 molecules and therefore an unequally shared nuclear distortion is expected. The full extent of the delocalization might be somewhat greater than $\sim$5.5 molecule. These results are consistent with the results of from Ref. [178] where the temperature dependence of the rate of superradiant emission from Tc thin films verses that of the monomer indicated an exciton delocalization onto $\sim$10 molecules. At the same time the altered electrostatic forces of the more delocalized exciton states are leveraged more strongly on intermolecular coordinates i.e. phonons. Once energy has relaxed out of the initial Raman wavepacket, the distortion of the nuclei and the exciton are bound together as a polaron.

From a comparison with previous impulsive stimulated Raman experiments as well as by modeling of the absorption-emission Stokes shift, we deduce that the S_1 exciton has a large contribution to the vibronic lineshape from three intermolecular phonon modes with frequencies 58, 123 and 130 cm^{-1} corresponding to librations about the M and L axes of the Tc molecules (Fig. 5.6). The two higher frequency phonons (123 and 130 cm^{-1}) constitute a reorientation of the short molecular axis and therefore a coordinate dependence of the transition dipoles. It is reasonable that these phonons contribute greatly to the vibronic spectral density of states and may affect the subsequent exciton dynamics.

Resonance Raman intensity analysis does not inherently give the direction or the phase of the excited state distortion along these ground state librational coordinates, but we can intuit this phase by inspecting the electron isosurfaces in Figure 5.4. The S_1 exciton involves an excitation from an linear combinations of occupied a_u orbitals to b_{1g} orbitals that are delocalized on about seven molecules. Excitation leaves a partial positive charge on the central molecule and a partial negative charge on the four surrounding molecules. The electropositive CH portion of the quadrupole interaction is weakened by the new partial positive

charge while the electronegative p_z portion of the quadrupole interaction is strengthened. The Raman wavepacket generated with excitation to S_1 should result in a planarization of the Tc molecules in the proximity of the exciton.

Not only does the altered electronic structure generate librations but the librational motion can also have a significant effect on electronic couplings and energies. This librational motion has been predicted to localize the electron density on a pair of molecules and tune the energies of the excited singlet states to near degeneracy with the ^{1}(TT).[127] The planarization of the Tc molecules results in increased overlap density of the p_z electrons. Michl et al. have shown that the two electron overlap density of these p_z orbitals modulates the rate of singlet fission in symmetric slipped-stack dimers.[182] These nuclear motions may be instrumental in efficiently coupling singlet and multiexciton states.[127, 183]

Having developed an coarse model for the lowest energy exciton S_1, we now seek to gain insight into the nuclear displacement in the S_n manifold of exciton states. The nuclear and electronic dynamics in the S_n manifold of exciton states are critical to understanding singlet fission as a coordinate dependent process since it has been postulated that efficient SF is energetically accessible from S_n. The calculated polarized absorption (Fig. 5.4) suggests that the S_1 exciton does not contribute to the b-polarized absorption corresponding to the UDS. Rather the b-polarized absorption is dominated by S_4 and S_5 at the red edge.

An estimate for how long these higher energy excitons states S_n persist is given by the peak width of the polarized absorption. The first peak of the UDS-polarized spectrum has a full-width at half-maximum of 0.056 eV (Fig. 5.4). This peak width yields a lower bound for the lifetime of these higher exciton states S_n of 36 fs. Since the peak width of the UDS-polarized absorption has contributions from pure dephasing, vibronic structure and inhomogenous broadening, 36 fs serves only as a minimum lifetime for relaxation of S_n to S_1 or ^{1}(TT). Transient absorption measurements indicate that the stimulated emission band (S_1-S_0) is formed in less than 200 fs yielding an upper bound for the relaxation time of S_n.[135] Therefore electronic relaxation out of S_n occurs on a timescale concurrent with nuclear wavepacket motion.

Detailed inspection of the lineshape of the UDS suggests that there is indeed a resemblance to the vibronic structure of the Tc monomer absorption (Fig. 5.5,B). Furthermore, when the excitation is resonant with the UDS states at 476.5 nm, the RR spectrum of Tc nanocrystal shows similar intensities and frequencies as that of Tc monomer with 413.1 nm excitation (Fig. 5.5 inset). These results suggest that the S_n states are more strongly displaced along high frequency intramolecular stretching modes as compared to the S_1 state which has more displacement along low frequency phonon librations. This observation can be understood by noting that the S_4 and S_5 excitons adopt structures where the electron and hole are localized on the same residue or on adjacent residues (charge transfer). Since excitation of the monomer and the S_4 and S_5 excitons involve similar orbitals, they are expected to have similar nuclear displacements and accordingly similar vibronic lineshapes.

It has been shown that in other organic semi-conductor systems varying the varying the excitation wavelength can have a robust effect on the short-time exciton dynamics and the yield of long lived photoproducts.[184] Crystalline Tc may show similar behavior where vary-

System	Intramolecular Reorganization Energy (cm^{-1})	Solvent/Phonon Reorganization Energy (cm^{-1})	Total (cm^{-1})
Monomer S_1	1760	70	1830
Crystal S_1	300 - 500	130	400 - 600

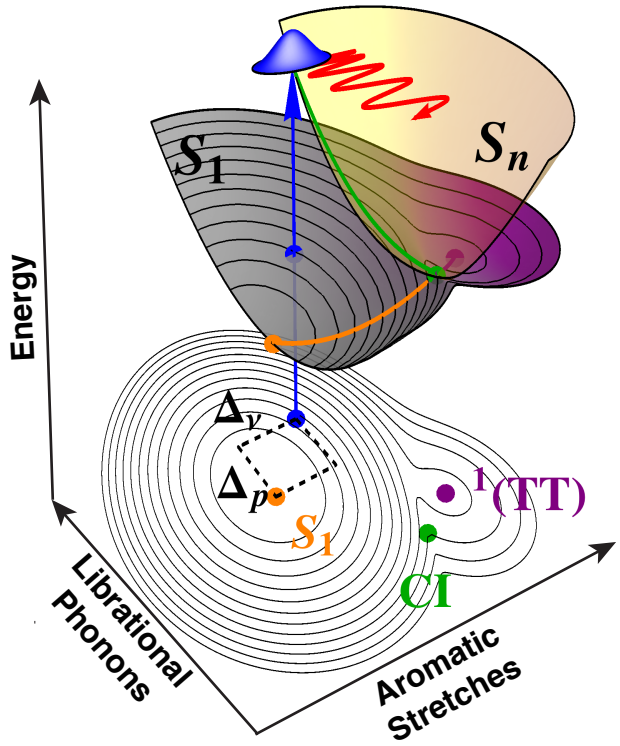

Figure 5.7: Schematic vibronic potential energy surfaces for singlet fission. A wavepacket is generated in a localized S_0 geometry, (blue arrow and dots) on S_n (yellow surface). The wavepacket follows a ballistic vibrational trajectory (red line) along high frequency aromatic stretches and low frequency librational phonon modes. In the first period of the librational phonon motion the wavepacket encounters a conical intersection between S_n and ^{1}(TT) (green sphere) and bifuricates. About half of the population transfers efficiently to ^{1}(TT) (purple sphere). Energy relaxes out of reactive high frequency aromatic stretches thereby trapping the remaining S_1 population (orange sphere) until an alternative incoherent thermal singlet fission pathway is activated. The displacement of the S_1 minimum relative to S_0 along aromatic stretches and librational phonons are indicated as Δ_ν and Δ_p respectively. The reorganization energies of the librational phonons (λ_p) and aromatic stretches (λ_ν) are indicated by the contour lines on S_1 each demarcating 200 cm^{-1}.

ing excitation wavelength effects the yield of sub-200 fs triplet formation.[184] A pump probe experiment involving changing the excitation wavelength from 525 to 400 nm is has been conducted in Ref. [135]. The authors observe significant change in the sub-2 ps response at 800 nm probe wavelength by varying the excitation wavelength although they have difficulty discerning the signals originating from the excited state absorption and those originating from coherent artifacts. More experiments are necessary to deduce this critical mechanism.

Figure 5.7 illustrates a hypothetical mechanism for SF in Tc that facilitates a discussion of our results. The total nuclear reorganization energy on S_1 (λ_{net} <600 cm^{-1}) is lower than the energy gap to the multiexciton state ($E_{^1(TT)} - E_{S_1} \approx 1500$ cm^{-1}). Consequently, an efficient SF channel should not be accessible from the vibrational levels of S_1 but only from higher energy exciton states (S_n, yellow surface). Following excitation to S_n, a wavepacket (red line) propagates ballisticly along low frequency librational phonon modes as well as intramolecular stretching coordinates. The high dimensionality of the reactive coordinates have been reduced to a two-dimensional representation for simplicity. The librational modes about the M molecular axis likely planarize the excited molecules allowing for an increase in p_z orbital overlap.[182] At the same time the high frequency aromatic stretching modes rapidly sample the high dimensional phase space around the conical intersection (green dot). When the wavepacket reaches the conical intersection, and SF is efficient, half of the excited state singlet population efficiently transfers to ^{1}(TT) (purple line).

Once the initial trajectory has dephased and vibrational energy has relaxed to a local minimum on S_1 (orange line and dot), the remaining S_1 population undergoes incoherent internal conversion to ^{1}(TT) on a 40-170 ps timescale largely governed by the temperature dependent rate of exciton diffusion to lattice sites with a suitable intermolecular geometry to make the process once again efficient.[129, 130, 135, 136] An alternative explanation for the fast SF dynamics could be that electronic coherence is responsible for efficient SF.[185] Given that the S_n states persist for longer than 36 fs and electronic decoherence is expected to occur on a time scales shorter than 10 fs[186, 187] it seems more likely that vibrational coherence is responsible for the coupling of S_n to ^{1}(TT) in Tc.

5.6 Conclusions

The mode specific reorganization energies for Tc monomer and nanocrystals have been determined. In the monomer, the excitation displaces primarily high frequency aromatic stretching coordinates ($\lambda_\nu = 1760$ cm^{-1}). In the nanocrystals, the reorganization energy for S_1 along these aromatic stretching coordinates is much smaller (300 <λ_ν <500 cm^{-1}) but there is an increased intermolecular reorganization energy ($\lambda_p \sim$130 cm^{-1}). These results are understood in the context of increased delocalization when going from the confined orbitals on a monomer to a delocalized exciton state in the molecular crystal. At the same time, there is evidence that the S_4 exciton state is more localized and its vibrational displacement resembles that of the monomer. Detailed inspection of the polarized absorption and literature transient absorption results indicate that there is an efficient singlet fission pathway from S_n

that occurs on a timescale concurrent with specific vibrational coherences (36 fs $<\tau_1<$200 fs). Using vdW-DFT, three highly displaced librational phonon modes in the nanocrystals were assigned and characterized. These phonon modes lead to a modulation of the intermolecular p_z orbital overlap. There is evidence that intermolecular p_z orbital overlap is necessary for efficient singlet fission to occur.[188] These results underpin the importance of resonance Raman analysis for developing a better understanding of vibronic spectral densities in complex periodic systems.

Acknowledgements

This work was supported by the Mathies Royalty Fund; the German Research Foundation (postdoctoral fellowship to Dr. D. Dietze, DFG grant DI1998/1-1); The Center for Computational Study of Excited-State Phenomena in Energy Materials at the Lawrence Berkeley National Laboratory, which is funded by the U.S. Department of Energy, Office of Science, Basic Energy Sciences, Materials Sciences and Engineering Division under Contract No. DE-AC02-05CH11231, as part of the Computational Materials Sciences Program. Work at the Molecular Foundry was supported by the Office of Science, Office of Basic Energy Sciences, of the U.S. Department of Energy under Contract No. DE-AC02-05CH11231. Computational resources provided by NERSC. We thank the Matt Francis lab for generous use of their fluorometer.

Chapter 6

Chemical and Solid State Examples of the Reciprocal Relation of Polaron Binding Energy and Polaron Size

This work will be submitted to the *Journal of Physical Chemistry C* by Scott R. Ellis, Myeongkee Park and Richard A. Mathies

6.1 Abstract

In systems where a delocalized electronic excitation has the same ground and excited state orbital symmetries or those that are isomorphic to a localized excitation the polaron binding energy (λ'), the energy that is deposited into phonons in the first half period after electronic excitation scales approximately reciprocally with the extent of the polaron size (ξ) which is the spatial extent over which an exciton or charge carrier acts on the nuclei. This principal informs vibronic excitations in small molecules and is also observed in the behaviour of solid state systems such as bulk semi-conductors nanomaterials.

6.2 Introduction

Chemists and physicists are increasingly interested in the interplay between optical excitations in delocalized electronic systems and the lattice distortion that accompanies them: what is referred to as a polaron. These systems can be difficult to model because of the scaling of many-bodied electron exchange interaction and the high dimensionality of the nuclear distortion. This problem motivates the development of a trend that allows us to compare the polaron binding energy, also called the vibration reorganization energy, of small systems to that of massive systems. To this end, we examine the vibrational reorganization energy in small molecules in solution, electronically coupled dimers[189], molecular crystals,[127] inorganic semi conductors, quantum dots[190], and metals. These systems were chosen because the lowest energy excitation involves electronic and vibrational states that are isomorphic to a more localized excitation so reasonable comparison can be made between the vibrational reorganization energies (λ_ν) and the polaron size (ξ). We find that the more delocalized excitations result in weaker lattice distorts.

Polarons are not exclusive to excitons; there is a binding energy associated with the annihilation of an electron from the valence band (oxidation) forming a hole polaron (λ_{h+}), or creation of an electron in the conduction band (reduction) forming an electron polaron (λ_{h+}). The binding energy of the exciton is typically greater than the binding energy of either the electron or the hole because the change in bond order of the exciton is twice as large and also the electron and hole act to localize each other when they are proximate in the case of an exciton.

In this work we us a simple molecular model so that the optical properties can be intuitively related to characteristics of the polaron. In a classical picture an excitation of an electron from an occupied to an unoccupied orbital alters the electrostatic environment around the nuclei and creates a strain field. The stain field accelerates the nuclei along specific vibrational or phonon coordinates on a femtosecond timescale thereby producing a wavepacket of vibrations or phonons, $|\chi_i(t)\rangle$.[162] The autocorrelation function of this wavepacket with the initial vibrational states $\langle\chi_i|\chi_i(t)\rangle$ determines the vibronic spectrum of the absorption and emission while cross-correlation of the wavepacket with excited vibrational states $\langle\chi_f|\chi_i(t)\rangle$ determines resonance Raman cross sections. We model the absorption, emission and reso-

nance Raman spectra with harmonic vibrational potential energy surfaces displaced along coordinates i in unit cell j by a dimensionless displacement parameter Δ_{ij}. When an exciton involves highly localized electronic states the alteration of electronic environment is stronger and leveraged across a few vibrational degrees of freedom while in a delocalized excitation each of many vibrational coordinates feels only a weak perturbation of its electronic environment. The dimensionless displacement of the nuclei is proportional to the change in bond order, which to first approximation is inversely related to the extent of delocalization. In this case as an excitation delocalizes across ξ isomorphic orbitals and the displacement of any one vibrational coordinate is diminished as:

$$\Delta' = \Delta_1/\xi \tag{6.1}$$

In the localized case the excitation displaces a vibrational coordinate by Δ_1 while in the delocalized case the excitation displaces ξ coordinates by Δ'. Therefore the polaron binding energy can be calculated as:

$$\lambda' = \sum_{j=1}^{\xi}\sum_{i=1}^{n} 1/2\hbar\omega_{ij}\Delta_{ij}'^2 \tag{6.2}$$

Where ω_{ij} and Δ'_{ij} are the frequency and displacement of vibration 'i' in unit cell 'j' respectively. The reorganization energy of the delocalized excitation is then diminished as

$$\lambda'(\xi) = \frac{\lambda_1}{\xi} \tag{6.3}$$

Where λ_1 is the vibrational reorganization energy of the localized single subunit excitation. This trend can be understood intuitively as delocalized electronic states more effectively screens the nuclei from a change in the electrostatic environment. Vibrational reorganization energy is an important parameter. The reorganization energy can result in an energy differential between electronic state and determines the exothermic electronic relaxation pathway. In Marcus theory the vibrational reorganization energy, λ', enters into the rate of electron transfer as:

$$k_{et} = \sqrt{\frac{\pi}{\hbar\lambda' k_b T}}|H_{ab}|^2 \mathrm{Exp}\left[\frac{-(\lambda' + \Delta G^0)^2}{4\lambda' k_b T}\right] \tag{6.4}$$

Here ΔG^0 is the difference in energy between electronic states, T is temperature, H_{ab} is the electronic coupling matrix element which typically decreases exponentially with the distance between electronic states 'a' and 'b'. This semi-classical model can be applied to excitations in periodic solids. In semiconductors the vibrational reorganization energy, λ', is called the polaron binding energy serves as a minimum potential barrier that must be overcome each time an exciton, or charge carrier 'hops' to an adjacent lattice site.[191] Therefore in solids the polaron binding energy controls charge carrier or exciton mobilities. In a solid

ΔG^0 is zero because each lattice site is identical with translation. From expression we surmise that semiconductors with localized electronic states (Frenkel-type excitons) typically have a larger reorganization energy and lower charge-carrier mobility while more delocalized excitons (Wannier-Mott excitons) typically have smaller polaron binding energies and exhibit higher carrier mobility. Moreover excitons in a bulk semiconductor crystal have an intrinsic electron hole binding energy. In such cases the delocalization cannot be infinite. In these systems, the reorganization energy asymptotes to a value (λ_{bulk}). We therefore fit the reorganization energy to the following.

$$\lambda'(\xi) = \frac{\lambda_1}{\xi} + \lambda_{bulk} \tag{6.5}$$

Where λ_1 is the polaron binding energy inherent to a single unit cell and λ_{bulk} is polaron binding energy in a infinite bulk semiconductor. This result helps explain photostability. UV or X-ray excitation involving confined electronic states of small molecules in the gas phase often results in photodissociation with quantum yields close to 100% because a large amount of energy is deposited into a few vibrational coordinates.[192] By contrast excitations involving delocalized electronic states are extremely photostable because the polaron binding energy is small and spread across many bound vibrational coordinates. For example, if passivated effectively quantum dots can be excited practically indefinitely without bleaching. We illustrate the broad applicability of this reciprocal relation and demonstrate how it can be applied to inform scientists about the electronic structure of periodic systems.

Small Molecules with Repeating Subunits

The simplest systems where the effect of delocalization can be observed are small molecules with electronically conjugated repeating subunits. The polyacenes are an ideal model system because the lowest energy B_{1u} electronic excited state is separated energetically from the next electronic state allowing for accurate measurement of the vibrational reorganization energy. The absorption and emission spectra of polyacenes with 3-6 conjugated rings is presented in Figure 6.1. By inspection of the ratio of the 0-1 vibronic transition to the electronic origin 0-0 transition the vibrational reorganization energy is shown to decrease with increasing conjugation length. The same effect is also apparent in the vibronic lineshapes of α-thiophene oligomers of chain length 2-6 (Fig D.1). In cases where the solvent relaxation is small and the lowest energy excited state is optically active the intramolecular vibrational reorganization energy can be well approximated by half of the Stokes shift, which is half the energy difference between absorbed and emitted light. Details of how the half Stokes shift ($1/2\nu_{St}$) was calculated is presented in the Section D.2. The measured half Stokes shift is presented in Fig. 6.1(B) along with a fit of the form $1/2\nu_{St} = (29 \pm 1) \times 10^4 cm^{-1}/\xi$. The anticipated trend is observed: the Stokes shift decreases with delocalization as $1/\xi$.[193, 194]

The term polaron is often used interchangeably to describe the nuclear distortion surrounding and exciton, or an electorn or hole. The electron and hole reorganization energies have been reported by density function theory and gas phase UV photoelectron spectroscopy

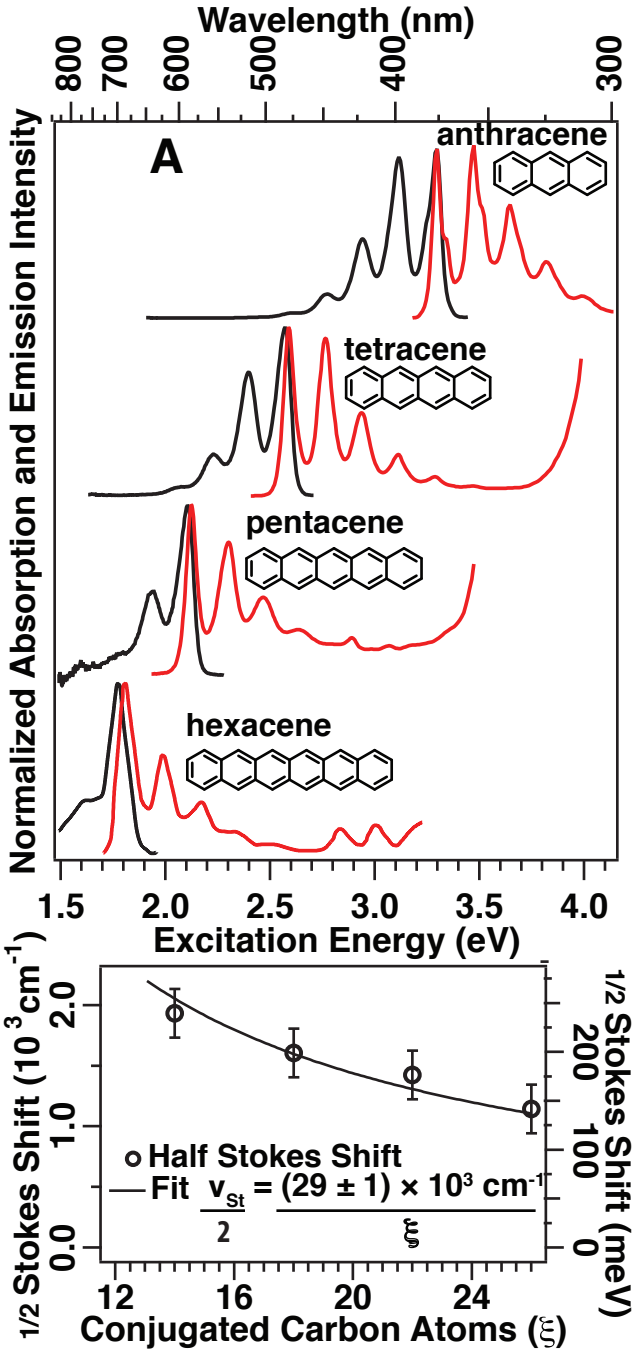

Figure 6.1: (A) Absorption (red) and emission (black) of polyacenes with between three to six conjugated rings. The spectra of hexacene were digitized from Ref. [193]. (B) Plot of measured Stokes shift verses number of conjugated carbon atoms.

for anthracene, tetracene, pentacene and rubrene. In these systems we find the free electron polaron binding energy is about 79% of the of the excitonic binding energy while the free hole polaron binding energy is about 56% of that of the exciton.[194, 195] The solution phase exciton reorganization is less than the sum of the gas phase electron and hole reorganization energy suggesting that in these systems polaron formation would drive exciton dissociation into free charge carriers.

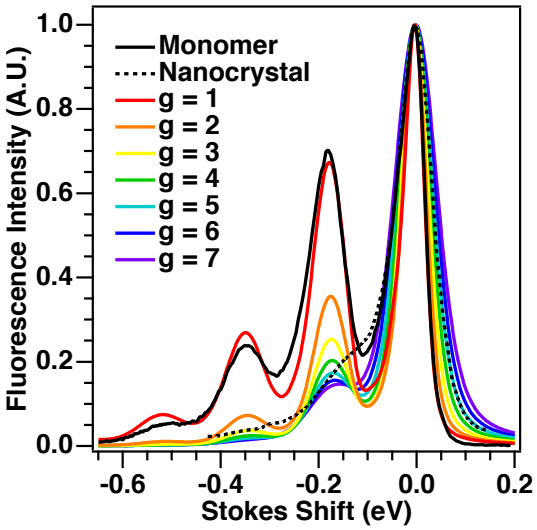

Figure 6.2: Model of the effect of wavepacket delocalization on the emission lineshape of a molecular crystal. The black solid line is the measured emission spectrum of tetracene monomer in acetone while the black dashed line is the measured emission from the tetracene as a nanocrystal. The red line is the wavepacket fit to the monomer emission with displacements Δ_i. The colored lines present calculated emission spectra in which the excitation is delocalized over 'ξ' molecules each with a displacement of Δ_i/ξ.

Exciton States in Dimers and Semiconductors

The effect of delocalization can be extended from excitations in small molecules to excitations in their corresponding dimers and then further to their behaviour in molecular crystals. When placed in close non-covalent contact the transition dipoles of the monomers interact and perturb the monomer states.[173, 196, 197] A manifold of exciton states are formed from linear combinations HOMO and LUMO states of the electronically coupled monomers. In these systems, the critical parameter that determines the vibrational reorganization energy is the extent of exciton delocalization.

Careful resonance Raman intensity analysis of non-covalent H-dimer[1] of merocyanine dye shows that the vibrational reorganization energy decreases from λ_1 ~370 cm^{-1} in the

[1]H-dimers are oriented with anti-parallel transition dipoles such that the optically allowed exciton state is antisymmetric and blue-shifted with respect to the monomer state.

monomer to $\lambda' \sim$130 cm^{-1}.[189] The authors note that "the reduced Franck-Condon activity [is] consistent with the electronic excitation being spread over both monomers".[189] The authors show that owing to the strongly coupled electronic states, the dimer can be treated as a super-molecule where the absorption and Raman cross-sections of the dimer can be effectively reproduced by decreasing the displacements of the monomer by a factor of $\sqrt{1/2}$. We show in the Section C.1 that this is equivalent to taking each displaced vibrational degree of freedom on the monomer, splitting it into two displaced coordinates each with a displacement of $\Delta_1/2$.

The polaron formation of dimers can be extended to that of bulk semi-conductors. To illustrate this we examine fluorescence spectrum of nanocrystalline tetracene. Importantly the bulk exciton Bohr radius of crystalline tetracene is much smaller than the size of tetracene nanocrystals used in this experiment.[120] Therefore the effect of confinement is negligible and the optical properties of the nanocrystals are nearly identical to that of a bulk tetracene crystal after averaging over isotropic orientations. Excited state electronic structure calculations show that absorption is complicated by the contribution of many exciton states. Furthermore if the energy separation between the lowest energy exciton state and the next state is somewhat larger than kbT then the fluorescence spectrum contains only vibronic transitions from the band-edge excition state S_1.[198] Therefore inspection of the emission lineshape is more indicative of purely vibrational reorganization energy. Figure 6.2 presents a comparison of the emission lineshape of tetracene monomer in solution (solid line) and tetracene nanocrystals (dashed line). The colored lines represent wavepacket model fits of the vibronic lineshape of an excitation evenly delocalized over ξ molecules. The best fit is found in the interval between $\xi = 5$ and $\xi = 6$ suggesting that the S_1 exciton is delocalized over approximately 5.5 molecules. This result is supported by the aforementioned electronic structure calculations as well as other experimental work.14, Using this knowledge a scientist can roughly estimate the extent electronic delocalization in a crystal or thin film by taking the ratio of the reorganization energies of the monomer to that of the solid. Rearranging Equation 6.2:

$$\xi = \frac{\lambda_1}{\lambda'} \tag{6.6}$$

the net reorganization energies are $\lambda_1 = 1830$ cm^{-1} and $\lambda' = 460$ cm^{-1} for the monomer and nanocrystal respectively leading estimate that the band-edge exciton is delocalized onto about 5.5 tetracene monomers.

Important implications arise from this analysis. First this implies that different exciton states have different extents of delocalization and therefore different vibrational potential energy surfaces. For example it is generally accepted that triplet states in molecular crystals are more localized than singlet states because of increased electron.[177] Therefore we would expect a triplets exciton state in molecular crystals would have a larger reorganization energy than would the singlet exciton states. A multiexciton state which is a spin couple pair of triplet excitons might have a still larger reorganization energy since two electrons have been promoted as compared to one in the singlet.

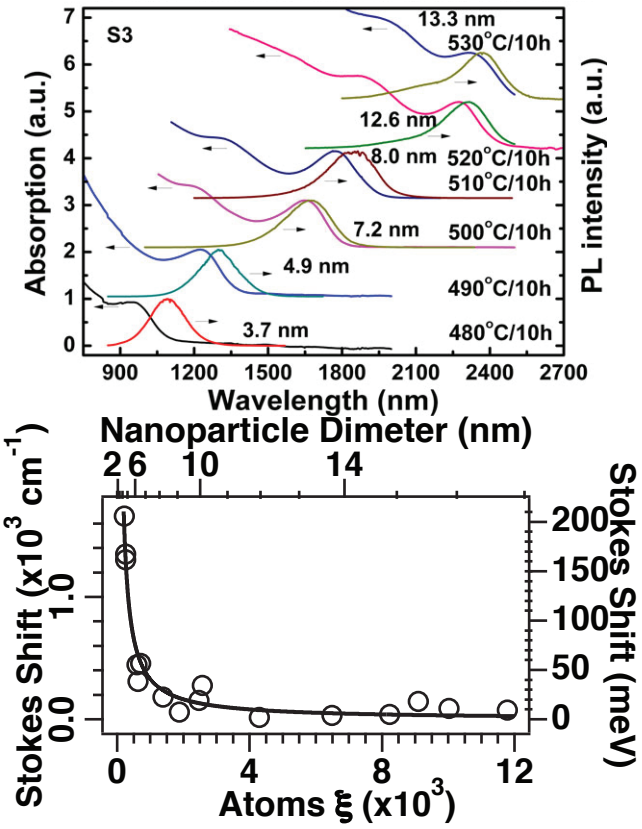

Figure 6.3: (Top) Absorption and photoluminescence spectra of PbS quantum dots of varying diameter annealed in a glass. (Bottom) Stokes shift verses number of sulfides. Red line is a least squares fit of the form $\lambda = (3.3 \times 10^5 \pm 1.7 \times 10^4 \text{cm}^{-1})/\xi$. Reprinted with permission from Ref. [199]. Copyright 2015. John Wiley & Sons, Inc.

Quantum Dots - Confined Semiconductor Nanoparticles

Semiconductors can be made into nanostructures which are smaller than the bulk exciton Bohr radius called quantum dots. Quantum confined nanoparticles have smaller polaron sizes and correspondingly a larger polaron binding energy. To illustrate this we once again inspect the half-Stokes shift of quantum dot systems; lead (II) sulfide and cadmium (II) selenide nanoparticles. Bulk PbS has a low energy direct bandgap of 410 meV at 300 K and a Bohr excition radius of about 18 nm. [199, 200] Annealing these nanoparticles at lower temperatures produces smaller nanoparticles and blue-shifts the absorption. For nanoparticles with diameters less than 18 nm the bulk exciton is confined and the bandgap blue-shifts. The electronic transition acts more strongly across fewer vibrational degrees of freedom, the net result of which is a larger vibrational reorganization. Figure 6.3(A) presents their absorption and emission of PbS nanoparticles annealed in silicate glasses.[199] In this case lineshapes are broad the Stokes shift is estimated from the offset between absorption and emission peak maxima. It is evident from the broad peaks that the magnitude of the Stokes shift increases

as the absorption blue-shifts. Figure 6.3(B) presents the magnitude of the Stokes shift as a function of estimated nanoparticle size in terms of number of sulfide atoms. The number of sulfide atoms were approximated as perfects spheres comprised of cubic unit cells of edge length 0.5936 nm, corresponding to that of bulk PbS at 300K.[200] A clear $\lambda'(\xi) = \lambda_1/\xi$ trend is observed. For nanoparticles on the order of the bulk exciton Bohr radius or greater, the nanoparticle size is not an accurate measure of delocalization. For large nanoparticles λ' should converge to some value greater than zero corresponding to the Stokes shift in bulk PbS although this effect is not obvious in this dataset. Various molar ratios of Pb:S ranging from $1:1$ to $2:0.8$ were used in synthesizing the nanoparticles from which this florescence data is taken. Despite varying the composition of nanopartices the λ_1/ξ trend dominates. This suggests that the observed trend is general to quantum confined systems and not limited to specific nanoparticles. A more famous example of electronic confinement is observed Stokes shift of CdSe nanoparticles. Bulk CdSe has a bandgap of about 1.84 eV near 0 K and a bulk exciton Bohr radius of about 5.6 nm.[201] Figure 6.4(A) presents the absorption and emission of werzite CdSe nanoparticles of varying sizes passivated and suspended in organo-phosphine glasses. It is clear from inspection that smaller nanoparticles have higher energy band gaps and larger Stokes shift.

The Stokes shift in quantum dots like PbS and CdSe is also commonly attributed to electronic relaxation through nearly degenerate spin states (band-edge exciton splitting, BEES) or surface-trapped states (STS). However, recently it has become clear that the polar polaron binding energy often accounts for a significant fraction of the observed Stokes shift.[190, 199] In an polydisperse ensemble of nanoparticles it is difficult to parse the energetic contribution of the electronic and vibrational relaxations which are both attributed to the Stokes shift.

Parsing the electronic and nuclear relaxations can be accomplished by inspecting the vibronic structure fluorescence line narrowing (FLN) spectra of CdSe nanoparticles of varying size (Fig. 6.5) taken from Ref. [190]. In this technique a tunable narrow-band laser is used to excite the red edge of the absorption band. Only the largest nanoparticles in the ensemble and excited therefore much of the inhomogeneity in the emission lineshape is circumvented. As a result the FLN spectra show a clear vibronic progression with a decreasing intensities of the 0-1 and 0-2 vibronic peaks in the larger nanoparticles. The peak spacing of the spectra corresponds to single displaced vibrational coordinate with a frequency of 206.6 cm^{-1} corresponding a gamma point energy of the longitudinal optical phonon mode which dominates the resonance Raman spectrum of CdSe nanoparticles.[202–204] The displacement of the these LO phonon mode can be estimated from the ratio of the intensity of the 0-1 vibronic transition to that of the 0-0 vibronic transition as $\Delta = (2I_{0-1}/I_{0-0})$.[192] (see Section D.3 for justification). The polaron binding energy can be calculated from the displacement according to Eq. 6.2. The polaron binding energy verses the estimated nanoparticle volume is presented in Figure 6.5(B). The numbers of unit cells was approximated by assuming CdSe nanoparticles were spheres of the reported radius with a unit cell volume of 0.1123 nm^3 consistent with bulk wertile CdSe at 300 K. The polaron binding energy decreases with increasing nanoparticle size, but the stokes shift does not asymptote to zero. The polaron binding energy does not asymptote to zero as would be expected if the exciton size contin-

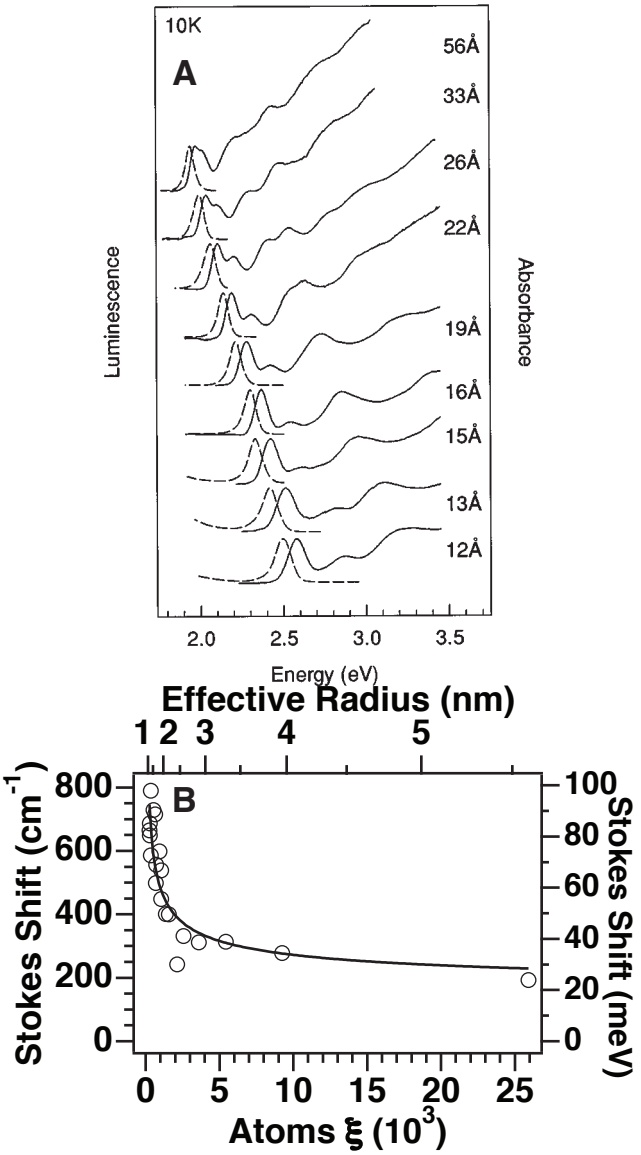

Figure 6.4: (Top) Normalized absorption and full luminescence spectra for CdSe QDâĂŹs with radii between 12 and 56 Å. A 300 W Xe arc lamp serves as the excitation source for both absorption and luminescence experiments. The excitation light is intentionally broad ∼50 nm FWHM! to prevent possible size selection of the dots. Detection of the transmission/luminescence signal is carried out with an OMA coupled to a 0.33 m spectrometer. The absorption spectra are indicated by solid lines; the corresponding luminescence spectra by dotted lines. Reprinted with permission from Ref [190]. Copyright 1996. Physical Review B.

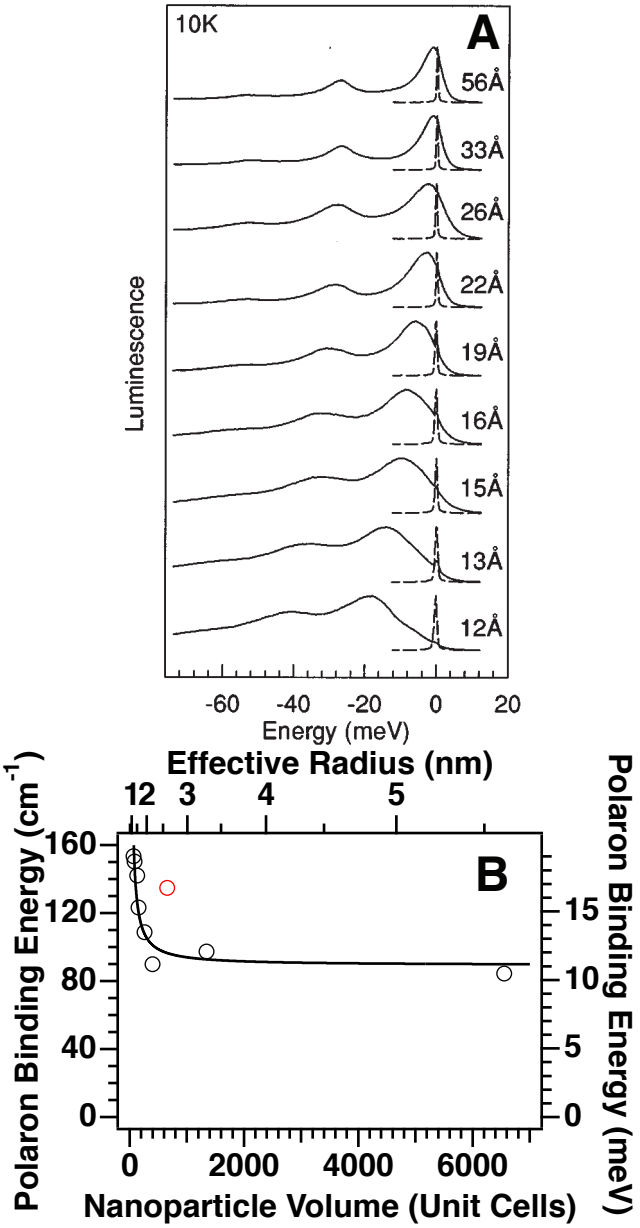

Figure 6.5: (A) Normalized Fluorescence Line Narrowing Spectra (black line) of for CdSe QD's with radii between 12 and 56 Å. The mean radii of the dots are determined from SAXS and TEM measurements. A 10 Hz Q-switched Nd:YAG/dye laser system (;7 ns pulses! serves as the excitation source. Detection of the FLN signal is accomplished using a time gated OMA. The laser line is included (dotted line) for reference purposes. All FLN spectra are taken at 10 K. B Relation between polaron binding energy along the LO phonon mode verses nanoparticle volume. The black line is a fit of the form $\lambda_{L.O.} = (4750 \pm 90\ \text{cm}^{-1})/\xi + (90 \pm 5)\ \text{cm}^{-1}$. The data point indicated by a red circle corresponding to a nanoparticle of 2.6 nm was not included in the fit as it was anomalous to the trend. Reprinted with permission from Ref. [190]. Copyright 1996. Physical Review B.

ued to delocalize indefinitely with nanoparticle size but rather it asymptotes to an energy of about 90 cm^{-1} corresponding to the lattice distortion energy of bulks CdSe. This result has been confirmed experimentally: the band edge emission of bulk CdSe has been reported and displays a clear vibronic progression with a spacing of ∼206.6 cm^{-1} and a polaron binding energy of ∼ 90 cm^{-1}.[205] This analysis considers only one displaced coordinate; however, we show in Section C.1 that a one dimensional displaced harmonic oscillator is equivalent to an ξ dimensional ensemble oscillator with the same frequencies if displacement along each coordinate is $\Delta_1/\xi^{0.5}$. For example the 1.2 nm is fit as a one dimensional wavepacket with a displacement of $\Delta_1 = 1.19$. We also know that a 1.2 nm nanoparticle can be approximated as 64 wertzite unit cells and there is one longitudinal optical (LO) phonon degree of freedom per unit cell. Finally we make the approximation that all the unit cells in the nanoparticle are uniformly displaced by the same amount. Equation 6.2 becomes:

Rearranging we can solve for Δ_{ij}. A physically realistic picture would describe the 1.2 nm CdSe nanoparticle polaron as a 64 dimensional displaced harmonic oscillator where each unit cell is displaced along the LO phonon by $\Delta' = 0.15$. By contrast the bulk CdSe polaron would be more aptly described as a distortion of the LO phonon coordinate in about 5000 unit cells each with a displacement $\Delta' = 0.01$. As mentioned previously the displacement on each unit cell need not be uniform; a still more physically realistic picture would include coordinates proximate to the exciton center that are displaced by more than that state while coordinates far form the exciton center would have practically no distortion. This back of the envelope calculation serves only as an approximation of the nuclear distortion. In a CdSe the electronic character of the bang-edge excitation is from the Se 4p orbitals to the Cd 5S orbital decreasing the ionic character of the crystal and lengthening the Cd-Se bondlength. Other salient features about the excited state are made clear by this vibronic analysis. The first emission peak maximum redshifts with respect to the excitation wavelength, assumed to be at the E_{00} electronic origin. This energy offset has been attributed band edge exciton splitting in previous works.[190] Unlike the polaron binding energy, the band edge exciton splitting asymptotes to zero in large nanoparticles. Another feature of the FLN spectra is that the vibronic peaks become broader in for smaller nanoparticles. It has been shown that this broadening is caused by dephasing from confined acoustic breathing modes which become increasingly optically active in the emission and resonance Raman spectra of small nanoparticles.[206, 207] By inspecting the fluorescence line narrowing spectra we are able to resolve the vibronic structure of the band edge exciton. This leads to some interesting observations of the nature of the excited state nuclear distortion of these important quantum dots.

Metals

In perfect metals like gold and graphene a plasmonic excitation is not localized in bonding orbitals. The electrons cloud resonates at the frequency of the incident light field and this effect largely screens the nuclei from experiencing a strain field.[198] Therefore there is no immediate lattice distortion of the nuclei and no appreciable polaron binding energy. The

photons' energy is deposited into kinetic energy of the conduction band electrons. Phonon emission occurs through a fundamentally different process than polaron formation. At room temperature the primary mechanism for electron phonon energy transfer is through scattering events of the hot conduction electron off of a nuclei at a lattice distortion after a finite time delay. Such a lattice distortion can originate from a phonon, a defect or impurity, at the boundary between crystal domains or at the edge of the metal.[198, 208] Metals do not fluoresce since the hot electron rapidly relaxes back to conduction band therefore we cannot inspect the half-Stokes shift to estimate the nuclear reorganization energy. Totally symmetric optical phonon modes are not displace and therefore do not appear in the resonance Raman spectra of a metal unless the electron and hole are localized at a defect or an edge in which case it cannot be considered a metal.[208]

6.3 Conclusion

There is a reciprocal relation between polaron binding energy and polaron size. This trend applies to vibronic transitions in all chemical and solid state systems. A combination of absorption, emission and resonance Raman analysis allows for precise identification of the vibrational degrees of freedom into which energy is deposited after excitation. When electronic relaxation to defects or trapped states is nominal over the timescales of fluorescence this relation can be inverted to gain a quick approximation of the polaron size. Comparison with simple vibrational structure calculations can then be used to determine geometry of the polaron. In practice, the nature and density of crystal defects and trap states limit the exciton or charge carrier mobility more so than does the polaron binding energy. However as technologies improve for growing more perfect crystals the upper limit for carrier mobility is determined by the polaron binding energy. These results suggest that localized excitons may not be ideally suited for photovoltaics because the large reorganization energy diminishes the exciton diffusion length. By understanding the basics of electron-phonon coupling we can begin the informed design of optoelectronic materials.

Chapter 7

Supramolecular $Ga_4L_6^{12-}$ Cage Photosensitizes 1,3-Rearrangement of Encapsulated Guest via Photoinduced Electron Transfer

7.1 Abstract

The $K_{12}Ga_4L_6$ supramolecular cage is photoactive and enables an unprecedented photoreaction not observed in bulk solution. $Ga_4L_6^{12-}$ cages photosensitize the 1,3-rearrangement of encapsulated cinnamylammonium cation guests from the linear isomer to the higher energy branched isomer when irradiated with UVA light. The rearrangement requires light and guest encapsulation to occur. The $Ga_4L_6^{12-}$ cage-mediated reaction mechanism was investigated by UV/vis absorption, fluorescence, ultrafast transient absorption, and electrochemical experiments. The results support a photoinduced electron transfer mechanism for the 1,3-rearrangement, in which the $Ga_4L_6^{12-}$ cage absorbs photons and transfers an electron to the encapsulated cinnamylammonium ion, which undergoes C-N bond cleavage, followed by back electron transfer to the cage and recombination of the guest fragments to form the higher energy isomer.

7.2 Summary

Photosynthesis inspires the development of systems capable of absorbing photons, transferring the harvested energy, and storing it in chemical bonds.[209] Artificial photosynthetic systems pair light-harvesting molecules, commonly porphyrins,[210] with energy acceptors such as quinones,[211] carbon nanotubes,[212] and fullerenes[213] to investigate the intricacies of energy transfer. Less explored are photosensitizing supramolecular nanovessels (cyclodextrins,[214] cavitands,[215] tubular hosts[216]) that transfer absorbed light energy to encapsulated guest acceptors and, in rare cases, elicit chemical transformations. For example, Fujita and co-workers reported a cationic palladium $M_6L_4^{12+}$ supramolecular assembly that participates in the photooxidation of alkanes.[217] In contrast to a polycationic photoreactive cage, a polyanionic photosensitizing cage would have significantly different photophysical properties and would preferentially react with a different class of substrates. For this reason, we investigated the water-soluble, highly anionic, gallium $M_4L_6^{12-}$ supramolecular assemblies[218] that have polyaromatic bridging ligands as potential photosensitizing agents. We hypothesized that the redox-active catecholate ligands could be photoexcited and donate excited-state energy to encapsulated guest molecules to induce chemical reactivity (Figure 7.1). Herein, we report that $Ga_4L_6^{12-}$ (L = diaminonaphthalene biscatecholamide) **1** photosensitizes an unprecedented allylic 1,3-photorearrangement[219] of encapsulated 1-cinnamylalkylammonium ions **2** to form the thermodynamically disfavored 3-substituted ammonium ion **3**. Chemical and photophysical studies implicate a photoinduced electron transfer (PET) mechanism for this process.

We envisioned that cationic allyldimethylcinnamylammonium ion **2a** would be strongly encapsulated[220] within **1**, and **1** could photosensitize the [2+2] cyclization of **2a** to form a bicyclic cyclobutane product (**5**, Scheme 7.1(1)) with UVA light, the triplet-photosensitized process that occurs in the absence of **1**.[221] Addition of **2a** (4.0 Îijmol, 6 mM) to a K_3PO_4-buffered (pD 8.0) aqueous solution of **1** (4.2 Îijmol) provides encapsulation complex **2a⊂1**

(⊂ denotes encapsulation) determined by 1H NMR spectroscopy (see SI).[222] Subsequent UVA irradiation of **2a⊂1** (14 h, 35 °C) provides not the expected encapsulated cyclobutane complex 5⊂1 but instead a new product, assigned by 1H NMR as encapsulated **3a**, resulting from allylic 1,3-rearrangement of the cinnamyl functional group (Scheme 7.1(2)). Independent synthesis of an authentic sample of 3a and subsequent formation of encapsulation complex 3a⊂1 confirmed that the product resulting from UVA irradiation was rearrangement product 3a, **4** kcal/mol higher in energy than linear isomer **2a** based on DFT calculations.

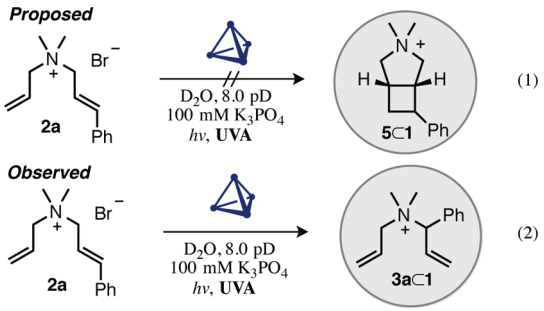

Scheme 7.1: Proposed and observed photochemical rearrangement reaction of allyldimethylcinnamylammoniumion

The photorearrangement can be extended to other encapsulated cinnamylammonium ions, although competitive cleavage to amines **4** is observed in some cases (see Table 1; vide infra). In the case of trimethylammonium substrate **2b**, broad resonances in the 1H NMR spectrum of **2b⊂1** indicate that **2b** is in rapid equilibrium[223] between the internal encapsulation complex **2b⊂1** and an external association complex.[224] Due to evidence for rapid guest exchange, it was important to assess whether the observed 1,3-rearrangement occurred in bulk solution or within the confines of **1**'s cavity. UVA irradiation of **2b** (without **1**) in K_3PO_4-buffered D_2O solution (pD 8.0, 14 h, 30 °C) provided only starting material. However,

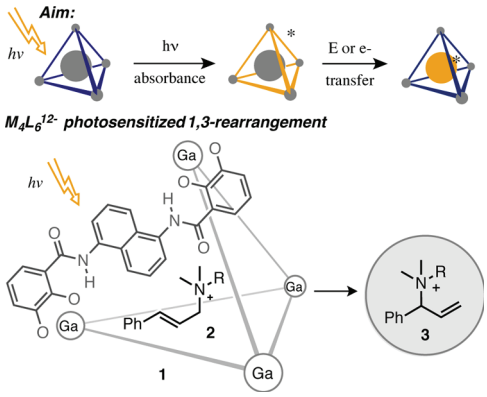

Figure 7.1: $K_{12}Ga_4L_6$ host **1** photosensitizes an allylic 1,3-rearrangement of encapsulated cinnamylammonium guests.

increasing the time of irradiation to 32 h showed 9cis-**2b**. In contrast, in the presence of **1** and UVA light, **2b** reacts completely after 14 h to form rearrangement product **3b**, trimethylamine **4b**, and cinnamyl alcohol.[1] Further evidence that formation of the 1,3-rearrangement product requires encapsulation is provided by a NEt_4^+-blocked host experiment.[225] UVA irradiation of a solution of $NEt_4 \subset$**1** and **2b** fails to provide rearrangement product **3b** after 12 h. A similar result is observed in an attempted catalytic reaction, in which **1** equiv of **2b** and 20 mol only 20 mol

Heating **2b⊂1** at 50 °C for 12 h in the absence of light fails to provide rearrangement product **3b** or trimethylamine **4b** and cinnamyl alcohol, and only encapsulated starting material **2b⊂1** is observed via 1H NMR. These experiments provide evidence that both UVA light and encapsulation in the cavity of **1** are necessary for the formation of products **3b** and **4b**. Formation of products **3b** and **4b** cannot be attributed to background thermal reactions that occur outside the confines of the supramolecular assembly.

Having established that the rearrangement is a photoinduced process mediated by assembly **1**, we carried out a further exploration of the factors that influence the rearrangement:cleavage ratio.[226] We found that N-alkyl substitution affects the ratio of rearrangement product **3** to tertiary amine **4** (Table 1). All substrates that undergo the rearrangement have an internal binding affinity of $\log(K_{int}) > 2$, as determined by competition studies with NMe_4^+.[222] N-Ethyl **2c**, N-propyl **2d**, and N-allyl **2a** are optimal substrates for the rearrangement; in these cases, **3** is formed in good yields, and tertiary amine side product is not observed by 1H NMR. Substrates that are weakly encapsulated, such as N-hexyl substrate **2g** with $\log(K_{int}) < 2$, do not form the rearrangement product **3g**, and only encapsulated tertiary amine **4g** is observed. These results suggest that weak binding of the substrate correlates with weak binding of the fragments formed upon photoreaction (see mechanistic discussion below).

To test whether the trialkylamine products **4** were the result of a decomposition pathway of rearrangement product **3**, encapsulated rearrangement product **3b⊂1** was irradiated with UVA, but no decomposition was seen after 12 h of irradiation. This suggests that the tertiary amine **4b** is the result of a photolytic process derived from the cinnamylammonium substrate **2b** as opposed to product **3b** decomposition.

To assess whether **1** was acting simply as a reaction vessel for the photo-rearrangement or also as a photosensitizing agent transferring absorbed energy to encapsulated **2**, we conducted UV/vis absorption studies of **1** and **2b**, respectively. The UV/vis absorption spectrum of **1** in H_2O shows absorption maxima at 224 and 330 nm (Figure 7.2A). The molar absorptivity (ϵ) for **1** was determined to be $(7.6 \times 10^4) \pm 0.3\ M^{-1}cm^{-1}$ at 330 nm. Importantly, the molar absorption coefficient of **1** is more than **4** orders of magnitude greater than that of **2b** in the portion of the spectrum where the UVA light source emits (315 - 400 nm). Thus, selective excitation of **1**, and not **2b**, is possible with a UVA light source. Use of a UVA light source in the photoreactions enables the unambiguous determination that **1** is a sensitizing agent in

[1] 1H NMR and mass spectral data indicate that a byproduct is the reaction of the cinnamyl cation with one ligand of **1**.

Table 7.1: Yields of Products Formed in the 1,3-Rearrangement of Variously Substituted Cinnamylammonium Ions Determined by 1H NMR integration

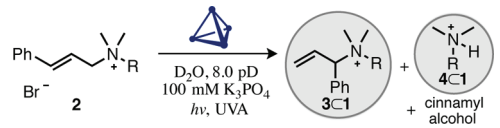

Entry	R	Rearrangement Product		3 (%)	4 (%)
1		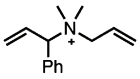	**3a**	66	0
2			**3b**	28	62
3		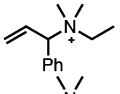	**3c**	82	0
4		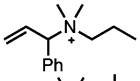	**3d**	83	0
5		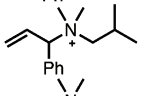	**3e**	40	51
6		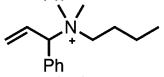	**3f**	20	47
7		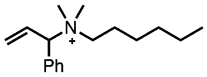	**3g**	0	65

the photo-rearrangement of **2b**. We carried out quantum yield studies of this rearrangement and found that the process occurs with a low quantum yield of $\phi_{R-\mathbf{2b}} = 0.010 \pm 0.007$. Quantum yields weredetermined using the Norrish type II cleavage of butyrophenone as an actinometer.[227]

Photosensitization of the encapsulated guest by the supramolecular host could occur by two means: energy transfer or electron transfer. For either Förster energy transfer (FRET) or Dexter energy transfer mechanisms to be operative, overlap of the

cinnamylammonium cation **2b** absorption spectrum with the $Ga_4L_6^{12-}$ fluorescence emission spectrum needs to be present.[228] However, an overlay of **2b** absorption and $Ga_4L_6^{12-}$ emission shows no overlap (Figure 7.2A), which means that a mechanism of exciton energy transfer to **2b** is not operative in this system. This leaves a PET mechanism as the likely mode of photosensitization.

Having identified **1** as the photosensitizing agent, we sought to understand the role of the excited state of **1** in activating the rearrangement of **2b** through transient absorption spectroscopy (see SI for details). Upon pulsed excitation with 400 nm light, an excited-state absorption band appears with (Figure 7.2B) and in the wavelength-separated absorption plot (Figure 7.2C). The excited-state absorption band corresponds to a transition from the first excited singlet state (S_1) to a higher energy electronic state (S_n). The signals were analyzed

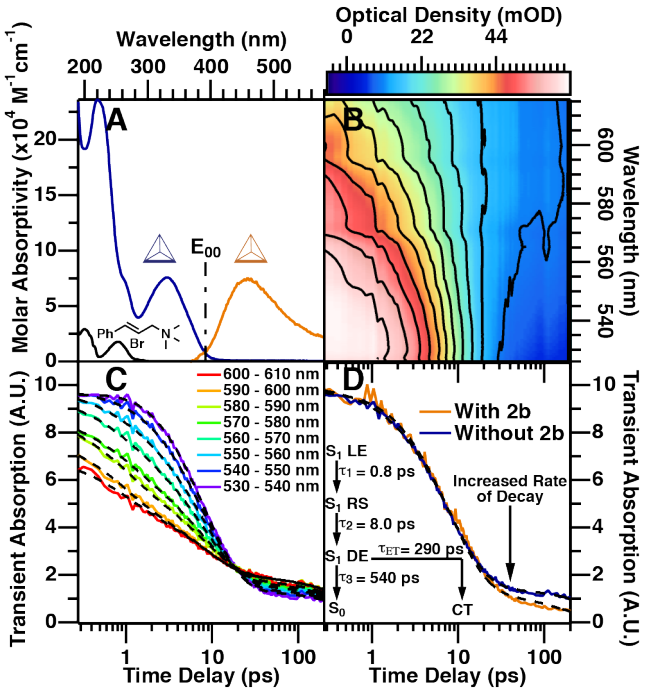

Figure 7.2: (A) UV/vis absorption spectra of $K_{12}Ga_4L_6$, **1** (blue) and cinnamylammonium **2b** (black) at 4×10^{-6} M in H_2O, 10 mM K_3PO_4, pH 8.0, overlaid with fluorescence emission of **1** (gold). (B) Contour plot of dispersed transient absorption of $K_{12}Ga_4L_6$ in H_2O from 200 fs to 200 ps after 400 nm actinic excitation. (C) Band integral over each 10 nm range in the transient absorption and the global exponential fits to the decay. (D) Comparison of transient absorption decay between 540 and 550 nm with and without **2b**.

in the context of first-order kinetics with three steps identified.

In the first resolvable step, the absorption blue-shifts ($\tau_1 = 0.8 \pm 0.3$ ps), corresponding to librational reorientation of the water solvent shell.[229] The next excited-state absorption decay step ($\tau_2 = 8.0 \pm 0.8$ ps) likely corresponds to exciton migration over the six ligands of tetrahedron 1. The highly symmetric tetrahedral structure allows excitons to "hop" between the orbitals of neighboring ligand residues through Förster-type dipole coupling.[230] This interpretation is supported by the depolarized fluorescence emission (see SI for details). In the final step, the excited-state population S_1 relaxes back to the ground electronic state S_0 ($\tau_3 = 540 \pm 40$ ps). In comparison with "empty" **1**, encapsulation complex **2b⊂1** shows that interactions with **2b** only weakly perturb the electronic structure of **1**. The greatest difference is apparent in the final relaxation step out of S_1. In the presence of **2b**, the excited-state population decays with a time constant of 190 ± 60 ps, as compared to 540 ± 40 ps in the absence of **2b** (Figure 7.2D). Thus, we estimate that the excited-state electron transfer occurs with a time constant of 290 ± 150 ps and a quantum yield of $\Phi_{ET} = 0.65 \pm 0.34$.

Additional evidence for the PET mechanism is provided by calculation of the Gibbs

energy of photoinduced electron transfer (eq 7.1).[228]

$$\Delta G^{o} = E^{o}_{D^{+}/D} + E^{o}_{A/A^{-}} + E^{*}_{D} - C \tag{7.1}$$

Gibbs energy of PET is approximated using the standard reduction potentials of donor **1** (E_D) and acceptor **2b** (E_A) and the electronic excited-state energy of the donor (E^*_D). Cyclic voltammetry was used to estimate that the E_D of **1** is 0.73 V vs SHE (16.8 kcal/mol), and the E_A of **2b** is estimated at -1.69 V vs SHE (-39.6 kcal/mol, see SI for details).[2] The electronic excitation energy (E^*_D) is estimated from the $E_{0,0}$ transition at 391 nm, found at the intersection of the absorption and emission spectra of **1** (Figure 2), to be 3.17 eV, or 73.1 kcal/mol. The Coulombic term, C, for solvent stabilization of opposite charges in H_2O is estimated to be 0.08 kcal/mol.[228] With the above information, we find a negative free energy of -17.2 kcal/mol for the transfer of an electron from excited singlet **1** to the charge-transfer state of **2b⊂1**. The negative free energy value provides support for a PET mechanism.

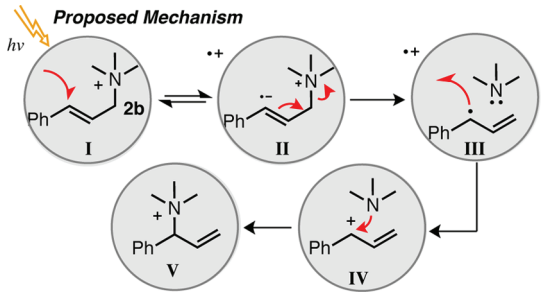

Scheme 7.2: Proposed mechanism of $K_{12}Ga_4L_6$-photosensitized 1,3-shift of cinnamylammonium cations

We propose that photoexcited assembly **2⊂1*** acts as a PET agent in the 1,3-rearrangement mechanism. In this pathway, **1** absorbs incoming light to generate the excited charge-transfer state **2⊂1***, in which an electron has been donated to the encapsulated cinnamylammonium acceptor **2** (I, Scheme 7.2). Excited-state electron donation to cation **2** results in heterolytic C-N cleavage (II), forming a tertiary amine and a geminal radical ion pair (RIP). In this case, the RIP is the stabilized allyl radical and a ligand-based radical cation moiety incorporated into the multi- cage (III). Back electron transfer from either the allyl radical or the tertiary amine to the ligand-based radical cation would form a stabilized allyl cation or tertiary amine radical cation and reestablish the original charge on the ligand (IV).[3] The

[2] Irreversible electrochemical cycles are observed after multiple scans for **1**, dependent on scan rate, and after a single scan for **2b**.

[3] We propose that the cinnamyl radical is the source of BET for several reasons. We observe tertiary amine **4**. We observe < 5% product where the cinnamyl has reacted with one cage ligand. We do not observe intramolecular cyclization onto a pendant alkene radical cation trap. [As an example, see: Newcomb, M.; Deeb, T. M. *J. Am. Chem. Soc.* **1987**, 109, 3163.] We do not observe hemiaminal or aldehyde products

encapsulated tertiary amine recombines with the allyl cation within the cavity to form the 3-substituted allyl product (V) or, in some cases, competitively escapes the cavity to give free amine. The cation either attacks one of the bridge ligands or reacts with H_2O to form cinnamyl alcohol.

In summary, we have found that $K_{12}Ga_4L_6$ supramolecular cages act as photosensitizers to transfer energy to encapsulated guest molecules, inducing transformations not observed in bulk solution. Encapsulation of the cinnamylammonium substrates is required for the 1,3-rearrangement to occur. Energy transfer was found to occur by a photoinduced electron transfer mechanism. Photosensitization and 1,3-rearrangement via PET are new modes of action enabled by the cavity of the $Ga_4L_6^{12-}$ cage.

that would result from amine radical cation decomposition. [As an example, see: Shono, T.; et al. *J. Am. Chem. Soc.* **1982**, 104, 5753.] Although we cannot rule out the formation of an amine radical cation, at this time we have not found evidence to support its formation.

Appendix A

Supporting Information: Difference Bands in Time Resolved Femtosecond Stimulated Raman Spectra of Photoexcited Intermolecular Electron Transfer from Chloronapthalene to Tetracyanoetheylene

This work will be submitted to the *The Journal of Physical Chemistry A* by Scott R. Ellis, David P. Hoffman, Myeongkee Park and Richard A. Mathies

A.1 Calculated Frequencies of $TCNE^{\bullet-}$

Frequency ω (cm^{-1})	IR Intensity (A.U.)	Raman Activity (A.U.)
45.8	0	0
111.2	2	0
130.3	0	19
149.9 ← ν_1	20	0
160.8	14	0
264	0	15
279.1	0	0
466.9	0	3
470.2	0	0
479.3	2	0
532.6 ← ν_2	0	31
543.9	0	1
562.4	12	0
623.3	0	3
627	0	0
639.2	0	1
1001.7	5	0
1187.8	8	0
1294.1	0	120
1424.6 ← ν_3	0	380
2215.8	0	1260
2226.6	410	0
2272.2	180	0
2279.3	0	1270

Table A.1: Frequencies, IR intensities and Raman activities of $TCNE^{\bullet-}$ calculated using the 6-311++G(d,p) basis set and uB3LYP functionals. The three modes that appear in the time domain impulsive spectrum and the femtosecond stimulated Raman spectra are indicated with arrows. The coordinates of these three modes are presented in Figure 3.4 of the main text.

A.2 Scaling of Observed Peak Frequency Shifts

Care must be taken when considering a time evolving peaks shift in a FSRS spectrum because the instantaneous frequency is convolved with "later" frequencies over the duration of the

Raman pump pulse. Consider a chirped signal where the instantaneous frequency changes exponentially with time constants τ_i

$$\frac{\partial \phi}{\partial t} = \omega_0 + \sum_i A_i e^{-t/\tau_i} \tag{A.1}$$

This frequency is measured over the duration of the Raman pump or the intrinsic dephasing of the peak.

$$W(t) = e^{-t/\tau_{peak}} \tag{A.2}$$

The observed frequency is the instantaneous frequency convolved over this dephasing time.

$$\begin{aligned}
\langle \Delta\omega(t) \rangle(\Delta t) &= \frac{\int_0^\infty (\omega(t+\Delta t) - \omega_0) W(t) dt}{\int_0^\infty W(t) dt} \\
&= \frac{\int_0^\infty \sum_i A_i e^{-(t+\Delta t)/\tau_i} e^{-t/\tau_{peak}} dt}{\int_0^\infty e^{-t/\tau_{peak}} dt} \\
&= \frac{\sum_i A_i e^{-\Delta t/\tau_i} \int_0^\infty e^{-(1/\tau_i + 1/\tau_{peak})t} dt}{\int_0^\infty e^{-t/\tau_{peak}} dt} \\
&= \frac{\sum_i - A_i e^{-\Delta t/\tau_i} \frac{e^{-(1/\tau_i + 1/\tau_{peak})t}}{\frac{1}{\tau_i} + \frac{1}{\tau_{peak}}} \Big|_0^\infty}{-\tau_{peak} e^{-t/\tau_{peak}} \Big|_0^\infty} \\
&= \sum_i \frac{A_i e^{-\Delta t/\tau_i}}{\frac{\tau_{peak}}{\tau_i} + 1}
\end{aligned} \tag{A.3}$$

Relating this to our measurement, the observed frequency shifts must be scaled to extract the instantaneous frequency shift.

$$\begin{aligned}
A_i &= A_{obs,i} \left(\frac{\tau_{peak}}{\tau_i} + 1 \right) \\
&= A_{obs,i} \left(\frac{\Gamma_i}{\Gamma_{peak}} + 1 \right)
\end{aligned} \tag{A.4}$$

Where $\pi\Gamma = 1/\tau$. The scaling factors presented above account for Fourier uncertainty. If a dynamic peak shift occurs faster than a peak's dephasing ($\tau_i < \tau_{peak}$) the magnitude of the

shift is stifled and a large scaling factor is required to account for the magnitude of the shift. If the shift occurs much slower than the dephasing ($\tau_i >> \tau_{peak}$) the time resolution is good and the scaling factor approaches unity.

A.3 Transient Absorption Anisotropy Analysis

The perpendicular polarized signal is analytically defined by two non-collinear electric field vectors.

$$OD_{\perp}(t) = \frac{OD_{MA}(t) - OD_{\parallel}(t)Cos^2(54.7356)}{Cos^2(90 - 54.7356)} \tag{A.5}$$

Thus the signal with perpendicular polarization must evolve with the same three time constants as the signals with parallel and magic angle polarizations. This is demonstrated in the subsequent analysis of transient absorption anisotropy.

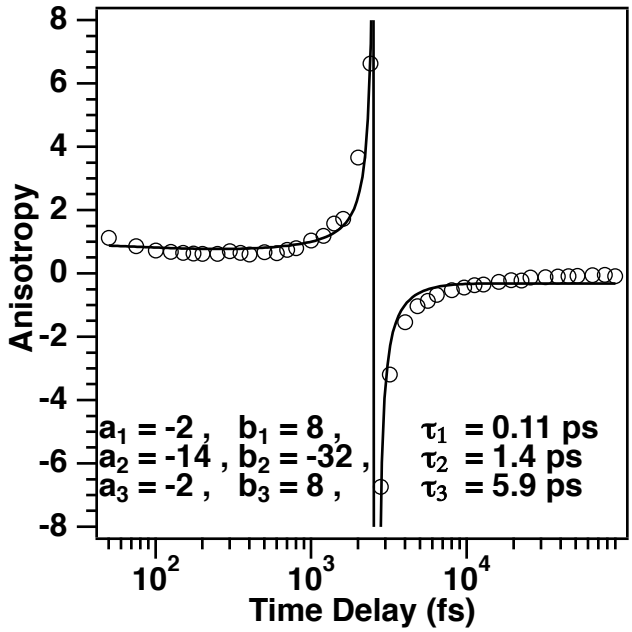

Figure A.1: Measured anisotropy (circles) of transient absorption signal integrated over the whole probe window (820 - 940 nm). The fit (black line) is described in the text. Relevant fit parameters are given.

Figure A.1 presents the time resolved transient absorption anisotropy. The anisotropy was calculated as

$$r(t) = \frac{OD_{\parallel} - OD_{\perp}}{OD_{\parallel} + 2OD_{\perp}} \tag{A.6}$$

$OD_{\parallel}$ and $OD_{\perp}$ are the band integrals of the optical density over the entire probe window with parallel and perpendicular polarizations. The measurements were acquired back to back. Given the nature of the decays in Fig. 3.5(a) a fit function was chosen of the form:

$$r(t) = \frac{a_1 e^{-t/\tau_1} + a_2 e^{-t/\tau_2} + a_3 e^{-t/\tau_3}}{b_1 e^{-t/\tau_1} + b_2 e^{-t/\tau_2} + b_3 e^{-t/\tau_3}} \tag{A.7}$$

Since the stimulated emission decays in 1.4 ps while the excited state absorption persists for 5.9 ps the TA anisotropy diverges at the logarithmic average of these two time constants 2.9 ps.

A.4 Comparison of Transition Polarizabilities of Difference Bands and Combination Bands

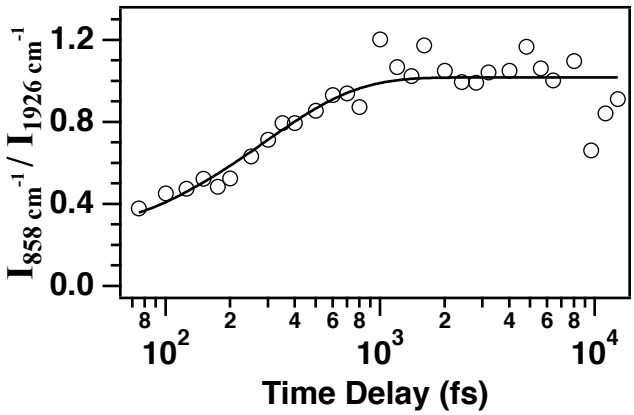

Figure A.2: The relative intensity of the 858 cm^{-1} mode to the 1926 cm^{-1} as a function of time delay after actinic excitation. The ordinate is unitless. The black line is a convoluted single exponential fit with a time constant of 300 ± 70 fs.

A comparison is made between the intensity of the difference band to that of a combination band since coupling occurs through the same Franck-Condon factors. Assume resonance with a single electronic state $|S_n\rangle$ through transition dipole μ_{S_n,S_1}. Assume also for simplicity that there are only two displaced harmonic coordinates: that of the high and low frequency modes. In this case the wave functions are separable and only these two coordinates contribute to the transition polarizability. Use an expanded notation. $|n_i, n_j\rangle = |\chi_{n_i}^{low}\rangle|\chi_{n_j}^{high}\rangle$

The intensity of a difference band follows as:

$$\begin{aligned}
\sigma_{R,01,10} = |\alpha_{01,10}|^2 &= \left| \frac{\mu_{S_n \leftarrow S_1}^2}{\hbar} \sum_{n_i,n_j} \frac{\langle 0,1|n_i,n_j\rangle\langle n_i,n_j|1,0\rangle}{(n_i-1)\omega_{low} + n_j\omega_{high} + \omega_0 - \omega_\ell + i\Gamma_{S_n}} \right|^2 \\
&= \left| \frac{\mu_{S_n \leftarrow S_1}^2}{\hbar} \sum_{n_i,n_j} \frac{\langle \chi_0^{low}|\langle \chi_1^{high}|\chi_{n_i}^{low}\rangle|\chi_{n_j}^{high}\rangle\langle \chi_{n_i}^{low}|\langle \chi_{n_j}^{high}|\chi_1^{low}\rangle|\chi_0^{high}\rangle}{(n_i-1)\omega_{low} + n_j\omega_{high} + \omega_0 - \omega_\ell + i\Gamma_{S_n}} \right|^2 \\
&= \left| \frac{\mu_{S_n \leftarrow S_1}^2}{\hbar} \sum_{n_i,n_j} \frac{\langle \chi_0^{low}|\chi_{n_i}^{low}\rangle\langle \chi_1^{high}|\chi_{n_j}^{high}\rangle\langle \chi_{n_i}^{low}|\chi_1^{low}\rangle\langle \chi_{n_j}^{high}|\chi_0^{high}\rangle}{(n_i-1)\omega_{low} + n_j\omega_{high} + \omega_0 - \omega_\ell + i\Gamma_{S_n}} \right|^2 \\
&= \left| \frac{\mu_{S_n \leftarrow S_1}^2}{\hbar} \sum_{n_i,n_j} \frac{\langle \chi_1^{low}|\chi_{n_i}^{low}\rangle\langle \chi_1^{high}|\chi_{n_j}^{high}\rangle\langle \chi_{n_i}^{low}|\chi_0^{low}\rangle\langle \chi_{n_j}^{high}|\chi_0^{high}\rangle}{(n_i-1)\omega_{low} + n_j\omega_{high} + \omega_0 - \omega_\ell + i\Gamma_{S_n}} \right|^2
\end{aligned} \tag{A.8}$$

In the last step we used the property of Franck-Condon factors to be real numbers and are equal to their complex conjugate. $\langle \chi_{n_x}|\chi_{n_y}\rangle = \langle \chi_{n_y}|\chi_{n_x}\rangle$

Now consider the intensity of a combination band

$$\begin{aligned}
\sigma_{R,11,00} = |\alpha_{11,00}|^2 &= \left| \frac{\mu_{S_n \leftarrow S_1}^2}{\hbar} \sum_{n_i,n_j} \frac{\langle 1,1|n_i,n_j\rangle\langle n_i,n_j|0,0\rangle}{n_i\omega_{low} + n_j\omega_{high} + \omega_0 - \omega_\ell + i\Gamma_{S_n}} \right|^2 \\
&= \left| \frac{\mu_{S_n \leftarrow S_1}^2}{\hbar} \sum_{n_i,n_j} \frac{\langle \chi_1^{low}|\chi_{n_i}^{low}\rangle\langle \chi_1^{high}|\chi_{n_j}^{high}\rangle\langle \chi_{n_i}^{low}|\chi_0^{low}\rangle\langle \chi_{n_j}^{high}|\chi_0^{high}\rangle}{n_i\omega_{low} + n_j\omega_{high} + \omega_0 - \omega_\ell + i\Gamma_{S_n}} \right|^2
\end{aligned} \tag{A.9}$$

Comparing A.8 and A.9 we find that the polarizabilities are similar except for the resonance denominator. However, if the incident light, ω_ℓ is somewhat tuned off of resonance or if the dephasing of the S_n state is fast (Γ_{S_n} is large) then the two polarizabilites should approach equivalence. In our experiment the resonant S_n excited state absorption is unstructured and highly transient (Γ_{S_n} is large). There is no reason to expect the difference in resonance condition differentiates the two polarizabilites within pathway (A).

A.5 Quantum Theory of Difference Frequencies in FSRS spectra

The time evolution of the density matrix via pathway (A) can be written as follow:

$$
\begin{aligned}
&[\rho^{(5)}(t)]_{(A)} \\
&= (\frac{1}{i\hbar})^5 \int_{-\infty}^{t} dt_1 \int_{-\infty}^{t_1} dt_2 \int_{-\infty}^{t_2} dt_3 \int_{-\infty}^{t3} dt_4 \int_{-\infty}^{t_4} dt_5 \sum_{n_i,n_j} \\
&\times e^{(i(\omega_{S_nS_1}+(n_i-1)\omega_{high}+(n_j+1)\omega_{low})-\Gamma_{S_nS_1})(t-t_1)} H'_{S_n,n_i,n_j,S_1,1,0}(E_{RPu},t_1) \\
&\times e^{-(\Gamma_{S_1S_1}+\Gamma_{1010})(t_3-t_4)} H'_{S_1,1,0,S_0,0,0}(E_{APu},t_4) \\
&\times |S_0\rangle|0,0\rangle\langle 0,0|\langle S_0| \\
&\times H'_{S_0,0,0,S_1,1,0}(E^*_{APu},t_5) e^{-(i(\omega_{S_0S_1}+\omega_{low})+\Gamma_{S_0S_1})(t_4-t_5)} \\
&\times H'_{S_1,1,0,S_n,n_i,n_j}(E^*_{RPu},t_3) e^{-(i(\omega_{S_nS_1}+(n_i-1)\omega_{low}+n_j\omega_{high})+\Gamma_{S_1S_n})(t_2-t_3)} \\
&\times H'_{S_n,n_i,n_j,S_1,0,1}(E^*_S,t_2) e^{(-(i(\omega_{high}-\omega_{low})+\Gamma_{1001})(t_1-t_2)}
\end{aligned}
\tag{A.10}
$$

Where Γ_{1010} corresponds to vibrational energy redistribution of the low frequency mode while Γ_{1001} corresponds to vibrational dephasing of the difference frequency. $\Gamma_{S_1S_1}$ corresponds to the rate of charge recombination. and $\Gamma_{S_1S_n}$ corresponds to electronic dephasing which is generally much faster than vibrational dephasing. The integrals can be solved analytically if the Raman pump is assumed to be a continuous wave light source while the actinic pump and the Stokes probe pulses are short with a Gaussian temporal envelope of duration τ_{APu} and τ_S respectively. The first two dipole field interactions prepares a vibrationally hot excited state population which decays as a function of Δt

$$
H'_{S_0,0,0,S_1,1,0}(E^*_{IPu},t_5) = -E^*_{IPu}\mu_{S_0S1}\langle 0,0|1,0\rangle\sqrt{2\pi}\tau_S e^{(-t_5-z/c)^2\tau^2_{APu}/2} e^{i\omega_S(t_5-z/c)} \tag{A.11}
$$

$$
H'_{S_1,1,0,S_0,0,0}(E_{IPu},t_4) = -E_{IPu}\mu_{S_1S_0}\langle 1,0|0,0\rangle\sqrt{2\pi}\tau_S e^{(-t_4-z/c)^2\tau^2_{Apu}/2} e^{-i\omega_S(t_4-z/c)} \tag{A.12}
$$

$$
H'_{S_1,0,1,S_n,n_i,n_j}(E^*_{RPu},t_3) = -E^*_{RPu}\mu_{S_1S_n}\langle 0,0|n_i,n_j\rangle e^{i\omega_{RPu}(t_3-z/c)} \tag{A.13}
$$

$$
\begin{aligned}
&H'_{S_n,n_i,n_j,S_1,0,1}(E^*_S,t_2) \\
&= -E^*_S\mu_{S_nS1}\langle n_i,n_j|0,1\rangle\sqrt{2\pi}\tau_S e^{(-t_2-z/c)^2\tau^2_S/2} e^{-i\omega_S(t_2-z/c)}
\end{aligned}
\tag{A.14}
$$

$$
H'_{S_1,1,0,S_n,n_i,n_j}(E_{RPu},t_1) = -E_{RPu}\mu_{S_1S_n}\langle 1,0|n_i+1,n_j\rangle e^{-i\omega_{RPu}(t_1-z/c)} \tag{A.15}
$$

$$
\begin{aligned}
&[\rho^{(5)}(t)]_{(A)} \\
&= (\frac{1}{i\hbar})^5 C(\ell, \tau_{APu}, \omega_{APu}) \left|E_{APu}\right|^2 \int_{-\infty}^{t} dt_1 \int_{-\infty}^{t_1} dt_2 \int_{-\infty}^{t_2} dt_3 \sum_{n_i,n_j} \\
&\times e^{(i(\omega_{S_nS_1}+(n_i-1)\omega_{high}+(n_j+1)\omega_{low})-\Gamma_{S_nS_1})(t-t_1)} H'_{S_n,n_i,n_j,S_1,1,0}(E_{RPu}, t_1) \\
&\times \frac{|S_1\rangle|1,0\rangle\langle 1,0|\langle S_1|\mu|S_0\rangle|0,0\rangle\langle 0,0|\langle S_0|\mu|S_1\rangle|1,0\rangle\langle 1,0|\langle S_1|}{(\omega_{APu}-\omega_{S_1S_0}-\omega_{low}-i\Gamma_{S_1S_0})(\omega_{APu}-\omega_{S_1S_0}-\omega_{low}+i\Gamma_{S_1S_0})} e^{-(\Gamma_{1010}+\Gamma_{S_1S_1})\Delta t} \\
&\times H'_{S_1,1,0,S_n,n_i,n_j}(E^*_{RPu}, t_3) e^{-(i(\omega_{S_nS_1}+(n_i-1)\omega_{low}+n_j\omega_{high})+\Gamma_{S_1S_n})(t_2-t_3)} \\
&\times H'_{S_n,n_i,n_j,S_1,0,1}(E^*_S, t_2) e^{(-(i(\omega_{high}-\omega_{low})+\Gamma_{1001})(t_1-t_2)}
\end{aligned}
\tag{A.16}
$$

The polarization that emits the signal is generated by the closure of the density matrix.

$$
\begin{aligned}
&P^{(5)}_{(A)}(t, \Delta t) \\
&= (\frac{1}{i\hbar})^5 C(\ell, \tau_{APu}, \omega_{APu}, \tau_S, \omega_S, \omega_{RPu}) \left|E_{APu}\right|^2 \left|E_{RPu}\right|^2 E^*_S \\
&\times \left|\mu_{S_1S_0}\right|^2 \left|\mu_{S_nS_1}\right|^4 \\
&\times \left|\frac{\langle 1,0^{S_1}|0,0^{S_0}\rangle}{(\omega_{APu}-\omega_{S_1S_0}-\omega_{low}-i\Gamma_{S_1S_0})}\right|^2 \sum_{n_i,n_j} \left|\frac{\langle 1,0^{S_1}|n_i,n_j^{S_n}\rangle\langle n_i,n_j^{S_n}|0,1^{S_1}\rangle}{\omega_{RPu}-\omega_{S_nS_1}-(n_i+1)\omega_{low}-n_j\omega_{high}-i\Gamma_{S_nS_1}}\right|^2 \\
&\times e^{(i(\omega_{RPu}-\omega_{high}+\omega_{low})-\Gamma_{1001})t} e^{-(\Gamma_{1010}+\Gamma_{S_1S_1})\Delta t}
\end{aligned}
\tag{A.17}
$$

Or Fourier transforming to the frequency domain yields.

$$
\begin{aligned}
&P^{(5)}_{(A)}(\omega_{FSRS}, \Delta t) \\
&= (\frac{1}{i\hbar})^5 C(\ell, \tau_{APu}, \omega_{APu}, \tau_S, \omega_S, \omega_{RPu}) \left|E_{APu}\right|^2 \left|E_{RPu}\right|^2 E^*_S \\
&\times \frac{\left|\mu_{S_1S_0}\right|^2 \left|\mu_{S_nS_1}\right|^4}{\omega_{FSRS}-\omega_{RPu}-\omega_{hi}+\omega_{low}-i\Gamma_{1001}} \\
&\times \left|\frac{\langle 1,0^{S_1}|0,0^{S_0}\rangle}{(\omega_{APu}-\omega_{S_1S_0}-\omega_{low}-i\Gamma_{S_1S_0})}\right|^2 \sum_{n_i,n_j} \left|\frac{\langle 1,0^{S_1}|n_i,n_j^{S_n}\rangle\langle n_i,n_j^{S_n}|0,1^{S_1}\rangle}{\omega_{RPu}-\omega_{S_nS_1}-(n_i+1)\omega_{low}-n_j\omega_{hi}-i\Gamma_{S_nS_1}}\right|^2 \\
&\times e^{-(\Gamma_{1010}+\Gamma_{S_1S_1})\Delta t}
\end{aligned}
\tag{A.18}
$$

To observe the Lorentzian lineshape of the signal multiply the numerator and denominator by $(\omega_{FSRS}-\omega_{RPu}-\omega_{hi}+\omega_{low}+i\Gamma_{1001})$. The signal is the imaginary part of the induced polarizaton:

$$
\begin{aligned}
&P^{(5)}_{(A)}(\omega_{FSRS}, \Delta t) \\
&= (\frac{1}{i\hbar})^5 C(\ell, \tau_{APu}, \omega_{APu}, \tau_S, \omega_S, \omega_{RPu}) \left|E_{APu}\right|^2 \left|E_{RPu}\right|^2 E_S^* \left|\mu_{S_1S_0}\right|^2 \left|\mu_{S_nS_1}\right|^4 \\
&\times \frac{\omega_{FSRS} - \omega_{RPu} - \omega_{hi} + \omega_{low} + i\Gamma_{1001}}{(\omega_{FSRS} - \omega_{RPu} - \omega_{hi} + \omega_{low})^2 + \Gamma^2_{1001}} \\
&\times \left| \frac{\langle 1, 0^{S_1} | 0, 0^{S_0} \rangle}{(\omega_{APu} - \omega_{S_1S_0} - \omega_{low} - i\Gamma_{S_1S_0})} \right|^2 \sum_{n_i, n_j} \left| \frac{\langle 1, 0^{S_1} | n_i, n_j^{S_n} \rangle \langle n_i, n_j^{S_n} | 0, 1^{S_1} \rangle}{\omega_{RPu} - \omega_{S_nS_1} - (n_i + 1)\omega_{low} - n_j\omega_{hi} - i\Gamma_{S_nS_1}} \right|^2 \\
&\times e^{-(\Gamma_{1010} + \Gamma_{S_1S_1})\Delta t}
\end{aligned}
\tag{A.19}
$$

Appendix B

Supporting Information: Reevalutation of Resonance Enhanced Two Dimensional Excited State Femtosecond Stimulated Raman Spectroscopy of Photoexcited Charge Transfer to H_4-TCNQ and F_4-TCNQ: Fifth-Order Coupling Within the Harmonic Approximation

by Scott R. Ellis, Daniel R. Dietze, Myeongkee Park and Richard A. Mathies

B.1 Data Analysis: Generation of the 2D-ES-FSRS spectrum

In an experiment when an off resonant impulsive pump pulse only a ground state vibrational coherence can be prepared, simplifying the analysis. The 2D-FSRS spectrum is generated by performing the Fourier transform across the time delay (Δt). However in an excited state 2D-FSRS experiment the impulsive pump prepares dynamic excited state populations, excited state coherences and ground state coherences. Therefore further data processing is required to extract the desired signal. Since the Raman pump and Stokes probe pulses are resonant with an excited state absorption band the experiment is not sensitive to the ground state coherences. The excited state population signal evolves as a slowly varying exponential and can therefore be extracted from the rapidly oscillating 2D-ES-FSRS signal. The procedure is illustrated in Figure B.1. Each frequency is fit from 280 to 2500 fs to a second order exponential rise. The population dynamics is subtracted from the signal yielding and oscillatory signal. The time-domain signals were zero padded to 256 points before they were Fourier transformed to improve the frequency resolution. After the Fourier transform a broad baseline remained across the FSRS axis at various impulsive frequencies. This baseline is likely the result of reabsorption of FSRS signal due to the oscillating excited state absorption. Since the 2D-ES-FSRS signal is expected to have narrow-band features, the unwanted baseline was removed by fitting each impulsive pumped frequency to a fifth-order polynomial as is illustrated in Figure B.2.

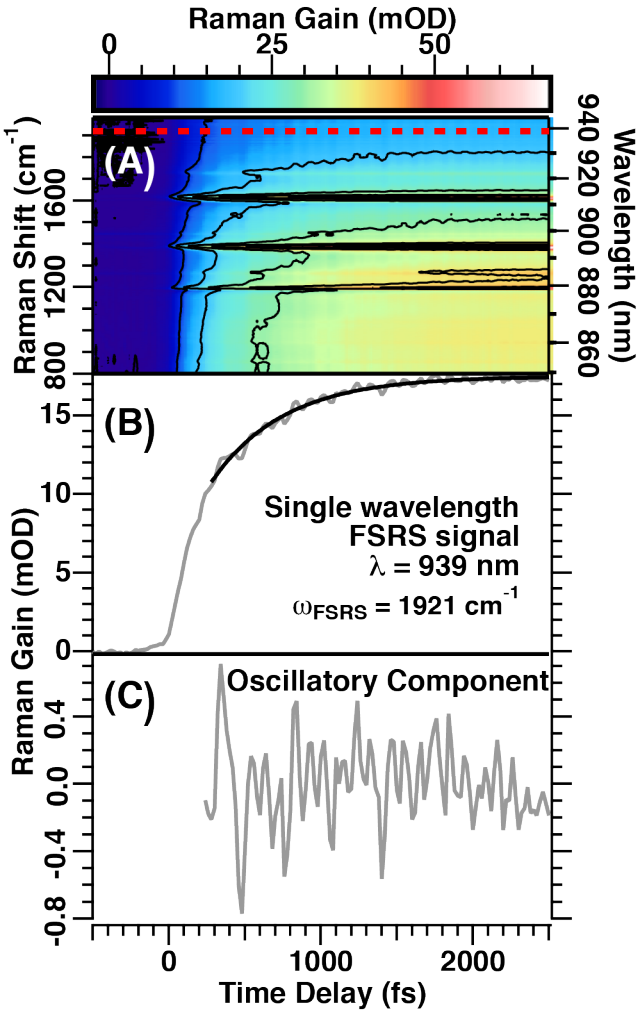

Figure B.1: (A) Contour plot of time evolving FSRS spectrum. The red dashed line indicate a random FSRS frequency chosen as an illustrative example of the fitting procedure. (B) Each FSRS frequency was trace (grey) is fit to a second order exponential rise from 280 - 2500 fs (black). (C) The oscillatory component is extracted and Fourier transformed yielding the impulsive spectrum at each FSRS frequency.

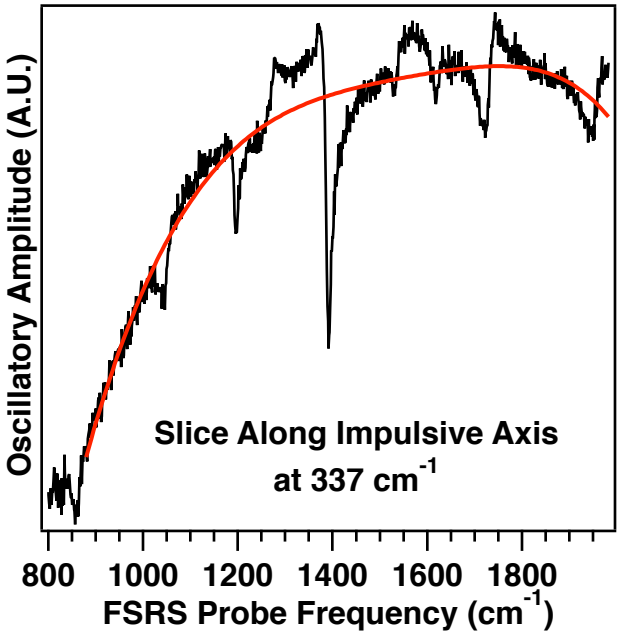

Figure B.2: Example of baseline removal of 2D-ES-FSRS spectrum. Each slice along the impulsive frequency axis (black) was fit to fifth order polynomial baseline (red). The residual contains only the desired narrow band interference features.

B.2 Modeling of Free Induction Decay Frequency Shift

The oscillatory excited state absorption signal presented in Figure 4.7 can be accounted for by frequency shifts over the course of the free induction decay. To extract the phase information while resolving the peaks in the free induction decay the Fourier transform amplitude was raised to the third power and divided by the absolute value of the amplitude.

$$\frac{I(\omega)^3}{|I(\omega)|} = \frac{(\int_0^\infty dt e^{2\pi i\omega t} S(t))^3}{|\int_0^\infty dt e^{2\pi i\omega t} S(t)|} \tag{B.1}$$

We assume a signal of the form:

$$S(t) = e^{-\Gamma_a t}\mathrm{Cos}((\omega + \Delta\omega e^{-\Gamma_b t})t + \Phi) \tag{B.2}$$

Setting the parameters ω= 330 cm^{-1}, $\Delta\omega$= 40 cm^{-1}, Γ_a = 15 cm^{-1}, Γ_b = 6 cm^{-1}, $\Phi = 6\pi/5$. The results are presented in Figure B.3.

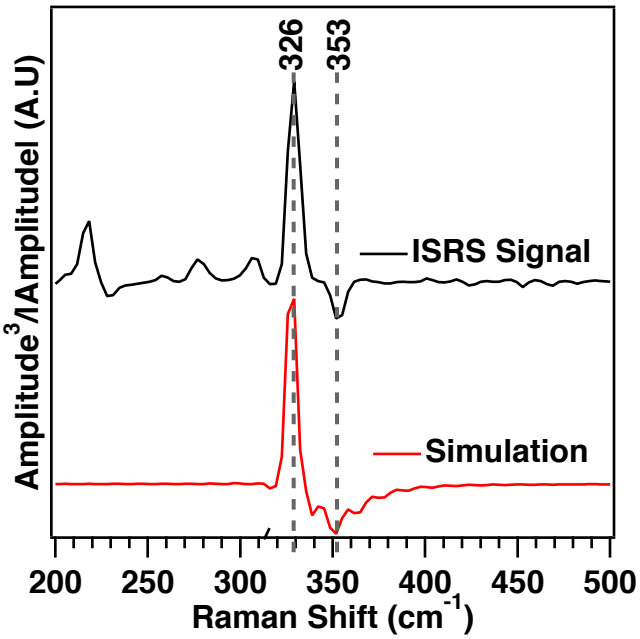

Figure B.3: Comparison of the measured and simulated impulsive excited state absorption signal from H_4-TCNQ. The amplitude of the Fourier transform have been raised to the third power and then divided by it's absolute value according to Eq. B.1. The input parameters are described in the text.

The parameters in the fit are underdetermined; however, this analysis indicates that the observed signal can be accounted for by a frequency shifting free induction decay.

B.3 2D-ES-FSRS at Fundamental Frequencies

Figure 4.1 presents the Wave-mixing energy level diagram of 2D-ES-FSRS (-) that is scattering at a difference frequency. Here we present the analogous 2D-ES-FSRS (F) and (+) pathways that result in scattering at a fundamental frequency and a combination frequency, respectively.

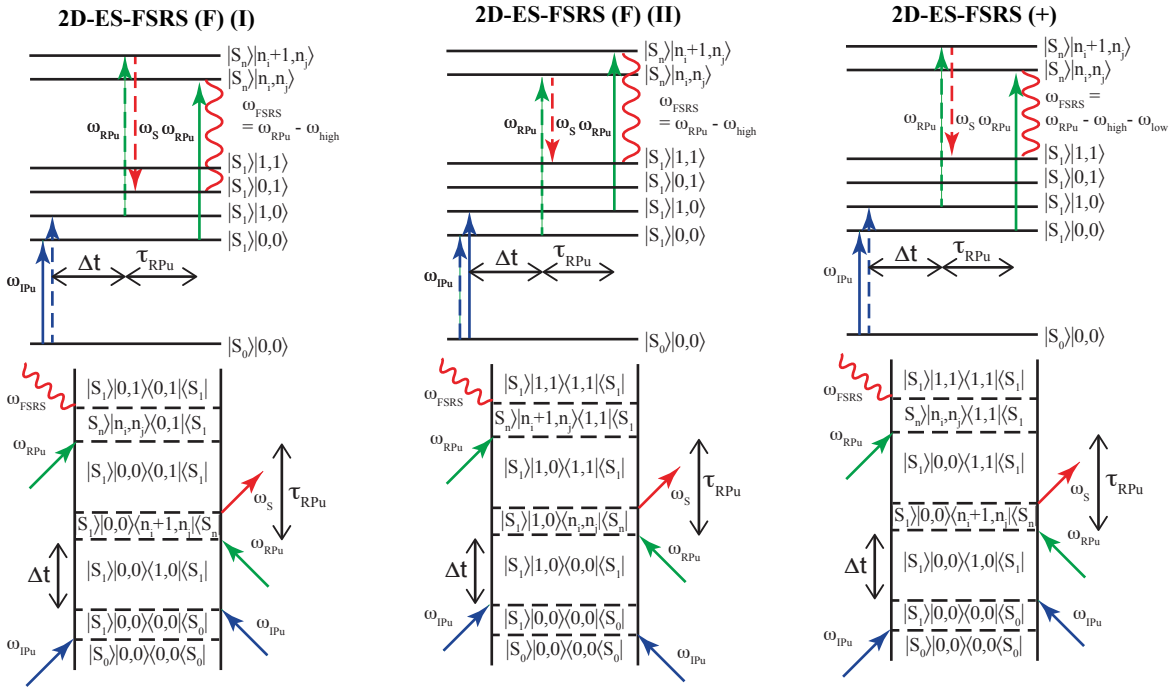

Figure B.4: Wave-mixing energy level diagrams and double sided Feynman diagrams of 2D-ES-FSRS at a fundamental FSRS probe frequency. The vibrational state within the manifold of a given electronic state is denoted as $|\nu_{low}, \nu_{hi}\rangle$ or the conjugate transpose as $\langle\nu_{low}, \nu_{hi}|$. The action of the impulsive pump (IPu, blue), Raman pump (RPu, green) and Stokes Probe (S, red) on the left and right side of the density matrix are indicated with solid and dash arrow respectively. The coherence evolution time is denoted Δt and the picosecond Raman pump pulse duration is labeled τ_{RPu}.

Appendix C

Supporting Information: Resonance Raman Characterization of Tetracene Monomer and Nanocrystals: Excited State Lattice Distortions Concurrent with Efficient Singlet Fission

This work will be submitted to *Physical Chemistry Chemical Physics*
Scott R. Ellis[1], Daniel R. Dietze[1,†], Tonatiuh Rangel[2], Florian Brown-Altvater[1], Jeffrey B. Neaton[2,*] and Richard A. Mathies[1,*]

[1] *Department of Chemistry, MC 1460, University of California at Berkeley, Berkeley, California 94720, USA*

[2] *Department of Physics, MC 7300, University of California at Berkeley, Berkeley, California 94720, USA*

*Corresponding authors, jbneaton@lbl.gov (JN) and ramathies@berkeley.edu (RM).

† Current address: OSRAM Opto-Semiconductors GmbH, 93055 Regensburg, Germany

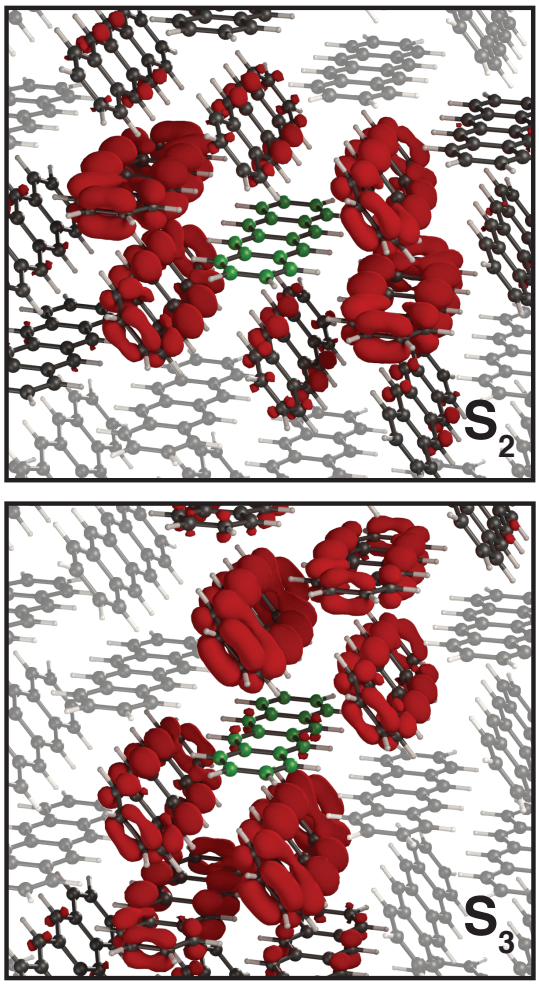

Figure C.1: electronic density surfaces for the second (S_2) and third (S_3) lowest energy exciton states with calculated energies of 2.355 and 2.431 eV. These state were calculated to have negligible oscillator strengths under polarized absorption.

Comparison of Optical Properties of Tetracene Nanocrystals and Bulk Crystalline Tetracene

Figure C.2 presents a comparison of the fluorescence spectrum of tetracene nanocrystals and thin films from this work and others.[131, 158, 231] The spectra consistently have a peak emission maxima of 528 ± 2 nm and display a similar lineshape suggesting that the singlet emission is a localized mechanism and does not depend on the bulk crystal structure. Thin films with a thickness greater than 100 nm display a red-shifted emission; however, this is likely the result of the self-absorption of the blue region of the emitted light by the optically dense sample.

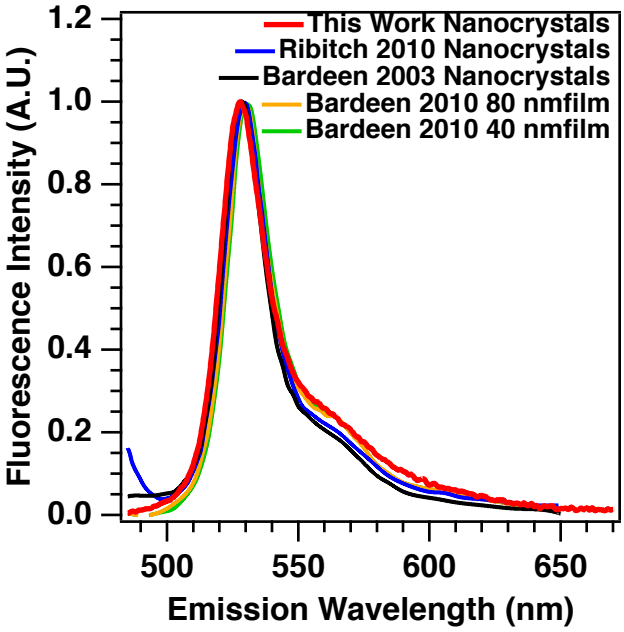

Figure C.2: Comparison of fluorescence spectra of crystalline tetracene from this work and various other publications. Both nanocrystals and thin films emit with maxima of 528 ± 2 nm.

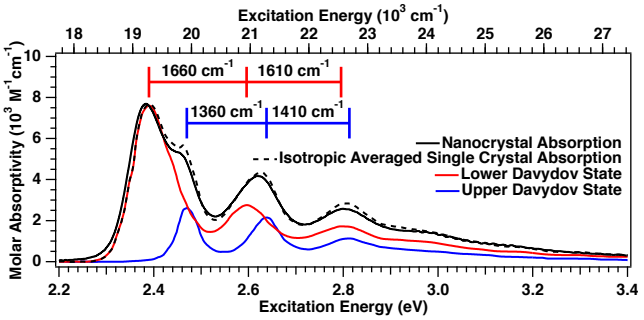

Figure C.3: Deconvolution of tetracene single crystal absorption into its two transition dipole transitions corresponding to lower Davydov state (red) and upper Davydov state (blue) digitized from [4]. The absorption spectrum from the nanocrystal agrees closely with isotropically oriented single crystals with increased inhomogeneity. The energy difference between adjacent peaks in the polarized absorption lineshapes is indicated by red and blue bars.

Figure C.3 presents a comparison of the polarized absorption spectra of tetracene single crystal from Ref. [147] with the measured absorption of a tetracene nanocrystal suspension. The spectra of the nanocrystals closely resemble that of the single crystal after isotropic averaging over all polarization contributions. The two absorption spectra differ by a slight red shift (56 cm^{-1}) of the nanocrystal absorption and broadening of the vibronic lineshape. The red shift and broadening could readily be accounted for by inhomogeneity and the effect

of the dielectric environment at the water-nanocrystal interface (surface boundary effects). X-ray crystal truncation rod scattering measurements have recently shown that in the outer surface monolayer of crystalline tetracene adopts a more coplanar close-packing conformation than in the bulk.[232] A wavepacket fit the bulk crystal absorption instead of the nanocrystal absorption would result in a larger reorganization energy in the low frequency modes (λ_p >130 cm^{-1}) by about 56 cm^{-1} and a smaller inhomogenous broadening (Θ <140 cm^{-1}) than in the nanocrystal fit (Table 5.2).

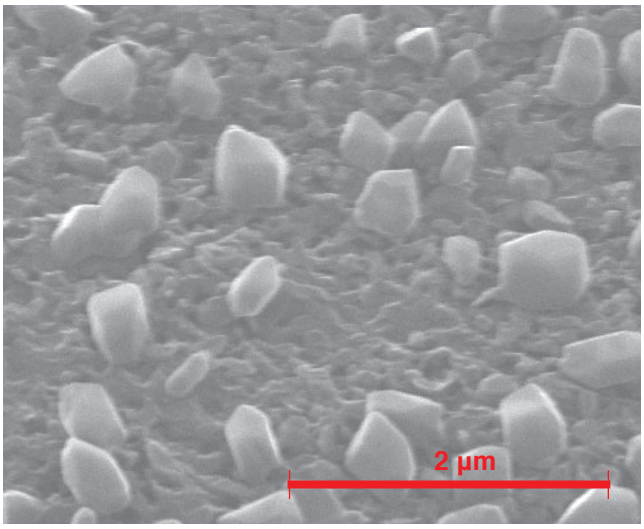

Figure C.4: Scanning electron microscope image of tetracene nanoparticles drop cast on a silicon surface. The image was acquired with a FEI Quanta 3D FIB using electron energies of 30 kV and a current of 280 pA. The tilt angle was 40°.

Comparison of Preresonance Enhancement of Phonon Modes in Tetracene Single Crystals

Figure C.6 presents the spontaneous Raman spectra of the six low frequency phonon modes at two different preresonant excitation wavelengths (653.6 and 752.5 nm, A and B respectively) digitized from Ref. [144] and Ref. [143]. Additionally four intramolecular vibrations in the region of 170 - 217 cm^{-1} are reported in both papers. The difference between the peak intensities in spectrum A and B is the result of preresonance enhancement. Preresonance enhancement reports on Frank Condon overlaps and nuclear displacements in the excited state.[233] The dashed line represents the 752.5 nm excited Raman spectrum, B., which has been scaled to show the same intensity of the 42.3 cm^{-1} mode as in spectrum A. The 42.3 cm^{-1} mode can be assumed to show little preresonance enhancement whilst the relative intensities of the five other phonon modes at 47.8, 58.5 88.4 117.1 and 129.8 cm^{-1} are enhanced by factors of 3.1, 3.8 7.1, 18.5 and 8.5 respectively. These results are consistent with those observed in the resonant impulsive transient absorption spectrum where modes at 58, 123 and 130 cm^{-1}

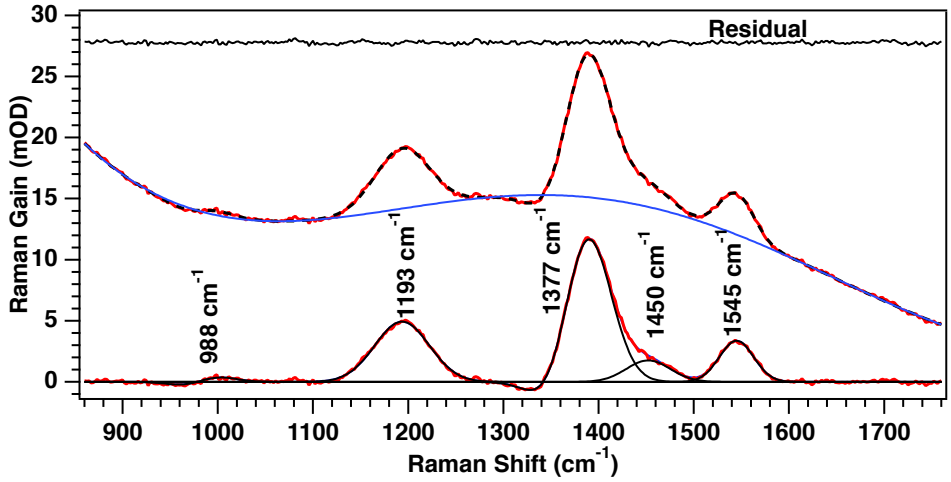

Figure C.5: Multi-peak fit to 520 nm excited femtosecond stimulated Raman spectrum of tetracene nanocrystals. The broad baseline is due to a ground state bleach induced by the early part of the Raman pump pulse interacting with the sample. The peak width of 42 cm^{-1} is the bandwidth of the picosecond Raman pump pulse. Fit was performed using five dispersive Gaussians and a 7th order polynomial baseline.

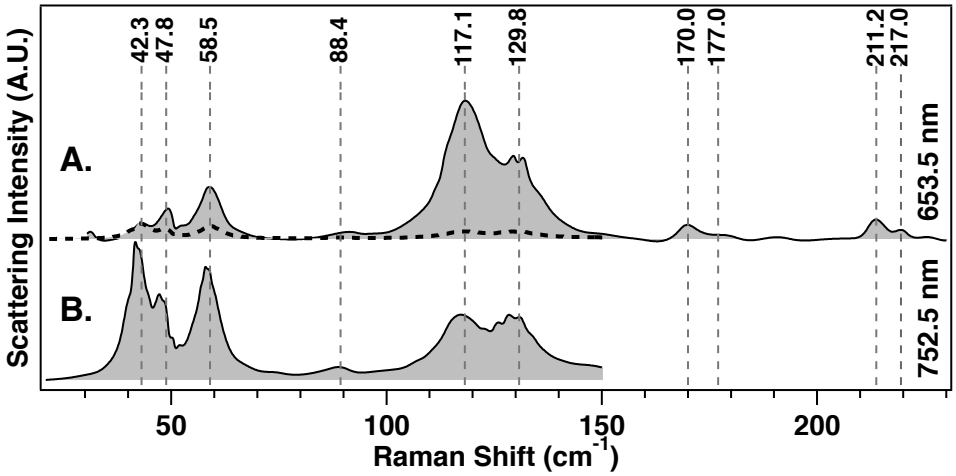

Figure C.6: Comparison of preresonance Raman spectra of tetracene single crystals with A 653.6 nm excitation from Ref. [144] and B 752.5 nm excitation from Ref. [143] The dashed spectrum is B which has been scaled such that the 42.3 cm^{-1} mode has the same intensity as that in A.

dominate the spectral power density.[146] The vdW-DFT calculated frequencies of the six gerade phonon modes are 47.7, 51.4, 62.7, 93.2, 131.6, 144.8 cm^{-1} making their assignment straightforward after a scaling factor of 0.914 is applied.

Table C.1: vdW-DF-cx calculated vibrational frequencies of Tc crystal structure. The parity of each vibration is denoted by 'g' for gerade and 'u' for ungerade.

ω (cm^{-1})	Γ	ω (cm^{-1})	Γ	ω (cm^{-1})	Γ	ω (cm^{-1})	Γ	ω (cm^{-1})	Γ	ω (cm^{-1})	Γ
0.0	u	384.0	g	745.6	g	950.7	g	1280.3	u	1599.0	g
0.0	u	390.0	g	746.9	u	952.7	g	1284.0	u	1601.2	g
0.0	u	431.7	u	748.1	g	963.0	g	1290.9	u	1606.3	g
37.8	u	432.8	u	748.1	u	967.1	u	1292.2	u	1610.1	g
47.7	g	452.1	u	752.5	u	970.8	g	1317.9	g	1622.5	u
51.4	g	463.6	g	755.5	u	973.6	u	1320.8	g	1624.9	u
62.7	g	467.0	u	765.4	g	1002.1	u	1368.0	u	3060.2	u
71.1	u	474.2	u	768.9	g	1003.6	g	1370.9	u	3061.2	g
73.3	u	475.7	g	769.6	g	1004.1	u	1373.8	u	3062.4	g
93.2	g	481.3	u	771.5	g	1004.6	g	1377.1	u	3063.6	u
105.0	u	487.4	g	829.8	u	1116.0	u	1396.8	g	3064.0	u
109.8	u	488.8	g	832.1	u	1116.2	g	1397.2	g	3064.5	u
131.6	g	499.2	g	834.2	g	1118.4	u	1397.9	g	3065.0	g
144.8	g	504.6	g	843.5	g	1119.7	g	1399.5	g	3065.2	g
146.3	u	544.9	u	845.6	g	1133.5	u	1406.5	u	3066.5	u
154.2	u	548.1	u	847.5	g	1138.3	u	1407.5	u	3067.1	u
165.1	u	555.4	u	856.5	g	1145.3	g	1436.9	g	3067.4	g
167.6	g	559.4	u	858.8	g	1151.9	u	1438.6	g	3068.8	g
172.6	g	602.0	u	875.6	u	1152.0	g	1440.8	g	3070.7	u
173.0	u	603.2	u	876.9	u	1153.4	u	1443.9	g	3071.8	g
214.5	g	610.8	g	883.9	g	1166.6	g	1461.6	u	3074.6	u
220.4	g	612.0	g	884.4	g	1168.4	g	1462.8	u	3074.7	g
269.5	u	617.5	u	897.6	u	1192.5	u	1512.7	g	3080.6	u
276.9	u	617.7	u	898.4	u	1193.7	u	1514.8	g	3081.1	g
298.4	g	712.7	g	901.1	g	1196.9	g	1531.3	g	3081.6	g
299.1	g	713.8	g	909.3	g	1198.0	g	1535.6	g	3081.8	u
312.8	g	728.0	u	917.8	u	1255.7	g	1537.4	u	3087.2	u
315.5	g	730.2	g	918.2	u	1255.8	g	1540.1	u	3087.4	g
322.5	u	736.8	g	949.6	u	1259.9	u	1556.6	u	3089.9	g
324.7	u	743.3	u	950.2	u	1260.3	u	1559.1	u	3091.0	u

C.1 Resonance Raman Intensity Analysis

The absorption, fluorescence, and Raman scattering cross-sections were simultaneously modeled using the time-dependent described in Section 1.3[4, 19, 26]. Recall the autocorrelation and cross correlation of the wavepacket.

$$\langle \chi_i | \chi_i(t) \rangle = \prod_{j=1}^{N} Exp\left[-\frac{\Delta_j}{\sqrt{2}} [1 - exp(-i\omega_j t)] \right] \tag{C.1}$$

$$\langle \chi_f | \chi_i(t) \rangle = \frac{\Delta_j}{\sqrt{2}} (e^{-i\omega_1} - 1) \prod_{j=1}^{N} Exp\left[-\frac{\Delta_j}{\sqrt{2}} [1 - exp(-i\omega_j t)] \right] \tag{C.2}$$

The Δ_j are the dimensionless displacements of the ground and excited state harmonic potential minima for the vibrational modes with frequencies ω_j. The mode specific reorganization energy, λ_ν, can be calculated as:

$$\lambda_\nu = \frac{\hbar \omega \Delta^2}{2} \tag{C.3}$$

In the fit to the nanocrystals (Fig. 5.1) a single displaced mode was used for each vibrational frequency observed in the Resonant FSRS spectra (Fig 5.3 & Fig. C.5). A more physically realistic model would include a distribution of displacements across ξ coordinates with the same frequency: one per molecule on which the excitation acts. It can be shown through simple arithmetic manipulation that equation C.3 is equal to:

$$\langle \chi_i | \chi_i(t) \rangle = \prod_{j=1}^{\xi N} Exp\left[-\frac{\Delta_j / \sqrt{\xi}}{\sqrt{2}} [1 - exp(-i\omega_j t)] \right] \tag{C.4}$$

Equation C.4 describes a multidimensional wavepacket autocorrelation where each dimension has been split into ξ degenerate dimensions each with a displacement of $\Delta_j / \xi^{1/2}$. Therefore a single displaced coordinate can reproduce the vibronic lineshape and resonance Raman cross sections of a multitude of degenerate displaced coordinates and the reorganization energies in both cases are the same.

Fitting the Dynamic Wavepacket Model to the Tc Monomer

The dynamic wavepacket model was fit iteratively by hand. The initial displacement factors were estimated from the cross sections as $\Delta = \sigma_R^{1/2} / \omega$. These initial estimated parameters were scaled together to match the overall width of the absorption. Next the electronic origin transition energy, E_{eg}, was adjusted to fit the peak energy of the calculated and measured absorption. The transition dipole length, Meg, was adjusted to match magnitude of the absorption cross section. The solvent relaxation energy, λ_s, was adjusted to match the magnitude of the Stokes shift between the absorption and the emission peak energies.

The inhomogenous broadening parameter, Θ, was increased to decrease the level of vibronic structure in the absorption lineshape. Once the absorption spectrum had been fit coarsely, the homogenous line-width parameter, Γ, was adjusted along with the displacements Δ_j to match the magnitude of the Raman cross sections and refine the width of the absorption. These parameters were adjusted iteratively to fit the absorption and resonance Raman cross sections.

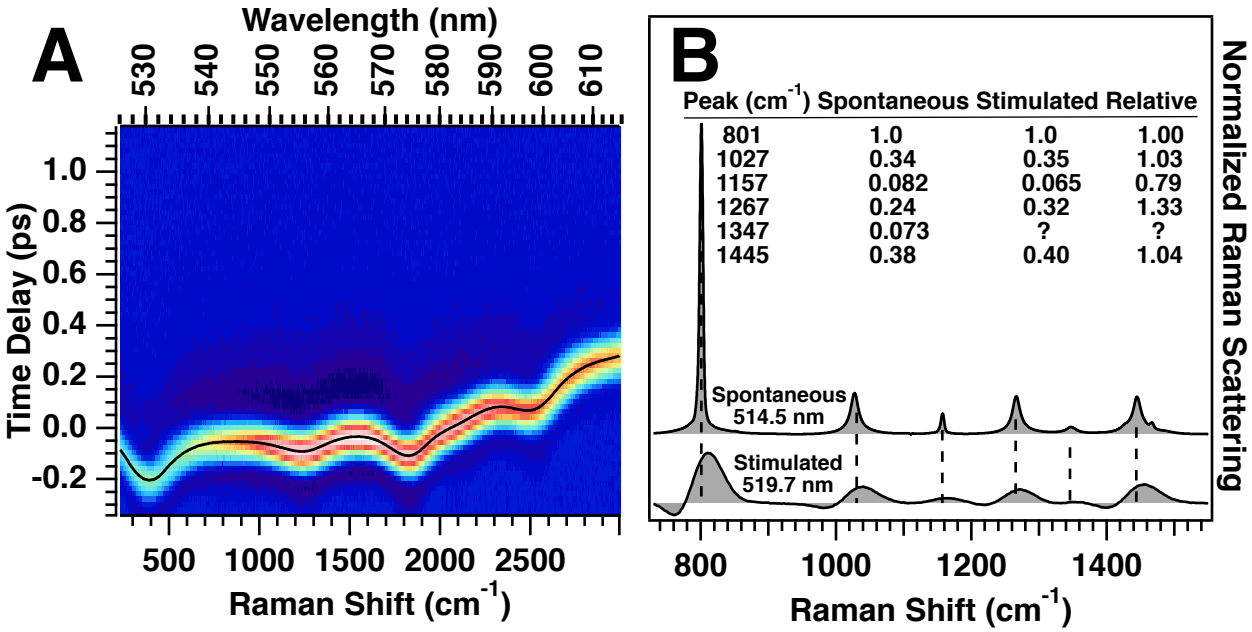

Figure C.7: Characterization of the femtosecond probe pulse for stimulated Raman measurement. A) Frequency resolved optical Kerr gated probe pulse used in 520 nm stimulated resonance Raman experiment. There is less than 70 fs of chirp in the probe pulse in the region of 750 -1600 cm^{-1} where intensity sensitive Raman cross-section measurements were performed. B) Comparison of spontaneous and stimulated Raman spectra of cyclohexane at 514.5 and 519.7 nm respectively. Fitting the stimulated Raman spectra to a dispersive Gaussian (Eqn. 5.3) faithfully reproduces the relative intensities within the limit of fitting errors caused by weak or congested signals.

Characterization of Femtosecond Probe (Stokes) Pulse for Resonant SRS

In order to accurately determine absolute Raman cross-sections from stimulated Raman spectroscopy the temporal chirp in the probe pulse was characterized by a frequency resolved Kerr gating experiment (Fig. C.7 A). Less than 60 fs of group velocity dispersion was present between the region 600 - 1650 cm^{-1} where Raman measurements were made. The effect of temporal chirp on the relative Raman intensities was checked by examining the Raman spectrum of cyclohexane as a test case (Fig. C.7 B). The stimulated Raman spectrum at

519.7 nm and the spontaneous Raman spectrum at 514.5 nm were fit as described in the main text. The two spectra were scaled such that the 801 cm^{-1} peak displays the same intensity. The inset in Fig. C.7 B presents the relative intensity of the peaks relative to the 801 cm^{-1} peak in columns two and three and relative to the stimulated Raman intensity in column four. The relative intensity of the 1027 and 1445 cm^{-1} peaks was accurately reproduced while that of the weak and congested peaks at 1157 and 1267 cm^{-1} deviated by $\sim 30\%$. The small peak at 1347 cm^{-1} could not be accurately fit. These results suggest that the relative intensity and correspondingly the absolute Raman cross section of strong well-separated peaks can be accurately measured by stimulated Raman spectroscopy. Figure C.5 presents the results of a least-squares multi-peak fitting routine of the five dispersive Gaussian functions and a 7th-order polynomial baseline to the resonant stimulated Raman spectrum of tetracene nanocrystals. An additional fit (not shown) was performed on the 600 - 800 cm^{-1} region of the spectrum where the baseline behaved differently.

Fluorescence vs Raman Intensities with 520 nm Excitation

Ratio of the intensity of the spontaneous 520 nm resonant Raman peak to the intensity of the fluorescence the same region can be estimated as follows. Our paper measures the molar absorptivity maximum of the nanocrystals to be $\epsilon_{520nm} = 7800$ $M^{-1}cm^{-1}$. From this value the absorption cross section is calculated as

$$\begin{aligned} \sigma_R &= \frac{1000ln(10)\epsilon}{6.022 \times 10^{23}} \times \frac{10^{16}\text{Å}^2}{1cm^2} \\ &= 3.82 \times 10^{-5}\epsilon \\ &= 0.29\text{Å}^2 \end{aligned} \tag{C.5}$$

A fluorescence quantum yield of about 0.002 has been reported.[132] We can estimate the fluorescence cross section with 520 nm excitation to be

$$\sigma_F = \phi_F \sigma_A = 5.9 \times 10^{-4}\text{Å}^2 \tag{C.6}$$

The strongest peak with 520 nm excitation is at 1386 cm^{-1} with a cross section of $\sigma_R = 2.82 \times 10^{-9}$ $Å^2$ (Table 5.2). Thus the emission cross section is about 200,000 times greater than a Raman cross section. The fluorescence is broad while the Raman is narrow. Since we seek an estimate of the relative intensities we will approximate the spectrum of the fluorescence as flat with a width of $\gamma_F = 960$ cm^{-1} which is the FWHM of the emission, and the Raman peak as flat with a width of $\gamma_R = 3$ cm^{-1}. The relative intensity in a given spectral region can then be calculated by dividing by the spectral linewidth.

$$I_F = \sigma_F/\gamma_F \tag{C.7}$$

The desired ratio can be calculated:

$$\begin{aligned}\frac{I_F}{I_R} &= \frac{\sigma_F \gamma_R}{\sigma_R \gamma_F} \\ &= \frac{1}{650}\end{aligned} \tag{C.8}$$

Therefor the emission is about 650 times more intense than the strongest spontaneous resonance Raman line. Stimulated resonance Raman spectroscopy is necessary to measure Raman intensities at the red edge of the absorption spectrum in crystalline tetracene.

Calculation of Raman Cross Section Confidence Intervals

The Raman cross sections are calculated as:

$$\sigma_{Tc} = \frac{8\pi}{3}\left(\frac{1+2\rho}{1+\rho}\right)\left[\left(\frac{\omega_l - \omega_{Tc}}{\omega_l - \omega_{std}}\right)^2 \left(\frac{I_{Tc}}{I_{std}}\right)\left(\frac{c_{std}}{c_{Tc}}\right)\left(\frac{\partial\sigma_{std}}{\partial\Omega}\right)\right] \tag{C.9}$$

The concentrations of tetracene and internal standard (C_{std} and C_{Tc}) as well as the laser frequencies to be known to an arbitrary degree of accuracy. The major sources of error arise from multi peak fitting and from the uncertainty in the differential cross section of the internal standard reported in the literature.[160, 161] The uncertainty of the fit peak areas A_{Tc} and A_{std} can be estimated from least squares data analysis as done in the Igor Pro software package. The uncertainty of inherent in the internal standard differential cross section is reported in Ref. [1] at ±10 % for acetone and in Ref. [158] at less than ±20 % for sulfate. The error was then propagated and the 95% confidence intervals were calculated according to equation S9.

$$\delta\sigma_{Tc} = \sigma_{Tc}\sqrt{\left(\frac{\delta A_{TC}}{A_{TC}}\right)^2 + \left(\frac{\delta A_{std}}{A_{std}}\right)^2 + \left(\frac{\delta A_{TC}}{A_{TC}}\right)^2} \tag{C.10}$$

Analysis of Non-totally Symmetric Modes in Tc Monomer

It came as a surprise that the b_{3g} fundamentals displayed strong resonance enhancement blue edge of the S_1 electronic state of the Tc monomer and nanocrystals. It has been shown that in naphthalene and anthracene both as a solution and as a polycrystalline solid these b_{3g} modes gain intensity with pre-resonance excitation through B-term vibronic coupling with the very optically active B_{1u} state.[29] The B-term Resonance Raman intensity is presented in Equation G.8 of Appendix G.

In Tc monomer there is a large energy separation between the B_{2u} and B_{1u} states at 2.626 and 4.41 eV respectively ergo the energy denominator should diminish the vibronic coupling stregth. With 3.00 eV excitation the Raman transition are above resonance with the M_{ge} B_{2u} transition and pre-resonant with the M_{re} B_{1u} transition. At this excitation wavelength the

totally symmetric a_g vibrations which are enhanced as M_{ge}^4 show intensity within the same order of magnitude as the b_{3g} vibrations which are enhanced as $M_{ge}^2 M_{rg}^2$. To reconcile this second point it should be noted that the B_{1u} transition (S_3) has an oscillator strength that is about twenty-fold greater than that of the low energy B_{1u} transition and can therefore enhance the non-totally symmetric modes and compete in vibronic intensity.[31] The high frequency of the b_{3g} modes at 1621 cm^{-1} and should have a strong resonance Raman intensity within B-term scattering as it should provide the strongest non-adiabatic perturbation of the electronic states.

Table C.2: Assignment of combinations and overtones bands in spontaneous resonance Raman spectra in Figure 2

Raman Shift (cm^{-1})	Excitation Wavelength (nm)	Assignment to Fundamental Frequencies
1063	476.5 & 457.9	752 + 316
1141	413.1	1198 - 58
1237	413.1	1179 + 58 or 2 × 619
1262	413.1	1198 + 58
1321	413.1	1198 + 130
1351	413.1	1396 - 58
1424	413.1	1369 + 58
1456	413.1	1396 + 58
1478	413.1	1159 + 316
1502	413.1	1448 + 58 or 752 × 2
1578	413.1	1448 + 130[a]
1601	476.5	1545 + 58
1666	476.5 & 413.1	1618 + 58[b]

Analysis of High Energy Resonance Raman Spectra in Tc Nanocrystals

A quantitative model could not be fit to the resonance Raman spectra of Tc Nanocrystals presented in Fig. 1 due to the contributions of higher energy exciton states. Still qualitative points can be made. The strongest peak in the 413.1 nm spectrum is the b_{3g} fundamental at 1618 cm^{-1}. Resonance enhancement of a b_{3g} fundamental with a frequency of 1630 cm^{-1} has been noted in polycrystalline samples of other linear polyacene such as anthracene and naphthalene. This enhancement has been attributed to B-term resonance involving coupling of both the B_{1u} and B_{2u} electronic states. High frequency non-totally symmetric vibrations such as this can provide a strong non-adiabatic perturbation of the electronic states.

The 413.1 nm spectrum contains a multitude of new peaks in the high frequency region of the spectrum while the low frequency peaks have diminished intensity. The most striking

peak is an intense broad shoulder centered at 1666 cm^{-1}. The frequencies of these peculiar bands do not correspond to any Raman active fundamental which have been measured previously.15,19,20 These new peaks could be combination bands of the high frequency intramolecular modes and the low frequency Raman active phonon modes. The new peaks could alternatively assigned to an IR active fundamental reported at 1670 cm^{-1} that gains intensity due to rapid symmetry breaking on the excited state. A careful Raman anisotropy investigation is required if definitive assignments are to be made.

The appearance of high frequency modes and damping of low frequency modes as in the 413.1 nm spectrum is typically caused by rapid multimode dephasing.[1] When the excited state potential is strongly sloped along multiple coordinates with dissimilar frequencies, there is insufficient time for the wavepacket to find Frank-Condon overlap with the first vibrationally excited state, ν_1, of the low frequency modes. Effectively the high frequency combination bands "steal" vibronic activity away from the low frequency fundamentals.[1] Rapid SF on a timescale shorter than multimode dephasing would also damp the low-frequency modes relative to the high frequency modes. The appearance of combination bands with the low frequency modes eg. 58, 123, 130, 316 cm^{-1} suggests that these modes are highly displaced.

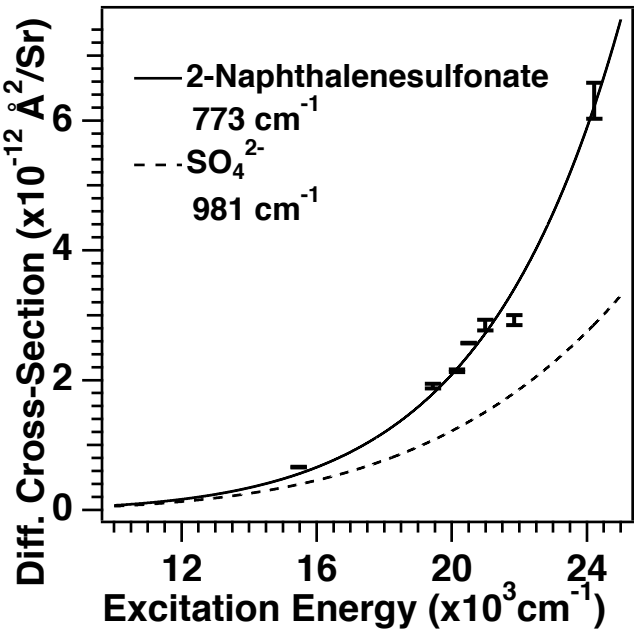

Figure C.8: Calibration of the differential Raman cross section of the 772 cm^{-1} line of 2-napthalene sulfonate by comparison with the intensity of the 981 $cmcm^{-1}$ symmetric stretching mode of sulfate as an external standard. The measured cross-sections were fit to Equation C.11 with fit parameters $K_e = 1.2 \times 10^{-27}$ cm^2, $\nu_e = 6.2 \times 10^4$ cm^{-1}.

Determination of Raman Cross Section of Internal Standard

The differential Raman cross section of the 772 cm^{-1} sulfonate bending mode of aqueous sodium 2-naphthalenesulfonate (SNS) was first determined by comparison with the 981 cm^{-1} symmetric stretching mode of aqueous sulfate (Fig. C.8) as an internal standard at six different excitation energies.[161] The differential cross sections were fit to the functional form of Equation C.11.

$$\frac{\partial\sigma}{\partial\Omega}(\omega) = K_e \omega \omega_S^3 \left[\frac{\tilde{\omega}_e^2 + \omega^2}{(\tilde{\omega}_e^2 + \omega^2)^2}\right]^2 \tag{C.11}$$

ω and ω_s are the frequencies of the incident and scattered shifted light respectively. K_e and $\tilde{\omega}_e$ are fit parameters determined to be 1.2×10^{-11} $Å^2$ and 6.2×10^4 cm^{-1} respectively.

Appendix D

Supporting Information: Chemical and Solid State Examples of the Reciprocal Relation of Polaron Binding Energy and Polaron Size

This work will be submitted to the *Journal of Physical Chemistry C* by Scott R. Ellis, Myeongkee Park and Richard A. Mathies

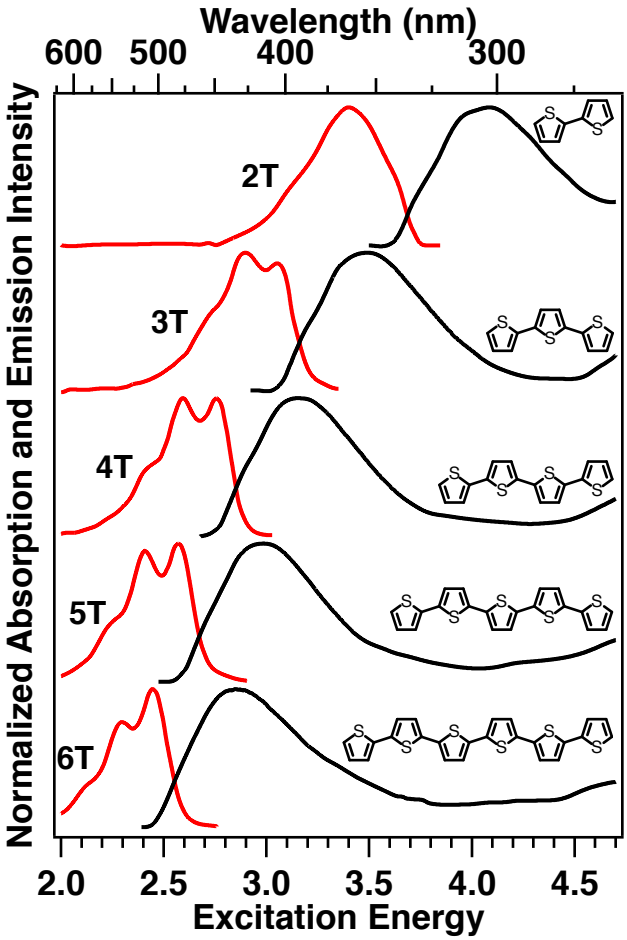

Figure D.1: Absorption (black) and fluorescence (red) spectra of oligothiophenes (nT) in dioxane for $n = 2 - 6$ repeating units. Data was digitized from Reference [234] The pixel resolution of the emission spectrum of the 2T was not sufficient to resolve the vibronic peaks in the published work.

D.1 Measurement of Spectra of Polyacenes

The spectra of anthracene were measured in a dilute solution of cyclohexane while the spectra of tetracene, pentacene were measured in solutions of 1,2,4-trichlorobenzene. The absorption and emission spectra of hexacene in cyclohexane solution were digitized from Ref. [193].

D.2 Stokes Shift Analysis

The total reorganization energy has contributions from intramolecular degrees of freedom as well as the solvent.

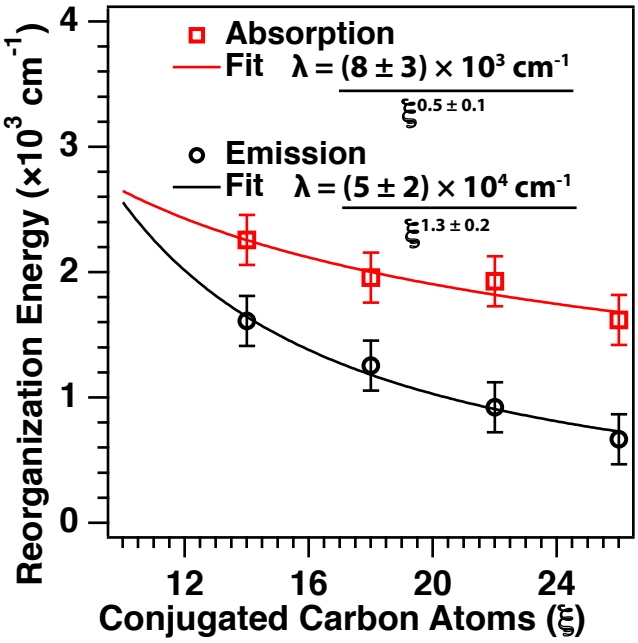

Figure D.2: Dependence of measured Stokes shift on the extent of delocalization (ξ) of polyacenes shown in Fig. 6.1. The solid lines are least squares fits to the absorption (red) and the emission (black) of the form $\nu_{St} = \nu_0/\xi_n$.

$$\lambda_{net} = \lambda_\nu + \lambda_S \tag{D.1}$$

In the case of polyacenes the solvent reorganization energy is an order of magnitude smaller than the intramolecular reorganization energy and will be neglected in this analysis. The Stokes shift is the energy difference between the absorbed and emitted light which is approximately twice the reorganization energy because nuclear reorganization accompanies both upward and downward optical transitions. Often the Stokes shift is estimated by the offset between peak maxima of the absorption and emission spectra, however this only works well when the lineshapes are approximately Gaussian and the maxima are at the center. For spectra with fine vibronic lineshapes it is necessary to evaluate the stokes shift by integration of the form:

$$\begin{aligned} \nu_{St} &= \nu_a^{e.g.} - \nu_f^{e.g.} \\ \nu_a^{e.g.} &= \int_0^\infty \nu_a \epsilon(\nu_a) d\nu_a / \int_0^\infty \epsilon(\nu_a) d\nu_a \\ \nu_f^{e.g.} &= \int_0^\infty \nu_f I(\nu_f) d\nu_f / \int_0^\infty I(\nu_f) d\nu_f \end{aligned} \tag{D.2}$$

ν_{St} is the stokes shift. $\epsilon(\nu_a)$ and $I(\nu_f)$ are the intensities of the absorption and the emission at each relevant frequency. ν_a and ν_f are the frequency offset from the electronic origin transition energy which is taken to be the energy at which the absorption and emission cross. $\nu_a^{e.g.}$ and $\nu_f^{e.g.}$ are intensity weighted averages over the absorption and emission spectral bands. Figure D.2 Presents the $\nu_a^{e.g.}$ and $\nu_f^{e.g.}$ verses the number of conjugated carbons in each polyacenes which is our metric for delocaization ξ. The solid lines are fits of the form $\nu^{e.g.} = \nu_0/\xi^n$. The absorption Stokes shift scales as $1/\xi^{0.5}$ while the emission scales as $1/\xi^{1.3}$. This deviation from the expected behavior $1/\xi$ reflects that the Stokes shift is an imperfect measure of the reorganization energy. Higher energy vibronic transitions in the absorption are enhanced by the energy dependence of the transition dipoles while the same vibronic transitions in the "mirrored" flurorescence are de-enhanced by an energy term raised to power of three. On the other hand the reorganization energy is determined solely by the Frank-Condon factors and assumes equal transition dipole couplings for all vibronic transitions. The true reorganization energy is a value between $\nu_a^{e.g.}$ and $\nu_f^{e.g.}$ which can determined by fitting the absorption or fluorescence with a time-dependent wave packet model. Still approximate $1/\xi$ behavior of the reorganization energy is observed in these simple systems.

D.3 Derivation of Displacement from Ratio of Peak Intensities

Within the displaced harmonic oscillator approximation the unitless displacement parameter Δ can be related to the ratio of the 0-1 vibronic peak intensity in the absorption or emission to the to 0-0 electronic origin peak intensity as follows. The electronic and vibrational components of a transition are often partitioned as $\langle\psi_{\nu'}|\psi_{\nu}\rangle\langle\psi_{e'}|\mu|\psi_{e}\rangle\langle\chi_{s'}|\chi_{s}\rangle$. For a given vibronic transition the ratio of the intensities is given by the ratio Frank Condon factors.

$$\frac{I_{0-1}}{I_{0-0}} = \left|\frac{\langle\psi_1'|\psi_0\rangle}{\langle\psi_0'|\psi_0\rangle}\right|^2 \tag{D.3}$$

Consider a harmonic oscillator which is displaced by q along coordinate x the ground and excited states.

$$\frac{I_{0-1}}{I_{0-0}} = \left|\frac{\int_{-\infty}^{\infty} dx \sqrt{\frac{m\omega}{\pi\hbar}}\sqrt{\frac{2m\omega}{\hbar}}(x-q)exp(\frac{-m\omega(x-q)^2}{2\hbar})exp(\frac{-m\omega(x)^2}{2\hbar})}{\int_{-\infty}^{\infty} dx \sqrt{\frac{m\omega}{\pi\hbar}}exp(\frac{-m\omega(x-q)^2}{2\hbar})exp(\frac{-m\omega(x)^2}{2\hbar})}\right|^2 \tag{D.4}$$

Let $a = m\omega/2\hbar$. Gaussian integrals are readily solved by completing the square and U-substitution.

$$\begin{aligned} &= \left|\frac{\frac{q}{2}exp(\frac{aq^2}{2})\sqrt{\frac{2m\omega}{\hbar}}\sqrt{\frac{\pi}{2a}}}{exp(\frac{aq^2}{2})\sqrt{\frac{\pi}{2a}}}\right|^2 \\ &= \left|q\sqrt{\frac{m\omega}{2\hbar}}\right|^2 \end{aligned} \tag{D.5}$$

The dimensionless displacement δ is defined as a standard deviation of the ground state wavefunction. So $\Delta = q\sqrt{\frac{\hbar}{m\omega}}$

$$\frac{I_{0-1}}{I_{0-0}} = \frac{|\Delta|^2}{2} \tag{D.6}$$

$$\Delta = \pm\sqrt{2\frac{I_{0-1}}{I_{0-0}}} \tag{D.7}$$

And the reorganization energy is

$$\lambda = \hbar\omega\frac{I_{0-1}}{I_{0-0}} \tag{D.8}$$

We can check the validity of these results against a wavepacket model for the emission lineshape. The fit spectra are overlaid with the data from Ref. [190].

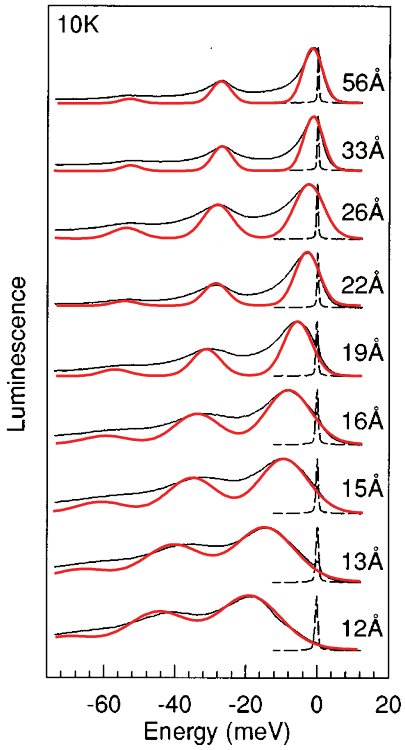

Radius (nm)	ξ (unit cells)	λ_v (cm^{-1})	Γ (cm^{-1})	ε_{BEES} (cm^{-1})	E_{00} (eV)	Δ_1	Δ'
1.2	64	148	50	309	1.92	1.20	0.15
1.3	82	144	48	238	1.98	1.18	0.13
1.5	126	139	40	154	2.05	1.16	0.10
1.6	153	120	37	132	2.13	1.08	0.09
1.9	256	105	23	90	2.21	1.01	0.06
2.2	397	89	20	47	2.30	0.93	0.05
2.6	656	134	24	39	2.35	1.14	0.04
3.3	1341	97	16	19	2.43	0.97	0.03
5.6	6553	86	16	22	2.49	0.91	0.01

Figure D.3: (Top) Normalized Fluorescence Line Narrowing Spectra (black line) of CdSe QD's between 12 and 56 Åin radius. Red lines are wavepacket fits modeled in this work with a single vibrational frequency reported in Table 1. The mean radii of the dots are determined from SAXS and TEM measurements. A 10 Hz Q-switched Nd:YAG/dye laser system (;7 ns pulses! serves as the excitation source. Detection of the FLN signal is accomplished using a time gated OMA. The laser line is included in the figure (dotted line) for reference purposes. All FLN spectra are taken at 10 K. Reprinted with permission from Ref. [190]. Copyright 1996. Physical Review B. (Bottom) Fit parameters for the emission spectra.

D.4 Derivation of a Physically Realistic Function for Exciton Delocalization in Nanoparticles

Consider a particle that is much larger than the bulk exciton Bohr radius. In this case the exciton doesnâĂŹt feel the effect of confinement. As the particle size is decreased the exciton will begin to feel the effect of confinement. In one limit the exciton electron and hole density would behave like a rigid sphere where the electron density is a step function. In this case at the point where the nanoparticle size is smaller then the bulk exciton Bohr radius, the excition would immediately adopt the size of the nanoparticle. A more physically realistic picture would account for the fact that the electron and hole density are not step functions but have some spatial decay to them. In this case the effect of confinement is more gradual. A complementary error function is chosen to model slope of the exciton volume (ξ) with respect to nanoparticle volume (V_{np}) because the delocalization should be unit linear for small nanoparticles and constant for large nanoparticles.

$$\frac{d\xi}{dV_{np}} = \frac{1}{2} erfc\left(\frac{V_{np} - V_{bulk}}{\sqrt{2}\sigma}\right) \tag{D.9}$$

Integrate with respect to V_{np} to get the exciton size dependence.

$$\xi(V_{np}) = \frac{1}{2}\int erfc\left(\frac{V_{np} - V_{bulk}}{\sqrt{2}\sigma}\right) dV_{np} \tag{D.10}$$

This is done by integration by parts and U-substitution.

$$\xi(V_{np}) = \frac{1}{2}\left((V_{np} - V_{bulk}) erfc\left(\frac{V_{np} - V_{bulk}}{\sqrt{2}\sigma}\right) - \frac{2\sigma}{\pi} exp\left[-\left(\frac{V_{np} - V_{bulk}}{\sqrt{2}\sigma}\right)\right]\right) + C \tag{D.11}$$

Use the limiting case of $\xi(0) = 0$ and to solve for C:

$$C = \frac{1}{2}\left(V_{bulk} erfc\left(\frac{V_{bulk}}{\sqrt{2}\sigma}\right) + \frac{2\sigma}{\pi} exp\left[-\left(\frac{-V_{bulk}}{\sqrt{2}\sigma}\right)^2\right]\right) \tag{D.12}$$

Plots of $d\xi/dV_{np}$ and $\xi(V_{np})$ for $V_{bulk} = 5$ and varying values of σ in Figure D.4 respectively. σ is phenomenolocial parameter 'exciton elasticity'. A small value of σ means the exciton electron and hole density behaves as a hard sphere while a large value of σ describes a soft exciton which feels the effects of confinement at long range and adjusts its wave function gradually. The reorganization energy now has the expected behaviour.

$$\lambda'(V_{np}) = \frac{\lambda_1}{\xi(V_{np})} \tag{D.13}$$

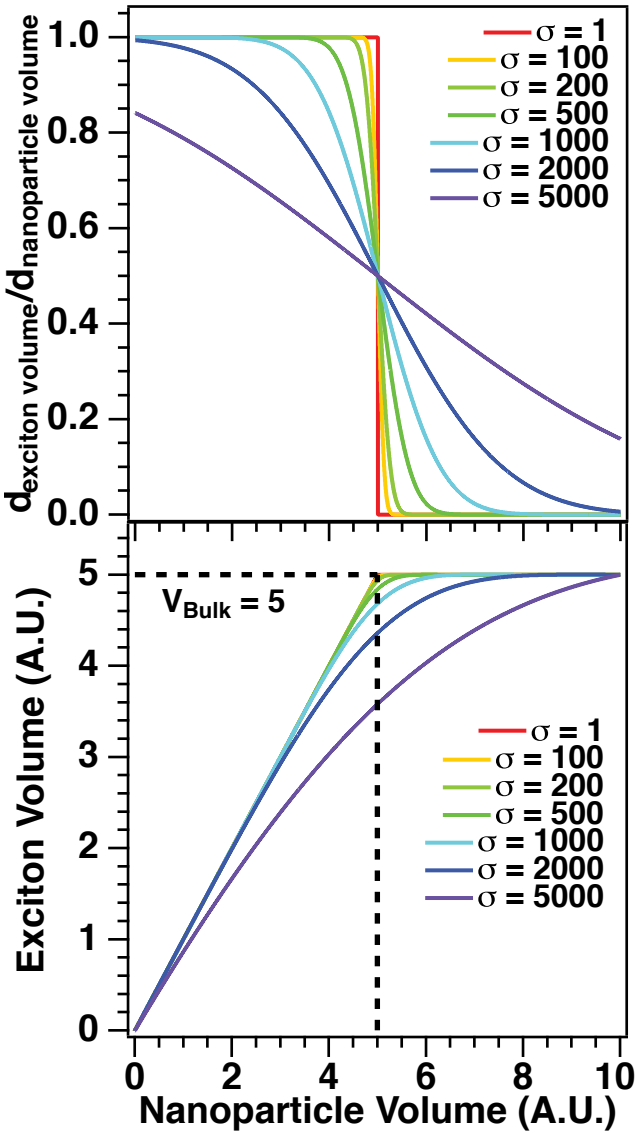

Figure D.4: Physically relevant analytical model for exciton size verses nanoparticle size. At some critical size the nanoparticle size (V_{np}) is the same as the bulk exciton Bohr radius V_{bulk}. How quickly the nanoparticle feels the effect of confinement is given by the parameter σ. For nanoparticles much larger than V_{bulk} the exciton size no longer increases on the nanoparticle size.

In this model the bulk semiconductor maintains a finite reorganization energy of:

$$\lambda' \left(\left(\frac{V_{np} - V_{bulk}}{\sigma} \right) \gg 1 \right) \tag{D.14}$$

Appendix E

Supporting Information: Supramolecular $Ga_4L_6^{12-}$ Cage Photosensitizes 1,3-Rearrangement of Encapsulated Guest via Photoinduced Electron Transfer

E.1 General Methods

Details of the synthesis and NMR characterization of $K_{12}Ga_4L_6$ and the alkyl ammonium salts can be found online at http://dx.doi.org/10.1021/jacs.5b06317. Additionally numerous control reactions were performed to indicate which substrates are photosensitized by $Ga_4L_6^{12-}$. Herein we present material pertaining to characterization of the electronic and optical properties of $K_{12}Ga_4L_6$ in solution.

Reaction solutions were magnetically stirred with the exception of those reactions performed in NMR tubes. Reactions were monitored using 0.25 mm pre-coated silica gel plates from Silicycle (TLGR10011B-323) containing a fluorescent indicator for visualization by UV light by thin layer chromatography. Various stains were used to visualize reaction products, including $KMnO_4$ and phosphomolybdic acid in ethanol. Flash chromatography was performed using MP Biomedicals SiliTech silica gel 32-63D.

Air sensitive materials were handled in an inert atmosphere N_2 glovebox. For moisture sensitive reactions, glassware was oven dried at 150 °C overnight prior to use or flame dried under vacuum immediately before use and back filled with dry N_2 using a vacuum line manifold. NMR spectra were recorded at ambient temperature using either Bruker AV-600, AV-500, DRX-500 or AV-400 MHz spectrometers. ^{1}H NMR chemical shifts (δ) are reported in parts per million (ppm) downfield of TMS relative to residual protic solvent resonances (7.26 ppm for $CDCl_3$, 5.30 ppm for CD_2Cl_2, 3.31 ppm for CD_3OD, 4.80 for D_2O, 2.50 for DMSO-d_6). ^{13}C-NMR chemical shifts (δ) are reported in ppm relative to the carbon resonance of the deuterated solvent (77.23 ppm for $CDCl_3$, 53.84 for CD_2Cl_2, 49.00 for CD_3OD, 39.52 for DMSO-d_6).

GC/MS experiments were conducted on a Perkin Elmer Mass spectrometer. Both low- and highresolution mass spectral data were obtained from the Micromass/Analytical Facility operated by the College of Chemistry, University of California, Berkeley. Infrared (IR) spectra were recorded on a as a Nujol mull or a thin film between NaCl plates. UV/Vis spectra were performed on a Hewlett Packard 8453 diode-array (deuterium/tungsten) spectrophotometer using quartz cuvettes. Fluorescence spectra were collected on a Varian Cary Eclipse fluorescence spectrophotometer at ambient temperature unless otherwise indicated. Melting points for all $K_{12}Ga_4L_6$ complexes are not reported as decomposition occurs above 190 °C. Photoreactions were conducted in a Rayonet photoreactor with a minimum of six UVB (280-315 nm) bulbs using N_2 degassed solvents under N_2 atmosphere in airtight pyrex ($<$ 275 nm filter) glassware.

E.2 UV-Vis Spectra and Determination of Molar Absorption Coefficient

$$\epsilon(\lambda) = \frac{A(\lambda)}{Cl} \tag{E.1}$$

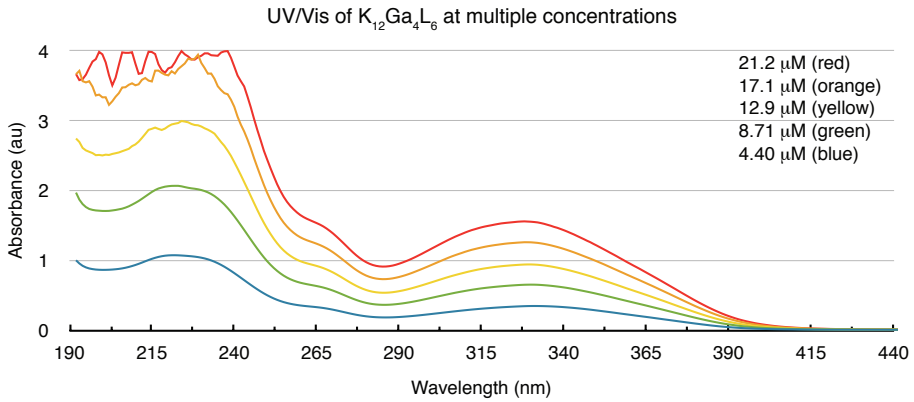

Figure E.1: UV-Vis absorbance spectrum of $K_{12}Ga_4L_6$ at variable concentrations.

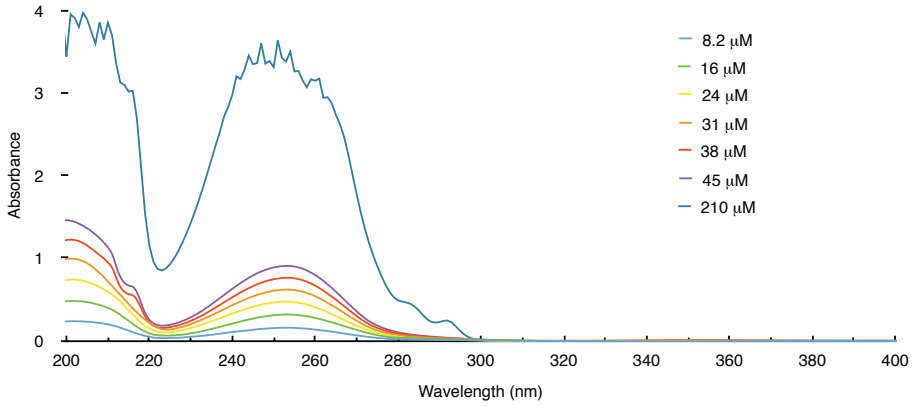

Figure E.2: Molar absorption coefficient plots of solvent filled **1** (blue) and **2b** (grey) at 330 nm. Concentrations are reported in μM.

Molar absorption coefficients (ϵ) for both $K_{12}Ga_4L_6$ **1** and **2b** were determined from a plot of absorbance versus concentration for a series of concentrations (Figure E.3). For $K_{12}Ga_4L_6$ ϵ is 7.6 x 10^4 $\pm$ 0.3 $M^{-1}cm^{-1}$ at 330 nm. For **2b**: Ît̨ is low with an upper limit of 26 $M^{-1}cm^{-1}$ at 330 nm.

Because the UV-Vis absorbance spectra were collected at concentrations much lower than the concentration that the 1,3-rearrangement takes place, we collected UV-Vis spectra for the cinnamyl ammonium at concentrations similar to that of the photorearrangement to determine whether the rearrangement was the result of direct absorbance of UV light or the result of energy transfer from the assembly. For **2b** under typical reaction conditions the concentration is 9.1 x 10^{-3} M. UV-Vis spectra were taken up to 2.1 x 10^{-4} M. Absorbance is not detected above 300 nm at the listed concentration (Figure E.3). The UVA light source used emits from 315 - 400 nm. This provides evidence that the rearrangement is the result of photosensitization by the assembly.

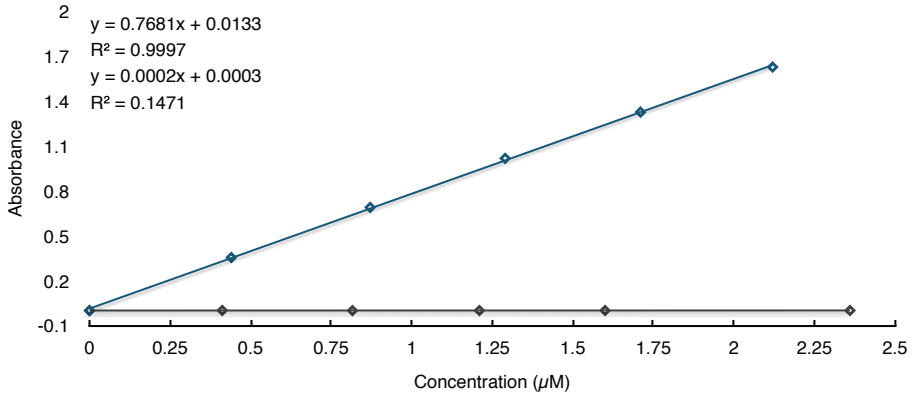

Figure E.3: UV-Vis spectra of **2b** at a range of concentrations. Spectra show no absorbance by **2b** above 300 nm. Absorbance.

E.3 Determination of Quantum Yield

Quantum yield experiments were conducted using a merry-go-round apparatus that has been described previously.[235] A 450 W Hanovia Hg lamp was used as the light source with borosilicate 4 test tubes containing a 2 mM K_2CrO_4 in 1% K_2CO_3 aqueous solution as the filter. Reactions were monitored by ^{1}H NMR. All quantum yield experiments were conducted in triplicate and 95conducted as previously described using C_6D_6 as solvent.[227]

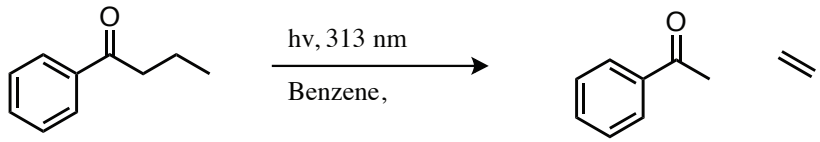

In an N_2 atmosphere glovebox, to a borosilicate NMR tube was added butyrophenone (0.0081 mmol) in degassed benzene-D_6 (0.9 ml, 0.009 M). The tube was capped and sealed with black electrical tape. NMR tubes were immersed in borosilicate test tubes with the previously mentioned chromate solution and irradiated for 14 h. Reaction progressed was monitored by NMR.

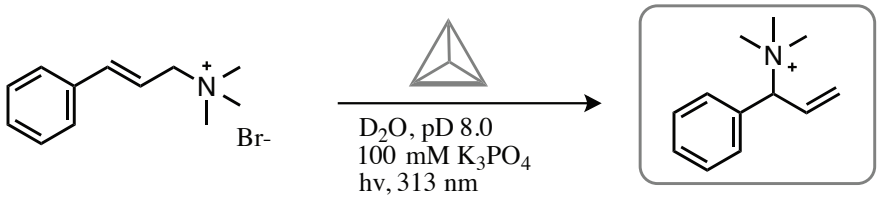

In a N_2 atmosphere glovebox, (E)-N,N,N-trimethyl-3-phenylprop-2-en-1-aminium bromide (**2b**, 2 mg, 0.0078 mmol) and $K_{12}Ga_4L_6$ (**1**, 15 mg, 4.2 mmol) were dissolved in de-

gassed D_2O (700 μL, pD 8.0, 100 mM K_3PO_4) and mixed until a homogeneous yellow solution formed. Solution was then transferred to a NMR tube, capped and sealed with black electrical tape. NMR tubes were immersed in borosilicate test tubes with the previously mentioned chromate solution and irradiated for 14 h. Reaction progressed was monitored by NMR.

E.4 DFT Calculations

Using Gaussian 09 software package, geometry optimizations were performed using DFT-B3LYP methods and basis set 6-311+G(d,p). Single point energy minima were determined in the gas phase using calculation method R-ωB97XD and basis set 6-311+G(d,p) for a single positive charge and singlet spin state. Relative energy differences were determined for **2b** and **3b**.

E.5 Electrochemical Methods

All electrochemical experiments were performed using a CH Instruments 660D potentiostat (Austin, TX) in a standard one-compartment, three-electrode electrochemical cell. Freshly polished glassy carbon (3 mm diameter, BASi; West Lafayette, IN) was used as the cathode in all experiments. Pt wire (electrochemical grade, purchased from Sigma Aldrich) was used as the anode in all experiments. Aqueous experiments were performed using a saturated Ag/AgCl reference purchased from BASi. Non-aqueous experiments were performed using Ag^0 wire as a quasi-reference, followed by addition of ferrocene as an internal standard at the conclusion of the experiment. Electrolytes were degassed by bubbling with Ar for 10 min. No iR compensation was applied.

E.6 Transient Absorption Spectroscopy

Materials and Methods

Solutions of $K_{12}Ga_4L_6$ and $K_{12}Ga_4L_6$ with trimethylcinnamyl ammonium (**2b** and **2b⊂1**) in water were filtered through a 40 μm Teflon filter to remove undissolved material. They were then diluted to an optical density of 0.6 at 400 nm and sealed inside a 2-mm path length cuvette with a Teflon stopper while under nitrogen gas to prevent oxidation during optical measurements. Additionally a Teflon covered 2-mm iron stir bar was placed in the cuvette. During the 4-hour acquisitions, the samples were simultaneously stirred magnetically and translated perpendicular to the beam path to replenish the irradiated volume mitigating photoalteration effects.

The transient absorption data were acquired on a femtosecond stimulated Raman instrument with the Raman pump pulse blocked. This setup has been described previously[159, 236]. Briefly, the fundamental from a femtosecond Ti:Sapphire oscillator amplifier is split

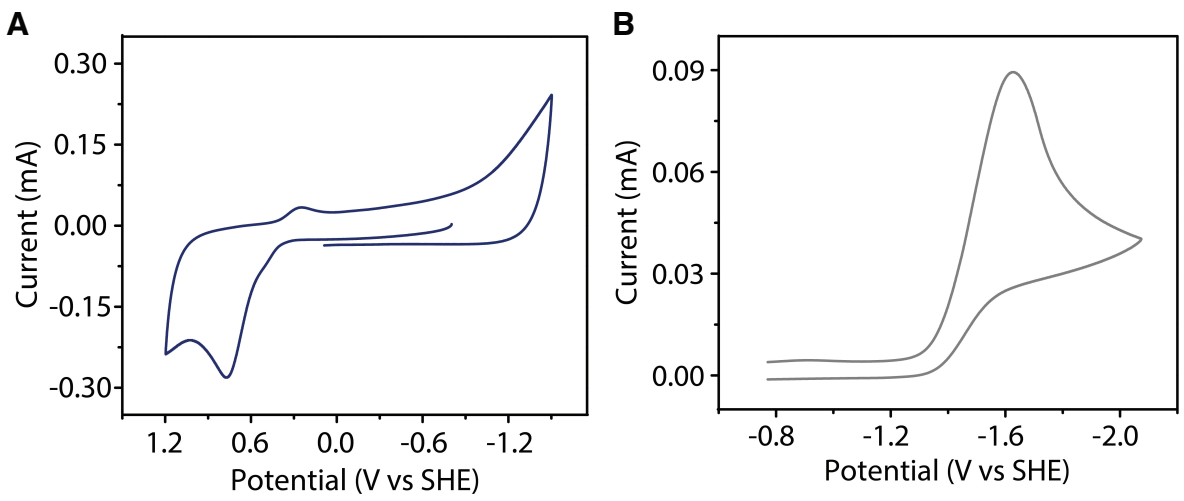

Figure E.4: A) Cyclic voltammograms of $K_{12}Ga_4L_6$ (1 mM) in H_2O with 100 mM K_3PO_4, pH 8.0, variable scan rates, sat. Ag/AgCl reference. B) Cyclic voltammogram of **2b** in DMF, 100 mM $nBuN_4PF_6$, Ferrocene reference, 100 mV/sec scan rate.

into two beams. The actinic pump pulse (400 nm, 460 nJ) was generated through SHG in a 0.4 mm thick Type 1 BBO crystal. The bandwidth of the actinic pump pulse did not warrant further compression. The probe pulse (7 nJ, 50 fs FWHM) was generated through super-continuum generation in a 3-mm thick sapphire window and then compressed with a BK7 prism compressor. The temporal cross-correlation between the actinic pump and the probe pulses was measured to be Gaussian with a width of 172 fs using the optical Kerr effect in water (Fig. E.5). The two pulses were polarized parallel to one another and overlapped spatially and temporally in the sample. The transmitted probe was focused through the slit of a single spectrograph (Spex 500, 600 gr/mm, 500 nm blaze) and the dispersed second-order diffraction was read out at 1 kHz on a front-illuminated CCD (Princeton Instruments, Pixis 100F). The actinic pump was chopped at 250 kHz generating a transient absorption signal in the direction of the probe calculated as

$$\Delta OD = -\log\left(\frac{\text{Transmittance}_{\text{probe, actinic pump on}}}{\text{Transmittance}_{\text{probe, actinic pump off}}}\right) \tag{E.2}$$

Data Analysis

Transient absorption spectra of **1** in H_2O were collected with pulsed 400 nm light excitation. The contour plots for the integrated transient absorption data of **1** and **2b⊂1** are shown in Figure E.6 plotted as change in optical density (OD) versus wavelength over time. Absorption data were collected in 10 nm intervals (150 CCD pixels) and integrated numerically from 530-610 nm. This resulted in eight kinetic decay traces. The decay traces are also plotted individually as absorbance versus time. A global least-squares fitting was performed on all

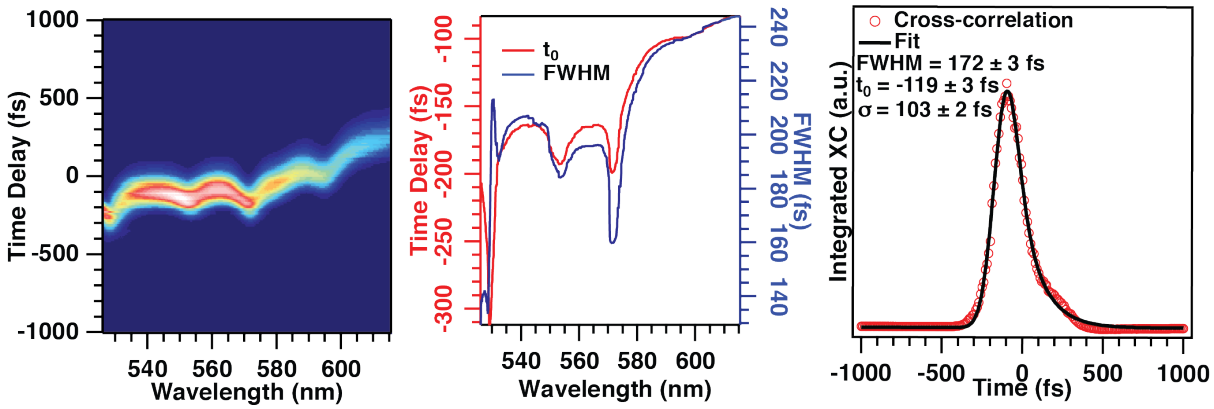

Figure E.5: (Left) Frequency resolved cross-correlation of the probe. The probe signal was gated by the Kerr rotation of the probe interacting with the actinic pump in the aqueous sample. (Middle) Pixel-by-pixel fit parameters to the cross-correlation signal. (Right) Integrated cross-correlation signal over all pixels and Kerr fitting.

decay traces simultaneously. The fitting function was a triple exponential decay convolved numerically with a Gaussian instrument response function of width σ_{IRF} and center t_0.

$$S(t) = \left\{ H(t-t_0) \left(A_1 Exp\left[\frac{t-t_0}{\tau_1}\right] + A_2 Exp\left[\frac{t-t_0}{\tau_2}\right] + A_3 Exp\left[\frac{t-t_0}{\tau_3}\right] \right) \right\} * \frac{1}{\sigma_{IRF}\sqrt{\pi}} Exp\left[\frac{-(t-t_0)}{2\sigma_{IRF}^2}\right] \tag{E.3}$$

H(t-t_0) is a Heaviside step function. Parameters An are the initial amplitudes and τ_n are the time constants of the decays. The parameters t_0 and σ_{IRF} were held fixed to the values measured using the cross correlation. Three time constants, τ_n, were globally fit to all wavelength intervals while the amplitudes, A_n, were fit independently at each wavelength because the signal was assumed to arise from a single excited state population involving dynamically correlated but spectrally unknown features.

The kinetics decays of the excited state absorption of **2b⊂1** were fit by holding the first two time constants (τ_1 and τ_2) fixed to values determined from solvent filled "empty" **1**. The assumption was that encapsulation of the substrate **2b** has a negligible impact on the early time dynamic processes but has a substantial impact on weak coupling processes observed at later times. This assumption seems justified as a high quality fit was found using a minimum number of adjustable parameters (Figure E.6).

The rate of electron transfer from **1** to encapsulated **2b** was estimated by assuming a kinetic model with two competing pathways: electron transfer to a charge transfer state and internal conversion to the ground state (Scheme E.1). The observed excited state decay rate

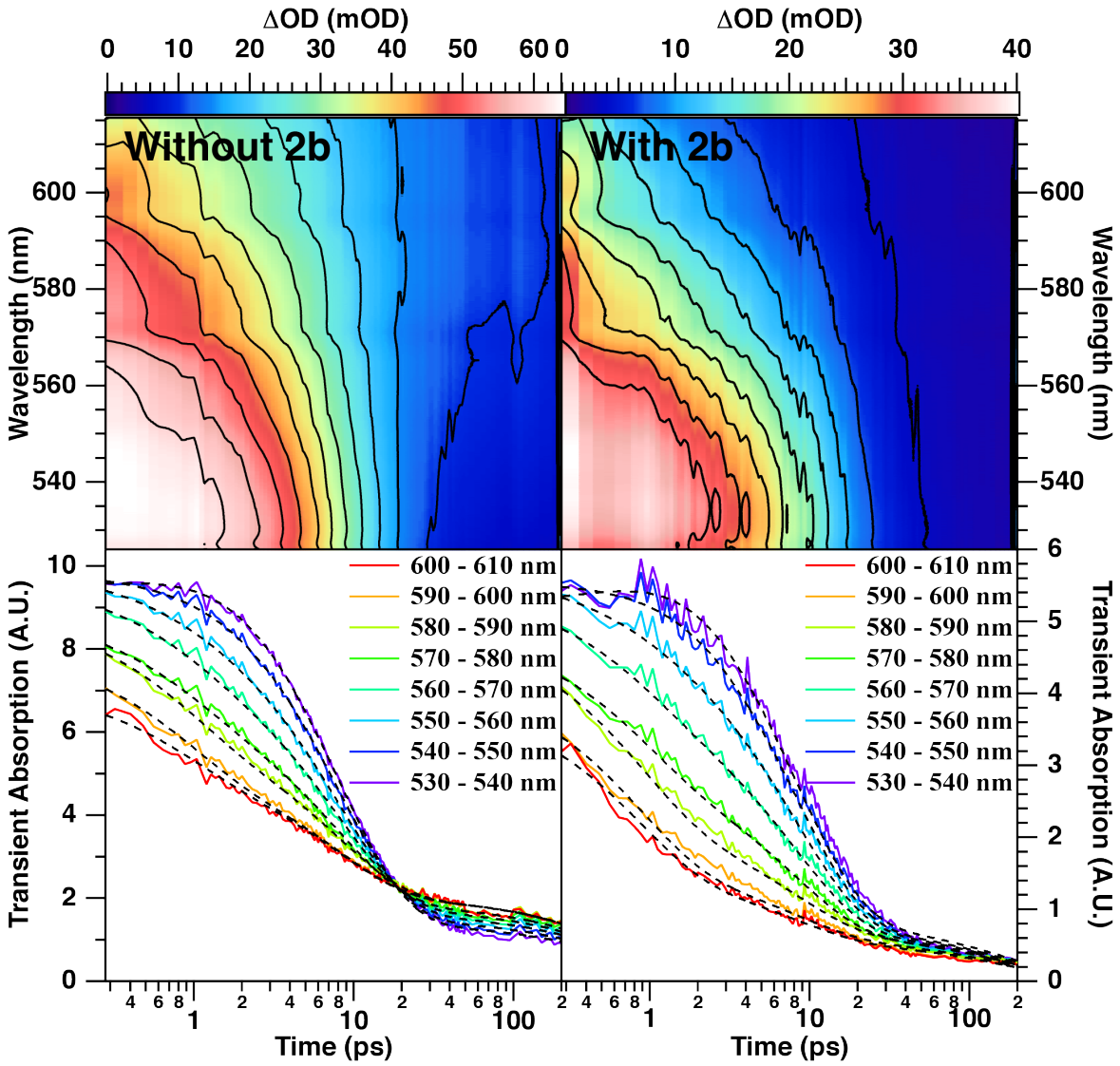

Figure E.6: Comparison of transient absorption signal of $K_{12}Ga_4L_6$ with encapsulation of cinnamylammonium substrate **2b** (right) and without any substrate (left) over the first 200 ps after 400 nm actinic excitation. (bottom) Band integral over each 10-nm range in the TA and the global exponential fits.

with **2b** (k_{obs}) is the sum of the two decay rates (k_3 and k_{ET}). From the rates, the electron transfer quantum yield (Φ_{ET}) can be calculated.

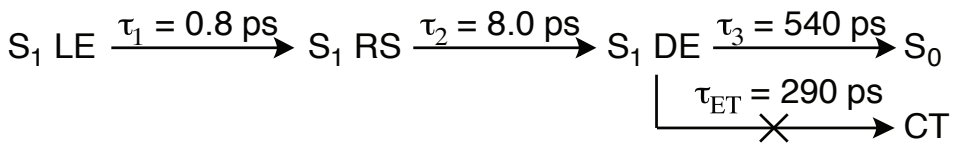

Scheme E.1: Kinetic model for relaxation of **1** after photoexcitation. S_1 LE is the first locally excited singlet state. RS indicates a relaxed solvent state. DE stands for a delocalized excitation state, S_0 is the ground electronic state. CT is a charge transfer state, which is only accessible when a cinnamylammonium substrate is encapsulated.

$$\begin{aligned} k_{ET} &= k_{obs} - k_3 \\ \tau_{ET} &= \frac{\tau_{obs}\tau_2}{\tau_3 - \tau_{obs}} \\ \Phi_{ET} &= \frac{k_{ET}}{k_{obs}} = \frac{\tau_{obs}}{\tau_{ET}} \end{aligned} \tag{E.4}$$

The 95% confidence intervals for the parameters reported were calculated using the Igor Pro least squares fitting software package as described in Numerical Recipes in C.[237] To better determine the uncertainty of the final long time constant, τ_3, once it had been decoupled from the other fit parameters, the first two time constants were held fixed and the global-fitting error analysis was performed again. This resulted in a decrease in the confidence interval, $\delta\tau_3$, by an order of magnitude. The error was then propagated in the following manner.

$$\begin{aligned} \delta\tau_{ET} &= \sqrt{\left(\frac{\partial\tau_{ET}}{\partial\tau_3}\right)^2(\delta\tau_3)^2 + \left(\frac{\partial\tau_{ET}}{\partial\tau_{obs}}\right)^2(\delta\tau_{obs})^2} \\ &= \sqrt{\left(\frac{\tau_{obs}}{\tau_3 - \tau_{obs}} - \frac{\tau_{obs}\tau_3}{(\tau_3 - \tau_{obs})^2}\right)^2(\delta\tau_3)^2 + \left(\frac{\tau_3}{\tau_3 - \tau_{obs}} + \frac{\tau_{obs}\tau_3}{(\tau_3 - \tau_{obs})^2}\right)^2(\delta\tau_3)^2} \\ \delta\Phi_{ET} &= \sqrt{\left(\frac{\partial\Phi_{ET}}{\partial\tau_{obs}}\right)^2(\delta\tau_{obs})^2 + \left(\frac{\partial\Phi_{ET}}{\partial\tau_{ET}}\right)^2(\delta\tau_{ET})^2} \\ &= \sqrt{\left(\frac{1}{\tau_{ET}}\right)^2(\delta\tau_{obs})^2 + \left(\frac{\tau_{obs}^2}{\tau_{ET}^2}\right)^2(\delta\tau_{ET})^2} \end{aligned} \tag{E.5}$$

Results and Discussion

An excited state absorption by **1** and **2b⊂1** appears after excitation with 400 nm light. For both **1** and **2b⊂1** the excited state decays with three time constants as described by eq E.1.

The character of these dynamic excited state processes can be understood by examining the wavelength-separated amplitudes of the global multi-exponential fitting (Fig. E.7).

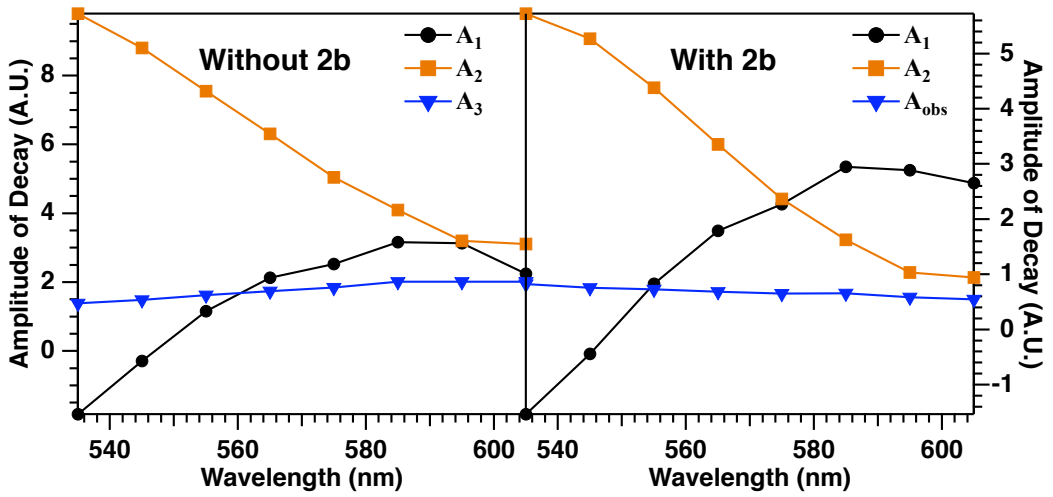

Figure E.7: Amplitude fit parameters, $A_n(\lambda)$, corresponding to transient absorption decay processes τ_n.

As seen in Figure E.7, an absorption feature that is decaying in intensity appears as a positive Gaussian while an absorption feature shifting in wavelength resembles a dispersive Gaussian (i.e. the first derivative of a Gaussian function). The first amplitude component A1, corresponding to $\tau_1 = 0.8 \pm 0.3$ ps, appears as a dispersive Gaussian, with a negative amplitude in the region blue of 545 nm. This can be interpreted as a blue shift of the excited state absorption as the blue part of the spectrum is actually gaining intensity while the red part is losing intensity. This 0.8 ps blue shift is the result of an increase in the $S_1 \rightarrow S_n$ transition energy as the S_1 is stabilized by water solvation. The same stabilization process that causes an increase in the $S_1 \rightarrow S_n$ transition energy also results in a decrease in the $S_1 \rightarrow S_0$ transition energy; therefore, dipole correlation time constants have been most commonly measured as a red shift in time-resolved fluorescence up-conversion experiments. In Barbara et al. (1988), a red shift of the fluorescence band was observed with two time constants of 0.16 ps and 1.2 ps.[229] The authors note however that if a single time constant was used in the analysis they find a time constant of 0.86 ps for the redshift. It is reasonable to assume that in our transient absorption measurement there is a faster component to the blue shift that is not resolved by the 170 fs time resolution of the instrument response. The second component of the transient absorption decay corresponding to $\tau_2 = 8.0 \pm 0.8$ ps appears as a large Gaussian feature with a maximum blue of the probe window. This decays in intensity is likely the result of rapid energy transfer between the six ligands of the tetrahedral cluster. Resonance energy transfer processes can occurs on time scales varying from less than 100 fs to greater than 1 ns. The rate of energy transfer depends on the molecular separation distance R_{DA}, the overlap integral of the absorption and fluorescence

bands J_{DA}, the dot product of the transition dipoles κ, the fluorescence quantum yield ϕ_D, and the fluorescence emission lifetime τ_D.[230a]

$$\frac{1}{\tau_{RET}} = \frac{9.76^{-26}\kappa^2 J_{DA}\phi_D}{\tau_D |R_{DA}|^6} \tag{E.6}$$

The light selectively excites to a singlet state where ligands are selected that have their transition dipoles oriented in the direction of the pump electric field. Through resonance energy transfer (Förster) the excitation then migrates such that it is evenly distributed among the six ligands at which point the transition dipoles are nearly isotropically oriented with respect to the initial excitation. To test this hypothesis we measured the fluorescence anisotropy of $K_{12}Ga_4L_6$ in water (λ_{EX} = 375 nm, λ_{EM} = 485 - 545 nm). If no rapid energy transfer occurs between the ligands, the anisotropy should decay with the rotational correlation time constant θ that can be approximated from a Stokes-Einstein radius calculation.[238]

$$\theta = \frac{\eta M V}{RT} \tag{E.7}$$

Where η is the viscosity. M is the molecular weight. V is the specific density. R is the gas constant and T is temperature. Taking the molecular weight of the cluster as 3300 g/mol and the specific volume to be 1 ml/g we find that the rotational correlation time constant is 1.2 ns. The steady state anisotropy, r, can then be calculated according to the following equation:

$$r = \frac{r_0}{1 + \tau_3/\theta} \tag{E.8}$$

Taking r_0 to be 0.4 and τ_3 to be 540 ps we find that the expected anisotropy to be r $\approx$ 0.28. However, with 375 nm excitation we measured an anisotropy of less than 0.05 suggesting that the transition dipole reorients on a timescale much faster than molecular rotation due to fast intramolecular energy transfer. In the final step of the excited state decay, a very broad absorption feature is observed to decay with a time-constant of τ_3 = 540 $\pm$ 40 ps. Although this process is not resolved fully within the time delay of the experiment, which is limited physically to 200 ps, a very clear slope is observed in the excited state decay both with and without inclusion of **2b**. This process shows the final relaxation out of S_1 and the disappearance of the excited state absorption signal.

The transient absorption signals with and without encapsulation of substrate **2b** are similar. The greatest discrepancy between the two signals is apparent in the final relaxation step. In the presence of cinnamylammonium substrate **2b** the excited state is quenched with τ_{obs} = 190 $\pm$ 60 ps. This substantial increase in the rate of decays suggest that the S_1 state efficiently couples into a charge transfer state with a time constant of τ_{ET} = 290 $\pm$ 150 ps and a quantum yield of quantum yield of Φ_{ET} = 0.65 $\pm$ 0.34. A comparison of the estimated electron transfer quantum yield with the reaction quantum yield $\Phi_{R\text{-}\mathbf{2b}}$ = 0.01 $\pm$ 0.007 suggests that once the charge transfer state has formed the rate of radical

recombination significantly outpaces the rate of the 1,3-rearrangement resulting in a marked decrease in reactivity and stored energy.

E.7 Pre-resonance Raman Spectroscopy

Materials and Methods

Solutions of 7×10^{-4} M naphthalene biscatecholamide ligand were prepared under nitrogen in a solution of potassium methoxide and methanol to stabilize the tetra-anionic basic structure most relevant to the supramolecular cage assembly. Additionally, solutions of 7×10^{-4} M of **1** and **2b⊂1** were prepared in methanol with an optical density of 0.15 at 413.1 nm per pathlength. Solutions were flowed through a capillary tube (I.D. = 1.5 mm) at a rate of 2 m/s and kept under a positive pressure of nitrogen gas. Samples were irradiated with 70 mW of 413.1 nm light focused to a spot less than 0.5 mm diameter and the signal was collected in the standard 90° scattering geometry. Spectra were read out on a liquid-nitrogen-cooled CCD (Roper Scientific, LN/CCD 1100).

Results and Discussion

To gain insight in to the vibrational and electronic structure of **1** we investigated the pre-resonance Raman spectra of three important constituents to the cluster in solutions of methanol: the naphthalene biscatecholamide ligand alone uncomplexed to gallium, and **1** with and without **2b**. The highly polarizable poly-anionic ligand and cluster afforded strong scattering intensity, which could easily be resolved over the weak fluorescence background.

Figure E.8 presents pre-resonance Raman spectra of the three constituents with 413.1 nm laser excitation at the red-edge of the lowest energy absorption band. The three spectra are very similar except for a few minor peak shift and changes in intensity. This similarity supports the idea that the tetraanionic form of the naphthalene biscatecholamide ligand is the relevant structure in the cage. Neither coordination with the gallium nor coupling between the ligand residues greatly perturbs the electronic or vibrational structure of ligand. Furthermore the similarity between spectra suggests weak electronic coupling between ligands and that the initial excitation has $\pi \rightarrow \pi*$ character localized on a single ligand residue and does not involve a collective excitation of all six ligands.

Notable changes in peak frequencies and the appearance of new peaks indicate important structural changes, which accompany the formation of the cluster. The vibrational character of these frequencies can be assigned by comparison with the Raman spectrum of naphthalene biscatecholamide ligand calculated from theory. The comparison between theory and measured Raman spectra is presented in Figure E.9. Most vibrations in the measured spectrum can be mapped onto Raman active vibrations with little ambiguity. The intensities of the calculated peaks only off-resonance polarizability and therefore only show weak congruence with the measured intensities. The following analysis focuses on the most robust changes in

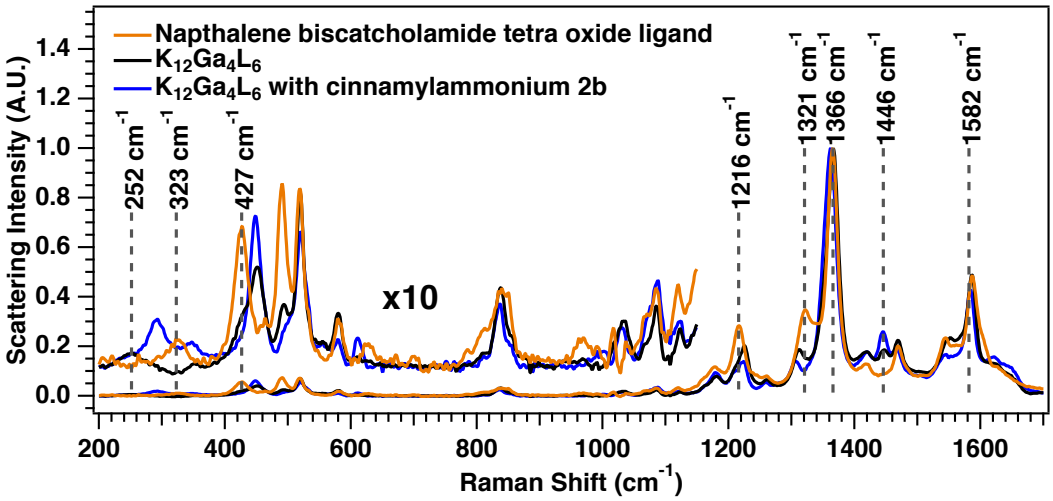

Figure E.8: Comparison of three pre-resonance Raman spectra excited with 413.1 nm light. Yellow is the naphthalene biscatecholamide ligand stabilized as a tetranionic base in potassium methoxide. Black is **1** in methanol. Blue is **2b⊂1** in methanol. The low frequency region has been amplified by a factor of 10. The contribution of the methanol Raman scattering and the fluorescence baseline have been subtracted for clarity.

the spectroscopic signals to gain a heuristic insight into the solution phase structure of the cluster.

When the ligand coordinates with the gallium forming **1**, the following spectroscopic changes occur: A new peak at 252 cm^{-1} appears which presumably involves Ga-O stretching character (Figure E.8). The peak at 323 cm^{-1} corresponding to in-plane bending of the catecholate oxygens blue shifts to 352 cm^{-1} as restoring force of this motion is strengthened by complexation with the gallium. The peak at 427 cm^{-1} corresponding to in plane distortion along the (O=CC)-(C-O-) angle blue shifts to 452 cm^{-1}. The peak at 1216 cm^{-1} corresponding to OC-NH stretching blue shifts to 1225 cm^{-1}. The peak at 1321 cm^{-1} corresponding to aromatic distortion on the catecholate redshifts to 1312 cm^{-1}. Finally a new peak appears at 1446 cm^{-1} which we propose may be an asymmetric C=O stretch which becomes Raman active as the ligand vibrations couple in the higher dimensional tetrahedral symmetry. These results are consistent with a breaking of aromaticity as the molecule distorts along the OC-C-CO dihedral angle of the catechol groups.

The Raman scattering from the cinnamylammonium substrate **2b** was too weak to be observed at the concentration employed because the excitation wavelength is far removed from its resonance. Thus the spectra presented above shows only spectroscopic changes in **1** indirectly induced by encapsulation of **2b** and not signals from **2b** itself. Assignment of vibrational mode character is made difficult because the **1** is too large to be modeled from density functional theory, however; a qualitative understanding of the vibrational character can be deduced by comparison with the ligand spectrum. Encapsulation of **2b** is accompanied a red shift of three pronounced peaks at 1317, 1366, and 1586 cm^{-1} to resultant

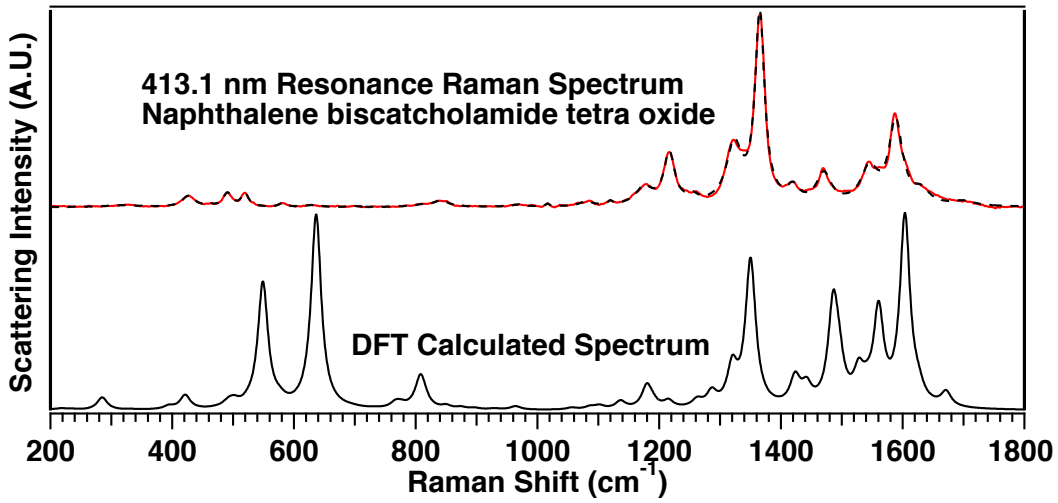

Figure E.9: Comparison of measured resonance Raman spectrum of naphthalene biscatecholamide ligand with the spectrum calculated from theory. The black dashed line is a least squares fit result of 24 Lorentzian functions to the measured data (red). The calculated peaks are represented by Lorentzians with a full width half maximum of 20 cm^{-1} in agreement with the average peak width of the measured spectrum. The frequencies and intensities have not been scaled.

frequencies of 1312, 1364 and 1582 cm^{-1} respectively. The vibrational character of these three modes is dominated by stretching of the catecholate and naphthalene rings. Additionally a new peak at 293 cm^{-1} is observed with unknown character. These results are consistent with a weakening the pi-bond strength when **2b** is introduced to the cavity.

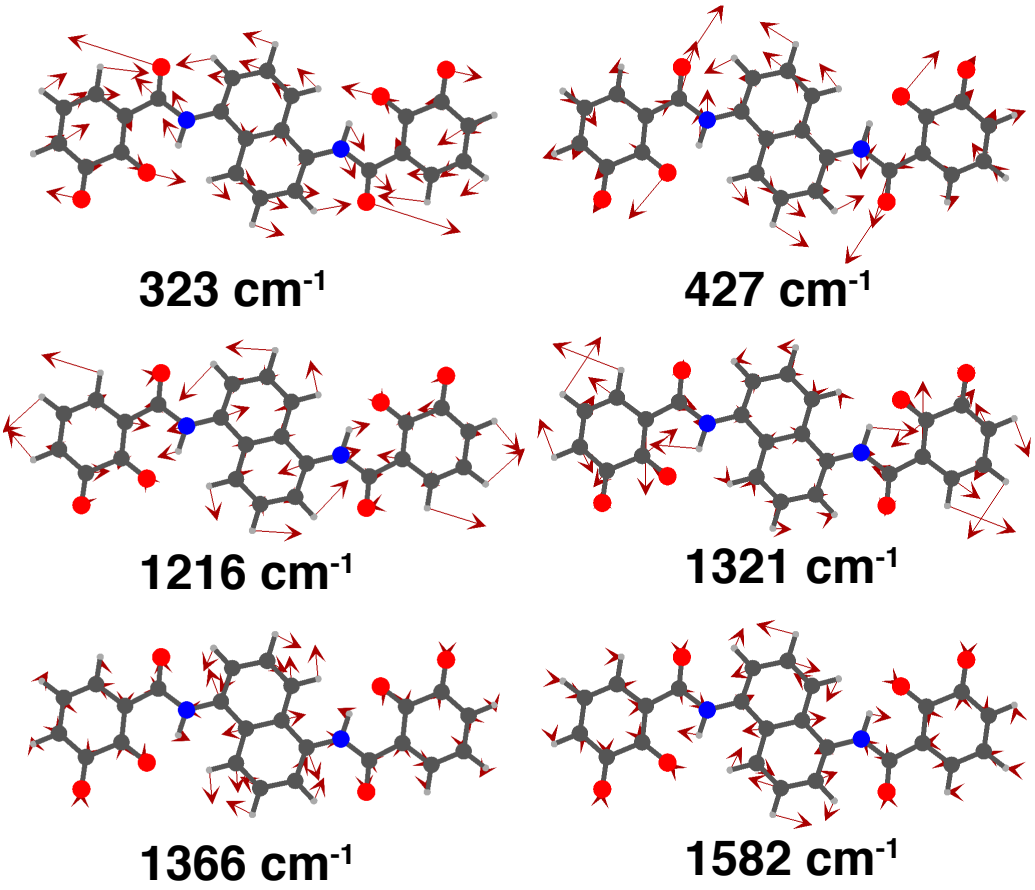

Figure E.10: Approximate mode character of six Raman active modes of naphthalene biscatecholamide ligand tetranionic base.

Appendix F

Derivation of Transition Polarizability

This derivation follows from Ref. [239], [240], [241].

The transition moment can be expanded leading to induced polarization terms of the form:

$$\begin{aligned}(p)_{ki} &= (p^{(0)})_{ki} + (p^{(1)})_{ki} + (p^{(2)})_{ki} + ... \\ &= (... + \langle\Psi_k^{(1)}| + \langle\Psi_k^{(0)}|)|\hat{M}|(|\Psi_i^{(0)}\rangle + |\Psi_i^{(1)}\rangle + ...) \\ &= \left\langle \Psi_k^{(0)} \middle| \hat{M} \middle| \Psi_i^{(0)} \right\rangle + \left\langle \Psi_k^{(1)} \middle| \hat{M} \middle| \Psi_i^{(0)} \right\rangle + \left\langle \Psi_k^{(0)} \middle| \hat{M} \middle| \Psi_i^{(1)} \right\rangle + \left\langle \Psi_k^{(1)} \middle| \hat{M} \middle| \Psi_i^{(1)} \right\rangle + ...\end{aligned} \tag{F.1}$$

$(p^{(0)})_{ki} = \langle\psi_k|\hat{\mu}|\psi_i\rangle$ describes a direct transition between unperturbed states i.e. an absorption event. The term $\langle\Psi_k^{(1)}|\hat{\mu}|\Psi_i^{(1)}\rangle$ falls in with $(p^{(2)})_{ki}$ which describes higher order terms like hyper-Raman and hyper-Rayleigh scattering. Linear Rayleigh and Raman scattering is described by $(p^{(1)})_{ki}$ for $k = i$ and $k = f$ respectively.

The time-dependent Schrödinger equation is:

$$(H^0 - i\hbar\frac{\partial}{\partial t})|\Psi_k^{(0)}(t)\rangle = 0 \tag{F.2}$$

The general solution is:

$$|\Psi_k^{(0)}\rangle = \sum_r b_r|\psi_r\rangle e^{-i\omega_r t} \tag{F.3}$$

If the system is in unperturbed state k or i then the solutions are:

$$|\Psi_k^{(0)}\rangle = |\psi_k\rangle e^{-i\omega_k t} \tag{F.4}$$

$$|\Psi_i^{(0)}\rangle = |\psi_i\rangle e^{-i\omega_i t} \quad . \tag{F.5}$$

The light field that is our perturbation has the form

$$H^1 = \widetilde{E}^* \hat{M} e^{i\omega_0 t} + \widetilde{E}\hat{M}e^{-i\omega_0 t} \tag{F.6}$$

Where $\widetilde{E}$ is a complex vector corresponding to the electric field and $\hat{M}$ is the transition dipole operator with elements $m_{ri} = \langle\psi_r|\mu|\psi_i\rangle$

$$(H^0 - H^1 - i\hbar\frac{\partial}{\partial t})|\Psi^{(0)}\rangle = 0 \tag{F.7}$$

$$|\Psi\rangle = |\Psi_k^{(0)}\rangle + |\Psi_k^{(1)}\rangle \tag{F.8}$$

$$(H^0 - i\hbar\frac{\partial}{\partial t})|\Psi^{(1)}(t)\rangle = H^1|\Psi_k^{(0)}(t)\rangle \tag{F.9}$$

Guess the solution of the form:

$$|\Psi_k^{(1)}(t)\rangle = |\psi_k^+\rangle e^{-i(\omega_k+\omega_0)t} + |\psi_k^-\rangle e^{-i(\omega_k-\omega_0)t} \tag{F.10}$$

Insert F.10 and F.4 into F.9.

$$\begin{aligned}
&(H^0 - i\hbar\frac{\partial}{\partial t})\left(|\psi_k^+\rangle e^{-i(\omega_k+\omega_0)t} + |\psi_k^-\rangle e^{-i(\omega_k-\omega_0)t}\right) \\
&= \widetilde{E}\hat{M}e^{-i\omega_0 t}e^{-i\omega_k t}|\psi_k\rangle + \widetilde{E}^*\hat{M}e^{i\omega_0 t}e^{-i\omega_k t}|\psi_k\rangle
\end{aligned}$$

$$\begin{aligned}
&H^0|\psi_k^+\rangle e^{-i(\omega_k+\omega_0)t} - \hbar(\omega_k+\omega_0)|\psi_k^+\rangle e^{-i(\omega_k+\omega_0)t} \\
&+H^0|\psi_k^-\rangle e^{-i(\omega_k-\omega_0)t} - \hbar(\omega_k-\omega_0)|\psi_k^-\rangle e^{-i(\omega_k-\omega_0)t} \\
&= \widetilde{E}\hat{M}e^{-i(\omega_k+\omega_0)t}|\psi_k\rangle + \widetilde{E}^*\hat{M}e^{-i(\omega_k-\omega_0)t}|\psi_k\rangle
\end{aligned}$$

Each time-dependent portion must also be equal.

$$H^0|\psi_k^+\rangle - \hbar(\omega_k+\omega_0)|\psi_k^+\rangle = \widetilde{E}\hat{M}|\psi_k\rangle$$

$$H^0|\psi_k^-\rangle - \hbar(\omega_k-\omega_0)|\psi_k^-\rangle = \widetilde{E}^*\hat{M}|\psi_k\rangle$$

Consider F.3 and apply the completeness relation $\sum_r |\psi_r\rangle\langle\psi_r| = \mathbf{1}$ to the left of $|\psi_k\rangle$.

$$(H^0 - \hbar(\omega_k+\omega_0))|\psi_k^+\rangle = \widetilde{E}\sum_r |\psi_r\rangle\langle\psi_r|\hat{\mu}|\psi_k\rangle$$

$$(H^0 - \hbar(\omega_k-\omega_0))|\psi_k^-\rangle = \widetilde{E}^*\sum_r |\psi_r\rangle\langle\psi_r|\hat{\mu}|\psi_k\rangle$$

The time-independent Schrödinger equation is true for any unperturbed eigenstate of H^0. The Hamiltonian can be evaluated if included in the sum over r.

$$H^0|\psi_r\rangle = \hbar\omega_r|\psi_r\rangle$$

Solve for $|\psi_k^+\rangle$ and $|\psi_k^-\rangle$ and insert into F.10. Let $\omega_{rk} = \omega_r - \omega_k$.

$$|\Psi_k^{(1)}(t)\rangle = \frac{1}{\hbar}\sum_r \left[\frac{|\psi_r\rangle\langle\psi_r|\hat{\mu}|\psi_k\rangle}{\omega_{rk}-\omega_0}\widetilde{E}e^{-i(\omega_k+\omega_0)t} + \frac{|\psi_r\rangle\langle\psi_r|\hat{\mu}|\psi_k\rangle}{\omega_{rk}+\omega_0}\widetilde{E}^*e^{-i(\omega_k-\omega_0)t}\right] \tag{F.11}$$

And the complex conjugate.

$$\langle\Psi_k^{(1)}(t)| = \frac{1}{\hbar}\sum_r \left[\frac{\langle\psi_k|\hat{\mu}|\psi_r\rangle\langle\psi_r|}{\omega_{rk}-\omega_0}\widetilde{E}^*e^{i(\omega_k+\omega_0)t} + \frac{\langle\psi_k|\hat{\mu}|\psi_r\rangle\langle\psi_r|}{\omega_{rk}+\omega_0}\widetilde{E}e^{i(\omega_k-\omega_0)t}\right]$$

We can finally calculate the induced polarization. Insert F.11, F.5 and F.5 into F.2. Let $\omega_{ki} = \omega_n - \omega_i$.

$$
\begin{aligned}
(p^{(1)})_{ki} & \\
&= \left\langle \Psi_k^{(1)} \left| \hat{\mu} \right| \Psi_i^{(0)} \right\rangle + \left\langle \Psi_k^{(0)} \left| \hat{\mu} \right| \Psi_i^{(1)} \right\rangle \\
&= \frac{1}{\hbar} \sum_r \frac{\langle \psi_k | \hat{\mu} | \psi_r \rangle \langle \psi_r | \hat{\mu} | \psi_i \rangle}{\omega_{ri} - \omega_0 - i\Gamma_r} \widetilde{E} e^{-i(\omega_0 - \omega_{ki})t} \\
&+ \frac{1}{\hbar} \sum_r \frac{\langle \psi_k | \hat{\mu} | \psi_r \rangle \langle \psi_r | \hat{\mu} | \psi_i \rangle}{\omega_{ri} + \omega_0 + i\Gamma_r} \widetilde{E}^* e^{i(\omega_0 + \omega_{ki})t} \\
&+ \frac{1}{\hbar} \sum_r \frac{\langle \psi_k | \hat{\mu} | \psi_r \rangle \langle \psi_r | \hat{\mu} | \psi_i \rangle}{\omega_{rk} - \omega_0 - i\Gamma_r} \widetilde{E}^* e^{i(\omega_0 + \omega_{ki})t} \\
&+ \frac{1}{\hbar} \sum_r \frac{\langle \psi_k | \hat{\mu} | \psi_r \rangle \langle \psi_r | \hat{\mu} | \psi_i \rangle}{\omega_{rk} + \omega_0 + i\Gamma_r} \widetilde{E} e^{-i(\omega_0 - \omega_{ki})t} \\
&= \boldsymbol{\alpha_{ki} E}
\end{aligned}
\tag{F.12}
$$

We have phenomenologically introduced term $i\Gamma_r$ to the resonant denominator corresponding to the lifetime or dephasing of states $|\psi_r\rangle$. The terms $\widetilde{E}^* e^{i(\omega_0 - \omega_{ki})t}$ and $\widetilde{E} e^{i(\omega_0 + \omega_{ki})t}$ correspond to an oscillating electric fields. If $k = i$ then the scattered frequency is the same as the initial frequency corresponding to Rayleigh scattering. If $k \neq f$ this term describes a Raman transition. Raman scattering with a frequency of $\omega_0 + \omega_{ki}$ is an induced emission of two quanta of energy and not observed in most practical situations. Oscillating terms of this frequency will not be considered further here. If $\omega_{fi} > 0$ the transition is called a Stokes Raman scattering. When $\omega_{fi} < 0$ the transition corresponds to an anti-Stokes Raman transition. In F.12 we have introduced the Raman transition polarizability α_{ki} as the time-independent part of the induced polarization that determines the Raman transition probability and therefore the scattering intensity.

$$
I_{ki} = |(\alpha)_{ki}|^2 = \left| \frac{1}{\hbar} \sum_r \left[\frac{\langle \psi_k | \hat{\mu} | \psi_r \rangle \langle \psi_r | \hat{\mu} | \psi_i \rangle}{\omega_{ri} + \omega_0 - i\Gamma_r} + \frac{\langle \psi_k | \hat{\mu} | \psi_r \rangle \langle \psi_r | \hat{\mu} | \psi_i \rangle}{\omega_{rk} - \omega_0 + i\Gamma_r} \right] \right|^2 \tag{F.13}
$$

Resonant Denominator

Under most normal circumstances the transition frequencies ω_{ri} and ω_{rk} are positive. As the light frequency ω_0 approaches an absorption band with transition frequency ω_{rk} the denominator of the second term $\omega_{rk} - \omega_0 - i\Gamma_r$ becomes small and the transition polarizability becomes large. A resonance enhancement of 10^6 can be observed. If the initial state is an excited state the incident light can also be resonant with a stimulated emission band. In such a case ω_{ri} is negative. In this case the first term with a sum in the denominator

dominates the transition polarizability and a similar resonance enhancement is observed as with absorption.

Appendix G

Herzberg-Teller Vibronic Coupling and the Albretch A,B,C,D terms

This is an abridged derivation of vibronic coupling which is described with more detail in [242], [243], and [239].

Using many zeroth order approximations, states $|\psi_k\rangle$ can be expressed as a product of the electronic, vibrational, rotational and spin wave functions.

$$|\psi_k\rangle = |e\rangle|\nu\rangle|r\rangle|s\rangle \tag{G.1}$$

The wave functions are separable as presented here only if there are no cross-terms in the overall Hamiltonian $\hat{\boldsymbol{H}} = \hat{H}_e + \hat{H}_\nu + \hat{H}_r + \hat{H}_s$. For example the electronic and spin wave functions can be separated if spin-orbit coupling is neglected. The vibrational and rotational wave functions can be separated in the absence of a centrifugal distortion. The electronic and vibrational wave function can be separated in the absence of vibronic coupling, if the electronic potential energy surfaces do not depend on nuclear coordinate. This section focus on the first order correction to the treatment of vibronic coupling and shows how vibronic coupling can elicits very complicated Raman transitions. To treat vibronic coupling analytically consider that the vibration along coordinates Q_m act as a perturbation of the electronic wavefunction which is a solution to the unperturbed Hamiltonian H_e^0 at equilibrium nuclear geometry Q_0. The perturbative Taylor series expansion is:

$$\hat{H}_e^m(Q) = (\hat{H}_e)_0 + \sum_m \left(\frac{\partial \hat{H}_e}{\partial Q_m})\right) Q_m + \sum_{mn} \left(\frac{\partial^2 \hat{H}_e}{\partial Q_m \partial Q_n})\right) Q_m Q_n + ... \tag{G.2}$$

The electronic wave function can now be separated from the vibrational wave function. Truncating the expansion at the first order, a distortion along vibration Q_m mixes the electronic state $|e^r\rangle$ with all the other electronic states $|e^s\rangle$

$$|\psi_{r'}\rangle = |e^{r'}\rangle|\nu^r\rangle = \left(|e^r\rangle + \frac{1}{\hbar}\sum_{e^s \neq e^r}\sum_m \frac{h_{sr}^m}{\omega_r - \omega_s}|e^s\rangle Q_m\right)|\nu^r\rangle \tag{G.3}$$

$$h_{sr}^m = \langle e^s|\frac{\partial \hat{H}_e}{\partial Q_m}|e^r\rangle \tag{G.4}$$

The matrix element h_{sr} determines the strength of vibronic coupling by coordinate Q_m. The denominator $\omega_r - \omega_s$ indicates that excited states that are energetically close together can be more strongly mixed. The perturbed vibronic wave function can inserted into each one photon transition moments from F.13.

$$\begin{aligned}&\langle\psi_{k'}|\mu|\psi_{r'}\rangle \\ &= \langle\nu^k|\left(\langle e^k| + \frac{1}{\hbar}\sum_{e^t \neq e^k}\sum_m \frac{h_{kt}^m Q_m}{\omega_r - \omega_t}\langle e^t|\right)\mu\left(|e^r\rangle + \frac{1}{\hbar}\sum_{e^s \neq e^r}\sum_m \frac{h_{sr}^m Q_m}{\omega_r - \omega_s}|e^s\rangle\right)|\nu^r\rangle\end{aligned} \tag{G.5}$$

Inserting G.5 into F.13 and then expanding we then sort the terms by their order with respect to Q. The first order terms are further separated into those where the vibronic coupling matrix element mixes the initial and final states ($|e^i\rangle$ and $|e^i\rangle$) and those where the matrix element mixes the intermediate state $|e^r\rangle$. Let matrix element $\mu_{ri} = \langle e^r|\mu|e^i\rangle$. As the electronic and vibrational wave functions have been separated the sum must run over both ν^r and e^r.

$$\alpha_{if} = A + B + C + D \tag{G.6}$$

$$A = \frac{1}{\hbar}\sum_{\nu^r,e^r}\left\{\frac{\mu_{e^f e^r}\mu_{e^r e^i}}{\omega_{e^r\nu^r} - \omega_{e^i\nu^i} - \omega_0 - i\Gamma_{e^r\nu^r}} + \frac{\mu_{e^f e^r}\mu_{e^r e^i}}{\omega_{e^r\nu^r} - \omega_{e^f\nu^f} + \omega_0 + i\Gamma_{e^r\nu^r}}\right\}\langle\nu^f|\nu^r\rangle\langle\nu^r|\nu^i\rangle \tag{G.7}$$

$$\begin{aligned} B = \frac{1}{\hbar^2}\sum_{\nu^r,e^r}\sum_{e^s\neq e^r}\sum_m \Bigg\{&\frac{\mu_{e^f e^s}\mu_{e^r e^i}}{\omega_{e^r\nu^r} - \omega_{e^i\nu^i} - \omega_0 - i\Gamma_{e^r\nu^r}} \\ &+\frac{\mu_{e^f e^s}\mu_{e^r e^i}}{\omega_{e^r\nu^r} - \omega_{e^f\nu^f} + \omega_0 + i\Gamma_{e^r\nu^r}}\Bigg\}\frac{h^m_{sr}}{\omega_{e^r} - \omega_{e^s}}\langle\nu^f|Q_m|\nu^r\rangle\langle\nu^r|\nu^i\rangle \\ +\frac{1}{\hbar^2}\sum_{\nu^r,e^r}\sum_{e^s\neq e^r}\sum_m \Bigg\{&\frac{\mu_{e^f e^r}\mu_{e^s e^i}}{\omega_{e^r\nu^r} - \omega_{e^i\nu^i} - \omega_0 - i\Gamma_{e^r\nu^r}} \\ &+\frac{\mu_{e^f e^r}\mu_{e^s e^i}}{\omega_{e^r\nu^r} - \omega_{e^f\nu^f} + \omega_0 + i\Gamma_{e^r\nu^r}}\Bigg\}\frac{h^m_{rs}}{\omega_{e^r} - \omega_{e^s}}\langle\nu^f|\nu^r\rangle\langle\nu^r|Q_m|\nu^i\rangle \end{aligned} \tag{G.8}$$

$$\begin{aligned} C = \frac{1}{\hbar^2}\sum_{\nu^r,e^r}\sum_{e^t\neq e^i,e^f}\sum_m \Bigg\{&\frac{\mu_{e^t e^r}\mu_{e^r e^i}}{\omega_{e^r\nu^r} - \omega_{e^i\nu^i} - \omega_0 - i\Gamma_{e^r\nu^r}} \\ &+\frac{\mu_{e^t e^r}\mu_{e^r e^i}}{\omega_{e^r\nu^r} - \omega_{e^f\nu^f} + \omega_0 + i\Gamma_{e^r\nu^r}}\Bigg\}\frac{h^m_{ft}}{\omega_{e^r} - \omega_{e^s}}\langle\nu^f|Q_m|\nu^r\rangle\langle\nu^r|\nu^i\rangle \\ +\frac{1}{\hbar^2}\sum_{\nu^r,e^r}\sum_{e^s\neq e^r}\sum_m \Bigg\{&\frac{\mu_{e^f e^r}\mu_{e^r e^t}}{\omega_{e^r\nu^r} - \omega_{e^i\nu^i} - \omega_0 - i\Gamma_{e^r\nu^r}} \\ &+\frac{\mu_{e^f e^r}\mu_{e^r e^t}}{\omega_{e^r\nu^r} - \omega_{e^f\nu^f} + \omega_0 + i\Gamma_{e^r\nu^r}}\Bigg\}\frac{h^m_{ti}}{\omega_{e^i} - \omega_{e^t}}\langle\nu^f|\nu^r\rangle\langle\nu^r|Q_m|\nu^i\rangle \end{aligned} \tag{G.9}$$

$$D = \frac{1}{\hbar^3} \sum_{\nu^r, e^r e^t, e^s \neq e^r} \sum_{m,n} \sum$$

$$\left\{ \frac{\mu_{e^f e^s} \mu_{e^t e^i}}{\omega_{e^r \nu^r} - \omega_{e^i \nu^i} - \omega_0 - i\Gamma_{e^r \nu^r}} \left(\frac{h^m_{rt}}{\omega_{e^r} - \omega_{e^t}} \right) \left(\frac{h^m_{sr}}{\omega_{e^r} - \omega_{e^s}} \right) \langle \nu^f | Q_m | \nu^r \rangle \langle \nu^r | Q_n | \nu^i \rangle \right. \tag{G.10}$$

$$\left. + \frac{\mu_{e^f e^t} \mu_{e^s e^i}}{\omega_{e^r \nu^r} - \omega_{e^f \nu^f} + \omega_0 + i\Gamma_{e^r \nu^r}} \left(\frac{h^m_{tr}}{\omega_{e^r} - \omega_{e^t}} \right) \left(\frac{h^m_{rs}}{\omega_{e^r} - \omega_{e^s}} \right) \langle \nu^f | Q_n | \nu^r \rangle \langle \nu^r | Q_m | \nu^i \rangle \right\}$$

Note that in all of these expressions the resonance is with the states $|e^r\rangle$ but the overall transition can be through other states $|e^s\rangle$ or $|e^t\rangle$ especially if these other states have similar energy to $|e^r\rangle$. The A term describes normal Resonance Raman scattering. The values $\langle \nu^r | \nu^i \rangle$ are Frank-condon factors which increase with the displacement of the e^r and e^i potential energy surfaces (see Appendix X). The A-term has no vibronic coupling term h^n_{rs}. The states are coupled directly by allowed transition dipoles. The B-term describes a Raman transition through two different allowed transition dipoles with vibronic coupling between electronic states. The C-term is peculair. It describes vibronic coupling between the initial final states and a transient state. The D-term describes a "resonant" Raman transition through a purely dipole forbidden state (μ_{ri} and μ_{fr} both are zero). The initial state projects up through a different transition dipole μ_{si}. vibronic coupling occurs to state $|e^r\rangle$ and then vibronic coupling occurs again to another optically active state. The transition is the projected down the the final state through a second transition dipole. The second transition dipole can be but is not necessarily the same as the complex conjugate of the first transition dipole ($\mu_{si} =_n \mu_{ft}* = \mu_{tf}$ if $|e^i\rangle = |e^f\rangle$ and $|e^s\rangle = |e^t\rangle$).

Bibliography

(1) Myers, A. B.; Mathies, R. A., *Biological Application of Raman Spectroscopy Spiro Vol 2: Resonance Raman Spectra of Polyenes and Aromatics*; Spiro, T. G., Ed.; John Wiley & Sons: New York, 1987, pp 1–58.

(2) McHale, J. L. In *Handbook of Vibrational Spectroscopy*; John Wiley & Sons, Ltd: 2006.

(3) McHale, J. L., *Molecular Spectroscopy*; Taylor & Francis, Group: 2017.

(4) Dietze, D. R., *rraman*; https://github.com/ddietze/FSRStools (accessed Feb 6, 2015).

(5) Ginsberg, N. S.; Cheng, Y.-C.; Fleming, G. R. *Accounts of chemical research* **2009**, *42*, 1352–1363.

(6) Courtney, T. L.; Fox, Z. W.; Estergreen, L.; Khalil, M. *The Journal of Physical Chemistry Letters* **2015**, *6*, PMID: 26262989, 1286–1292.

(7) Lewis, N. H. C.; Gruenke, N. L.; Oliver, T. A. A.; Ballottari, M.; Bassi, R.; Fleming, G. R. *The Journal of Physical Chemistry Letters* **2016**, *7*, 4197–4206.

(8) Hill, A. D.; Zoerb, M. C.; Nguyen, S. C.; Lomont, J. P.; Bowring, M. A.; Harris, C. B. *The Journal of Physical Chemistry B* **2013**, *117*, PMID: 23844833, 15346–15355.

(9) Kukura, P.; McCamant, D. W.; Yoon, S.; Wandschneider, D. B.; Mathies, R. A. *Science* **2005**, *310*, 1006–1009.

(10) Park, M.; Kim, C. H.; Joo, T. *The Journal of Physical Chemistry A* **2013**, *117*, 370–377.

(11) Champenois, E. G.; Shivaram, N. H.; Wright, T. W.; Yang, C.-S.; Belkacem, A.; Cryan, J. P. *The Journal of Chemical Physics* **2016**, *144*, 014303.

(12) Harris, D. C.; Bertolucci, M. D., *Symmetry and spectroscopy: an introduction to vibrational and electronic spectroscopy*; Courier Corporation: 1978.

(13) Griffiths, D. J.; Harris, E. G. *American Journal of Physics* **1995**, *63*, 767–768.

(14) Hamm, P. *University of Zurich* **2005**.

(15) Dietze, D. R.; Mathies, R. A. *Chem. Phys. Chem.* **2016**, *17*, 1224–1251.

(16) Hoffman, D. P. Molecular Choreography of Isomerization and Electron Transfer Using One and Two Dimensional Femtosecond Stimulated Raman Spectroscopy., Ph.D. Thesis, University of California, Berkeley, 2014.

(17) Creelman, M. R. Time Resolved Structural Studies of Photochemical Processes Using Resonance Raman., Ph.D. Thesis, University of California, Berkeley, 2013.

(18) A., T. Lecture Notes: Introductory Quantum Mechanics II: Diagramatic Perturbation Theory., https://ocw.mit.edu/courses/chemistry/, (accessed Oct 22, 2017).

(19) Myers, A. B. *Chemical Physics* **1994**, *180*, 215–230.

(20) Strickler, S. J.; Berg, R. A. *The Journal of Chemical Physics* **1962**, *37*, 814–822.

(21) Ziegler, L. D.; Hudson, B. S. *The Journal of Chemical Physics* **1983**, *79*, 1197–1202.

(22) Imre, D.; Kinsey, J. L.; Sinha, A.; Krenos, J. *The Journal of Physical Chemistry* **1984**, *88*, 3956–3964.

(23) Stuart, C. M.; Frontiera, R. R.; Mathies, R. A. *The Journal of Physical Chemistry A* **2007**, *111*, PMID: 17985852, 12072–12080.

(24) Hoffman, D. P.; Ellis, S. R.; Mathies, R. A. *The Journal of Physical Chemistry A* **2013**, *117*, PMID: 24138073, 11472–11478.

(25) Myers, A. B.; Pranata, K. S. *The Journal of Physical Chemistry* **1989**, *93*, 5079–5087.

(26) Kulinowski, K.; Gould, I. R.; Myers, A. B. *J. Phys. Chem.* **1995**, *99*, 9017.

(27) Asher, S. A. *Analytical chemistry* **1984**, *56*, 720–724.

(28) Musser, A. J.; Liebel, M.; Schnedermann, C.; Wende, T.; Kehoe, T. B.; Rao, A.; Kukura, P. *Nat Phys* **2015**, *11*, 352–357.

(29) Ohta, N.; Ito, M. *Chem. Phys.* **1977**, *20*, 71–81.

(30) Yamakita, Y.; Kimura, J.; Ohno, K. *J. Chem. Phys.* **2007**, *126*, 064904–1.

(31) Bree, A.; Lyons, L. E. *J. Chem. Soc.* **1957**, *26*, 5206–5212.

(32) Rumelfanger, R.; Asher, S. A.; B, M. P. *Applied Spectroscopy*, *42*, 267–272.

(33) Peteanu, L. A.; Schoenlein, R. W.; Wang, Q.; Mathies, R. A.; Shank, C. V. *Proceedings of the National Academy of Sciences* **1993**, *90*, 11762–11766.

(34) Hoffman, D. P.; Mathies, R. A. *Phys. Chem. Chem. Phys.* **2012**, *14*, 6298.

(35) Lambert, A. G.; Davies, P. B.; Neivandt, D. J. *Applied Spectroscopy Reviews* **2005**, *40*, 103–145.

(36) *Hyper-Raman Spectroscopy*; John Wiley & Sons, Ltd: 2006.

(37) Klessinger, M.; Michl, J., *Excited States and Photochemistry of Organic Molecules*; VCH: New York, 1995.

(38) Domcke, W.; Yarkony, D.; Köppel, H. E., *Conical Intersections: Electronic Structure, Dynamics and Spectroscopy*; World Scientific: River Edge, NJ, 2004.

(39) Rosspeintner, A.; Lang, B.; Vauthey, E. *Annu. Rev. Phys. Chem.* **2013**, *64*, 247.

(40) Thompson, B. C.; Fréchet, J. M. J. *Angew. Chem., Int. Ed.* **2008**, *47*, 58.

(41) McHale, J. L.; Merriam, M. J. *J. Phys. Chem.* **1989**, *93*, 526.

(42) Britt, B. M.; McHale, J. L.; Friedrich, D. M. *J. Phys. Chem.* **1995**, *99*, 6347.

(43) Myers, A. B. *Chem. Rev.* **1996**, *96*, 911.

(44) Wynne, K.; Galli, C.; Hochstrasser, R. M. *J. Chem. Phys.* **1994**, *100*, 4797.

(45) Rubtsov, I. V.; Yoshihara, K. *J. Phys. Chem. A* **1999**, *103*, 10202.

(46) Chiu, C.-C.; Hung, C.-C.; Chen, C.-L.; Cheng, P.-Y. *J. Phys. Chem. B* **2013**, *117*, 9734.

(47) Cina, J. A.; Kovac, P. A. *J. Phys. Chem. A* **2013**, *117*, 6084.

(48) Fingerhut, B. P.; Dorfman, K. E.; Mukamel, S. *J. Chem. Theory Comput.* **2014**, *10*, 1172.

(49) Fang, C.; Frontiera, R. R.; Tran, R.; Mathies, R. A. *Nature* **2009**, *462*, 200.

(50) Rhinehart, J. M.; Challa, J. R.; McCamant, D. W. *J. Phys. Chem. B* **2012**, *116*, 10522.

(51) Fujisawa, T.; Creelman, M.; Mathies, R. A. *J. Phys. Chem. B* **2012**, *116*, 10453.

(52) Kukura, P.; McCamant, D. W.; Mathies, R. A. *Annu. Rev. Phys. Chem.* **2007**, *58*, 461.

(53) Weigel, A.; Ernsting, N. P. *J. Phys. Chem. B* **2010**, *114*, 7879.

(54) Weigel, A.; Dobryakov, A.; Klaumünzer, B.; Sajadi, M.; Saalfrank, P.; Ernsting, N. P. *J. Phys. Chem. B* **2011**, *115*, 3656.

(55) Wilson, K. C.; Lyons, B.; Mehlenbacher, R.; Sabatini, R.; McCamant, D. W. *J. Chem. Phys.* **2009**, *131*, 214502.

(56) Dunlap, B.; Wilson, K. C.; McCamant, D. W. *J. Phys. Chem. A* **2013**, *117*, 6205.

(57) Mehlenbacher, R. D.; Lyons, B.; Wilson, K. C.; Du, Y.; McCamant, D. W. *J. Chem. Phys.* **2009**, *131*, 244512.

(58) Sun, Z.; Lu, J.; Zhang, D. H.; Lee, S.-Y. *J. Chem. Phys.* **2008**, *128*, 144114.

(59) Zhao, B.; Sun, Z.; Lee, S.-Y. *J. Chem. Phys.* **2011**, *134*, 024307.

(60) Webster, O.; Mahler, W.; Benson, R. *J. Org. Chem.* **1960**, *25*, 1470.

(61) McCamant, D. W.; Kukura, P.; Yoon, S.; Mathies, R. A. *Rev. Sci. Instrum.* **2004**, *75*, 4971.

(62) Hoffman, D. P. FSRS-LabVIEW., https://github.com/david-hoffman/FSRS-LabVIEW, (accessed Jul 15, 2013).

(63) Tufts, D.; Kumaresan, R. *IEEE Trans. Acoust. Speech Signal Process.* **1982**, *30*, 671.

(64) Barkhuijsen, H.; de Beer, R.; Bovée, W. M. M. J.; van Ormondt, D. *J. Magn. Reson. 1969* **1985**, *61*, 465.

(65) Barkhuijsen, H.; de Beer, R.; van Ormondt, D. *J. Magn. Reson. 1969* **1986**, *67*, 371.

(66) Hoffman, D. P. Igor-Data-Analysis., https://github.com/david-hoffman/Igor-Data-Analysis, (accessed Jul 15, 2013).

(67) Benesi, H. A.; Hildebrand, J. H. *J. Am. Chem. Soc.* **1949**, *71*, 2703.

(68) Jeanmaire, D. L.; Van Duyne, R. P. *J. Am. Chem. Soc.* **1976**, *98*, 4029.

(69) Frisch, M. J.; Trucks, G. W.; Schlegel, H. B.; Scuseria, G. E.; Robb, M. A.; Cheeseman, J. R.; Scalmani, G.; Barone, V.; Mennucci, B.; Petersson, G. A., *Gaussian 09 Revision C.01*; Gaussian Inc.: Wallingford, CT, 2009.

(70) Horng, M. L.; Gardecki, J. A.; Papazyan, A.; Maroncelli, M. *J. Phys. Chem.* **1995**, *99*, 17311.

(71) Pollard, W. T.; Mathies, R. A. *Annu. Rev. Phys. Chem.* **1992**, *43*, 497.

(72) Girlando, A.; Pecile, C. *Spectrochim. Acta: Mol. Spectrosc.* **1973**, *29*, 1859.

(73) Khatkale, M. S.; Devlin, J. P. *J. Chem. Phys.* **1979**, *70*, 1851.

(74) Pawlukojć, A.; Natkaniec, I.; Bator, G.; Sobczyk, L.; Grech, E.; Nowicka-Scheibe, J. *Spectrochim. Acta, A: Mol. Biomol. Spectrosc.* **2006**, *63*, 766.

(75) McCamant, D. W.; Kukura, P.; Mathies, R. A. *J. Phys. Chem. B* **2005**, *109*, 10449.

(76) Niu, K.; Zhao, B.; Sun, Z.; Lee, S.-Y. *J. Chem. Phys.* **2010**, *132*, 084510.

(77) Patuwo, M. Y.; Lee, S.-Y. *J. Chem. Phys.* **2013**, *139*, 234101.

(78) Zhang, Y.; Improta, R.; Kohler, B. *Phys. Chem. Chem. Phys.* **2014**, *16*, 1487.

(79) Heider, N.; Fischer, S. F. *Chem. Phys.* **1984**, *88*, 209.

(80) Frontiera, R. R.; Shim, S.; Mathies, R. A. *The Journal of Chemical Physics* **2008**, *129*, 064507.

(81) Qiu, X.; Li, X.; Niu, K.; Lee, S.-Y. *The Journal of Chemical Physics* **2011**, *135*, 164502.

(82) Dobryakov, A. L.; Quick, M.; Ioffe, I. N.; Granovsky, A. A.; Ernsting, N. P.; Kovalenko, S. A. *The Journal of Chemical Physics* **2014**, *140*, 184310.

(83) Batignani, G.; Pontecorvo, E.; Giovannetti, G.; Ferrante C Fumero, G.; Scopigno, T.

(84) Fumero, G.; Batignani, G.; Dorfman, K. E.; Mukamel, S.; Scopigno, T. *ChemPhysChem* **2015**, *16*, 3438–3443.

(85) Kivala, M.; Boudon, C.; Gisselbrecht, J.-P.; Enko, B.; Seiler, P.; Müller, I.; Langer, N.; Jarowski, P.; Gescheidt, G.; Diederich, F. *Chemistry - A European Journal* **2009**, *15*, 4111–4123.

(86) Jeanmaire, D. L.; Suchanski, M. R.; Van Duyne, R. P. *J. Am. Chem. Soc.* **1975**, *97*, 1699–1707.

(87) Gould, I. R.; Ege, D.; Moser, J. E.; Farid, S. *Journal of the American Chemical Society* **1990**, *112*, 4290–4301.

(88) Frey, J. E.; Andrews, A. M.; Combs, S. D.; Edens, S. P.; Puckett, J. J.; Seagle, R. E.; Torreano, L. A. **1992**, 6460–6466.

(89) Jiwan, J. H.; Soumillion, J. P. *The Journal of Physical Chemistry* **1995**, *99*, 14223–14230.

(90) Marcus, R. A. *The Journal of Chemical Physics* **1956**, *24*, 966–978.

(91) Closs, G.; Calcaterra, L.; Green, N.; Penfield, K.; Miller, J. *The Journal of Physical Chemistry* **1986**, *90*, 3673–3683.

(92) Wynne, K.; Reid, G. D.; Hochstrasser, R. M. **1996**, *105*, 2287–2297.

(93) Rubtsov, I. V.; Yoshihara, K. **1997**, *5639*, 6138–6140.

(94) Kim, S. Y.; Kim, C. H.; Park, M.; Ko, K. C.; Lee, J. Y.; Joo, T. *The Journal of Physical Chemistry Letters* **2012**, *3*, 2761–2766.

(95) Song, Y.; Clafton, S. N.; Pensack, R. D.; Kee, T. W.; Scholes, G. D. **2014**, *5*, 4933.

(96) Hayashi, M.; Yang, T.-S.; Yu, J.; Mebel, A.; Lin, S. H. *The Journal of Physical Chemistry A* **1997**, *101*, 4156–4162.

(97) Rossi, M.; Haselbach, E. *Helvetica Chimica Acta* **1979**, *62*, 140–151.

(98) Michiya, I. *Bulletin of the Chemical Society of Japan* **1972**, *45*, 1947–1950.

(99) Hinkel, J. J.; Devlin, J. P. **1973**, *4750*.

(100) Lee, S.-Y.; Zhang, D.; McCamant, D. W.; Kukura, P.; Mathies, R. A. *The Journal of Chemical Physics* **2004**, *121*, 3632–3642.

(101) Wilson, K. C.; Lyons, B.; Mehlenbacher, R.; Sabatini, R.; McCamant, D. W. *The Journal of Chemical Physics* **2009**, *131*, 214502.

(102) Liu, W.; Tang, L.; Oscar, B. G.; Wang, Y.; Chen, C.; Fang, C. *The Journal of Physical Chemistry Letters* **2017**, *8*, PMID: 28195486, 997–1003.

(103) Quick, M.; Dobryakov, A. L.; Kovalenko, S. A.; Ernsting, N. P. *The Journal of Physical Chemistry Letters* **2015**, *6*, PMID: 26262974, 1216–1220.

(104) Hoffman, D. P.; Mathies, R. A. *Accounts of Chemical Research* **2016**, *49*, PMID: 27003235, 616–625.

(105) Itoh, M. **1970**, *3678*, 886–889.

(106) Phillips, W. D.; Phillips, W. D. **1958**, *2703*, 2778–2782.

(107) Hoffman, D. P.; Ellis, S. R.; Mathies, R. A. *The Journal of Physical Chemistry A* **2014**, *118*, 4955–4965.

(108) Eom, I.; Park, S.; Han, H.-S.; Yee, K.-J.; Baik, S.-H.; Jeong, D.-Y.; Joo, T.; Lim, Y.-S. *Nano Letters* **2012**, *12*, 769–773.

(109) Izumi, I.; Atsushi, Y.; Takayoshi, K. *Bulletin of the Chemical Society of Japan* **2011**, *84*, 164–171.

(110) Shimada, R.; Kano, H.; Hamaguchi, H.-O. *Journal of Raman Spectroscopy* **2006**, *37*, 469–471.

(111) Shimada, R.; Kano, H.; Hamaguchi, H.-o. *The Journal of Chemical Physics* **2008**, *129*, 024505.

(112) Abraham, B.; Nieto-Pescador, J.; Gundlach, L. *The Journal of Physical Chemistry Letters* **2016**, *7*, PMID: 27482847, 3151–3156.

(113) Hunger, J.; Stoppa, A.; Thoman, A.; Walther, M.; Buchner, R. *Chemical Physics Letters* **2009**, *471*, 85–91.

(114) Schnedermann, C.; Muders, V.; Ehrenberg, D.; Schlesinger, R.; Kukura, P.; Heberle, J. *Journal of the American Chemical Society* **2016**, *138*, PMID: 26999496, 4757–4762.

(115) Casado, J.; Burrezo, P. M.; Ramírez, F. J.; Navarrete, J. T. L.; Lapidus, S. H.; Stephens, P. W.; Vo, H.-L.; Miller, J. S.; Mota, F.; Novoa, J. J. *Angewandte Chemie International Edition* **2013**, *52*, 6421–6425.

(116) Valley, D. T.; Hoffman, D. P.; Mathies, R. A. *Physical Chemistry Chemical Physics* **2015**, *17*, 9231–9240.

(117) Von Benten, R. S.; Liu, Y.; Abel, B. *The Journal of Physical Chemistry A* **2010**, *114*, PMID: 20931954, 11522–11528.

(118) Lynch, M. S.; Van Kuiken, B. E.; Daifuku, S. L.; Khalil, M. *The Journal of Physical Chemistry Letters* **2011**, *2*, 2252–2257.

(119) Kaufman, L. J.; Heo, J.; Ziegler, L. D.; Fleming, G. R. *Phys. Rev. Lett.* **2002**, *88*, 207402.

(120) Ellis, S. R.; Hoffman, D. P.; Park, M.; Mathies, R. A. *Journal of Physical Chemistry B* **2017**, In Submission.

(121) Sun, Z.; Fu, B.; Zhang, D. H.; Lee, S.-Y. *The Journal of Chemical Physics* **2009**, *130*, 044312.

(122) Eldridge, J.; Lin, Y.; Mayadunne, T.; Montgomery, L.; Kaganov, S.; Miebach, T. *Solid State Communications* **1998**, *105*, 427–431.

(123) McCamant, D. W. *The Journal of Physical Chemistry B* **2011**, *115*, PMID: 21650454, 9299–9305.

(124) Smith, M. B.; Michl, J. *Annu. Rev. Phys. Chem.* **2013**, *64*, 361–386.

(125) Bakulin, A. A.; Morgan, S. E.; Kehoe, T. B.; Wilson, M. W. B.; Chin, A. W.; Zigmantas, D.; Egorova, D.; Rao, A. *Nat. Chem.* **2015**, *8*, 16–23.

(126) West, B. A.; Womick, J. M.; McNeil, L. E.; Tan, K. J.; Moran, A. M. *J. Phys. Chem. C* **2010**, *114*, 10580–10591.

(127) Zimmerman, P. M.; Bell, F.; Casanova, D.; Head-Gordon, M. *J. Am. Chem. Soc.* **2011**, *133*, 19944–19952.

(128) Chien, C.-T.; Lin, C.-C.; Watanabe, M.; Lin, Y.-D.; Chao, T.-H.; Chiang, T.-c.; Huang, X.-H.; Wen, Y.-S.; Tu, C.-H.; Sun, C.-H.; Chow, T. J. *J. Mater. Chem.* **2012**, *22*, 13070–13075.

(129) Birech, Z.; Schwoerer, M.; Schmeiler, T.; Pflaum, J.; Schwoerer, H. *J. Chem. Phys.* **2014**, *140*, 114501.

(130) Thorsmølle, V. K.; Averitt, R. D.; Demsar, J.; Smith, D. L.; Tretiak, S.; Martin, R. L.; Chi, X.; Crone, B. K.; Ramirez, A. P.; Taylor, A. J. *Phys. Rev. Lett.* **2009**, *102*, 017401.

(131) Burdett, J. J.; Müller, A. M.; Gosztola, D.; Bardeen, C. J. *J. Chem. Phys.* **2010**, *133*, 144506.

(132) Merrifield, R.; Avakian, P.; Groff, R. *Chem. Phys. Lett.* **1969**, *3*, 386–388.

(133) McGlynn, S. P.; Azumi, T.; Kasha, M. *J. Chem. Phys.* **1964**, *40*, 507–515.

(134) Mitsui, M.; Ando, N.; Nakajima, A. *J. Phys. Chem. A* **2007**, *111*, 9644–9648.

(135) Wilson, M. W. B.; Rao, A.; Johnson, K.; Gélinas, S.; di Pietro, R.; Clark, J.; Friend, R. H. *J. Am. Chem. Soc.* **2013**, *135*, 16680–16688.

(136) Piland, G. B.; Bardeen, C. J. *J. Phys. Chem. Lett.* **2015**, *6*, 1841–1846.

(137) Reineke, S.; Baldo, M. a. *Sci. Rep.* **2014**, *4*, 3797.

(138) Burdett, J. J.; Bardeen, C. J. *J. Am. Chem. Soc.* **2012**, *134*, 8597–8607.

(139) Kukk, P.; Freiberg, A. *J. Chem. Phys.* **1992**, *97*, 118.

(140) Amirav, A. *J. Chem. Phys.* **1981**, *75*, 3770.

(141) Sidorov, A. N.; Aleksandrov, I. V.; Bobovich, Y. S. **1975**, *I*, 418–420.

(142) Alajtal, A. I.; Edwards, H. G. M.; Elbagerma, M. A.; Scowen, I. J. *Spectrochim. Acta Part A Mol. Biomol. Spectrosc.* **2010**, *76*, 1–5.

(143) Venuti, E.; Della Valle, R. G.; Farina, L.; Brillante, A.; Masino, M.; Girlando, A. *Phys. Rev. B* **2004**, *70*, 1–8.

(144) Weinberg-Wolf, J. R.; McNeil, L. E.; Liu, S.; Kloc, C. *J. Phys.* **2007**, *19*, 276204.

(145) Puschnig, P.; Meisenbichler, C.; Draxl, C. *arXiv:1306.3790 [cond-mat.mtrl-sci]* **2013**.

(146) Grumstrup, E. M.; Johnson, J. C.; Damrauer, N. H. *Phys. Rev. Lett.* **2010**, *105*, 1–4.

(147) Tavazzi, S.; Raimondo, L.; Silvestri, L.; Spearman, P.; Camposeo, A.; Polo, M.; Pisignano, D. *J. Chem. Phys.* **2008**, *128*, 154709.

(148) Davydov, A. S. *Sov. Phys. Uspekhi* **1964**, *7*, 145.

(149) Roth, F.; Mahns, B.; Hampel, S.; Nohr, M.; Berger, H.; Büchner, B.; Knupfer, M. *Eur. Phys. J. B* **2013**, *86*, 66.

(150) Ambrosch-Draxl, C.; Nabok, D.; Puschnig, P.; Meisenbichler, C. *New J. Phys.* **2009**, *11*, 125010.

(151) Rangel, T.; Berland, K.; Sharifzadeh, S.; Brown-Altvater, F.; Lee, K.; Hyldgaard, P.; Kronik, L.; Neaton, J. B. *Phys. Rev. B* **2016**, *Submitted.*

(152) Brown-Altvater, F.; Rangel, T.; Neaton, J. B. *Phys. Rev. B* **2016**.

(153) Fedorov, I. A.; Marsusi, F.; Fedorova, T. P.; Zhuravlev, Y. N. *J. Phys. Chem. Solids* **2015**, *83*, 24–31.

(154) Kronik, L.; Neaton, J. B. **2016**, DOI: 10.1146/annurev-physchem-040214-121351.

(155) Tiago, M. L.; Northrup, J. E.; Louie, S. G. **2003**, 1–6.

(156) Sharifzadeh, S.; Biller, A.; Kronik, L.; Neaton, J. B. *Phys. Rev. B* **2012**, *85*, 125307.

(157) Cudazzo, P.; Sottile, F.; Rubio, A.; Gatti, M. *J. Phys.* **2015**, *27*, 113204.

(158) Kim, H. Y.; Bjorklund, T. G.; Lim, S.-H.; Bardeen, C. J. *Langmuir* **2003**, *19*, 3941–3946.

(159) Shim, S.; Mathies, R. A. *J. Phys. Chem. B* **2008**, *112*, 4826–4832.

(160) Colles, M. J. *J. Chem. Phys.* **1972**, *56*, 3384.

(161) Dudik, J. M.; Johnson, C. R.; Asher, S. A. *J. Chem. Phys.* **1985**, *82*, 1732–1740.

(162) Lee, S.-Y.; Heller, E. J. *J. Chem. Phys.* **1979**, *71*, 4777–4788.

(163) Perdew, J. P.; Burke, K.; Ernzerhof, M. *Phys. Rev. Lett.* **1996**, *77*, 3865–3868.

(164) Gonze et al., X. *Comput. Phys. Commun.* **2016**, *205*, 106–131.

(165) Campbell, R. B.; Robertson, J. M.; Trotter, J. *Acta Crystallogr.* **1962**, *15*, 289–290.

(166) *Comput. Phys. Commun.* **2012**, *183*, 1269–1289.

(167) Hybertsen, M. S.; Louie, S. G. *Phys. Rev. B* **1986**, *34*, 5390–5413.

(168) Shao, M.; Da Jornada, F. H.; Yang, C.; Deslippe, J.; Louie, S. G. *Linear Algebra Appl.* **2016**, *488*, 148–167.

(169) Giannozzi, P.; Baroni, S.; Bonini, N.; Calandra, M.; Car, R.; Al., E. *J. Phys.* **2009**, *21*, 395502.

(170) Berland, K.; Hyldgaard, P. *Phys. Rev. B* **2014**, *89*, 35412.

(171) Perdew, J. P.; Ruzsinszky, A.; Csonka, G. I.; Vydrov, O. A.; Scuseria, G. E.; Constantin, L. A.; Zhou, X.; Burke, K. *Phys. Rev. Lett.* **2008**, *100*, 136406.

(172) Petrenko, T.; Krylova, O.; Neese, F.; Sokolowski, M. *New J. Phys.* **2009**, *11*, 015001.

(173) Spano, F. C. *The Journal of Chemical Physics* **2004**, *120*, 7643–7658.

(174) He, R.; Tassi, N. G.; Blanchet, G. B.; Pinczuk, A. *Phys. Rev. B - Condens. Matter Mater. Phys.* **2011**, *83*, 1–6.

(175) Giblin, J.; Kuno, M. *J. Phys. Chem. Lett.* **2010**, *1*, 3340–3348.

(176) Jankowiak, R.; Kalinowski, J.; Konys, M.; Buchert, J. *Chem. Phys.* **1979**, *65*.

(177) Köhler, A.; Bässler, H. *Mater. Sci. Eng. R Reports* **2009**, *66*, 71–109.

(178) Lim, S.-H.; Bjorklund, T. G.; Spano, F. C.; Bardeen, C. J. *Phys. Rev. Lett.* **2004**, *92*, 107402.

(179) Camposeo, A.; Polo, M.; Tavazzi, S.; Silvestri, L.; Spearman, P.; Cingolani, R.; Pisignano, D. *Phys. Rev. B* **2010**, *81*, 33306.

(180) Kasha, B. Y. M. *Discuss. Faraday Soc.* **1950**, *9*, 14–19.

(181) Irkhin, P.; Ryasnyanskiy, A.; Koehler, M.; Biaggio, I. *Phys. Rev. B* **2012**, *86*, 1–13.

(182) Smith, M. B.; Michl, J. *Chem. Rev.* **2010**, *110*, 6891–6936.

(183) Takeuchi, S.; and Tahei Tahara* *J. Phys. Chem. A* **2005**, *109*, 10199–10207.

(184) Grancini, G.; Maiuri, M.; Fazzi, D.; Petrozza, a.; Egelhaaf, H.-J.; Brida, D.; Cerullo, G.; Lanzani, G.; Binda, M.; Criante, L.; Perissinotto, S. *Nat. Mater.* **2012**, *11*, 1–5.

(185) Monahan, N. R.; Sun, D.; Tamura, H.; Williams, K. W.; Xu, B.; Zhong, Y.; Kumar, B.; Nuckolls, C.; Harutyunyan, A. R.; Chen, G.; Dai, H.-L.; Beljonne, D.; Rao, Y.; Zhu, X.-Y. *Nat. Chem.* **2016**, *9*, 341–346.

(186) Arnold, C.; Vendrell, O.; Santra, R. *Phys. Rev. A - At. Mol. Opt. Phys.* **2017**, *95*, 1–7.

(187) Vacher, M.; Bearpark, M. J.; Robb, M. A.; Malhado, J. P. *Phys. Rev. Lett.* **2017**, *118*, 1–5.

(188) Müller, A. M.; Avlasevich, Y. S.; Schoeller, W. W.; Müllen, K.; Bardeen, C. J. *J. Am. Chem. Soc.* **2007**, *129*, 14240–14250.

(189) Leng, W.; Wu, F.; Kelley, A. M. **2004**, 10284–10294.

(190) Rosen, M.; Kuno, M.; Nirmal, M.; Norris, D. J.; Bawendi, M. **1996**, *54*, 4843–4856.

(191) Kwiatkowski, J. J.; Nelson, J.; Li, H.; Bredas, J. L.; Wenzel, W.; Lennartz, C. *Phys. Chem. Chem. Phys.* **2008**, *10*, 1852–1858.

(192) Ashfold, M. N. R.; Cronin, B.; Devine, A. L.; Dixon, R. N.; Nix, M. G. D. *Science* **2006**, *312*, 1637–1640.

(193) Nijegorodov, N.; Ramachandran, V. *Spectrochim. Acta Part A* **1997**, *53*, 1813–1824.

(194) Coropceanu, V.; Malagoli, M.; Gruhn, N. E.; Bill, T. G.; Bre, J. L. **2002**, 1–4.

(195) Duhm, S.; Xin, Q.; Hosoumi, S.; Fukagawa, H.; Sato, K.; Ueno, N.; Kera, S. *Adv. Mater.* **2012**, *24*, 901–905.

(196) Fulton, R. L.; Gouterman, M. *The Journal of Chemical Physics* **1964**, *41*, 2280–2286.

(197) Kelley, A. M. *The Journal of Chemical Physics* **2003**, *119*, 3320–3331.

(198) Kittel, C., *Introduction to Solid State Phyics*, 7th ed.; John Wiley & Sons: 1996, p 297.

(199) Han, N.; Liu, C.; Zhao, Z.; Zhang, J.; Xie, J.; Han, J.; Zhao, X.; Jiang, Y. *International Journal of Applied Glass Science* **2015**, *6*, 339–344.

(200) Madelung, O., *Semiconductors: Data Handbook*, 3rd ed.; Springer-Verlag: New York, 2004, pp 226–230.

(201) Ekimov, A. I.; Hache, F.; Ricard, D.; Flytzanis, C.; Polytechnique, E.; Minchen, T. U. *J. Opt. Soc. Am. B* **1993**, *10*, 100–107.

(202) Kelley, A. M.; Dai, Q.; Jiang, Z.-j.; Baker, J. A.; Kelley, D. F. *Chem. Phys.* **2013**, *422*, 272–276.

(203) Baker, J. A.; Kelley, D. F.; Kelley, A. M.; Baker, J. A.; Kelley, D. F.; Myers, A. **2013**, *024702*, DOI: 10.1063/1.4812499.

(204) Widulle, F.; Kramp, S.; Pyka, N. M.; Go, A.; Ruf, T.; Debernardi, A.; Lauck, R.; Cardona, M. **1999**, *264*, 448–451.

(205) Reynolds, D. C.; Litton, C. W.; Collins, T. C. **1967**, *156*, 881–889.

(206) Ferne, M. J.; Littleton, B. N.; Cooper, S.; Rubinsztein-dunlop, H.; Mulvaney, P. **2008**, 1878–1884.

(207) Woggon, U.; Gindele, F.; Wind, O.; Klingshirn, C. **1996**, *54*, 1506–1509.

(208) Ferrari, A. C.; Meyer, J. C.; Scardaci, V.; Casiraghi, C.; Lazzeri, M.; Mauri, F.; Piscanec, S.; Jiang, D.; Novoselov, K. S.; Roth, S.; Geim, A. K. **2006**, *187401*, 1–4.

(209) Gust, D.; Moore, T. A.; Moore, A. L. *Acc. Chem. Res.* **2001**, *34*, 40.

(210) Fukuzumi, S.; Honda, T.; Kojima, T. *Coord. Chem. Rev.* **2012**, *256*, 2488.

(211) Kurreck, H.; Huber, M. *Angew. Chem., Int. Ed. Engl.* **1995**, *34*, 849.

(212) Ito, O.; D'Souza, F. *Molecules* **2012**, *17*, 5816.

(213) D'Souza, F.; Ito, O. *Coord. Chem. Rev.* **2005**, *249*, 1410.

(214) (a) Yang, C.; Mori, T.; Wada, T.; Inoue, Y.; New, J. *Chem.* **2007**, *31*, 697; (b) Wu, S.; Luo, Y.; Zeng, F.; Chen, J.; Chen, Y.; Tong, Z. *Angew. Chem., Int. Ed.* **2007**, *46*, 7015; (c) Fukuhara, G.; Mori, T.; Wada, T.; Inoue, Y. *Chem. Commun.* **2006**, 1712.

(215) (a) Jagadesan, P.; Mondal, B.; Parthasarathy, A.; Rao, V. J.; Ramamurthy, V. *Org. Lett.* **2013**, *15*, 1326; (b) Porel, M.; Jockusch, S.; Parthasarathy, A.; Rao, V. J.; Turro, N. J.; Ramamurthy, V. *Chem. Commun.* **2012**, *48*, 2710; (c) Porel, M.; Chuang, C.-. H.; Burda, C.; Ramamurthy, V. *J. Am. Chem. Soc.* **2012**, *134*, 14718.

(216) Hitosugi, S.; Ohkubo, K.; Iizuka, R.; Kawashima, Y.; Nakamura, K.; Sato, S.; Kono, H.; Fukuzumi, S.; Isobe, H. *Org. Lett.* **2014**, *16*, 3352.

(217) (a) Furutani, Y.; Kandori, H.; Kawano, M.; Nakabayashi, K.; Yoshizawa, M.; Fujita, M. *J. Am. Chem. Soc.* **2009**, *131*, 4764; (b) Yamaguchi, T.; Fujita, M. *Angew. Chem., Int. Ed.* **2008**, *47*, 2067; (c) Yoshizawa, M.; Miyagi, S.; Kawano, M.; Ishiguro, K.; Fujita, M. *J. Am. Chem. Soc.* **2004**, *126*, 9172.

(218) (a) Caulder, D. L.; Powers, R. E.; Parac, T. N.; Raymond, K. N. *Angew. Chem., Int. Ed.* **1998**, *37*, 1840; (b) Caulder, D. L.; Raymond, K. N. *J. Chem. Soc., Dalton Trans.* **1999**, 1185.

(219) (a) Lee, G. A.; Israel, S. H. *J. Org. Chem.* **1983**, *48*, 4557; (b) Takuwa, A.; Kanaue, T.; Yamashita, K.; Nishigaichi, Y. *J. Chem. Soc., Perkin Trans. 1* **1998**, 1309.

(220) Parac, T. N.; Caulder, D. L.; Raymond, K. N. *J. Am. Chem. Soc.* **1998**, *120*, 8003.

(221) Steiner, G.; Munschauer, R.; Klebe, G.; Siggel, L. *Heterocycles* **1995**, *40*, 319.

(222) Davis, A. V.; Fiedler, D.; Seeber, G.; Zahl, A.; van Eldik, R.; Raymond, K. N. *J. Am. Chem. Soc.* **2006**, *128*, 1324.

(223) Pluth, M. D. M.; Bergman, R. G. R.; Raymond, K. N. K. *Science* **2007**, *316*, 85.

(224) Sgarlata, C.; Mugridge, J. S.; Pluth, M. D.; Tiedemann, B. E. F.; Zito, V.; Arena, G.; Raymond, K. N. *J. Am. Chem. Soc.* **2010**, *132*, 1005.

(225) Hart-Cooper, W. M. W.; Clary, K. N.; Toste, F. D.; Bergman, R. G. R.; Raymond, K. N. K. *J. Am. Chem. Soc.* **2012**, *134*, 17873.

(226) (a) Brown, C. J.; Bergman, R. G.; Raymond, K. N. *J. Am. Chem. Soc.* **2009**, *131*, 17530; (b) Hastings, C. J.; Fiedler, D.; Bergman, R. G.; Raymond, K. N. *J. Am. Chem. Soc.* **2008**, *130*, 10977; (c) Fiedler, D.; Bergman, R. G.; Raymond, K. N. *Angew. Chem., Int. Ed.* **2004**, *43*, 6748.

(227) Wagner, P. J.; Kemppainen, A. E. *J. Am. Chem. Soc.* **1972**, *94*, 7495.

(228) Turro, N. J.; Ramamurthy, V.; Scaiano, J. C., *Modern Molecular Photochemistry of Organic Molecules*; University Science Books: Sausalito, California, 2010.

(229) Jarzeba, W.; Walker, G. C.; Johnson, A. E.; Kahlow, M. A.; Barbara, P. F. *J. Phys. Chem.* **1988**, *92*, 7039–7041.

(230) (a) Langhals, H.; Esterbauer, A. J.; Walter, A.; Riedle, E.; Pugliesi, I. *J. Am. Chem. Soc.* **2010**, *132*, 16777; (b) Hwang, I.-W. *J. Photochem. Photobiol., A* **2006**, *178*, 130.

(231) Köstler, S.; Rudorfer, A.; Haase, A.; Satzinger, V.; Jakopic, G.; Ribitsch, V. *Adv. Mater.* **2009**, *21*, 2505–2510.

(232) Morisaki, H.; Koretsune, T.; Hotta, C.; Takeya, J.; Kimura, T.; Wakabayashi, Y. *Nat Commun* **2014**, *5*.

(233) Warshel, A.; Dauber, P. *J. Chem. Phys.* **1977**, *66*.

(234) Grebner, D.; Helbig, M.; Rentsch, S. *J. Chem. Phys.* **1995**, *99*, 16991–16998.

(235) Winston, M. S.; Wolf, W. J.; Toste, F. D. *J. Am. Chem. Soc.* **2014**, *136*, 7777–7782.

(236) Creelman, M.; Kumauchi, M.; Hoff, W. D.; Mathies, R. A. *J. Phys. Chem. B* **2014**, *118*, 659–667.

(237) Press, W. H.; Teukolsky, S. A.; Vetterling, W. T., *Numerical Recipes in C: The Art of Scientific Computing, 2*; Cambridge University Press: L Cambridge CB2 1TN, 2002.

(238) Lakowicz, J. R., *Fluorescence Anisotropy. Principles of Fluorescence Spectroscopy, 2*; Plenum Publishers: ew York, NY, 1999.

(239) A., L. D., *The Raman Effect: A Unified Treatment of the Theory of Raman Scattering by Molecules*; John Wiley & Sons Ltd: West Sussex PO19 IUD, England, 2002.

(240) R., S., *Principals of Quantum Mechanics*; Springer US: 1994.

(241) G, P., *Handbuch der Radiologie: Rayleigh-Streuung und Raman Effekt*; Academische Verlag: Leipig, 1934.

(242) J, T.; C., A. A., *Raman Spectroscopy*; Plenum Press: New York, 1970.

(243) Albrecht, A. C. *The Journal of Chemical Physics* **1961**, *34*, 1476–1484.